

Faculty of Engineering

Scalable Microwave Applicators for High-Temperature Processing

Jose Miguel Rodriguez Oyarzun

Thesis submitted to the University of Nottingham for the degree of Doctor of Philosophy

March 2019

Abstract

There have been numerous attempts to develop microwave-based processes for applications including waste treatment, metallurgy and advanced material synthesis. At a laboratory scale improvement in energy efficiency and reduction in the environmental impact for many of these applications has been demonstrated to be potentially significant. Unfortunately, very few if any applications of high-temperature microwave processes, with products reaching more than 250 °C, have ever reached a commercial scale. A multiplicity of factors have hindered such developments including a lack of understanding of microwave-material interactions and their variation during real processing conditions and also lack of consideration of material transport techniques for moving the products through the microwave heating systems and their robustness and scalability to full scale. A clear gap in the development of high-temperature microwave applications has been highlighted, with no or very few, clear scale-up strategies or hardware solutions able to meet the requirements around robustness for continuous operation and ultimately commercial implementation. In this work, three concepts have been developed which have enabled a range of scalable options for microwave applicators that can both underpin proof of concept and full-scale processes, crucially at high temperature. An elliptical cylindrical cavity applicator, a hybrid toroidal fluidised bed, and a metallic conveyor belt system are presented. All of these concepts have been developed to the prototype stage, and the design and performance have been studied by numerical simulation and validated through experimental measurements and cross-platform simulation. The simulation framework was also validated against a number of different processing systems with several test materials evidencing suitability for the design and evaluation of microwave heating systems for high-temperature application.

For liquids and fine powders, and especially when high power densities within the product are required, an elliptical cylindrical cavity provides a stable and practical replacement to more traditional single-mode cavities. Simulated and experimental results showed good agreement with a -10 dB bandwidth of 9 MHz and 8 MHz and quality factors of 198 and 233 respectively. The treatment of waste oils and plastics, as well as the purification of minerals like quartz powders, could be potentially suitable applications for this class of applicator. For particulates from 1 to 20 mm, the hybrid fluidised bed system demonstrates significant potential for use in high-temperature processes, especially for medium to high microwave loss products. Only a 1 MHz difference between experimental and measurement -10 dB bandwidth and practically the same resonant frequency was observed. Potential applications are considered to be the pyrolysis of biomasses, coals and various carbonaceous materials and the reduction of iron ores. The system overcomes particulate size limitations found in conventional fluidised beds as well as reduce microwave field homogeneity issues by thorough mixing of the product without integrated moving parts. For larger particles, greater than 10 mm in size, the metal conveyor belt system provides a suitable candidate for high-throughput processes in which the major limitation is the lack of robustness and microwave compatibility of conveying technology. Similar resonant levels of -32 dB, and 69 MHz and 76 MHz -10 dB bandwidth for the experimental and simulation respectively were produced, with a similar heating behaviour. Envisaged potential applications include coke-making from low ranking coals and the direct reduction of iron.

Further work includes the finalisation of commissioning for experimental use in a variety of applications. The performance of test work that validates the power handling capabilities and robustness of the different systems under a variety of conditions and materials. The implementation of continuous processing strategies in the developed systems to study their engineering performance and commercial prospects.

Dedication

To Claudia, my beloved daughter

Acknowledgements

Firstly, I would like to express my sincere gratitude to my supervisors Professor Sam Kingman and Dr Chris Dodds for the continuous support of my studies, for their patience and encouragement, and for giving me the opportunity to be a part of their team. Their guidance and support has been an essential part of both the research and writing of this thesis.

I would also want to express my special gratitude to my late supervisor, Dr Hector Carrasco, who motivated me to pursue my doctoral studies and, unfortunately, died too young while I was working on it.

My sincere thanks also goes to my research teammates, technical staff and colleagues who have been a crucial part in my work either by support, discussion or companionship.

Beside them, I would like to mention my parents and brothers and the rest of my kin who gave me their love, logistic support and much-appreciated advice from a distance.

Last but not the least, I would like to thank my dear family, Cristina and Claudia, for embarking with me in this adventure, supporting and standing beside me in both the good and bad times.

Index

Abstract ..... **i**

Dedication ..... **iii**

Acknowledgements ..... **iv**

Index ..... **v**

List of figures ..... **x**

List of tables ..... **xxii**

Chapter 1 Introduction **1**

1.1 Aims 5

1.2 Objectives 6

1.3 Contributions 6

1.4 List of publications 7

Chapter 2 Microwave heating fundamentals **8**

2.1 Maxwell's equations and constitutive relations 8

2.2 Electromagnetic power 9

2.3 Electromagnetic properties variability 10

2.4 Scattering parameters 15

2.4.1 Smith chart 18

2.5 Quality factor and resonant frequencies 20

2.6 Dielectric properties characterisation 22

2.6.1 Open-ended probe 22

2.6.2 Cavity perturbation technique 23

2.6.3 Transmission line method 23

2.7 Heating mechanisms 25

2.7.1 Dipolar losses 28

2.7.2 Interfacial losses 28

2.7.3 Conduction losses 28

2.7.4 Magnetic hysteresis 29

2.7.5 Eddy currents 29

2.7.6 Remarks 30

2.8 Heating strategies 30

2.9 Sample shape and electric field orientation influence on heating efficiency 30

2.10 Legal framework 32

2.10.1 Industrial heating frequencies and applications 32

2.10.2 Safety regulations 34

2.11 Microwave processing system 35

2.12 Waveguides 36

2.13 Waveguide cavity resonators 39

2.13.1 Resonance frequency 40
2.14 Main issues in high-temperature microwave systems 41
2.14.1 Penetration depth 41
2.14.2 Arcing 43
2.14.3 Thermal runaway 45
2.14.4 Thermal insulation materials 47
2.14.5 Metrology and control 47
2.15 Microwave heating fundamentals summary 50
2.16 Applicator technologies 51
2.16.1 Radio-frequency (RF) applicator technologies 51
2.16.2 Microwave applicator technologies for heating 53
Chapter 3 High-temperature microwave applications 59
3.1 Waste treatment 59
3.1.1 Waste plastics 60
3.1.2 Automotive industry wastes 65
3.1.3 Biomass 68
3.1.4 Discussion of microwave waste-treatment processes 72
3.2 Ferrous Pyrometallurgy 74
3.2.1 Microwave-material properties 75
3.2.2 Coke-making 76
3.2.3 Iron ore reduction 79
3.3 Sintering of advanced materials 83
3.3.1 Microwave ceramic sintering 84
3.3.2 Powder metallurgy 85
3.3.3 Discussion of microwave sintering of materials 88
3.4 Conclusions 89
Chapter 4 Methods, materials and modelling framework 91
4.1 Measurement of scattering parameters 91
4.2 Measurement of Q-factor 92
4.2.1 Two-port measurement of Q-factor 93
4.2.2 One-port measurement of Q-factor 94
4.3 Power measurements 99
4.3.1 Direct power measurements 99
4.3.2 Average power loss density 99
4.3.3 Power uniformity index 100
4.3.4 Power conversion efficiency 100
4.4 Dielectric measurement methodology 100
4.4.1 Cavity perturbation technique 101
4.4.2 Transmission line technique 103
4.5 Thermal pattern using infrared imaging 104
4.6 Test materials 106
4.6.1 FOAMGLAS® T4 107
4.6.2 Quartz powder 108
4.6.3 Ecoal50 coal briquettes 109
4.6.4 Copper ore 110
4.6.5 Sample support and holder materials 111
4.6.6 Metals 111

4.7 Electromagnetic simulation general framework 111
4.7.1 COMSOL simulation framework 112
4.7.2 Single-mode resonant cavity validation 117
4.7.3 Multimode cavity validation 124
4.7.4 Electromagnetic simulation framework conclusions 126
4.8 Summary 126
Chapter 5 Applicator for liquids and fine powders 127
5.1 Potential applications 129
5.1.1 Waste engine oil treatment 129
5.1.2 Waste plastic pyrolysis and depolymerization 130
5.1.3 Ceramic sintering 131
5.1.4 Quartz powder fracture and purification 131
5.1.5 Mineral ore treatment 132
5.1.6 Discussion on potential applications 132
5.2 Elliptical cavities 132
5.3 Modal analysis and design charts 134
5.4 Cavity design methodology and case study 139
5.4.1 Design requirements for a case study 139
5.4.2 Microwave properties characterisation 140
5.4.3 Material feeding 140
5.4.4 TM elliptical cylinder cavity 143
5.4.5 Cavity selection 150
5.4.6 The microwave feeding 151
5.4.7 Resonant cavity 154
5.4.8 System schematic drawing 154
5.4.9 Results and model validation 155
5.4.10 Heating system 160
5.4.11 System scale-up 162
5.5 Conclusions 173
Chapter 6 Applicator for granular products 175
6.1 Potential applications 178
6.1.1 Fast/flash pyrolysis of waste biomass and coals 178
6.1.2 Direct reduction of iron ore 179
6.2 Reactor design 180
6.2.1 Reactor geometry 182
6.2.2 Microwave feeding 186
6.2.3 Open waveguide radiation alternatives 188
6.2.4 Waveguide slot radiation 189
6.3 Microwave fluidised bed concepts simulation results 197
6.3.1 Waveguide fed 197
6.3.2 Narrow wall slot fed 203
6.3.3 Broad wall slot fed 207
6.3.4 Microwave fluidised bed simulations results summary 212
6.4 Microwave fluidised bed prototype design 213
6.4.1 Prototype and validation 213
6.4.2 Torbed T400 CBRMW reactor 216
6.4.3 Initial heating trials 221
6.5 Microwave fluidised bed system scale-up 222

6.5.1 Effect of bed position variation 225
6.5.2 The increase of reactor diameter 226
6.6 Conclusions 227

Chapter 7 Applicator for large products 229
7.1 Metallic conveyor belts in the literature 230
7.2 Prototype applicator concept 233
7.3 Potential applications 234
7.3.1 Coke-making 234
7.3.2 Direct reduction of iron 236
7.4 Conductive conveyor belt applicator concept and initial design 237
7.4.1 Slotted waveguide feed 238
7.4.2 Field shapers 241
7.4.3 Product load 242
7.4.4 Model simplification 243
7.4.5 Initial results 244
7.4.6 Microwave enclosure 247
7.5 Prototype development 248
7.6 Coupling sensitivity to material property change 250
7.7 Penetration of power and conversion efficiency 251
7.7.1 Product directly over the belt 255
7.7.2 The dielectric interface between product and belt 256
7.8 Transverse uniformity 258
7.9 Cross-coupling in a mirrored setup 259
7.10 Coupling tolerance to change of position 260
7.11 Experimental validation 260
7.12 Scale-up 263
7.13 Conclusions 264

Chapter 8 Conclusions 267
8.1 Design and validation framework 268
8.2 Applicator technology for processing of liquids and fine powders 269
8.3 Applicator technology for processing of granular products 270
8.4 Applicator technology for processing of large granular products 272
8.5 Future work 274
8.5.1 Applicator technology for processing of liquids and fine powders 274
8.5.2 Processing of waste plastics 277
8.5.3 Applicator technology for processing of granular products 278
8.5.4 Applicator technology for processing of large granular products 279

Appendix A – Bessel function roots 281

Appendix B – TM_{010} cavity study 282

Appendix C – DEM simulation 285

Appendix D – Dielectric properties of some materials 288

Appendix E – Rectangular TE_{103} applicator versus elliptical 290

References 292

List of figures

Figure 1.1 Electromagnetic spectrum and industrial, scientific and medical microwave frequency bands. 1

Figure 1.2 Conceptual representation of (a) conventional heating via thermal conduction from the surface and (b) microwave volumetric heating. 2

Figure 1.3 Conceptual representation of microwave selective heating of a two-phase material composed of an electromagnetically transparent and an absorbent phase component. 3

Figure 1.4 Developed concepts and their application relative to product particle size and microwave properties. 5

Figure 2.1 (a) Dielectric constant and (b) loss factor of oat and barley straw versus temperature in nitrogen atmosphere at 915 and 2,450 MHz up to 450 °C after [26], measured by cavity perturbation technique. 11

Figure 2.2 (a) Dielectric constant and (b) loss factor of oat and barley straw versus temperature in nitrogen atmosphere at 915 and 2,450 MHz up to 700 °C after [26], measured by cavity perturbation technique.. 12

Figure 2.3 Dielectric loss factors versus temperature of wet and dry wood chippings at 2.45GHz after [27], measured by cavity perturbation technique. 12

Figure 2.4 Dielectric properties of Vermiculite versus bulk density at 934 and 2,143 MHz after [31]. 13

Figure 2.5 Dielectric constant (a) and loss factor (b) of water versus frequency for different temperatures based on the Debye model, reproduced from [34]. 14

Figure 2.6 N-port network scattering matrix sketch. 15

Figure 2.7 Scattering parameter nomenclature 16

Figure 2.8 Standing wave pattern example after [37]. 17

Figure 2.9 Smith chart construction overview after [37]. 19

Figure 2.10 Impedance smith chart, normalised impedance reading. 19

Figure 2.11 Impedance smith chart, reflection coefficient and VSWR reading. 20

Figure 2.12 Illustration of the cavity perturbation effect on the resonance upon insertion of a small dielectric load. 23

Figure 2.13 Transmission line setup for measurement of microwave properties in reflection mode (one-port) 24

Figure 2.14 Transmission line setup for measurement of microwave properties in reflection/transmission mode (two-port) 24

Figure 2.15 Microwave heating qualitative profile. 27

Figure 2.16 Representation of dipolar loss mechanism in water. 28

Figure 2.17 Representation of a hysteresis loop on a ferromagnetic material exposed to a varying magnetic field after [61]. 29

Figure 2.18 Illustration of boundary conditions for tangential component of the electric field on a dielectric-dielectric interface. 31

Figure 2.19 Illustration of boundary conditions for normal component of the electric flux density on a dielectric-dielectric interface. 31

Figure 2.20 Electric field (a) polarised perpendicular to the surface and (b) parallel to the surface of a cylindrical sample, reproduced from [67]. 32

Figure 2.21 Generic microwave processing system 36

Figure 2.22 Generic cross section waveguide sketch. 37

Figure 2.23 Attenuation per meter of different modes in a circular copper waveguide with radius $a = 2.54$ cm, after [22]..... 37

Figure 2.24 Rectangular and circular cross-section waveguide sketches. 38

Figure 2.25 Penetration depth of bituminous coal after [28]. 42

Figure 2.26 Penetration depth of magnetite concentrate at a density of 2.8g/cm^3 after [81]. 43

Figure 2.27 Zirconia dielectric properties at 2.45GHz adapted from [111]. 46

Figure 2.28 Simulated temperature distribution in the system at 2.441 GHz after (a) 100 s, (b) 200 s and (c) 208 s of microwave processing of a zirconia sample, after [111]. 46

Figure 2.29 RF induction system sketch. 52

Figure 2.30 RF capacitive treatment system sketch. 53

Figure 2.31 Multi-mode resonant cavity for batch processing sketch. 54

Figure 2.32 Microwave conveyor belt system sketch. 55

Figure 2.33 Schematic of continuous microwave treatment for treatment of contaminated soil based on dual applicator for processing at 150 kg/h throughput, after [79]. 55

Figure 2.34 Sketch of pilot plant dual single-mode applicator system for treatment of ores with a 150 tonne per hour throughput after [148]. 56

Figure 2.35 Microwave serpentine travelling wave applicator sketch after [43]. 57

Figure 2.36 Rectangular waveguide section travelling wave applicator after [43]. 57

Figure 3.1 Typical microwave polymer processing system example, reproduced from [121]. 62

Figure 3.2 PET depolimerization applicator sketch for 12.5 kg/h throughput. WR430 waveguide feeding an external cylinder with internal slotted cylinder, reproduced from [180]. 63

Figure 3.3 Simplified BRC environmental process for pyrolysis of tyres, reproduced from [13]. 66

Figure 3.4 Lam et al. oil pyrolysis system schematic, reproduced from [194]. 68

Figure 3.5 Microwave assisted pyrolysis plant conceptual sketch, reproduced from [220]..... 70

Figure 4.1 Example transmission coefficient of an iris passband filter with a small dielectric insert. . 93

Figure 4.2 Smith chart plot of three example of resonant cavities. Under-coupled (blue line), critically coupled (green line), and over-coupled (red line). 95

Figure 4.3 Auxiliary circle for smith-chart calculation of coupling factor, with lossy coupling structure. 96

Figure 4.4 Generic representation of a microwave resonant cavity system. 96

Figure 4.5 Circuital model representation as parallel RLC circuit, of a generic microwave resonant cavity system. 96

Figure 4.6 Representation of a resonator resonant circle from a measurement plane (blue circles) and a calibrated to the detuned short port position with an adequate delay (green circles). 97

Figure 4.7 Smith chart representation of the half power frequency points for the calculation of the different quality factors, reproduced from [300]. 98

Figure 4.8 Schematic representation the cavity perturbation measurement rig..... 101

Figure 4.9 Electric field distribution of resonant modes of the cavity for dielectric measurements. .. 101

Figure 4.10 NEC H2640 Thermal camera minimum distance from target depending on sample size. 106

Figure 4.11 Dielectric constant and loss factor versus temperature up to 400 °C of FOAMGLAS® T4 measured by CPT at 2,470 MHz at a packing density of 0.115 g/cm^3 – Average of three measurements. 108

Figure 4.12 Dielectric constant and loss factor versus temperature up to 400 °C of Quartz powder measured by CPT at 2,470 MHz at a packing density of 1.16 g/cm^3 – average of three measurements. 109

Figure 4.13 Charcoal briquettes (a) commercial shape, (b) cylindrical cut-out for microwave tests, (c) cross-cut, and (d) pulverised. 109

Figure 4.14 Dielectric constant and loss factor versus temperature up to 400 °C of charcoal briquette powder measured by CPT at 2,470 MHz at a packing density of 1 g/cm3, normal (blue circles) and pre-dried (red circles) – average of three measurements. 110

Figure 4.15 COMSOL suggested solver module according to electrical size after [331] 113

Figure 4.16 WR430 TE_{10n} applicator with 82 mm diameter extension tube, and 25 mm diameter choking section, for monitoring. 117

Figure 4.17 Simulated (blue line) and experimental (red line) S_{11} (dB). Single-mode loaded with FOAMGLAS®T4 sample. 119

Figure 4.18 Simulated (blue line) and experimental (red line) impedance plot Smith chart. Single-mode loaded with FOAMGLAS®T4 sample. 119

Figure 4.19 Simulated (blue line) and experimental (red line) S11 (dB). Single-mode loaded with quartz powder sample..... 120

Figure 4.20 Simulated (blue line) and experimental (red line) impedance plot Smith chart. Single-mode loaded with quartz powder sample. 120

Figure 4.21 Power input (blue line) power absorbed (red line) during quartz powder treatment. 121

Figure 4.22 Simulated temperature distribution (a), photography after quartz heating experiment (b) and simulated power loss density distribution (c) at the top surface..... 122

Figure 4.23 Simulated (blue line) and experimental (red line) S11 (dB). Single-mode loaded with charcoal briquette sample. 123

Figure 4.24 Simulated (blue line) and experimental (red line) impedance plot Smith chart. Single-mode loaded with charcoal briquette powder sample. 123

Figure 4.25 Simulated power loss density (W/m^3) and experimental temperature distribution (°C) of a 5min run at 83W at the top surface of the sample. 124

Figure 4.26 Multimode system sketch 124

Figure 4.27 Experimental thermal image and simulation of power loss density at the surface of a FOAMGLAS®T4 tile, heated in the floor of the multimode cavity. 125

Figure 4.28 Experimental thermal image and simulated of power loss density at the surface of a FOAMGLAS®T4 tile, heated 39 mm from the floor of the multimode cavity. 125

Figure 4.29 Experimental thermal image and simulated power loss density distribution at the surface of a FOAMGLAS®T4 tile, heated 66 mm from the floor of the multimode cavity. 125

Figure 4.30 Experimental thermal image and simulated power loss density distribution at the surface of a FOAMGLAS®T4 tile, heated 93 mm from the floor of the multimode cavity 125

Figure 5.1 Sketch of typical circular and rectangular single-mode applicators. 127

Figure 5.2 Sketch of elliptical cylinder applicator. 133

Figure 5.3 First 12 TM modes of an elliptical cylinder cavity $D2 = 220$ mm $h = 50$ mm and an $ecc = 0.7$..... 135

Figure 5.4 First 12 TM modes of an elliptical cylinder cavity $D2 = 220$ mm $h = 50$ mm and an $ecc = 0.7$, cross-planes. 136

Figure 5.5 Normalised cut-off wavelength ($\lambda c/a$) of five TM modes of an elliptical cylinder cavity waveguide adapted from the polynomials published in [355] and [341]. 137

Figure 5.6 Design chart for the empty elliptical cavity, first four modes, at 2,450 MHz..... 138

Figure 5.7 Design chart for the empty elliptical cavity, first four modes, at 915 MHz..... 138

Figure 5.8 Design chart for the empty elliptical cavity, first four modes, at 433 MHz..... 138

Figure 5.9 Normalised power loss density of a sample with a PUI = 0.18, uniformly treated in the vertical coordinate. 139

Figure 5.10 Maximum diameter for self-choking behaviour at ISM frequencies 2,450 MHz (blue line), 915 MHz (red line) and 433 MHz (yellow line) for different dielectric constant materials. 141

Figure 5.11 Below cut-off attenuation per centimetre versus tube diameter for 2,450 MHz, with different dielectric filling material. 142

Figure 5.12 Below cut-off attenuation per centimetre versus tube diameter for 915 MHz, with different dielectric filling material. 142

Figure 5.13 TM_2 mode electric field distribution in central cut-plane. Empty $e \approx 0.7, a = 83$ mm, $b = 59.2$ mm cavity. 144

Figure 5.14 TM_2 mode electric field distribution along the major axis. Empty $e \approx 0.7, a = 83$ mm, $b = 59.2$ mm cavity. 145

Figure 5.15 TM_4 mode electric field distribution in central cut-plane. Empty $e \approx 0.7, a = 112$ mm, $b = 80$ mm cavity. 145

Figure 5.16 TM_4 mode electric field distribution along the major axis. Empty $e \approx 0.7, a = 112$ mm, $b = 80$ mm cavity. 146

Figure 5.17 Loaded cavity size and load positioning adjustment procedure summary. 147

Figure 5.18 Electric field distribution at the vertical middle cut plane, TM_2 cavity (red line), TM_4 cavity (blue line). The dashed lines represent the sample boundaries. 148

Figure 5.19 TM_2 Electric field distribution at the horizontal middle cut plane. Loaded cavity with $e \approx 0.7, a \approx 73.6$ mm, $b \approx 52.5$ mm, load at 38.8 mm from the centre..... 148

Figure 5.20 TM_2 Electric field distribution at the vertical middle cut plane. Loaded cavity with $e \approx 0.7, a \approx 73.6$ mm, $b \approx 52.5$ mm, load at 38.8 mm from the centre..... 148

Figure 5.21 TM_4 Electric field distribution at the horizontal middle cut plane. Loaded cavity with $e \approx 0.73, a \approx 102$ mm, $b \approx 70$ mm, load at 74.4 mm from the centre. 149

Figure 5.22 TM_4 Electric field distribution at the vertical middle cut plane. Loaded cavity with $e \approx 0.73, a \approx 102$ mm, $b \approx 70$ mm, load at 74.4 mm from the centre. 149

Figure 5.23 Sketch of waveguide feeding of the elliptical cavity. 151

Figure 5.24 Sketch of monopole (i.e. coaxial) feeding of the elliptical cavity..... 151

Figure 5.25 Sketch of monopole (i.e. coaxial) feeding of an elliptical cavity with two loads. 152

Figure 5.26 Electric field distribution in the horizontal middle cut-plane for the waveguide-fed elliptical cavity. 153

Figure 5.27 Electric field distribution in the vertical middle cut-plane for the waveguide-fed elliptical cavity. 153

Figure 5.28 Adjustable grounded coaxial probe sketch. 153

Figure 5.29 Fabricated adjustable grounded coaxial probe. 153

Figure 5.30 Picture of the internal part of the prototype. 154

Figure 5.31 Schematic of fabricated prototype elliptical cylinder applicator with main dimensions. 155

Figure 5.32 Electric field distribution (V/m) simulated by CST Microwave at 2.46 GHz. 156

Figure 5.33 Electric field distribution simulation (V/m) simulated by COMSOL at 2.46 GHz. 157

Figure 5.34 Power loss density simulation (W/m3) simulated by CST at 2.46 GHz. 157

Figure 5.35 Power loss density simulation (W/m^3) simulated by COMSOL at 2.46 GHz. 158

Figure 5.36 Reflection scattering parameter S11 (dB) experimental measurement (red line), COMSOL simulation (blue line) and CST simulation (yellow line). 159

Figure 5.37 Generator output versus applicator frequency bands after [364]. 160

Figure 5.38 Typical magnetron output spectrum for different types of power supplies, reproduced from [368] 161

Figure 5.39 Heating system. Cooling circuit omitted, and cavity orientation rotated for clarity. 162

Figure 5.40 Controlled feeder concept sketch for material handling for elliptical cylinder applicator164

Figure 5.41 Merrick 970N weight belt feeder from [371]. 165

Figure 5.42 Conical hopper schematic, being D the outlet diameter and θ the semi-included angle. 165

Figure 5.43 Estimated conical hopper discharge rate calculated from equation (5.5) (blue line) and equation (5.6) (red line). 168

Figure 5.44 Estimated conical hopper discharge rate for a 9 mm particle size and 53.6 mm outlet diameter, calculated from equation (5.6) 169

Figure 5.45 Large diameter product through series of off centred applicators conceptual sketch. 170

Figure 5.46 Estimated conical hopper discharge rate for a 25.4 mm particle size and 161 mm outlet diameter, calculated from equation (5.6) 170

Figure 5.47 Choke structure based on resonating corrugations. 171

Figure 5.48 Choke scattering parameters – TE_{11} to TE_{11}. 172

Figure 5.49 Choke scattering parameters – TM_{01} to TM_{01}. 172

Figure 5.50 Choke scattering parameters – TE_{11} to TM_{01}. 172

Figure 5.51 Choke scattering parameters – TM_{01} to TE_{11}. 172

Figure 5.52 Choke electric field distribution at 915MHz for a TE11 excitation. 173

Figure 5.53 Choke electric field at 915MHz for a TM01 excitation. 173

Figure 6.1 Torbed CBR operation principles sketch after [412]. 181

Figure 6.2 Torbed T400 CBR schematic. 184

Figure 6.3 Reactor general dimensions and a typical bed geometry. 185

Figure 6.4 Central cut planes electric field distribution resonant mode at 2,449 MHz for empty cavity (only one polarisation shown). XY cut-plane at expected bed position centre (~26 mm from base). 185

Figure 6.5 Central cut planes electric field distribution for polarisation rotated modes resonant at 2,458 MHz for empty cavity (only one polarisation shown). Additional XY cut-plane at expected bed position centre (~26 mm from base). 185

Figure 6.6 Schematic of different feeding arrangement for Torbed T400 CBRMW reactor. (a) Waveguide through central cone, (b) waveguide from lid, (c) waveguide through reactor wall, (d) broad wall slotted waveguide ring through central cone, (e) narrow wall slotted waveguide ring through central cone, (f) slotted waveguide ring through reactor wall. 187

Figure 6.7 Cone waveguide fed reactor sketch. 188

Figure 6.8 Lid waveguide fed reactor sketch 1. 189

Figure 6.9 Lid waveguide fed reactor sketch 2. 189

Figure 6.10 TE_{10} rectangular waveguide surface current on its broad-side. Overlay of possible positions for radiating and non-radiating slots. 190

Figure 6.11 TE_{10} rectangular waveguide surface current on its narrow-side. Overlay of possible positions for radiating and non-radiating slots. 190

Figure 6.12 TE_{10} rectangular waveguide surface current and electric field distribution on its broad-side with two slots, one in the middle and one shifted to one side. 191

Figure 6.13 Maximum slot power handling according to slot width at room temperature air. 192

Figure 6.14 Maximum slot peak power handling versus air temperature for various slot widths. 2 mm (blue line), 4 mm (red line), 6 mm (yellow line), 8 mm (purple line), and 10 mm (green line). 193

Figure 6.15 E tee splitter electric field behaviour, arm outputs in opposite phase. 194

Figure 6.16 Electric field distribution within the waveguide ring designed for narrow wall slot feeding. 195

Figure 6.17 H tee splitter electric field behaviour, arm outputs in phase. 196

Figure 6.18 Electric field distribution within the waveguide ring designed for broad wall slot feeding. 197

Figure 6.19 Reflection coefficient magnitude of a waveguide fed reactor with a product bed with a dielectric constant of 1.5 and loss factor of 0.05 (blue line), 0.1 (green line), 0.5 (red line), 1 (cyan line), 2 (purple line) and 4.5 (yellow line). 198

Figure 6.20 Reflection coefficient magnitude of a waveguide fed reactor with a product bed with a dielectric constant of 4.5 and loss factor of 0.05 (blue line), 0.1 (green line), 0.5 (red line), 1 (cyan line), 2 (purple line) and 4.5 (yellow line). 199

Figure 6.21 Reflection coefficient magnitude of a waveguide fed reactor with a product bed with a dielectric constant of 7.5 and loss factor of 0.05 (blue line), 0.1 (green line), 0.5 (red line), 1 (cyan line), 2 (purple line) and 4.5 (yellow line). 199

Figure 6.22 Reflection coefficient magnitude of a waveguide fed reactor with a product bed with a dielectric constant of 1.5 and loss factor of 0.05, tuned for 2.45 GHz. 201

Figure 6.23 Electric field distribution of a waveguide fed reactor with a product bed with a dielectric constant of 1.5 and loss factor of 0.05, tuned for 2.45 GHz. XY cut-plane at bed centre. 201

Figure 6.24 Power loss density distribution of a waveguide fed reactor with a product bed with a dielectric constant of 1.5 and loss factor of 0.05, tuned for 2.45 GHz. XY cut-plane at bed centre... 201

Figure 6.25 Reflection coefficient magnitude of a waveguide fed reactor with a product bed with a complex permittivity of 3.96-j1.23 (blue line), 4.26-j1.48 (green line), and 5.78-j4.99 (red line), tuned for a 4.26-j1.48 load at 2.45 GHz. 202

Figure 6.26 Electric field distribution of a waveguide fed reactor with a product bed with a dielectric constant of 4.26 and a loss factor of 1.48, tuned for 2.45 GHz. XY cut-plane at bed centre. 203

Figure 6.27 Power loss density distribution of a waveguide fed reactor with a product bed with a dielectric constant of 4.26 and a loss factor of 1.48, tuned for 2.45 GHz. XY cut-plane at bed centre. 203

Figure 6.28 Reflection coefficient magnitude of a narrow wall slot fed reactor with a product bed with a dielectric constant of 1.5 and loss factor of 0.05 (blue line), 0.1 (green line), 0.5 (red line), 1 (cyan line), 2 (purple line) and 4.5 (yellow line)..... 203

Figure 6.29 Reflection coefficient magnitude of a narrow wall slot fed reactor with a product bed with a dielectric constant of 4.5 and loss factor of 0.05 (blue line), 0.1 (green line), 0.5 (red line), 1 (cyan line), 2 (purple line) and 4.5 (yellow line)..... 204

Figure 6.30 Reflection coefficient magnitude of a narrow wall slot fed reactor with a product bed with a dielectric constant of 7.5 and loss factor of 0.05 (blue line), 0.1 (green line), 0.5 (red line), 1 (cyan line), 2 (purple line) and 4.5 (yellow line)..... 204

Figure 6.31 Reflection coefficient magnitude of a narrow wall slot fed reactor with a product bed with a dielectric constant of 1.5 and loss factor of 0.05, tuned for 2.45 GHz. 205

Figure 6.32 Electric field distribution of a narrow wall slot fed reactor with a product bed with a dielectric constant of 1.5 and loss factor of 0.05, tuned for 2.45 GHz. XY cut-plane at bed centre... 205

Figure 6.33 Power loss density distribution of a narrow wall slot fed reactor with a product bed with a dielectric constant of 1.5 and loss factor of 0.05, tuned for 2.45 GHz. XY cut-plane at bed centre... 205

Figure 6.34 Reflection coefficient magnitude of a narrow wall slot fed reactor with a product bed with a complex permittivity of 3.96-j1.23 (blue line), 4.26-j1.48 (green line), and 5.78-j4.99 (red line), tuned for a 4.26-j1.48 load at 2.45 GHz. 206

Figure 6.35 Electric field distribution of a narrow wall slot fed reactor with a product bed with a dielectric constant of 4.26 and loss factor of 1.48, tuned for 2.45 GHz. XY cut-plane at bed centre. 207

Figure 6.36 Power loss density distribution of a narrow wall slot fed reactor with a product bed with a dielectric constant of 4.26 and loss factor of 1.48, tuned for 2.45 GHz. XY cut-plane at bed centre. 207

Figure 6.37 Reflection coefficient magnitude of broad wall slot fed reactor with a product bed with a dielectric constant of 1.5 and loss factor of 0.05 (blue line), 0.1 (green line), 0.5 (red line), 1 (cyan line), 2 (purple line) and 4.5 (yellow line). 208

Figure 6.38 Reflection coefficient magnitude of broad wall slot fed reactor with a product bed with a dielectric constant of 4.5 and loss factor of 0.05 (blue line), 0.1 (green line), 0.5 (red line), 1 (cyan line), 2 (purple line) and 4.5 (yellow line). 208

Figure 6.39 Reflection coefficient magnitude of broad wall slot fed reactor with a product bed with a dielectric constant of 7.5 and loss factor of 0.05 (blue line), 0.1 (green line), 0.5 (red line), 1 (cyan line), 2 (purple line) and 4.5 (yellow line). 209

Figure 6.40 Reflection coefficient magnitude of a broad wall fed reactor with a product bed with a dielectric constant of 1.5 and loss factor of 0.05, tuned for 2.45 GHz. 210

Figure 6.41 Electric field distribution of a broad wall slot fed reactor with a product bed with a dielectric constant of 1.5 and loss factor of 0.05, tuned for 2.45 GHz. XY cut-plane at bed centre. 210

Figure 6.42 Power loss density distribution of a broad wall slot fed reactor with a product bed with a dielectric constant of 1.5 and loss factor of 0.05, tuned for 2.45 GHz. XY cut-plane at bed centre... 210

Figure 6.43 Reflection coefficient magnitude of a broad wall fed reactor with a product bed with a complex permittivity of 3.96-j1.23 (blue line), 4.26-j1.48 (green line), and 5.78-j4.99 (red line), tuned for a 4.26-j1.48 load at 2.45 GHz. 211

Figure 6.44 Electric field distribution of a broad wall slot fed reactor with a product bed with a dielectric constant of 4.26 and loss factor of 1.48, tuned for 2.45 GHz. XY cut-plane at bed centre. 212

Figure 6.45 Power loss density distribution of a broad wall slot fed reactor with a product bed with a dielectric constant of 4.26 and loss factor of 1.48, tuned for 2.45 GHz. XY cut-plane at bed centre. 212

Figure 6.46 Initial prototype waveguide feeding ring. 214

Figure 6.47 FOAMGLAS® static bed triangular profile with 30 mm height and 34 mm width, 395 mm outer diameter, 327 mm internal diameter. 215

Figure 6.48 Simulation (red line) and measurement (blue line) of initial Torbed T400 CBRMW prototype, with a static FOAMGLAS® load..... 216

Figure 6.49 Torbed MWCBR400 with PTFE window shell (3 mm) and FOAMGLAS® load – Power loss density simulation vs thermal imaging measurement, for 300 W microwave input for 10 seconds. 216

Figure 6.50 Torbed T400 CBRMW prototype external view. 217

Figure 6.51 Torbed T400 CBRMW prototype internals 217

Figure 6.52 Inlet and exhaust choke testing rig..... 218

Figure 6.53 Honeycomb structure picture 15 mm x 100 mm cells. 219

Figure 6.54 Empty tube choke attenuation..... 219

Figure 6.55 Transmission range of optical materials, adapted from [430]..... 220

Figure 6.56 IR viewing port configuration – germanium window. 220

Figure 6.57 Germanium window with AR/AR coating – 3 mm thick, after [431]..... 221

Figure 6.58 Hybrid heating test on the Torbed MWCBR400 with PTFE window shell (3 mm) and 500 g load of corn –Thermal imaging (a) after convection heating to 150 °C (b) after 2 kW microwave input for 20 seconds (full absorbed power). 221

Figure 6.59 Purely microwave heating test on the Torbed MWCBR400 with PTFE window shell (3 mm) and 300 g load of malt –Thermal imaging (a) after convection heating to 150 °C (b) after 2 kW microwave input for 20 seconds (full absorbed power, cold matched). 222

Figure 6.60 Reflection coefficient magnitude of a broad wall fed reactor with a product bed with a complex permittivity of 1.5-j0.05 tuned for 896 MHz. 223

Figure 6.61 Reflection coefficient magnitude of a broad wall fed reactor with a product bed with a complex permittivity of 4.32-j1.86 (blue line), 4.67-j2.26 (green line), and 7.26-j5.64 (red line), tuned for a 4.67-j2.26 load at 896 MHz. 223

Figure 6.62 Electric field distribution of a broad wall slot fed reactor with a product bed with a dielectric constant of 1.5 and loss factor of 0.05, tuned for 2.45 GHz. XY cut-plane at bed centre. 224

Figure 6.63 Power loss density distribution of a broad wall slot fed reactor with a product bed with a dielectric constant of 1.5 and loss factor of 0.05, tuned for 2.45 GHz. XY cut-plane at bed centre... 224

Figure 6.64 Electric field distribution of a broad wall slot fed reactor with a product bed with a dielectric constant of 4.67 and loss factor of 2.26, tuned for 2.45 GHz. XY cut-plane at bed centre. 224

Figure 6.65 Power loss density distribution of a broad wall slot fed reactor with a product bed with a dielectric constant of 4.67 and loss factor of 2.26, tuned for 2.45 GHz. XY cut-plane at bed centre. 224

Figure 6.66 Reflection coefficient magnitude for original bed position (red line), shifted upwards by 0.5 cm (blue line) and 1 cm (green line). 226

Figure 6.67 Electric field distribution of 1,000 mm waveguide ring with WR975 waveguide cross-section..... 227

Figure 6.68 Electric field distribution of a 1,000 mm waveguide ring with custom 189.9 x 97.79 mm cross-section. 227

Figure 7.1 Suspended metallic belt in microwave tunnel, adapted from [441] 232

Figure 7.2 Parallel plate applicator schematic, based on the design proposed in [443] 233

Figure 7.3 Hybrid heating conveyor belt concept for coke-making 235

Figure 7.4 Microwave compatible hearth concept. 237

Figure 7.5 Standing wave electric field pattern of a short circuited TE_{10} waveguide 238

Figure 7.6 Standing wave surface current pattern of a short circuited TE_{10} waveguide. 239

Figure 7.7 Slotted waveguide feed for parallel plate applicator at S-band, 6 mm slot thickness. 239

Figure 7.8 Free space model of slotted waveguide design 240

Figure 7.9 Far-field radiation pattern 240

Figure 7.10 Electric field X polarisation component (horizontal) 240

Figure 7.11 Electric field Y polarisation component (vertical) 240

Figure 7.12 Electric field Z polarisation component (horizontal) 241

Figure 7.13 Electric field distribution components (a) total, (b) X direction, (c) Y direction and (d) Z direction..... 242

Figure 7.14 Complex permittivity versus temperature of material m1. 242

Figure 7.15 Product presentation, (a) 50 mm x 50 mm x 25 mm lump matrix with uniform 20 mm spacing, and (b) continuous 25 mm height bed. 243

Figure 7.16 Reflection coefficient magnitude of the full mirrored model (red line) and simplified half model (blue line). 244

Figure 7.17 Reflection coefficient magnitude of matrix load for different temperature properties. ... 244

Figure 7.18 Power loss density at 350 °C properties, vertical and horizontal middle cut plane through the bed. 245

Figure 7.19 Power loss density at 450 °C properties, vertical and horizontal middle cut plane through the bed. 246

Figure 7.20 Power loss density at 550 °C properties, vertical and horizontal middle cut plane through the bed. 246

Figure 7.21 Power loss density at 650 °C properties, vertical and horizontal middle cut plane through the bed. 247

Figure 7.22 Parallel plate metal conveyor belt prototype conceptual schematic. 248

Figure 7.23 Parallel plate metal conveyor belt prototype main dimensions schematic..... 249

Figure 7.24 S_{11} parameter in (dB) for a 25 mm load with $\varepsilon r' = 1.5$ and $\varepsilon r'' = 0.1$ (solid line), $\varepsilon r'' = 0.5$ (dash line), $\varepsilon r'' = 1$ (dot line) and $\varepsilon r'' = 2$ (dash-dot line)..... 250

Figure 7.25 S_{11} parameter in (dB) for a 25 mm load with $\varepsilon r' = 4$ and $\varepsilon r'' = 0.1$ (solid line), $\varepsilon r'' = 0.5$ (dash line), $\varepsilon r'' = 1$ (dot line) and $\varepsilon r'' = 2$ (dash-dot line)..... 251

Figure 7.26 S_{11} parameter in (dB) for a 25 mm load with $\varepsilon r' = 8$ and $\varepsilon r'' = 0.1$ (solid line), $\varepsilon r'' = 0.5$ (dash line), $\varepsilon r'' = 1$ (dot line) and $\varepsilon r'' = 2$ (dash-dot line)..... 251

Figure 7.27 S_{11} parameter in (dB) for a 25 mm load with $\varepsilon r' = 15$ and $\varepsilon r'' = 0.1$ (solid line), $\varepsilon r'' = 0.5$ (dash line), $\varepsilon r'' = 1$ (dot line) and $\varepsilon r'' = 2$ (dash-dot line)..... 251

Figure 7.28 Power loss density (W/m^3) for a 25 mm load with $\varepsilon r' = 1.5$ and $\varepsilon r'' = 0.1$ (a), $\varepsilon r'' = 0.5$ (b), $\varepsilon r'' = 1$ (c) and $\varepsilon r'' = 2$ (d). 252

Figure 7.29 Power loss density (W/m^3) for a 25 mm load with $\varepsilon r' = 4$ and $\varepsilon r'' = 0.1$ (a), $\varepsilon r'' = 0.5$ (b), $\varepsilon r'' = 1$ (c) and $\varepsilon r'' = 2$ (d)..... 253

Figure 7.30 Power loss density (W/m^3) for a 25 mm load with $\varepsilon r' = 8$ and $\varepsilon r'' = 0.1$ (a), $\varepsilon r'' = 0.5$ (b), $\varepsilon r'' = 1$ (c) and $\varepsilon r'' = 2$ (d)..... 254

Figure 7.31 Power loss density (W/m^3) for a 25 mm load with $\varepsilon r' = 15$ and $\varepsilon r'' = 0.1$ (a), $\varepsilon r'' = 0.5$ (b), $\varepsilon r'' = 1$ (c) and $\varepsilon r'' = 2$ (d). 254

Figure 7.32 Power loss density (W/m^3) for a 25 mm FOAMGLAS® load, at its top surface. 255

Figure 7.33 Power loss density (W/m^3) for a 25 mm FOAMGLAS® load, at its middle point. 256

Figure 7.34 Power loss density (W/m3) for a 25 mm FOAMGLAS® load, at its bottom surface. 256

Figure 7.35 Power loss density (W/m^3) for a 25 mm FOAMGLAS® load, at its top surface, with a 1 cm refractory layer ($\varepsilon r = 3 - j0.01$) between belt and product. 257

Figure 7.36 Power loss density (W/m^3) for a 25 mm FOAMGLAS® load, at its middle point, with a 1 cm refractory layer ($\varepsilon r = 3 - j0.01$) between belt and product. 257

Figure 7.37 Power loss density (W/m3) for a 25 mm FOAMGLAS® load, at its bottom surface, with a 1 cm refractory layer ($\varepsilon r = 3 - j0.01$) between belt and product. 258

Figure 7.38 Linear projection of the power loss density (W/m^3) for a 25 mm load with $\varepsilon r' = 4$ and $\varepsilon r'' = 1$ at its top surface. 259

Figure 7.39 Cross-coupling for a 25 mm load with $\varepsilon r' = 4$ and $\varepsilon r'' = 1$ 260

Figure 7.40 Simulation of the reflection coefficient magnitude versus vertical position of the bed for a 25 mm tall FOAMGLAS® bed. 260

Figure 7.41 Parallel plate applicator testing rig. 261

Figure 7.42 Parallel plate applicator testing rig product load. 262

Figure 7.43 Experimental thermal image of a 25 mm tall FOAMGLAS® heated for 1 minute at 135 W and cooled for 2 minutes. 262

Figure 7.44 Power loss density distribution simulation of a 25 mm height FOAMGLAS® load (300 W input) at 2.45 GHz. 263

Figure 7.45 Metal conveyor applicator reflection coefficient magnitude simulation (blue line) and experimental measurement (red line). 263

Figure 7.46 Electric field distribution simulation of a 68 mm height FOAMGLAS® load (300 W input) at 896 MHz. 264

Figure 7.47 Power loss density distribution simulation of a 68 mm height FOAMGLAS® load (300 W input) at 896 MHz. 264

Figure 7.48 Metal conveyor applicator reflection coefficient magnitude simulation for a scaled 896 MHz design. 264

Figure 8.1 Simulated electric field distribution on TM4 elliptical applicator for oil treatment. 275

Figure 8.2 Simulated electric field distribution around the maximum for different dielectric constants. 275

Figure 8.3 Simulated power uniformity index and quality factor for different dielectric constants. .. 276

Figure 8.4 Liquid product processing conceptual sketch based on various applicators in series. 277

Figure 8.5 Plastic waste microwave processing system conceptual sketch. 278

Figure 8.6 Large scale microwave hearth furnace conceptual schematic. Only one microwave heating section represented for simplicity. 279

Figure 8.7 Laboratory scale rotary hearth furnace Nabertherm DH 3020, from [445]. 280

Figure 8.8 Laboratory scale rotary hearth furnace Nabertherm DH 3020 internals with high-temperature steel plating from [445]. 280

List of tables

Table 2.1 Summary of microwave properties measurement techniques 22

Table 2.2 Scattering parameters to permittivity methods 25

Table 2.3: ISM frequency allocations 33

Table 2.4: ISM equipment in current use, reproduced from [69] 33

Table 2.5. Exposure limit values for 300MHz – 6GHz, adapted from [71] 34

Table 2.6. Exposure action levels, adapted from [71] 35

Table 2.7. Summary of main parameters for rectangular waveguides adapted from [22] 38

Table 2.8. Summary of main parameters for circular waveguides adapted from [22] 38

Table 2.9 Standard rectangular waveguide sizes, adapted from [76] 39

Table 3.1 Commercial fuels calorific value or high heating values (HHV) [164]. 60

Table 3.2 Selected product yields from microwave waste plastic pyrolysis, all with MW operation at a frequency of 2.45 GHz. Solid/Liquid/Gas (%wt) yield and oil high heating value (HHV). 64

Table 3.3 Selected product yields from microwave end-of-life tyre pyrolysis, all with MW operation at a frequency of 2.45 GHz. Solid/Liquid/Gas (%wt) yield and high heating value (HHV). 67

Table 3.4 Ferrous metallurgy microwave material studies 75

Table 4.1 Dielectric constant and loss tangent measured at 2.45 GHz vs literature [24] for Nylon66 and Teflon - average of twelve measurements. 104

Table 4.2 Incandescent body temperature estimation based on colour for ultra-high temperature materials adapted from [316] 106

Table 4.3 Relative magnetic permeability and conductivity of metals 111

Table 4.4 Aluminium rectangular resonator of 70 mm x 35 mm x 100 mm simulated at different meshing densities compared to analytical values. 114

Table 4.5 Skin depth of some metallic materials at 2.45 GHz 116

Table 5.1 UK domestic plastic waste stream general composition after [348] 130

Table 5.2 Resonant frequencies in (GHz) for the first 31 modes of an elliptical cylinder cavity $a = 110$ mm $h = 50$ mm and an $e = 0.7$. 134

Table 5.3 Estimated maximum diameter for self-choking behaviour of a feeding tube for different applications 141

Table 5.4 Properties of TM_2 and TM_4 elliptical cavities loaded with product. 149

Table 5.5 Properties of TM_2 and TM_4 elliptical cavities loaded with product for varying heights (d). 149

Table 5.6 Dimensions of prototype elliptical cylinder applicator 155

Table 5.7 Measured and simulated results for TM_4 elliptical cavity with a 2 mm - 4 mm ore load. .. 159

Table 5.8 Frequency scale-up first-pass estimation for elliptical applicator prototype. 163

Table 5.9 Product properties for the estimation of discharge rates – unreferenced values comes from initial sizing and measurements. 167

Table 5.10 Second-pass estimation for elliptical applicator prototype. 168

Table 6.1 Summary of microwave fluidised beds in the scientific literature. 176

Table 6.2 Summary of results for waveguide (WG), narrow wall slot (NWS) and broad wall slot (BWS) fed reactor at 2.45GHz, for a 6 kW microwave power input. 212

Table 6.3 Summary of results for the broad wall slot fed reactor at 896 MHz for a 100 kW microwave power input. 225

Table 7.1 Metallic conveying solutions in the literature – apparent weakness 231

Table 7.2 Dimensions of prototype parallel plate metal conveyor belt applicator 249

Table 7.3 Power loss density uniformity across the heating zone. 259

Table 8.1 UK domestic plastic waste stream general composition after [348] 277

Chapter 1 Introduction

Microwaves are defined as a part of the electromagnetic spectrum with frequencies spanning from 300 MHz to 300 GHz. This type of non-ionizing radiation is used in several fields of application including wireless communications, radio astronomy, navigation, radar, imaging, spectroscopy, cooking, and material processing [1], [2]. For both research and industrial microwave processing systems, the most used frequency bands are the industrial, scientific and medical (ISM) ones, due to readily available high-power equipment and legal clearance for use, in particular, the 915 MHz and 2,450 MHz bands are considered [3]. A representation of the electromagnetic spectrum with the important ISM bands is shown in Figure 1.1.

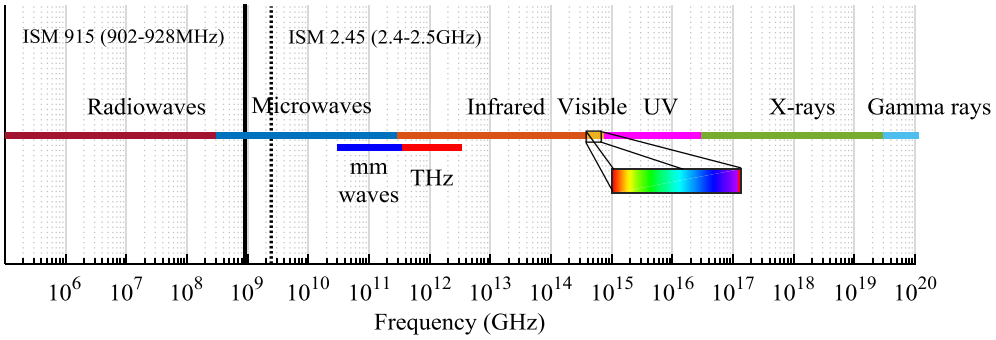


Figure 1.1 Electromagnetic spectrum and industrial, scientific and medical microwave frequency bands.

The application of microwaves for material processing has been considered for a variety of applications. However, given the complexity of microwave-material interactions, the design of these systems requires a detailed understanding of the material property variation during processing and an in-depth comprehension and integration of the different techniques involved in the heating, transport, by-product handling, maintenance, monitoring and control [4]. This requirement makes the development of large scale microwave processing systems a multidisciplinary effort which requires a compromise between electromagnetic, material handling and process engineering to deliver techno-economically viable solutions [4], [5].

Material processing can use microwave energy as an alternative to the more traditional electric and fossil-fuel based heating. Conventional methods deliver heat mostly through convection, radiation and thermal conduction, which propagates from the source to the product surface and then to its core as illustrated in Figure 1.2 (a). In microwave heating, power is dissipated directly within the product volume through molecular-level interaction with the varying electromagnetic fields, generating an inverse temperature gradient due to heat-loss at the product surface, as shown in Figure 1.2 (b) [4], [6]–[10].

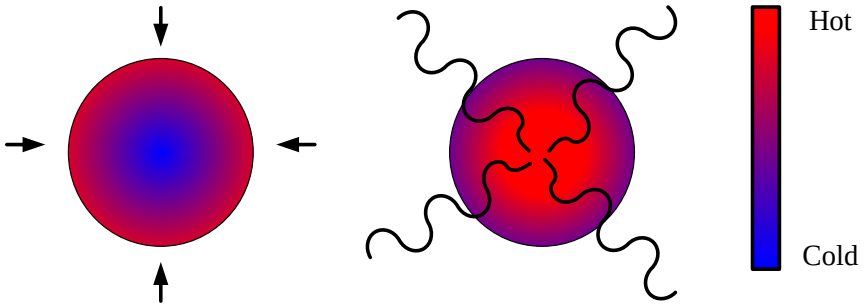


Figure 1.2 Conceptual representation of (a) conventional heating via thermal conduction from the surface and (b) microwave volumetric heating.

Microwaves can be regarded as an expensive form of heat delivery as its directly driven by expensive electrical energy [11]. Therefore, usage needs to be carefully weighed, as the most likely successful applications are the ones that can gain a significant competitive advantage over alternative conventional heating methods. Moreover, not every product is readily suitable for microwave heating, often requiring a particular presentation or a specific technique to be processed effectively, if possible at all [12].

A myriad of advantages can be exploited, depending on the particularities of each application, based on three main microwave-heating characteristics. First, the volumetric heating nature of the process, illustrated in Figure 1.2 (b), can provide a fast, uniform and efficient temperature increase of the whole product [6], [13], [14]. Second, rapid on/off operation can be achieved without significant thermal inertia, as microwaves heat the product

directly, rather than its surroundings [15], [16]. Thirdly, there is the possibility of selective heating, which allows targeting specific parts of the samples to be treated based on its different electromagnetic properties, so called selective heating (Figure 1.3) [15]–[17]. Processes which benefit from one or more of these characteristics have shown potential to develop much faster processing, ability to treat larger feedstocks without as much pre-processing, delivery of superior product quality (or unique product properties), energy savings, footprint reduction, lower environmental impact, or significantly improve or ease downstream processing steps [18]–[21].

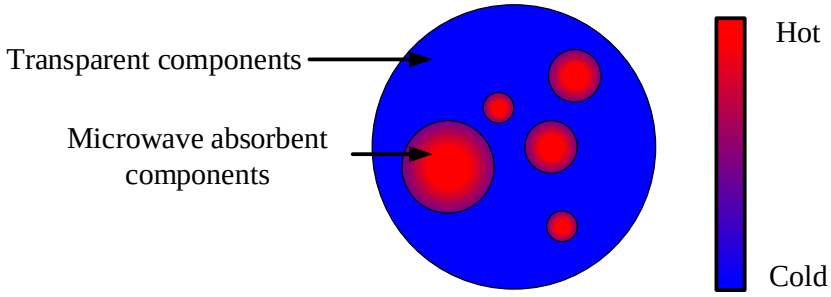


Figure 1.3 Conceptual representation of microwave selective heating of a two-phase material composed of an electromagnetically transparent and an absorbent phase component.

Unfortunately, much of the research to date has not considered the scaling up aspects of the different techniques widely applied in laboratory setups as these are not directly transferable to larger scales, especially for applications where products can reach high temperatures (i.e. over 250 °C), for which few if any robust engineering solutions are currently available. The development of concepts with clear scalable paths is needed to provide the step-change that will lead to the design of large batch and continuous processes that can open the way to successful commercial application. In addition, the use of promising hybrid heating techniques (i.e. a combination of microwaves with conventional heat sources) which may help to reduce process variables and to open the scope of microwave processing to a whole new range of materials, remains mostly unexplored [4].

In order to develop a scalable solution, the process should be analysed from a holistic view point. The characterisation of the electromagnetic properties of the product should lead to a range of possibly suitable microwave application techniques if any, and to general estimations on processing requirements. The physical properties of the product during processing, including its presentation, size, geometry, physical states, and the possible generated by-products should lead to a range of possible material handling techniques, structural and thermal material requirements. Also, the process itself should give information about expected throughputs and performance in commercial scenarios.

The compatibility between material handling, construction, structural, processing requirements and microwave application techniques needs to be evaluated, and possible concepts that can meet the basic process requirements can be drafted, which define a clear scale-up path. Detailed engineering development should be carried out to evaluate such concepts further, considering electromagnetic design and optimisation, microwave hardware sizing, robustness and materials of constructions, material handling implementation, monitoring, control and safety solutions. However, there is a notorious lack of scalable concepts in the literature or at least lack of attempts to resolve scale-up issues particularly for high temperature processes.

In this thesis three concepts for higher temperature microwave processing with clear scale-up paths are proposed and evaluated; selected to cover as large range of material presentations and microwave properties as possible, (as illustrated in Figure 1.4) and to provide a platform of alternatives for the development of new large scale microwave processes currently under investigation. These concepts can be implemented in a hybrid heating setting if needed. Firstly, an elliptical cylindrical cavity for the continuous treatment of pumpable liquids and fine powders. This is considered particularly suitable for products that require high power densities (i.e. low microwave absorption properties), but with usage also for applications with higher

microwave absorption for example microwave flow chemistry applications. Secondly, a novel hybrid convection/microwave fluidised bed system for products with particle sizes ranging from few millimetres to up to 2 cm, with medium and high microwave absorption properties. Finally, a robust metal conveyor solution able to handle hot particles bigger than 2 cm, suitable for operation under harsh conditions, for medium to high microwave absorption product properties is considered.

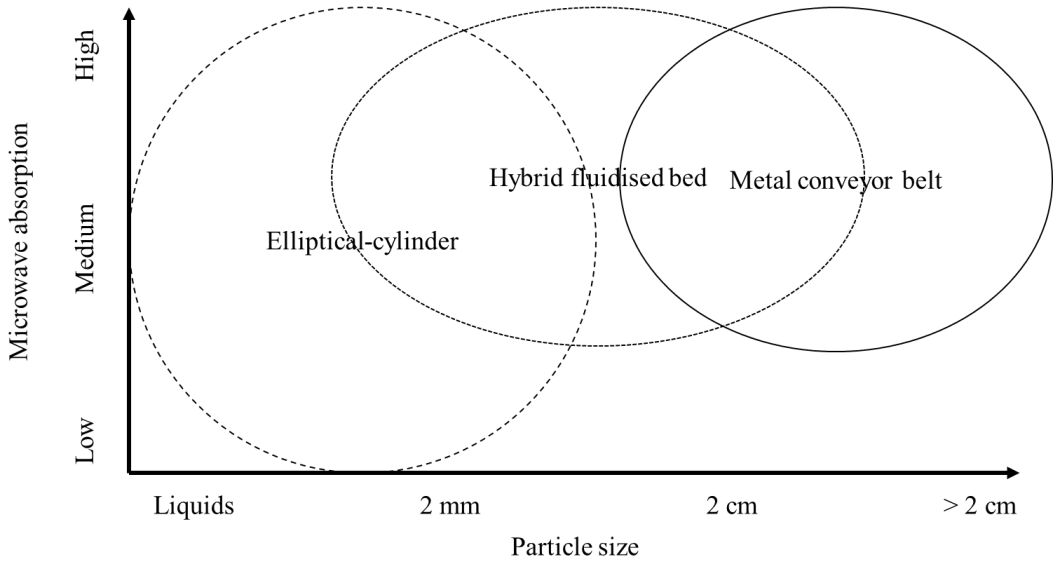


Figure 1.4 Developed concepts and their application relative to product particle size and microwave properties.

Prototypes for each of the proposed concepts were designed and fabricated and used to validate the used design methodologies. These systems are being used to provide proof of concept studies in a variety of applications, and a full-scale system is currently being developed for the hybrid fluidised bed system.

1.1 Aims

The specific aims of this work are to create a platform of scalable high temperature microwave applicator prototypes that can be used for proof of concept for different applications and to serve as an initial step for the development of full-scale processes.

1.2 Objectives

- Produce a literature review to identify critical aspects and opportunities for developing scalable solutions, with a focus on high-temperature processes (i.e. over 250 °C).
- Perform electromagnetic characterisation of products of interest, benchmark materials, insulation materials and any required auxiliary material in close to expected processing conditions, to serve as the basis of the applicator design.
- Design, development, validation and evaluation of applicator solutions that can be used for a wide range of bulk materials (i.e. from liquids to large lumps) and of a variety of dielectric properties, with clear scale-up prospects, to serve as the basis for the ongoing investigation of different high temperature microwave processing applications.
- Make recommendations as to suitable applicator classes for development and scale up of high temperature microwave processes.

1.3 Contributions

- Development of a scalable microwave elliptical cylinder applicator and design methodology as an alternative to the common single mode systems for applications for fluids and small powders.
- Development of a scalable novel hybrid heating microwave toroidal fluidised bed for granular materials, which gives an unprecedented solution to the microwave treatment uniformity conundrum.
- Development of a scalable and robust metal conveyor belt system for microwave heating of large particles in extreme conditions.
- Contribution to the art with publications that deals with microwave material properties characterisation and further the understanding of hybrid conventional-

microwave heating techniques in high-temperature systems, and also with other purely microwave high temperature processing techniques (see next section).

1.4 List of publications

- Durán-Jiménez, G., Hernández-Montoya, V., Rodríguez Oyarzun, J., Montes-Morán, M. Á., & Binner, E. (2019). Pb(II) removal using carbon adsorbents prepared by hybrid heating system: Understanding the microwave heating by dielectric characterization and numerical simulation. Journal of Molecular Liquids, 277, 663–671. https://doi.org/10.1016/j.molliq.2018.12.143

- Buttress, A. J., Rodriguez, J. M., Ure, A., Ferrari, R. S., Dodds, C., & Kingman, S. W. (2019). Production of high purity silica by microfluidic-inclusion fracture using microwave pre-treatment. Minerals Engineering, 131, 407–419. https://doi.org/https://doi.org/10.1016/j.mineng.2018.11.025

Chapter 2 Microwave heating fundamentals

This chapter introduces microwave-heating fundamental principles in a high-temperature context, summarising the critical parameters and phenomena involved in system design.

2.1 Maxwell's equations and constitutive relations

The physical laws that govern electromagnetic fields are represented in Maxwell's equations of which detailed explanation can be found in most fundamental electromagnetism and microwave engineering textbooks [1], [2], [22], [23]. Phasor-form time-harmonic equations are given by [1], [22].

$$\nabla \times \overline{\mathrm{E}} = -\mathrm{j}\omega\overline{\mathrm{B}} \qquad \text{Faraday's law} \qquad (2.1)$$

$$\nabla \times \bar{H} = j\omega\bar{D} + \bar{J} \qquad \text{Ampère's Law} \qquad (2.2)$$

$$\nabla \cdot \bar{D} = \rho \qquad \text{Gauss' Law} \qquad (2.3)$$

$$\nabla \cdot \bar{B} = 0 \qquad \text{Gauss' Law for magnetism} \qquad (2.4)$$

where $\bar{E}$ and $\bar{H}$ are the electric and magnetic fields, $\bar{D}$ and $\bar{B}$ are the electric and magnetic flux density, $\bar{J}$ is the electric current sources and ρ is the electric charge density.

The interaction between electromagnetic radiation and materials depends on the material's constitutive parameters, electric permittivity (ε), magnetic permeability (μ) and electric conductivity (σ). For practical reasons, these parameters are generally presented relative to the corresponding free space quantities ($\varepsilon_0 = 8.8541878176 \times 10^{-12}$ F/m and $\mu_0 = 4\pi \times 10^{-7}$ H/m) as $\varepsilon_r = \varepsilon/\varepsilon_0$ and $\mu_r = \mu/\mu_0$. It is also useful to separate real from imaginary parts due to their physical implications, as will be implied from the following sections, as $\varepsilon_r = \varepsilon_r{}' - j\varepsilon_r{}''$ and $\mu_r = \mu_r{}' - j\mu_r{}''$. The constitutive relations that describe the macroscopic characteristics of a linear media can be written as [1], [22]

$$\bar{D} = \varepsilon\bar{E} = \varepsilon_0(\varepsilon_r' - j\varepsilon_r'')\bar{E} \tag{2.5}$$

$$\bar{B} = \mu\bar{H} = \mu_0(\mu_r' - j\mu_r'')\bar{H} \tag{2.6}$$

$$\bar{J} = \sigma\bar{E} \tag{2.7}$$

2.2 Electromagnetic power

The Poynting's theorem states the energy (power) conservation in electromagnetics. For a volume V enclosed by a surface S it can be derived from Maxwell's equations as [1], [22]

$$-\frac{1}{2}\int_V (\bar{E}\cdot\bar{J}_s^* + \bar{H}^*\bar{M}_s)\,dv \tag{2.8}$$

$$= \frac{1}{2}\oint_S (E\times H^*)ds + \frac{\sigma}{2}\int_V |\bar{E}|^2\,dv$$

$$+\frac{\omega}{2}\int_V (\varepsilon_0\varepsilon_r''|\bar{E}|^2 + \mu_0\mu_r''\bar{H}^2)dv$$

$$+\frac{j\omega}{2}\int_V (\mu'|\bar{H}|^2 - \varepsilon'|\bar{E}|^2)dv$$

Each term represents:

$$\mathrm{P_s} = -\frac{1}{2}\int_V (\bar{E}\cdot\bar{J}_s^* + \bar{H}^*\bar{M}_s)\,dv$$ Power delivered by the current sources. (2.9)

$$P_0 = \frac{1}{2}\oint_S (E\times H^*)ds$$ Power flow out of the surface S. (2.10)

$$P_l = \frac{\sigma}{2}\int_V |\bar{E}|^2\,dv$$ Power dissipated due to conductivity, dielectric and magnetic losses. (2.11)

$$+\frac{\omega}{2}\int_V (\varepsilon_0\varepsilon_r''|\bar{E}|^2 + \mu_0\mu_r''\bar{H}^2)dv$$

$$P_{st} = \frac{j\omega}{2}\int_V (\mu'|\bar{H}|^2 - \varepsilon'|\bar{E}|^2)dv$$ Stored power. (2.12)

The Poynting's theorem can be written as $P_s = P_0 + P_l + P_{st}$. This balance equation shows that the power from the sources is equal to the transmitted power out of the surface, plus the power loss and the stored power [22]. Equation (2.11) shows that electric field dissipation is dependent upon the imaginary part of the electric permittivity and conductivity, while magnetic field dissipation depends upon the imaginary part of the magnetic permeability. Meanwhile, equation (2.12) shows that energy storage in the form of the electric and magnetic fields is a function of the real part of the electrical permittivity and magnetic permeability respectively.

2.3 Electromagnetic properties variability

The characterisation of microwave properties as described above is paramount for the design and operation of any microwave processing system. The material's microwave properties change under different processing conditions as they are dependent upon its composition, moisture content, temperature, frequency and bulk or solid density [12], [24], [25].

The dielectric properties of oat and barley straw during pyrolysis are a useful example to illustrate dielectric properties dependency of materials to these parameters; these are shown in Figure 2.1 and Figure 2.2 for temperatures up to 700 °C, measured by the cavity perturbation technique. Low-temperature absorption is mostly due to the high water content and the impact this has on the loss factor, but loss sharply decreases as temperature increases effectively drying the material. Then, during pyrolysis, the measured properties keep descending due to the release of any remaining bound water and due to weight loss; however, the material permittivity is independent of mass, this reduction being artifacts of the measurement method, as it is calibrated for the original volume. After 450 °C, a dramatic increase in the dielectric properties follows, as shown in Figure 2.2, due to the transformation to char with the consequent increase

in conductivity, making the material a highly microwave absorbent product (carbon) [26]. Limitations of this measurement technique are discussed in section 4.4.1. In particular, for biomass characterisation, the technique does not provide an accurate representation of the behaviour during microwave processing, as are based on heating up a small sample in a conventional furnace and then measure its dielectric properties in a microwave cavity, with the related rapid heat loss and lack of representation of heating profile and chemical evolution as will occur during volumetric heating of within a bulk material bed.

Similar behaviour can be seen in other materials, for example, pyrolysis of wood pellets [27], bituminous coal [28], hay [29], nutshells [30], among many others. Nonetheless, significant variation in dielectric properties with temperature are not exclusive for just carbonaceous materials in pyrolysis processes, as there are many other materials which also exhibit considerable changes with temperature [24], [25]. The effect of pre-drying of wood chips on the dielectric loss factor shown in Figure 2.3 clearly illustrates the moisture influence at low temperatures.

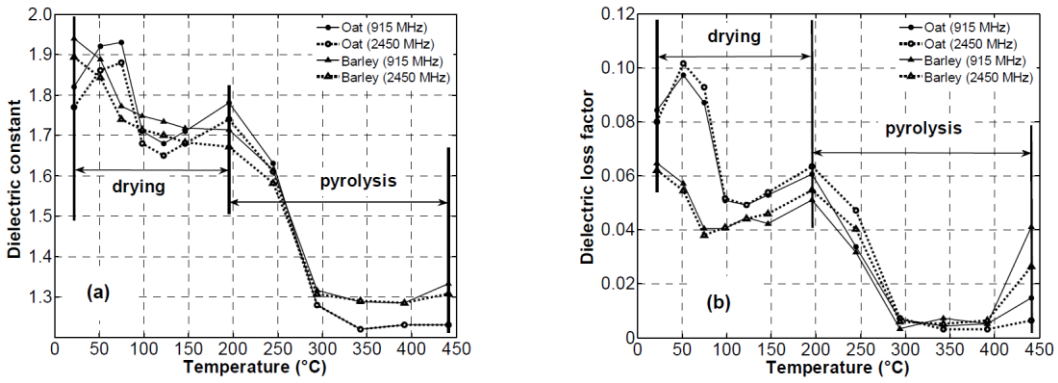


Figure 2.1 (a) Dielectric constant and (b) loss factor of oat and barley straw versus temperature in nitrogen atmosphere at 915 and 2,450 MHz up to 450 °C after [26], measured by cavity perturbation technique.

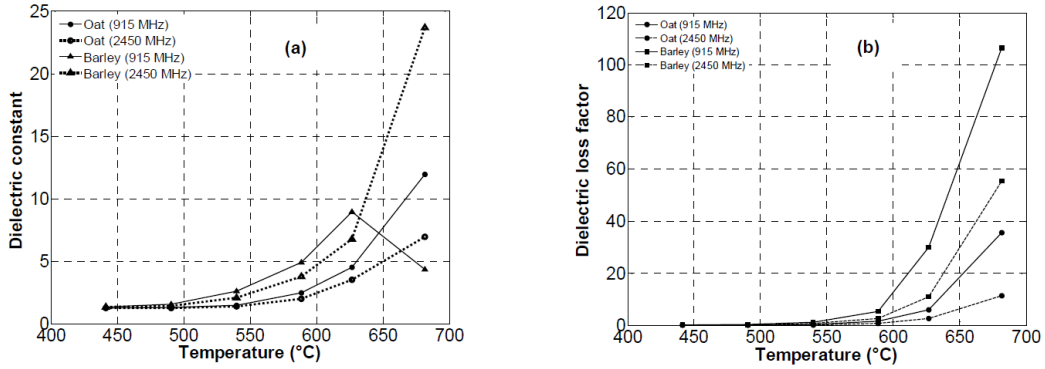


Figure 2.2 (a) Dielectric constant and (b) loss factor of oat and barley straw versus temperature in nitrogen atmosphere at 915 and 2,450 MHz up to 700 °C after [26], measured by cavity perturbation technique..

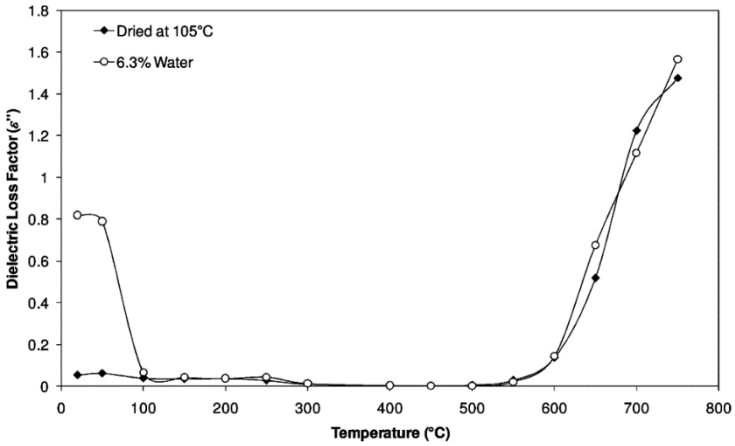


Figure 2.3 Dielectric loss factors versus temperature of wet and dry wood chippings at 2.45GHz after [27], measured by cavity perturbation technique.

To exemplify dielectric dependency upon bulk density of a material, vermiculite dielectric properties are shown in Figure 2.4. The dielectric property measurements represent the macroscopic response of a volume filled with the material and air, in which the air portion of the volume is given by the bulk density of the material. Therefore, as air approximates vacuum, the measured dielectric properties increase with an increase in bulk density (i.e. decrease of air and increase of product), as can be seen in Figure 2.4. Several mixing equations have been developed and are commonly used to estimate dielectric properties at different bulk densities [31], [32].

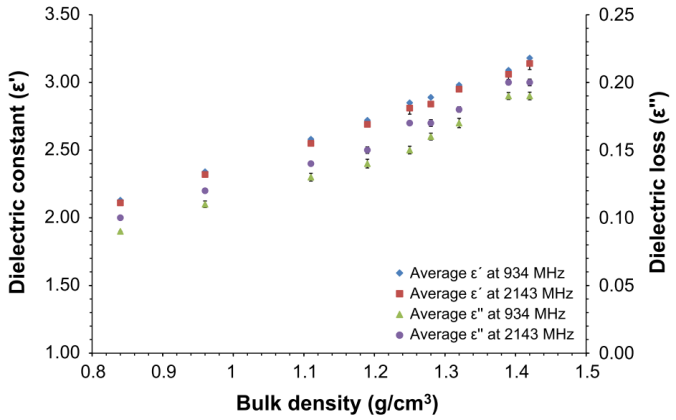


Figure 2.4 Dielectric properties of Vermiculite versus bulk density at 934 and 2,143 MHz after [31].

Moreover, the ability to penetrate the material effectively will depend on its size, shape, positioning, microwave absorption properties and the configuration of the electromagnetic fields [9]. In high-temperature processing, materials are subject to a broad range of temperatures and processing conditions, and thus to a wide variation of its response to microwaves. These variable behaviours imply the need for specific and sometimes sophisticated strategies to process materials under various conditions [33].

Frequency dependency of the complex permittivity can usually be expressed by the Debye model for linear polar dielectrics as [34]

$$\varepsilon_r = \varepsilon_\infty + \frac{\varepsilon_s - \varepsilon_\infty}{1 + j\omega\tau} \tag{2.13}$$

where ε_s is the material low frequency dielectric constant, ε_∞ is the material high frequency dielectric constant, ω is the angular frequency, and τ is the relaxation time which is the time required for dipole reorientation after external electric field is removed. Separating into real and imaginary terms we can write [34]

$$\varepsilon_r{}' = \varepsilon_\infty + \frac{\varepsilon_s - \varepsilon_\infty}{1 + \omega^2\tau^2} \tag{2.14}$$

$$\varepsilon_r'' = \varepsilon_\infty + \frac{(\varepsilon_s - \varepsilon_\infty)\omega\tau}{1 + \omega^2\tau^2} \tag{2.15}$$

When the relaxation time is the inverse of angular frequency ($\omega = 1/\tau$), a resonant response occur in which a local maximum occur. A useful material to illustrate this is water, the of which the real (k') and imaginary part (k'') of the complex permittivity for different temperatures is shown in Figure 2.5. For frequencies below the relaxation, an increase in temperature results in a decrease of the loss factor, and for frequencies above relaxation an increase in it.

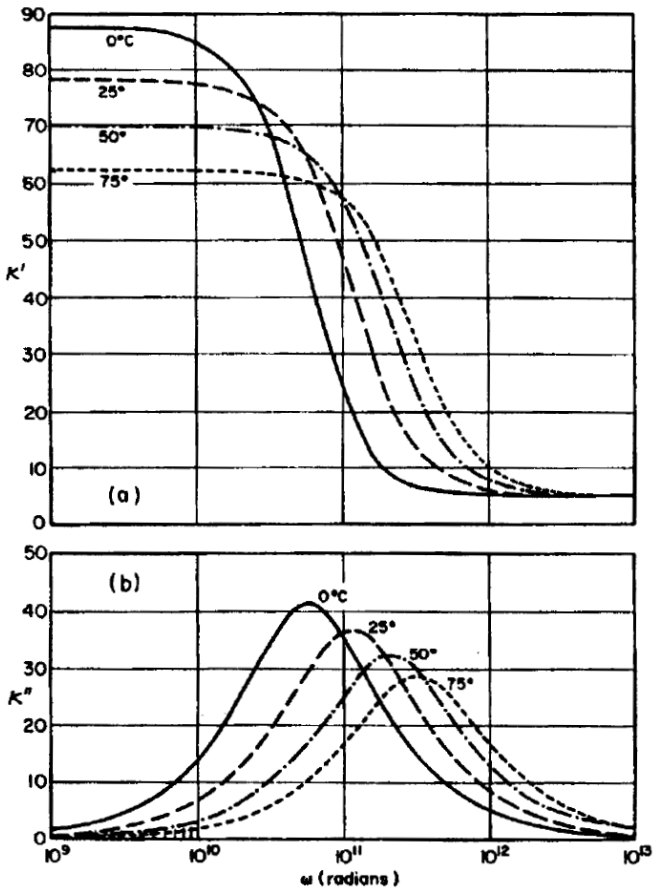


Figure 2.5 Dielectric constant (a) and loss factor (b) of water versus frequency for different temperatures based on the Debye model, reproduced from [34].

2.4 Scattering parameters

At microwave frequencies, the direct measurement of impedance or admittance of a network require very accurate open-circuit and short-circuits which are hard to manufacture at these frequencies. On the other hand, the measurement of scattered waves from a port require only matched loads, which are much easier to produce, making network representation based on wave scattering more practical [1], [2], [22], [35].

The scattering parameters can be used to describe the network frequency response, relating the incident, reflected and transmitted waves. Several properties of microwave components can be expressed in terms of its scattering parameters including reflection coefficient, voltage standing wave ratio, return and insertion loss, cross-coupling, impedance, admittance, among others [22]. Considering a network with N ports as illustrated in Figure 2.6, The scattering matrix is defined in relation to the incident and reflected waves in each port as [2]

$$\begin{bmatrix} V_1^- \\ V_2^- \\ \vdots \\ V_N^- \end{bmatrix} = \begin{bmatrix} S_{11} S_{12} & \cdots & S_{1N} \\ S_{21} & \ddots & \vdots \\ \vdots & & \\ S_{N1} & & S_{NN} \end{bmatrix} \begin{bmatrix} V_1^+ \\ V_2^+ \\ \vdots \\ V_N^+ \end{bmatrix}$$

Where V_n^+ is an incident wave to port n and V_m^- outgoing from port m.

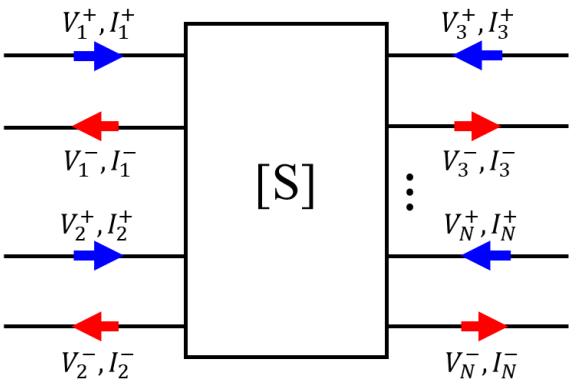


Figure 2.6 N-port network scattering matrix sketch.

Each element of the matrix can be determined for an incident wave from port j and the outgoing wave at port i, when the incident wave from every other port is zero (i.e. matched load), as [2]

$$S_{ij} = \left.\frac{V_i^-}{V_j^+}\right|_{V_k^+=0\ for\ k\neq j} \tag{2.16}$$

The S-matrix row index represents the output ports, while the column index represents the corresponding input port, as illustrated in Figure 2.7.

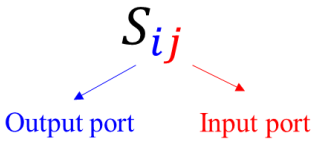


Figure 2.7 Scattering parameter nomenclature

In a one-port network, the scattering matrix that describes the device under test consists of a single element as $S_{11} = \Gamma = V_1^-/V_1^+$. This ratio of the reflected wave to incident wave on the same port is called the reflection coefficient [36]. It can be defined as a function of the DUT impedance (Z_L) and the line characteristic impedance (Z_0) as

$$\Gamma = \frac{Z_L - Z_0}{Z_L + Z_0} \tag{2.17}$$

The power distribution of the network can be defined as a function of the incident power from port 1 (P_i) as

$$P_{r1} = |S_{11}|^2 P_{i1} \qquad \text{Power reflected from the DUT} \tag{2.18}$$

$$P_a = (1 - |S_{11}|^2) P_{i1} \qquad \text{Power absorbed by the DUT} \tag{2.19}$$

A measure of how well matched the impedance of the DUT is to the impedance of the line is the standing wave ratio ($VSWR$). It is defined as the ratio of the maximum (E_{max}) to

minimum (E_{min}) value of the standing wave (Figure 2.8). The $VSWR$ can be expressed in terms of the reflection coefficient magnitude as [35], [37]

$$VSWR = \frac{E_{max}}{E_{min}} = \frac{1 + |S_{11}|}{1 - |S_{11}|} \tag{2.20}$$



Figure 2.8 Standing wave pattern example after [37]**.**

In a two-port network, the scattering matrix consists of 4 parameters which can be calculated as

$$S_{11} = \left.\frac{V_1^-}{V_1^+}\right|_{V_2^+=0} \qquad S_{21} = \left.\frac{V_2^-}{V_1^+}\right|_{V_2^+=0} \qquad S_{12} = \left.\frac{V_1^-}{V_2^+}\right|_{V_1^+=0} \qquad S_{22} = \left.\frac{V_2^-}{V_2^+}\right|_{V_1^+=0} \tag{2.21}$$

S_{11} and S_{22} represent the reflection coefficient of port 1 and port 2 respectively. S_{21} represents the transmission coefficient from port 1 to port 2, while S_{12} represent the transmission coefficient from port 2 to port 1.

The absorbed power by the applicator is given by the difference of the incident power minus the reflected and transmitted powers as $P_a = P_i - P_r - P_t$. As a function of the incident power, the power absorbed by the applicator is given by

$$P_{a1} = (1 - |S_{11}|^2 - |S_{21}|^2)\, P_{i1} \qquad \text{Power from port 1} \tag{2.22}$$

$$P_{a2} = (1 - |S_{22}|^2 - |S_{12}|^2)\, P_{i2} \qquad \text{Power from port 2} \tag{2.23}$$

In a microwave applicator context, for multiple feeding port systems, the power used for processing can be lost due to reflected power to the same port, transmitted to other ports

(i.e. cross-coupling) or absorbed in the applicator by other elements rather than the product (e.g. applicator walls, insulation). For convenience, scattering parameters magnitudes are usually noted in decibels. Decibels express a power ratio as

$$A(dB) = 10\log_{10}\frac{p_2}{p_1} \qquad \text{Ratio of power } p_2/p_1 \text{ in dB} \qquad (2.24)$$

Hence, $S(dB) = 10\log_{10}|S|^2 = 20\log_{10}|S|$. For example, if $S_{11} = -10dB$, the reflected power will be $P_r = 10^{(S11dB/10)}P_i = 0.1P_i$. Common metrics used to characterise microwave devices defined by the scattering parameters are

$$RL_1 = -20\log_{10}|S_{11}| \qquad \text{Return loss (dB) at port 1} \qquad (2.25)$$

$$RL_2 = -20\log_{10}|S_{22}| \qquad \text{Return loss (dB) at port 2} \qquad (2.26)$$

$$IL_1 = -20\log_{10}|S_{21}| \qquad \text{Insertion loss (dB) from port 1 to 2} \qquad (2.27)$$

$$IL_2 = -20\log_{10}|S_{12}| \qquad \text{Insertion loss (dB) from port 2 to 1} \qquad (2.28)$$

2.4.1 Smith chart

The Smith chart is a useful graphical tool that allows displaying impedance, admittances, reflection coefficient, VSWR, and any scattering parameter of a port simultaneously. Impedances can be represented as real and imaginary part in a Cartesian plane; however, open circuits, having an infinite impedance, cannot be shown in a useful manner. Instead, the whole impedance range can be represented in a polar plot. Circles of constant resistance and arcs of constant reactance overlaid in the polar plot form the impedance Smith chart [37], this is illustrated in Figure 2.9. Similarly, circles of constant conductance and arcs of constant susceptance form the admittance Smith chart (the same as impedance chart rotated in 180°).

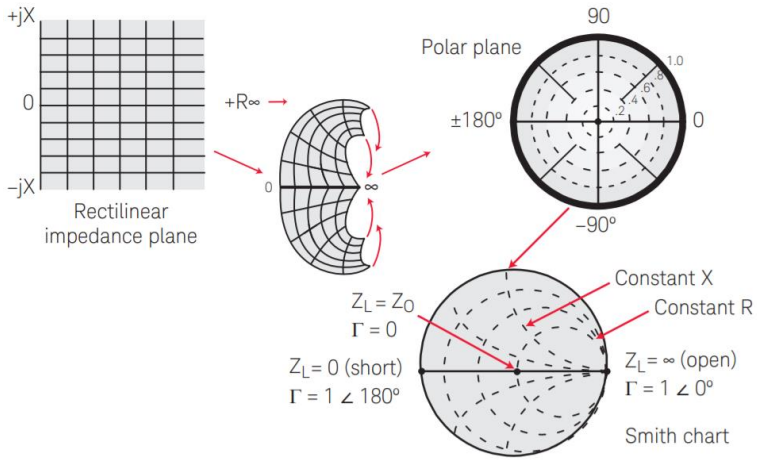


Figure 2.9 Smith chart construction overview after [37]**.**

Impedance normalised to the line impedance as $z = r + jx = Z/Z_0$ and can be plotted using the resistance circles (r - blue lines), and reactance arcs (x - green lines) as shown in Figure 2.10.

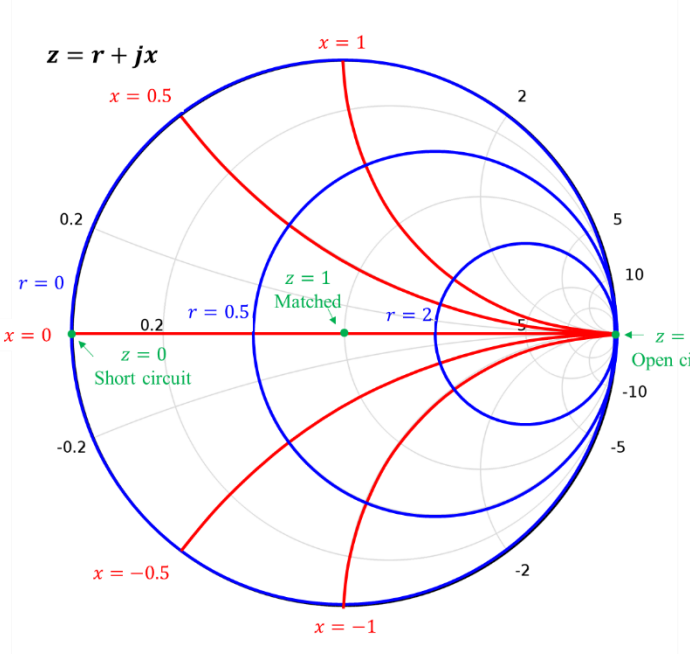


Figure 2.10 Impedance smith chart, normalised impedance reading.

The reflection coefficient can be read as the vector formed in the complex plane as in Figure 2.11. The horizontal axis ($Re(\Gamma)$) represent positions of minimum (i.e. left side, negative $Re(\Gamma)$) and maximum (i.e. right side, positive $Re(\Gamma)$) of the standing wave pattern. The

normalised impedance at a maximum location of a standing wave pattern is equal to its VSWR. Hence, the $VSWR$ can be obtained in the chart by drawing a circle of constant reflection coefficient magnitude (purple line) and intersecting to the right side of the horizontal axis, the reading of the respective constant resistance circle (orange) at this point represent the $VSWR$ value.

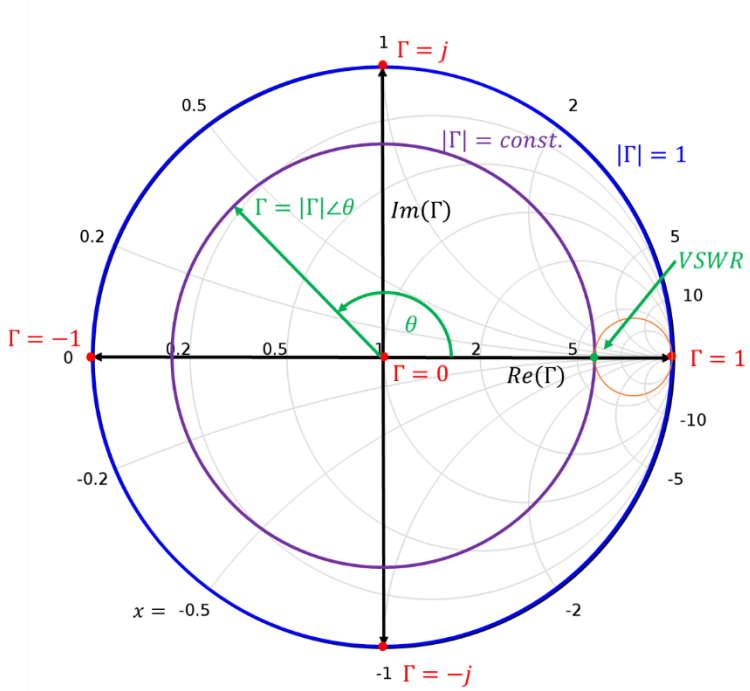


Figure 2.11 Impedance smith chart, reflection coefficient and VSWR reading.

2.5 Quality factor and resonant frequencies

This quantity gives a measure of how sharp the response of a resonant component is to an excitation and is inversely proportional to the rate of power dissipation to average stored energy. The quality factor of a resonant cavity can be defined as [1], [12]

$$Q = \omega \frac{U_{em}}{P} \tag{2.29}$$

Where ω is the angular frequency, U_{em} is the average stored electromagnetic energy and P is the dissipated power (i.e. energy loss per second). Alternatively, this parameter can also be defined as the ratio of the resonant frequency to the half-power bandwidth as [1], [12]

$$Q = \frac{f_0}{\Delta f} \tag{2.30}$$

The contribution to the quality factor can be separated depending on where the power is being dissipated in the form [38]

$$\frac{1}{Q_L} = \frac{1}{Q_0} + \frac{1}{Q_{ext}} \tag{2.31}$$

The first term related to the loaded quality factor (Q_L) represent the damping in the whole system. The first term on the right side related to the empty quality factor (Q_0) represents the damping in the resonator, and the second term on the right side related to the external quality factor (Q_{ext}) represent the damping on the coupling line. This effectively represents the link budget of power in the microwave system.

For generality, let's define Q_c as the quality factor due to the loss in the applicator metallisations (generally walls), and Q_d due to losses in the samples and dielectric furniture. Then, the quality factor for these contributions combined, generally called unloaded quality factor, is given by

$$Q_0 = \frac{1}{\frac{1}{Q_c} + \frac{1}{Q_d}} \tag{2.32}$$

This metric along with its resonance frequency is used to characterise microwave resonant components performance.

2.6 Dielectric properties characterisation

A variety of techniques to characterise the microwave properties of materials exists, such as cavity perturbation, transmission line, and open-ended probe [39]. The major driving factors to select an appropriate technique are the frequency of interest, physical properties (e.g. liquid or solid, granular size, and sample size restrictions), required the property to characterise (ε_r and μ_r), and the expected properties of the material [40]–[42]. A summary of the applicability and characteristics of the methods are shown in Table 2.1, which are detailed in the following subsections.

Table 2.1 Summary of microwave properties measurement techniques

Method	Frequency	Measurable properties	Expected properties	Remarks
Coaxial probe	10 MHz – 50 GHz	ε_r	High loss	Extremely Broadband. Lossy liquids and powders.
Transmission line	50 MHz - 60 GHz	ε_r, μ_r	Low to mid loss	Broadband. Best for low to mid loss machinable solids, powders and liquids.
Resonant cavity	300 MHz – 30 GHz	ε_r, μ_r	Low loss	Discrete frequencies. Best for low-loss small solids, powders and liquids.

2.6.1 Open-ended probe

An open-ended probe for dielectric measurements consists in an open transmission line which radiates fringing fields into a bulk of a material sample [43]. Implementations of this include waveguides [44] and coaxial probes [41]. The probe is inserted into the sample or rested in its surface depending if the material is a liquid or solid [41]. The reflection scattering parameter (S_{11}) is measured, and the complex permittivity of the material under test is calculated from it using models associated with the physical properties of the probe [45]. This technique provides a broadband measurement depending on the analyser and probe properties, with commercial alternatives ranging 10 MHz to 50 GHz [46]. This technique is mostly adequate for high-loss liquids and, to less extent, powdered materials [40], [41].

2.6.2 Cavity perturbation technique

A resonant cavity resonance frequency will shift, and its quality factor will change, upon the perturbation of its fields by the insertion of an object as illustrated in Figure 2.12. This principle can be used to measure the microwave properties of a material that is inserted into a resonant cavity, by measuring the variation in resonant frequency and quality factor [47]. Only a set of discrete frequencies can be measured in the same cavity at frequencies where it exhibits a resonant behaviour.

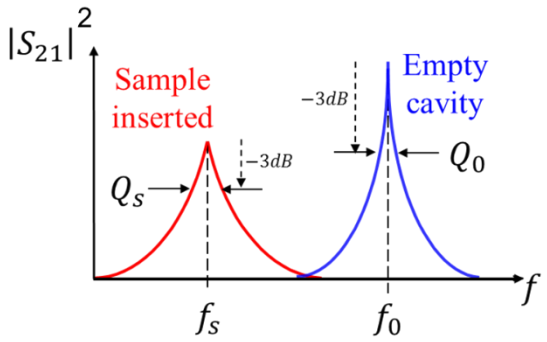


Figure 2.12 Illustration of the cavity perturbation effect on the resonance upon insertion of a small dielectric load.

This method is commonly used for electric permittivity measurements by putting the sample in a zone where the resonant mode is known to have an electric field maximum and magnetic field minimum. Alternatively, the method can be used for magnetic permeability measurement by locating the sample in a magnetic field maximum and electric field minimum [48].

This technique is suitable for analysing solid, liquid or powder materials. The sample should be of electrically small and low loss, as the method formulation assumes minimal alteration of the fields, an aspect that only holds under the conditions mentioned above [47].

2.6.3 Transmission line method

This method is based on filling a section of a transmission line and measuring the scattering parameters of such network element, in reflection (Figure 2.13) and/or transmission (Figure 2.14) modes [49]. These parameters can be then converted to permittivity and

permeability by a variety of methods/algorithms based on the physical properties of the transmission line, sample and holder [42]. Most commonly used setups are based on coaxial lines and waveguides in reflection/transmission mode. Nonetheless, high-temperature systems might be easier to implement in a reflection setup as one end of the fixture can be heated [50], [51].

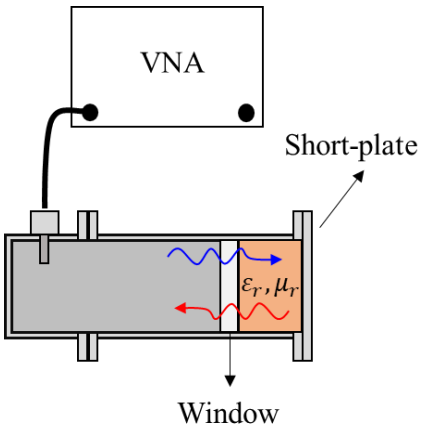


Figure 2.13 Transmission line setup for measurement of microwave properties in reflection mode (one-port)

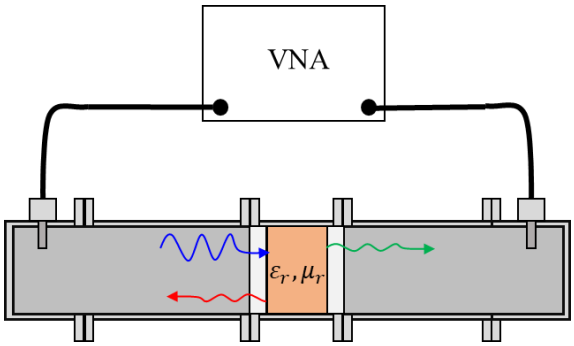


Figure 2.14 Transmission line setup for measurement of microwave properties in reflection/transmission mode (two-port).

Coaxial lines can produce considerably broad measuring frequency bands and can be used for measurement as low as 50 MHz where the use of waveguides is unpractical due to its size, whereas waveguides system bandwidth is limited by its waveguide band, and are used between 900 MHz up to mm-waves [41]. The use of co-planar waveguides has been reported for up to 220 GHz [52].

Coaxial line samples are compact and require a toroidal shape [53], [54]. This type of construction generally requires more sample preparation, and the holders can be harder to build [41]. Waveguide systems can handle large samples, which in turn, can be more representative of the bulk, considering a material that might be locally heterogeneous.

This method can be used to measure low and medium loss samples accurately and is especially well suited for solid machined samples, as air gaps are usually the largest source of

error [41], [42]. Granular and liquids can be tested with this method too, provided the sample holder walls can confine the material without significant air gaps. Accurate high-temperature implementations have been made, but do require complex error correction strategies to compensate for thermal expansion and waveguide deformation [55].

S-parameter to permittivity conversion methods include Nicholson-Ross-Weir (NWR) [56], new non-iterative (NNI, alternative simplified formulation of NWR) [57], NIST iterative [58], transmission phase shift (TPS), iterative polynomial fits (IPF) [59]. Other unpublished methods exist and are implemented in commercial software [41].

The selection of an adequate algorithm will depend on the sample size, magnetic properties, and expected microwave properties. A summary of the method suitability is shown in Table 2.2 based on the information given in [41], [42], [56]–[59].

Table 2.2 Scattering parameters to permittivity methods

Method	Quantity measurement	Sample size	Sample loss	Comments
NWR	ε_r, μ_r	Small	Low to high	Divergence in low-loss materials near $\lambda_g/2$
NNI	ε_r	Arbitrary	Low	Fast and accurate
NIST	ε_r	Arbitrary	Low to high	Slow and accurate, needs good initial guess ε_r
TPS	ε_r	Small	Low	Fast and accurate, independent sample position, needs accurate machining
IPF	ε_r, μ_r	Arbitrary	Low	Good for magnetic materials.

2.7 Heating mechanisms

At microwave frequencies, electromagnetic heating can be produced by various physical mechanisms such as polarisation and conduction losses, magnetic hysteresis and eddy currents [9], [33].

A useful quantity to assess heating distribution in a volume and the effectiveness of treatment is the power loss density. This quantity represents the power loss per unit of volume and can be derived from equation (2.11) as

$$P_d = \frac{\omega}{2}\left(\left(\frac{\sigma}{\omega} + \varepsilon_0\varepsilon_r''\right)|\bar{E}|^2 + \mu_0\mu_r''\bar{H}^2\right) \tag{2.33}$$

Including the electric conductivity (σ) as part of the effective imaginary electric permittivity ($\varepsilon_{reff}'' = \sigma/(\varepsilon_0\omega) + \varepsilon_r''$), equation (2.33) can be rewritten as

$$P_d = \frac{\omega}{2}\left(\varepsilon_0{\varepsilon_{reff}}''|\bar{E}|^2 + \mu_0\mu_r''|\bar{H}|^2\right) \tag{2.34}$$

where ${\varepsilon_{reff}}''$ and μ_r'' are usually called electric and magnetic loss factors as they represent the power loss due to the effect of the electric and magnetic field interaction with the media. In this workthe imaginary part of the complex permittivity will represent effective values unless otherwise stated.

The dissipated power will act as heating source, transforming the electromagnetic energy in an increase of temperature within the material. A simplified model of such behaviour can be modelled as a heat transfer function [60]

$$P_d = \rho C_p\frac{\partial T}{\partial t} + \frac{hA}{V}(\mathrm{T} - \mathrm{T_0}) \tag{2.35}$$

where ρ is the material density, C_p is the material heat capacity, T is the temperature, h is the heat transfer coefficient, A is the surface area, V is the volume, and T_0 is the ambient temperature. Solving the differential equation (2.35) considering an initial temperature equal to ambient gives a solution of the form

$$T(t) = T_0 + \frac{P_d V}{Ah}\left(1 - e^{\left(-\frac{Ah}{\rho C_p V}\right)t}\right) \tag{2.36}$$

An example temperature profile based on equation (2.36) is shown in Figure 2.15.

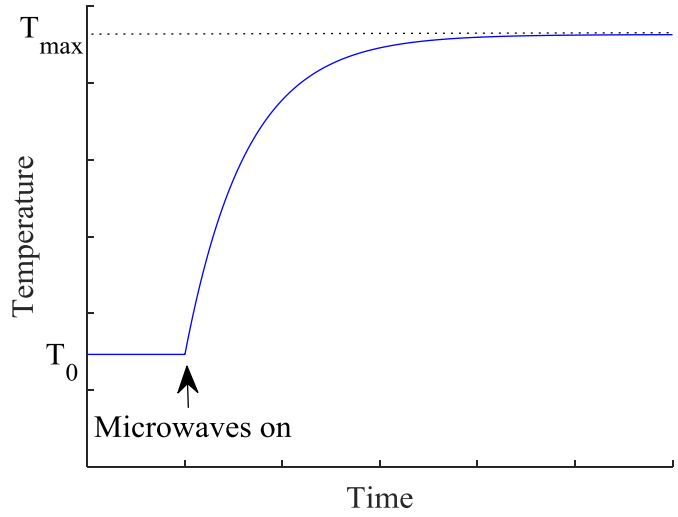


Figure 2.15 Microwave heating qualitative profile.

The maximum attainable temperature is given by $T_0 + (P_d V)/(Ah)$, highlighting the effect of the sample volume and surface area in this limit. The higher the volume and smaller surface area the bigger the maximum temperature. Furthermore, the power density also affects the maximum temperature directly. The heating rate is given by the derivative of the temperature profile as

$$\frac{\partial T}{dt} = \frac{P_d}{\rho C_p} e^{\left(-\frac{Ah}{\rho C_p V}\right)t} \tag{2.37}$$

which present a maximum at the start of the heating ($t = 0$), being directly proportional to the power loss density, with a rate of $P_d/(\rho C_p)$.

2.7.1 Dipolar losses

At microwave frequencies, the dominant polarisation that affects microwave heating is dipolar (i.e. material's permanent dipoles) [33]. When subjected to varying electric fields, the dipoles will try to align to the field polarisation. Due to the high-frequency oscillation of the electric field, the molecule alignment will lag and their movement will result in intermolecular collisions that will generate heat by friction [9], [33]. A representation of this behaviour in water is shown in Figure 2.16.

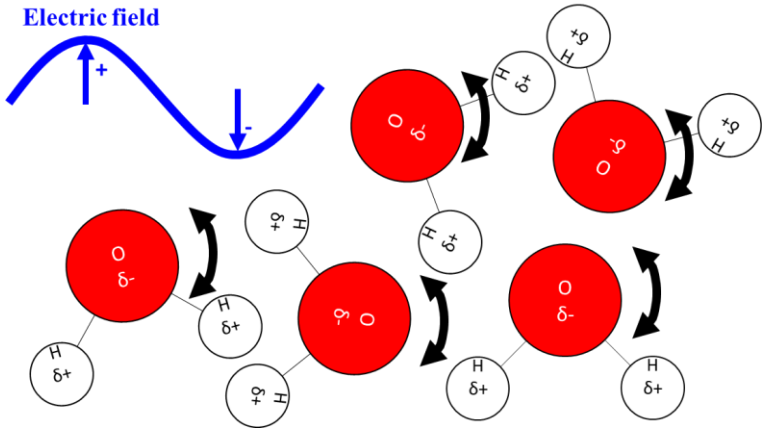


Figure 2.16 Representation of dipolar loss mechanism in water.

2.7.2 Interfacial losses

This heating mechanism, also known as Maxwell-Wager, occur in heterogeneous material mixtures with free charged particles exists within a non-conductive media. Charge can build up in the interface between the materials as response to an applied electromagnetic field, resulting in effective polarisation and, similarly to dipolar losses, dissipation in the form of heat [12].

2.7.3 Conduction losses

A conductive material subjected to electric fields will experience a movement of its free charge aligned with the field polarisation, developing a current flow. These flowing currents are dissipated as heat as a function of the material resistivity (i.e. electron, ions, atomic and

molecular collisions resulting in heat generation). This mechanism is also commonly known as Ohmic, resistive or Joule losses [9], [33].

2.7.4 Magnetic hysteresis

Ferromagnetic materials present magnetic dipoles which, analogously to dipolar losses for the electric field, try to align with the fast-varying magnetic fields, lagging and generating oscillatory friction and heat. Magnetisation by an alternating magnetic field results in a hysteresis loop, once magnetised in one direction the material will not relax by itself needing an opposing field [33], [61]. A representation of this loop is shown in Figure 2.17.

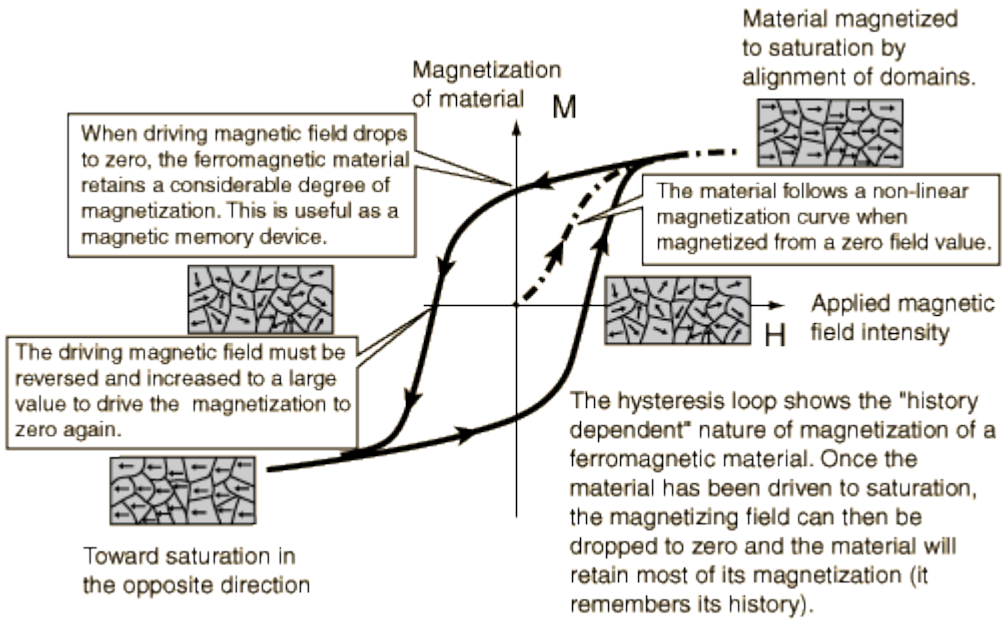


Figure 2.17 Representation of a hysteresis loop on a ferromagnetic material exposed to a varying magnetic field after [61]**.**

2.7.5 Eddy currents

These are the currents induced in a conductive material due to being exposed to a magnetic field. These currents will dissipate as a function of the material resistivity generating heat (i.e. conduction loss) [9], [33]. This mechanism is generally exploited in induction heating where a workpiece surface is heated by the induced currents (i.e. skin heating).

2.7.6 Remarks

The dipolar loss is the primary mechanism for microwave heating of most electrical insulators. Conduction loss and eddy currents drive microwave heating of conductor and semiconductor materials. Hysteresis loss only affects magnetic materials [9], [33].

2.8 Heating strategies

When materials exhibit good microwave absorbent properties, a direct heating method can be used efficiently, in which the material is directly exposed to microwave energy. For highly transparent materials indirect methods are more suitable, in which auxiliary absorbent materials are used to couple the microwave energy efficiently, which will then heat the product through thermal conduction [33], [62]. Another strategy for transparent materials is the use of hybrid heating, in which a combination of conventional and microwave heating is carried out. This is usually done as pre-treatment by conventional heating methods up to a state in which materials become sufficiently microwave susceptible [63].

The significant variation of temperatures with the resulting change of the materials microwave properties introduces the need for sophisticated approaches to achieve adequate treatment. Strategies can mix both direct and indirect microwave heating and combine with conventional heating and can comprise several treatment stages of different nature or varying operational parameters. The use of hybrid techniques and susceptors opened the microwave processing scope to several applications where its use was considered unpractical, such as bulk metals and microwave transparent materials [62], [64], [65]. Several examples of susceptor-assisted microwave processing can be found in [66].

2.9 Sample shape and electric field orientation influence on heating efficiency

The effectiveness of the interaction of a material sample with the electromagnetic fields depends on the field boundary conditions. Depolarisation, where there is a component of the

electric field normal to a material boundary, can reduce the electric field within a material and this can have a major effect on the heating efficiency. Considering an interface between two dielectric mediums of permittivity ε_1 and ε_2 respectively, as shown in Figure 2.18 and Figure 2.19.

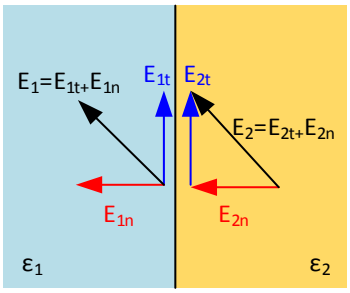


Figure 2.18 Illustration of boundary conditions for tangential component of the electric field on a dielectric-dielectric interface.

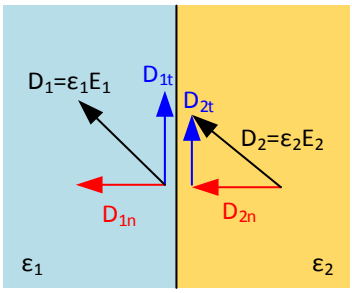


Figure 2.19 Illustration of boundary conditions for normal component of the electric flux density on a dielectric-dielectric interface.

The boundary conditions for the electric field on a dielectric-dielectric interface are that the tangential component is continuous across the interface ($E_{1t} = E_{2t}$) and that the normal component of the electric flux density is continuous across the dielectric boundary ($D_{1n} = D_{2n}$). Therefore, the dielectric boundary conditions for tangential and normal electric field components can be written as

$$E_{1t} = E_{2t}$$

$$\varepsilon_1 E_{1n} = \varepsilon_2 E_{2n}$$

This suggest that arranging the sample surface tangential to the polarisation of the electric field will ensure a higher power loss density as the field is maximised (equal to the external field in the boundary). If the sample surface present itself perpendicular to the field

polarisation a depolarisation effect (i.e. reduction of the internal field) will occur given by the ratio of permittivity of both materials.

The reduction of the electric field due to depolarisation can result in a drastic reduction of the heating rate for materials with high dielectric constant. This can be illustrated for a cylindrical sample with an applied electric field E_0 as shown in Figure 2.20.

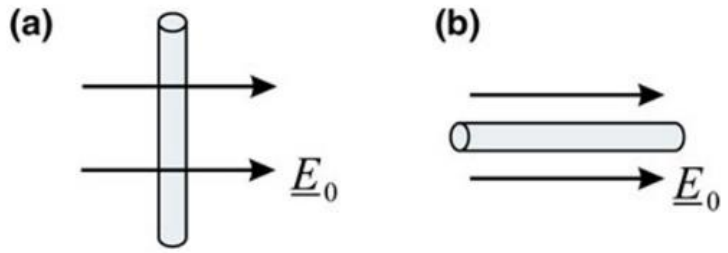


Figure 2.20 Electric field (a) polarised perpendicular to the surface and (b) parallel to the surface of a cylindrical sample, reproduced from [67].

The ratio of internal electric fields and powers between both polarisations is [67]

$$\frac{E_{\parallel}}{E_{\perp}} \approx \frac{1}{2}\left((\varepsilon_1 + 1) - j\varepsilon_2\right)$$

$$\frac{P_{\parallel}}{P_{\perp}} \approx \frac{1}{4}\left((\varepsilon_1 + 1)^2 + \varepsilon_2^2\right)$$

For example for water at 900 MHz, the power dissipation ratio is greater than 1,600, resulting in a dramatic difference in heating rates [67].

2.10 Legal framework

2.10.1 Industrial heating frequencies and applications

Electromagnetic heating systems operate in the industrial, scientific and medical (ISM) frequency bands. The International Telecommunications Union (ITU) radio regulations define these bands for the *operation of equipment or appliances designed to generate and use locally radio frequency energy for industrial, scientific, medical, domestic or similar purposes, excluding applications in the field of telecommunications* [68]. These bands are portions of the

electromagnetic spectrum (Figure 1.1) allocated to avoid interference with telecommunication applications [69]. However, numerous telecommunication systems that can withstand potential interference exist, and are commonly used, such as Wi-Fi, Bluetooth, Zigbee, wireless telephones, RFID and NFC [70]. Table 2.3 shows the designated ISM bands and Table 2.4 summarises some of the current applications that make use of ISM frequencies. Most industrial microwave heating systems operate at 433, 915 and 2,450 MHz.

Table 2.3: ISM frequency allocations

Centre frequency	Frequency band
6.78 MHz	6.765-6.795 MHz
13.567 MHz	13.553-13.567 MHz
27.12 MHz	26.957-27.283 MHz
40.68 MHz	40.66-40.70 MHz
433.92 MHz	433.05-434.79 MHz
915 MHz*	902-928 MHz
2 450 MHz	2 400-2 500 MHz
5.8 GHz	5.725-5.825 GHz
24.125 GHz	24.00-24.25 GHz
61.25 GHz	61.00-61.50 GHz
122.5 GHz	122-123 GHz
245 GHz	244-246 GHz

*896MHz in the United Kingdom

Table 2.4: ISM equipment in current use, reproduced from [69]

Frequency (MHz)	Major applications	RF power (typical)	Estimated No. in use
Below 0.15	Industrial induction heating (welding and melting of metals) Ultrasonic cleaning (15-30 kHz) Medical applications (ultrasonic diagnostic imaging)	10 kW-10 MW 20-1,000 W 100-1,000 W	> 100,000 > 100,000 > 10,000
0.15-1	Induction heating (heat treating, package sealing, welding and melting of metals) Ultrasonic medical diagnostics	1 kW-1 MW 100-1,000 W	> 100,000 > 100,000
1-10	Surgical diathermy (1-10 MHz dampened wave oscillator) Wood gluing and wood curing (3.2 and 6.5 MHz) Valve induction generators production of semi-conductor material RF arc stabilized welding (1-10 MHz dampened wave oscillator)	100-1,000 W 10 kW-1.5 MW 1-200 kW 2-10 kW	> 100,000 > 1,000 > 10,000

10-100	Dielectric heating (the majority operate on frequencies in the ISM bands at 13.56, 27.12 and 40.68 MHz, but many also operate on frequencies outside the ISM bands)		
	– ceramics	15-300 kW	< 1,000
	– foundry core drying	15-300 kW	< 1,000
	– textile drying	15-200 kW	> 1,000
	– business products (books, paper, gluing and drying)	5-25 kW	> 1,000
	– food (post baking, meat and fish thawing)	10-100 kW	< 1,000
	– solvent drying		
	– wood drying and gluing (veneer and lumber drying)	5-400 kW	> 10,000
	– general dielectric drying	5-1,000 kW	> 100,000
	– plastic heating (die sealing and plastic embossing)	1-50 kW (most < 5 kW)	> 10,000
	Medical applications		
	– medical diathermy (27 MHz)	100-1,000 W	> 1,000
	– magnetic resonance imaging (10-100 MHz in large shielded rooms)		
100-1 000	Food processing (915 MHz)	< 200 kW	< 1,000
	Medical applications (433 MHz)		
	RF plasma generators		
	Rubber vulcanization (915 MHz)		< 1 000
Above 1 000	RF plasma generators		
	Domestic microwave ovens (2,450 MHz)	600-1,500 W	> 200 million
	Commercial microwave ovens (2,450 MHz)	1.5-200 kW	
	Rubber vulcanization (2,450 MHz)	6-100 kW	< 1,000
	RF excited ultraviolet curing		

2.10.2 Safety regulations

The British Standards BS EN 60335-2-25:2002 and BN EN 60335-2-90:2006 specify a microwave leakage limit of 50 W/m^2 at any point 50 mm or more from the external surface of the device. In the United Kingdom, the Health and Safety Executive provide control of electromagnetic fields at work regulations [71]. Compliance limits for typical industrial microwave frequencies are summarised in Table 2.5 and Table 2.6.

Table 2.5. Exposure limit values for 300MHz – 6GHz, adapted from [71]

Health effects		
Area of exposure	SAR (W/kg)*	SA (mJ/kg)**
Whole body	0.4 (average over whole body)	
Head and trunk	10	
Limbs	20	
Sensory effects		
Head		10

*Specific absorption rate (SAR) is the rate at which energy is absorbed per

unit mass of body tissue in watts per kilogram.

**Specic energy abosption (SA) is the energy absorbed per unit mass of biological tissue in joules per kilogram.

Table 2.6. Exposure action levels, adapted from [71]

Frequency range	External electric field strength ALs (E) [V/m]	Magnetic flux density ALs (B) [μT]
400MHz – 2GHz	$3 \times 10^{-3}\, f^{1/2}$	$1 \times 10^{-5}\, f^{1/2}$
2GHz – 6GHz	1.4×10^{2}	4.5×10^{-1}

f is the frequency in GHz

If exposure levels are below this ALs, it will comply with the limits specified in Table 2.5.

2.11 Microwave processing system

A microwave processing system is usually comprised of four major sub-systems as shown in Figure 2.21. A generator unit which will provide the microwave energy, a power coupling unit that will ensure an effective delivery of the energy, an applicator unit that will provide a means for the interaction between the energy and the product, and a unit for the monitoring and general control of the process. Generator, power coupling and applicator units are interconnected by means of microwave transmission lines. This thesis is centred around the design of applicator solutions for a variety of materials and processing conditions. Details on microwave processing sub-systems and components including microwave generators, transmission line theory, matching techniques, filters, etc, can be found elsewhere [1], [2], [7], [12], [19], [22], [23], [35], [72].

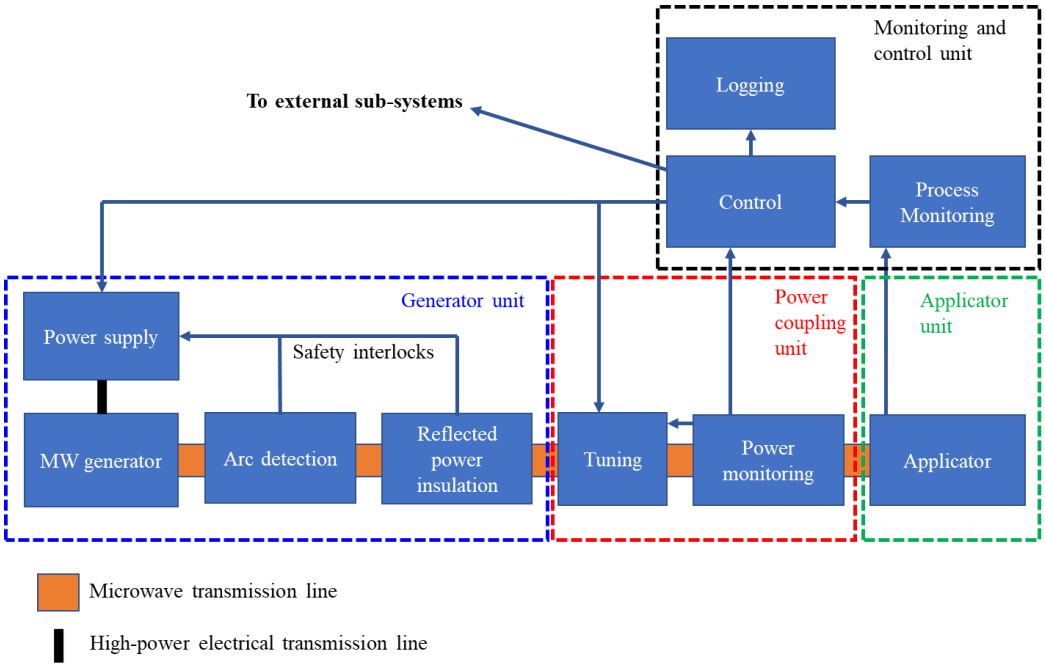


Figure 2.21 Generic microwave processing system

2.12 Waveguides

Waveguides are a type of transmission line with extremely low-loss and high-power handling abilities [73]. They consist of an electrically conductive hollow tube that allows the propagation of electromagnetic waves through it in defined propagating modes (Figure 2.22). These modes can only be transverse electric (TE) or transverse magnetic (TM), with the electric or magnetic field perpendicular to the direction of propagation respectively, due to the conditions imposed by the electrically conductive boundary (i.e. the electric and magnetic field cannot be simultaneously transverse to the propagation direction as in transverse electromagnetic waves (TEM)) [2]. TE waves are defined by having $E_z = 0$ and $H_z \neq 0$, while TM waves are defined with $E_z \neq 0$ and $H_z = 0$.

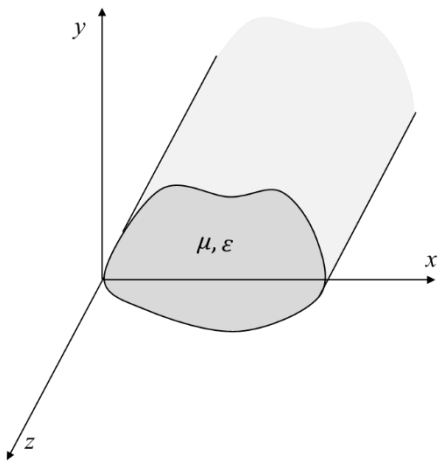


Figure 2.22 Generic cross section waveguide sketch.

Each propagation mode has specific cut-off frequencies determined by the waveguide cross-section geometry and size, allowing its propagation only above this frequency, hence acting as a high-pass filter structure [74]. Waveguides are generally operated in what is called the dominant mode, which is the one with lower cut-off frequency. Single-mode operation is guaranteed when the generator frequency band lies within the dominant and the next mode cut-off frequencies. In multi-mode regime, several propagation patterns coexist, and power can be transformed from one mode to another [75]. Attenuation in a circular waveguide is shown in Figure 2.23.

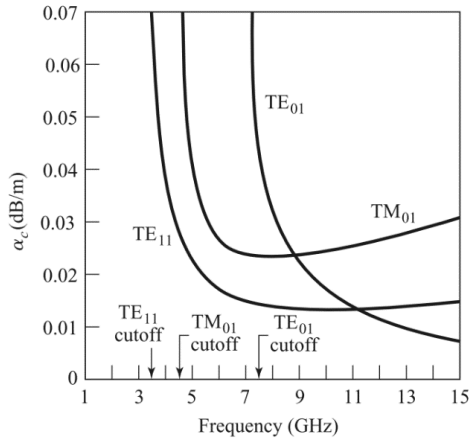


Figure 2.23 Attenuation per meter of different modes in a circular copper waveguide with radius $a = 2.54$ cm, after [22].

Rectangular and circular cross-section waveguide geometries are shown in Figure 2.24. A summary of the rectangular waveguide and circular waveguide main parameters are shown in Table 2.7 and Table 2.8 respectively. The electromagnetic field expressions for both type of

waveguides for TE and TM modes can be found in most electromagnetics fundamental and microwave engineering textbooks [1], [22], [23], [74], [75].

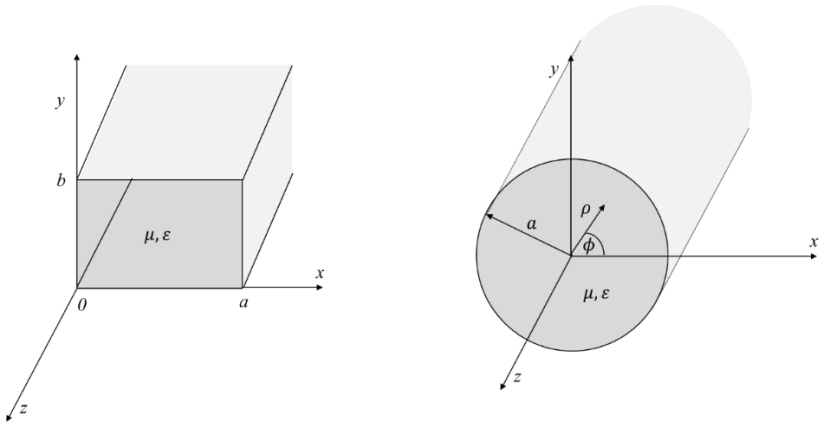


Figure 2.24 Rectangular and circular cross-section waveguide sketches.

Table 2.7. Summary of main parameters for rectangular waveguides adapted from [22]

Quantity	Description	Equation	
k	Wave number	$\omega\sqrt{\mu\varepsilon}$	(2.38)
k_c	Cut-off wave number	$\sqrt{(m\pi/a)^2 + (n\pi/b)^2}$	(2.39)
β	Phase constant	$\sqrt{k^2 - k_c^2}$	(2.40)
λ_c	Cut-off wavelength	$2\pi/k_c$	(2.41)
f_c	Cut-off frequency	$k_c/(2\pi\sqrt{\mu\varepsilon})$	(2.42)
λ_g	Guided wavelength	$2\pi/\beta$	(2.43)
v_p	Phase velocity	ω/β	(2.44)
η	Intrinsic impedance	$377/\sqrt{\varepsilon_r}$	(2.45)
Z_{TE}	Wave impedance TE mode	$k\eta/\beta$	(2.46)
Z_{TM}	Wave impedance TM mode	$\beta\eta/k$	(2.47)
R_s	Surface resistivity	$\sqrt{\omega\mu_0/(2\sigma)}$	(2.48)

$m, n \neq 0$ for TM modes

TE_{00} do not exist

Table 2.8. Summary of main parameters for circular waveguides adapted from [22]

Quantity	Description	Equation	
k	Wave number	$\omega\sqrt{\mu\varepsilon}$	(2.49)
k_c (TE)	Cut-off wave number for TE modes	p'_{nm}/a	(2.50)
k_c	Cut-off wave number for TM modes	p_{nm}/a	(2.51)

(TM)			
β	Phase constant	$\sqrt{k^2 - k_c^2}$	(2.52)
λ_c	Cut-off wavelength	$2\pi/k_c$	(2.53)
f_c	Cut-off frequency	$k_c/(2\pi\sqrt{\mu\varepsilon})$	(2.54)
λ_g	Guided wavelength	$2\pi/\beta$	(2.55)
v_p	Phase velocity	ω/β	(2.56)
η	Intrinsic impedance	$377/\sqrt{\varepsilon_r}$	(2.57)
Z_{TE}	Wave impedance TE mode	$k\eta/\beta$	(2.58)
Z_{TM}	Wave impedance TM mode	$\beta\eta/k$	(2.59)
R_s	Surface resistivity	$\sqrt{\omega\mu_0/(2\sigma)}$	(2.60)

p_{nm} is the m^{th} root of the bessel function of the first kind $J_n(x)$.

p'_{nm} is the m^{th} root of the derivative of the bessel function of the first kind $J_n{}'(x)$.

Refer to Appendix A for value tables.

Standard waveguide sizes that might be usable in the microwave ISM frequencies are summarised in Table 2.9.

Table 2.9 Standard rectangular waveguide sizes, adapted from [76]

ISM band	Name	WG#	Recommended band (GHz)	Inside dimensions (mm)	f_cTE_{10} (GHz)	f_cTE_{20} (GHz)
433 MHz	WR-2100	0	0.35-0.50	533.40 × 266.7	0.28	0.56
	WR-1800	1	0.45-0.63	457.20 × 228.6	0.33	0.66
	WR-1500	2	0.50-0.75	381.00 × 190.5	0.39	0.79
915 MHz	WR-1150	3	0.63-0.97	292.10 × 146.5	0.51	1.03
	WR-975	4	0.75-1.15	247.7 × 123.8	0.61	1.21
	WR-770	5	0.97-1.45	195.58 × 97.79	0.77	1.53
2,450 MHz	WR-430	8	1.72-2.60	109.22 × 54.61	1.37	2.75
	WR-340	9A	2.20-3.30	86.63 × 43.18	1.74	3.47
	WR-284	10	2.60-3.95	72.136 × 34.036	2.08	4.16

2.13 Waveguide cavity resonators

A closed waveguide can be used as a cavity resonator. Such resonator will store energy in the form of electric and magnetic fields, while power is dissipated in its wall and in materials within it. Coupling to such type of resonator is generally done by means of an aperture, a probe

or a loop, positioned according the desired mode excitation. The field patterns or modes within the resonator depends on its geometry and dimensions.

2.13.1 Resonance frequency

The resonance frequencies of a rectangular resonator can be calculated as [22]

$$f = \frac{c}{2\pi\sqrt{\mu_r\varepsilon_r}}\sqrt{\left(\frac{m\pi}{a}\right)^2 + \left(\frac{n\pi}{b}\right)^2 + \left(\frac{q\pi}{d}\right)^2} \tag{2.61}$$

where d is the longitudinal dimension of the cavity and q the longitudinal mode number. For a given desired resonant frequency, the cavity length is given by

$$d = \frac{c}{\sqrt{\mu_r\varepsilon_r}}\frac{abq}{\sqrt{4a^2b^2f^2 - a^2\left(\frac{c}{\sqrt{\mu_r\varepsilon_r}}\right)^2 n^2 - b^2\left(\frac{c}{\sqrt{\mu_r\varepsilon_r}}\right)^2 m^2}} \tag{2.62}$$

Similarly, for a circular cylinder cavity the resonant frequency is given as [22]

$$f = \frac{c}{2\pi\sqrt{\mu_r\varepsilon_r}}\sqrt{\left(\frac{s}{a}\right)^2 + \left(\frac{q\pi}{d}\right)^2} \tag{2.63}$$

where $s = p'_{nm}$ for TE modes and $s = p_{nm}$ for TM modes. For modes with index q = 0 (e.g. TM_{0n0}), the frequency is independent form the cavity length. For a given desired resonant frequency, the cavity length is given by

$$d = \frac{c}{\sqrt{\mu_r\varepsilon_r}}\frac{\pi aq}{\sqrt{4a^2\pi^2f^2 - \left(\frac{c}{\sqrt{\mu_r\varepsilon_r}}\right)^2 s^2}} \tag{2.64}$$

Some common loading arrangement resonant frequencies can be estimated analytically [3], [43]. However, arbitrary cross section cavities or more complex loading are bound to a numerical analysis approach due to the high complexity of a possible analytical solution [3].

2.14Main issues in high-temperature microwave systems

During thermal treatment, materials experience chemical and physical transformations with the generation of hot gaseous, liquid and solid by-products that add to an already complex and harsh operational environment. Contamination, accumulation of debris, or deficient handling of any of these variables can result in destructive results [19]. Arcing, overheating, thermal run-away, hot spots, burning or melting of structural or thermal insulation components are typical occurrences in high-temperature setups, where products are heated over 250 °C [77], [78]. Having control over these conditions can be troublesome in continuous systems for large-scale implementations, due to the constant exposure to radiation, gases and chemicals of insulation and structural elements; the continuous generation of waste and debris; dust from material handling; among others [12], [19], [77]–[79]. On top of these issues, there is a lack of practical ways to measure and control temperature accurately [79], [80]. Further details on penetration depth, arcing, thermal run-away, hotspots, thermal insulation, and metrology and control are given next.

2.14.1 Penetration depth

This quantity is defined as the distance at which the power flux decays by $1/e$ of its surface value and is a useful parameter to estimate the feasibility of processing products of different sizes. A general formulation taking into account both electric and magnetic losses is given in equation [65], [81].

$$Dp = \frac{\lambda_0}{2\sqrt{2}\pi} \frac{1}{\sqrt{\varepsilon_r''\mu_r' - \varepsilon_r'\mu_r' + \sqrt{(\varepsilon_r'\mu_r')^2 + (\varepsilon_r''\mu_r'')^2 + (\varepsilon_r'\mu_r'')^2 + (\varepsilon_r''\mu_r')^2}}} \tag{2.65}$$

where λ_0 is the free space wavelength.

For non-magnetic materials, the penetration depth can be expressed simply as [81]

$$dp = \frac{\lambda_0}{2\pi\sqrt{2\varepsilon_r'}} \frac{1}{\sqrt{\sqrt{1+\left(\frac{\varepsilon_r''}{\varepsilon_r'}\right)^2}-1}} \tag{2.66}$$

For low loss tangent materials (i.e. when $\varepsilon_r''/\varepsilon_r' \ll 1$), it can be further simplified as

$$dp = \frac{\lambda_0\sqrt{\varepsilon'}}{2\pi\varepsilon''} \tag{2.67}$$

Treatment uniformity problems are inherent to large absorptive products, as the decay can happen to a degree in which only superficial heating will occur. In such cases, the rest of the volume will be heated by thermal conduction. This issue is particularly troublesome in high-temperature processing, as it is common that the material's microwave-absorption rates increase rapidly after surpassing a critical temperature and therefore suddenly reducing the penetration depth, making the process difficult to control [28], [82]–[84]. Typical examples of this include processes such as coke-making, pyrolysis of carbonaceous materials, ferrous concentrates, where after surpassing 600°C the microwave absorption increase sharply [26]–[30], [81]–[83], [85] making penetration depth an issue, creating uniformity and thermal runaway concerns. To illustrate this type of behaviour, the penetration depth versus temperature of bituminous coal is shown in Figure 2.25 and of a magnetite concentrate in Figure 2.26.

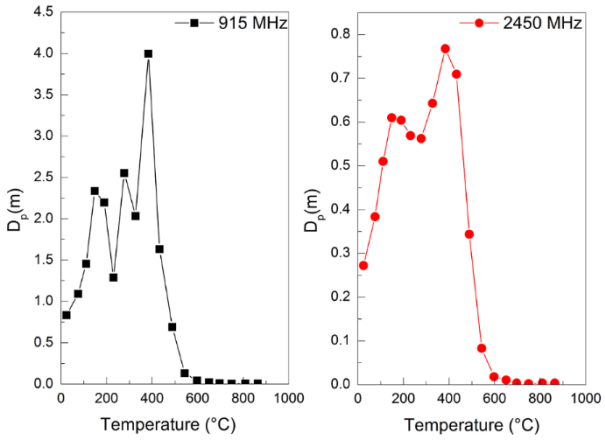


Figure 2.25 Penetration depth of bituminous coal after [28].

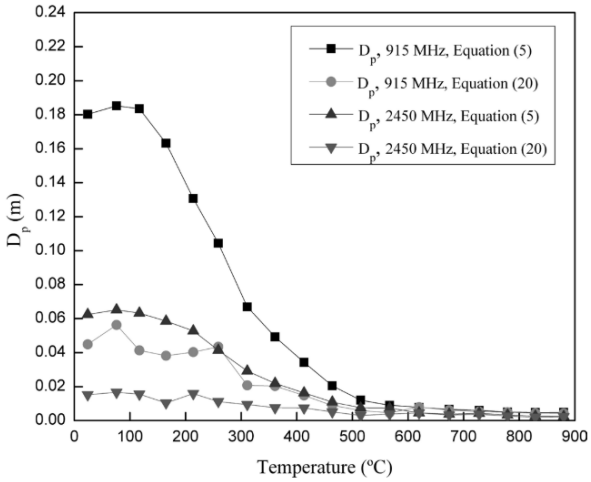


Figure 2.26 Penetration depth of magnetite concentrate at a density of 2.8g/cm^3 after [81]**.**

Larger frequencies result in lower penetration depths, if the dielectric properties remain similar, so treating large absorptive products at lower frequencies can be more practical [83].

2.14.2 Arcing

In the presence of high-intensity electric fields, ionisation can occur due to the increase in particle's kinetic energy. The charged particles will then ionise others leading to the formation of electrically conductive paths which can sustain an electric discharge [86]–[88].

Gases are prone to sustain discharges, as their dielectric strengths (i.e., maximum voltage or electric field amplitude that a material can withstand before breakdown) are orders of magnitudes lower than for liquids or solids [87]. In high-frequency gas discharges, primary ionisation due to electron motion controls the breakdown (i.e. not always needing an extra source of electrons) [88], [89], as the electrons are not swept from the discharge. The breakdown will occur when electron density due to ionisation becomes equal to electron loss [88].

The dielectric strength of a gas is proportional to the absolute pressure (or density), according to Paschen's laws [88]–[90]. At constant pressure, density falls with increasing temperature, and thus, the dielectric strength of gases decreases as temperature rises [89]. This behaviour is because at lower gas densities, the kinetic energy is easily accumulated due to reduced friction between particles [88]. The required electric field for dielectric breakdown is

decreased with the increase of gas temperature [86], [91], making hot-gas environments in high-temperature processes particularly susceptible to discharges. Humidity can also contribute to increasing arcing risks [92], [93].

The presence of conductive materials within the microwave fields can also promote arc generation. Typically, charge density and electric fields can reach very high values in sharp edges and tips, and if the charges accumulate sufficient kinetic energy, it can start the above-described ionisation [12], [87]. Such materials will also supply electrons for initiating and sustaining the discharge [9]. Thus, highly conductive debris and contamination accumulation pose a significant arc generating risk inside a microwave applicator, making constant cleaning and maintenance critical. Furthermore, the product under treatment shape and packing is critical, with sharp edges and small gaps increasing the likelihood of arcing.

The electric field intensity to sustain an arc can be considerably lower than the one needed to trigger it [19], as the lower resistivity in the gas allow to sustain the same current with lower voltages. When the discharge is started, the high-temperature in its vicinity make the ionisation process partially thermal [94] with low particle recombination (i.e. deionisation) [89] and with a significantly lower breakdown threshold [86], [91]. This behaviour makes on/off strategies better suited to stop arcs securely rather than just power control, allowing enough time for the ionised gas to disperse.

Arcing can lead to significantly destructive results with possible damage to the product, applicator, and critical equipment [77]. It can also represent a significant waste of power [95]. However, in some applications, the generation of discharges or micro-plasmas can be useful if the dissipated power serves to heat the product [96]–[99]. Moreover, the use of microwave-driven plasma is common in electronics and chemical processing for non-thermal applications, such as etching, chemical vapour deposition, and surface treatment [43], [100]–[103]. In such

systems, the microwave energy couples to the plasma directly, as it becomes an electrically conductive volume, and serves to keep the gas ionised. Microwave-plasma thermal processing have been recently explored in gasification applications, for small-scale on-site gasification [104]–[106] yet, its efficiency is uncertain.

2.14.3 Thermal runaway

If the increase in temperature changes the material in such a way that it accelerates heating rates, then it can enter a positive feedback loop which may produce sudden extreme heating rates. This type of behaviour is often called thermal runaway when it becomes uncontrollable [107].

In microwave heating, thermal runaway is usually related to changes in a material's complex permittivity and conductivity with temperature. Various dielectric materials show an increasing microwave absorption as the temperature rises [20], [24], [25], [108]–[110]. The combination of non-uniform electromagnetic fields, heterogeneous material composition and fast variations of the material microwave properties with temperature, can result in significant local temperature differences within the product. In some cases, a critical stage can be reached where the absorption rate increases extremely rapidly, allowing few if any control in the reaction resulting in thermal runaway [4], [109].

One of the many high-temperature processes in which this can happen is in microwave processing of ceramics, e.g. zirconia [111], for which dielectric properties are shown in Figure 2.27. The authors simulated their microwave multi-mode system where localised (i.e. non-uniform) heating occur. This uneven treatment resulted in the fast heating of a local area which in turns resulted in an increase in loss factor and preferential microwave energy deposition in the same spot (i.e. hot-spot) as shown in Figure 2.28. This accelerated heating keeps increasing in a positive loop ending in sudden thermal-runaway, which agrees with their experimental observations.

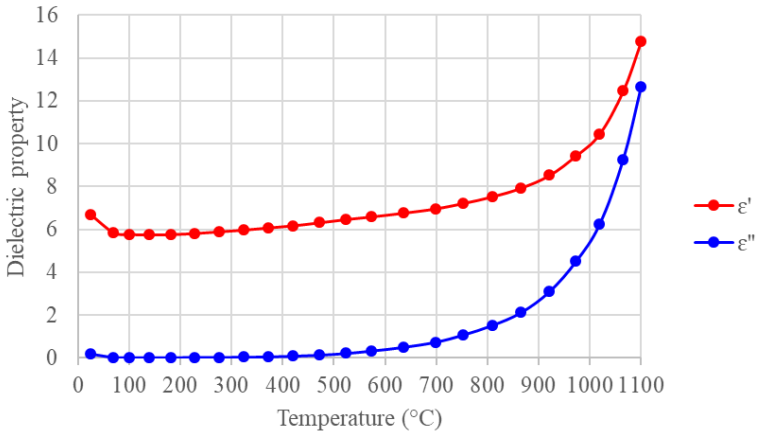


Figure 2.27 Zirconia dielectric properties at 2.45GHz adapted from [111]**.**

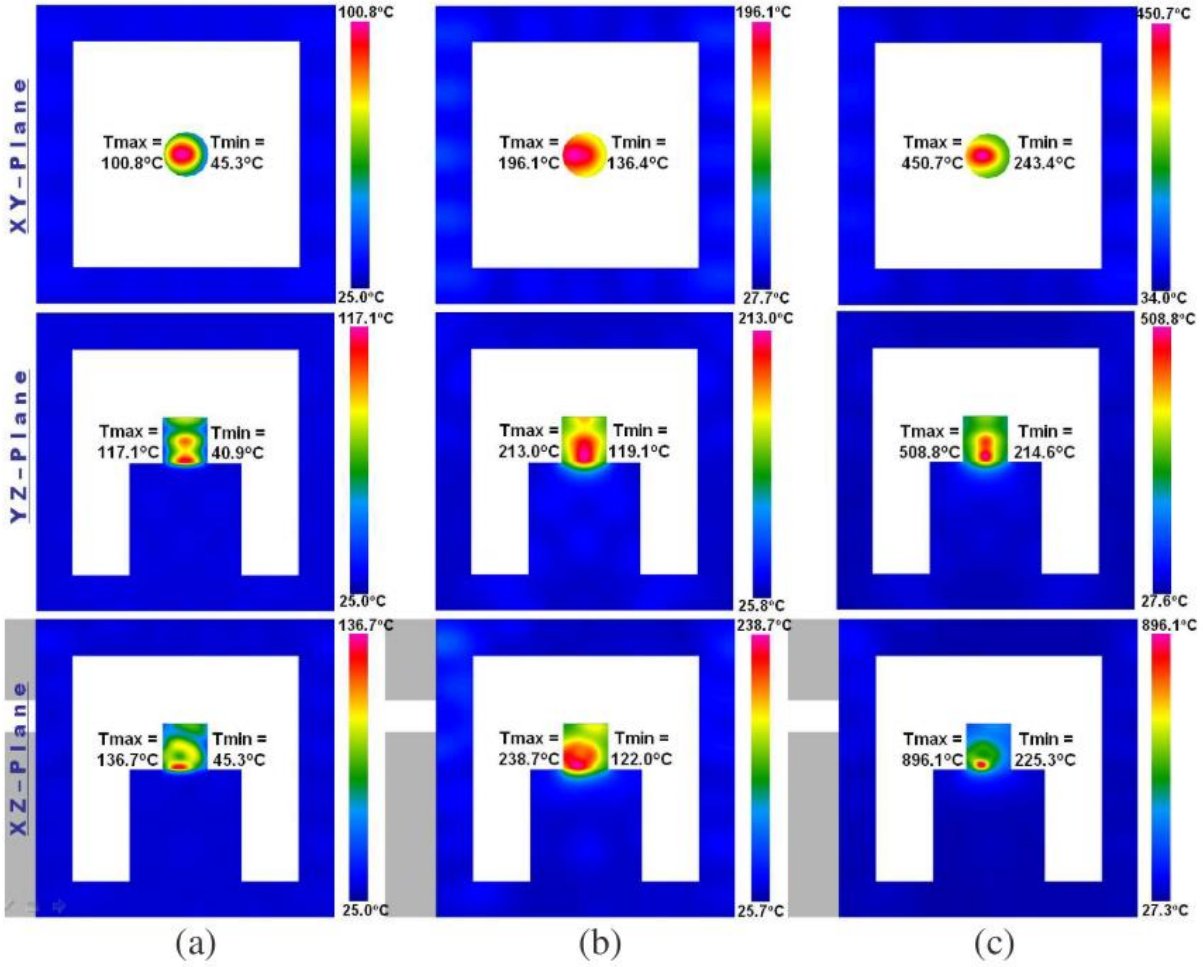


Figure 2.28 Simulated temperature distribution in the system at 2.441 GHz after (a) 100 s, (b) 200 s and (c) 208 s of microwave processing of a zirconia sample, after [111]**.**

Monitoring and control, if any, is usually focused on the bulk material or in a few specific points, making hot-spots hard to detect [20]. This can lead to thermal runaway and

destructive results including non-uniform treatment, arc generation, overheating and burning of the product, the melting of conveyor belts and linings [12]. The most common control strategies are adjusting input powers [108] or cavity's physical dimensions [112]. Mode-stirring, product mixing and moving (e.g. stirring, turntables, conveying, vibrating, etc), the use of multiple microwave sources, and frequency sweeping can help increasing uniformity and thus reducing hot-spots [3], [113]. Moreover, the use of hybrid heating, susceptors, and insulation can help to reduce the likelihood of thermal runaway by effectively reducing the thermal gradients during processing [4].

2.14.4 Thermal insulation materials

Thermal insulation materials that are transparent to microwaves have a high thermal shock resistance, chemical and mechanical stability, are critical for high-temperature microwave systems. Its use can result in dramatic enhancement of efficiency as well as improvement of treatment uniformity by reducing thermal gradients [4].

Alumina and mullite refractories, as well as zirconia-based ceramic fibres, and fused quartz or borosilicate glasses are common in most high-temperature microwave implementations [114]. The transmission properties of alumina and mullite during microwave high-temperature heating at 915 MHz and 2.45 GHz are reported in [115], providing an analytical approach that can be useful in selecting the adequate isolation on applicator design. Boron-nitride and yttrium oxide granules, and zirconia, alumina and silica based fibres, have been used in high-product value ceramic sintering applications [4], [116].

2.14.5 Metrology and control

One of the most desirable parameters to measure for control purposes in most applications is the temperature, making the lack of accurate measurement techniques during microwave processing a significant obstacle to the development of high-temperature systems.

Technological solutions include thermocouples, fibre-optics sensors and infrared pyrometers [80], [117].

Thermocouples experience several problems when operating in microwave systems. Their presence can create strong field distortions, it can be heated instead of the product drawing significant amounts of power, and it can be a considerable heat loss element from the product, and thermocouples are generally susceptible to interference from the electromagnetic fields [117]–[120]. Thermocouple-based measurements tend to misrepresent the actual sample behaviour [120]. Shielded thermocouples to be used during microwave off cycles were suggested as a plausible alternative in some particular applications, helping to mitigate, to some extent, the above-described limitations [117], [121], [122].

Fibre-optics thermometers have less influence on the system behaviour and are not significantly affected by microwaves yet are mostly limited to moderate temperatures. Probes are delicate and prone to contamination [80], [117], [119].

Infrared pyrometers, being a non-contact method can be safely used in most microwave setups. Nonetheless, this technology can only measure surface temperatures and is sensitive to the emissivity of the target, which can lead to significant errors [80], [119]. Experimental approaches can be used calibrating optical and infrared pyrometers with thermocouple measurements during microwave off periods, leading to more precise measurements during microwave presence [119].

Relying on the measurement of incident and reflected powers, and thus, absorbed powers, rather than just temperatures [120], [123], [124] and the use of temperature profile prediction models based on simulations [125] have been reported as alternatives to temperature measurements. The temperature and reflected power measurements can be used to control the generator output power or the stub positions in an automatic tuner system.

2.14.5.1 Temperature mapping

Several techniques can be used to characterise the microwave heating behaviour of an applicator experimentally. Infrared sensor spot measurements, thermocouple measurement (post-treatment), thermal camera imaging, and thermal paper mapping (i.e. fax or thermochromic paper).

Comparison between measured thermal patterns and simulated power density distributions, as well as measured and simulated scattering parameters, are the generally accepted simulation validation approaches in microwave applicators, as directly probing field distributions is generally unpractical [126]. The temperature pattern distribution after microwave treatment gives a measure of the power density distribution. This has been used to provide experimental validation of numerical simulations [127]–[129]. Therefore, this constitute a useful tool to assist the design of microwave heating applications [129].

This technique has limitations given that the dielectric properties of materials change with temperature, making it accurate for materials with stable dielectric properties in the studied heated range [126]. Online measurements are complicated and require the use of a multiplicity of sensors during operation of the cavity [130], whereas the in-situ use of thermal cameras are generally limited to small apertures.

When the cavity being studied cannot be opened fast or monitored in-situ, the heat-loss and temperature spread through the sample will reduce its quality as a representation of the power loss density distribution. Thermal sensitive paper (i.e. fax paper) can be used to print the temperature pattern, avoiding the heat-loss limitation. The paper itself is microwave transparent, so it should be used in conjunction with a microwave susceptible material [3]. This technique can only produce monochromatic results (e.g. black for highly heated, white for lowly or not heated). The thermal paper generally blackens upon reaching 100 to 150°C and is very sensitive to overexposure [130]. Using cobalt chloride impregnated filter paper produce a

gradual pattern associated to temperature generating pink-blue patterns; however, the colour pattern it is affected by the heat-loss [131] so intrinsically have the same limitations as regular thermal imaging.

2.15 Microwave heating fundamentals summary

Microwave energy can be used for thermal processing of a variety of products especially if volumetric, selective heating or low thermal inertia is beneficial. The ability for a material to interact with such energy is governed by its constitutive parameters, the electric permittivity (ε_r) and magnetic permeability (μ_r). These generally exhibit considerable variation with composition, density, frequency and temperature, making their characterisation paramount to system design.

The conversion of the electromagnetic energy into heat, in this frequency region is mostly dominated by conductive and dipolar loss for electric field dissipation, and eddy currents and magnetic hysteresis loss for magnetic field dissipation. The exploited mechanism will generally depend on the type of product to be treated and required processing conditions. Moreover, there are three major heating strategies; direct heating where microwaves are directly deposed into the product, indirect heating where a susceptor material is heated which then heats the actual product by thermal conduction, and hybrid approaches mixing microwave with conventional heating methods.

A legal framework establishes specific frequency bands for operation and leakage and exposure safety limits for the usage of high frequency electromagnetic waves. The approved ISM bands for industrial use are the 433, 915 and 2,450 MHz, chosen to avoid interference with telecommunication systems. A broad range of applications have been successfully developed in these bands, however, they are mostly for relatively low temperature processes of less than 250 °C.

Microwave processing systems are generally composed of generators that provide the energy, matching systems that ensure efficient delivery, applicators that allow the interaction of the radiation with the product and general monitoring and control systems to manage production and safety. A variety of applicator systems exist that allow widely different processing conditions and product throughputs and it is important that the appropriate applicator is selected for the heating outcomes required from the process.

Microwave processing, in particular for high-temperature systems, can be complex and special consideration should be given to selection of thermal insulation, structural materials, metrology, and control equipment. Most commonly used microwave transparent insulation materials become lossy at high-temperatures, and the broad temperature range encompass significant product properties variation, making processes hard to monitor and control. Moreover, the harsh environment calls for the use of particularly robust structural materials and ancillary equipment. Also, it is vital that variable and sometimes unpredictable effects such as penetration depth, arcing and thermal runaway should be accounted during process design to ensure that a material is processed to the correct degree and consistently so.

2.16 Applicator technologies

2.16.1 Radio-frequency (RF) applicator technologies

2.16.1.1 Induction heating

In RF, the most widespread technology is induction heating for metallurgical applications is induction heating with applications including melting, hardening, curing, forging and brazing. It shows the highest heating efficiency and speed among metal processing techniques with low power consumption and environmental impact [69], [132], [133].

The principle of operation is based on the induction of eddy currents (see section 2.7.5) within an electrically conducting workpiece via a magnetic coil as represented in Figure 2.29.

A current is set through the coil generating a magnetic field that induce currents in the workpiece which creates heat by resistive loss.

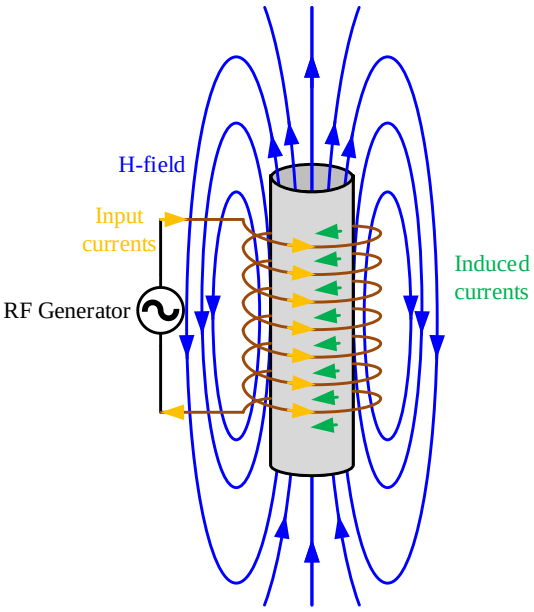


Figure 2.29 RF induction system sketch.

These systems mostly operate in frequencies up to 400 kHz depending on the workpiece size and type, and the nature of the treatment. Lower frequencies results in a deeper heated layer and are more common in bulk heating applications, whereas higher frequencies have been used mostly for surface hardening. Some systems have been developed up to 27 MHz for thin surface hardening [132], [133]. Given the relatively low magnetic field produced in induction heating there is no need for electromagnetic containment measures such as choking to guarantee operator safety.

2.16.1.2 Dielectric heating

RF dielectric heating by dipolar loss finds applications in food, pharmaceutics, textiles, fibre-glass, woods, ceramics and advanced materials industries. Conventional processes include drying and moisture control, glueing, curing, preheating, disinfestation, sterilisation, pasteurisation, baking and thawing [43], [69], [134], [135]. These systems operate at the ISM

frequencies of 6.78, 13.56, 27.12 and 40.68 MHz, relying mostly on capacitive applicators (**Error! Reference source not found.**) and variations of this concept [43], [69], [134], [135].

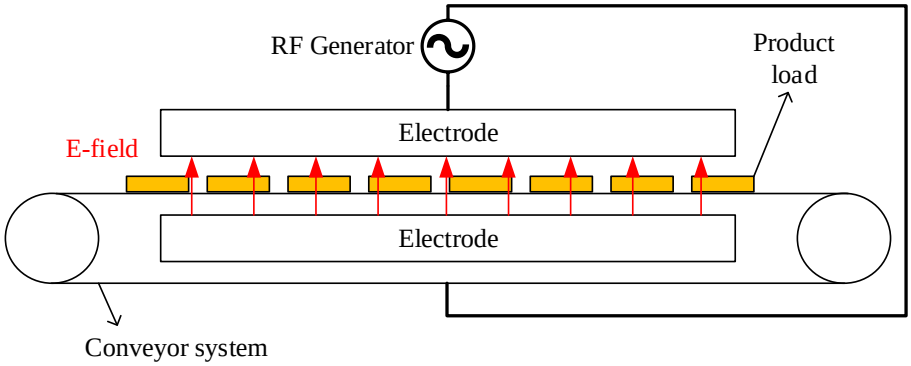


Figure 2.30 RF capacitive treatment system sketch.

The major advantages of RF heating over microwave technologies are its higher penetration depths and better heating uniformities due to larger wavelengths; nonetheless, capacitive applicators are limited to a highly homogeneous bed of product, and might its uniformity qualities may become non-existent for high loss or non-uniform products [43], [136], [137]. Furthermore, according to equation (2.34), the achievable power density is proportional to frequency. For applications limited by electrical breakdown, the power density can be much higher in a microwave system [138] with RF systems more susceptible to arcing, making vacuum and possibly high temperature applications, where arcing likelihood is even higher, better suited for microwave heating [137].

2.16.2 Microwave applicator technologies for heating

2.16.2.1 Resonant cavities for microwave heating

Technological implementations of microwave heating are generally based upon resonant cavities. These are electrically conductive enclosures which can store electromagnetic energy by resonating within the microwave frequency range [3]. The electromagnetic fields bounce back and forth between the cavity walls generating standing wave patterns at its

resonant frequencies which are constrained by the cavity geometry and dimensions [1], [22]. If a microwave absorbent product is set in the cavity, it will eventually dissipate this stored energy through heating it up [3], [43], [139]. Resonant cavities for heating applications are usually classified according to the number of resonant modes they can sustain. Single-mode cavities, as the name implies, are intended to operate with a well defined unique standing wave pattern or mode with highly concentrated field, while multi-mode cavities allow a multiplicity of varying patterns [3]. In the following section, a brief overview of both types of cavities and their usage in material processing is given. Please note that detailed explanation of both applicator types is provided in the subsequent chapters.

2.16.2.1.1 Multi-mode cavities

The use of batch type processes with multi-mode cavities (**Error! Reference source not found.**) is the most popular microwave heating approach [3]. Typical uses are found in food, pharmaceutical, chemical processing and ceramics [3], [12], [19]. Devices such as turntables or mode-stirrers are used to ensure uniform heating, moving the product and stirring the electric fields respectively [43], [139].

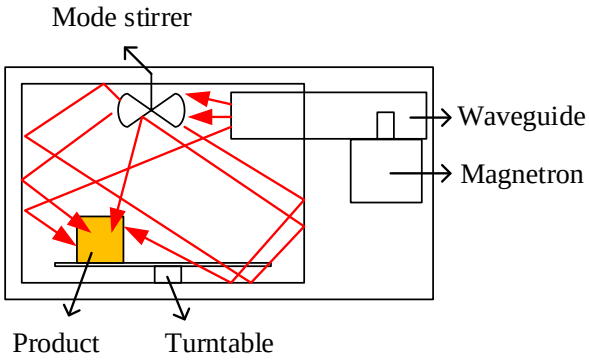


Figure 2.31 Multi-mode resonant cavity for batch processing sketch.

For large-scale processes, continuous systems are essential to achieve commercial throughputs [19], [140]. Conveyor systems with microwave transparent belts that move materials through one or several multi-mode resonant cavities (Figure 2.32) have been used

successfully for a wide variety of processes such as fermenting, cooking, curing, drying, heating, melting of fats, pasteurization, roasting, sterilization, tempering, thawing, and vulcanization [12]. In such systems, the conveying movement enhances the uniformity of the product treatment [79], [141], [142]. An example system is shown in Figure 2.33, used in the study of contaminated soil remediation with 150 kg/h throughputs.

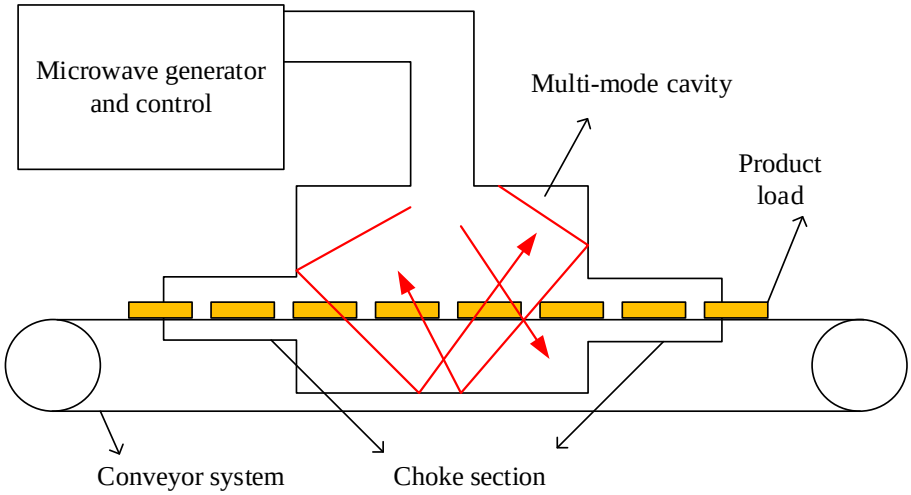


Figure 2.32 Microwave conveyor belt system sketch.

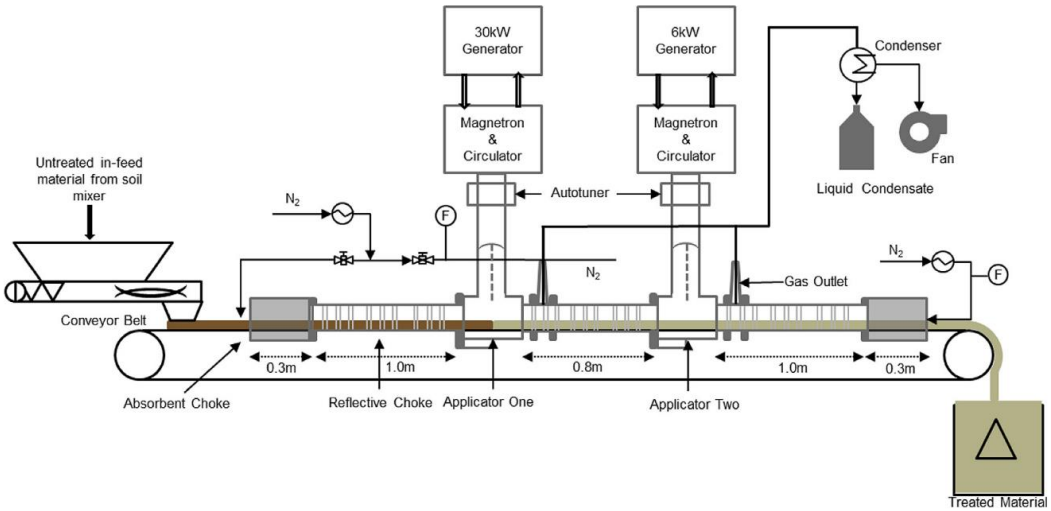


Figure 2.33 Schematic of continuous microwave treatment for treatment of contaminated soil based on dual applicator for processing at 150 kg/h throughput, after [79]**.**

2.16.2.1.2 Single-mode cavities

Single-mode systems have been used widely for research purposes, however, for large-scale continuous processing, applications are typically limited to liquids, emulsions, purees,

and fine granular materials. Some examples of this are continuous flow microwave chemistry [143]–[145], food processing [146], [147] and minerals treatment [148], [149]. These and most systems at a industrial scale operate at 915 MHzdue to the ability of handling larger loads. A sketch of a pilot plant system based on two single-mode applicators for treatment of ores able to reach a throughput of 150 tonnes per hour is shown in Figure 2.34.

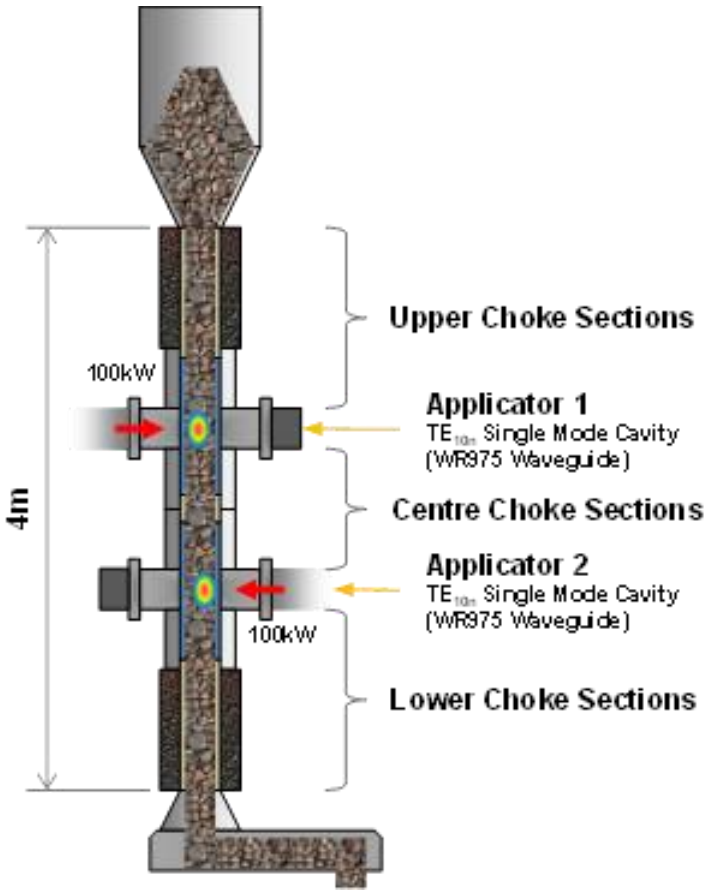


Figure 2.34 Sketch of pilot plant dual single-mode applicator system for treatment of ores with a 150 tonne per hour throughput after [148]**.**

2.16.2.2 Travelling wave applicators

Other approaches include travelling wave applicators, where a dummy load dissipates the leftover energy at the termination of a transmission line, the applicator being the transmission line itself [43]. Travelling wave applicators have been used to some extent in continuous processing of lossy laminar or web-like products and liquids, primarily in drying,

curing and flow chemistry [12], [19], [43], [150], [151]. The serpentine (Figure 2.35) and the rectangular waveguide section (Figure 2.36) are classic examples of this class of applicator.

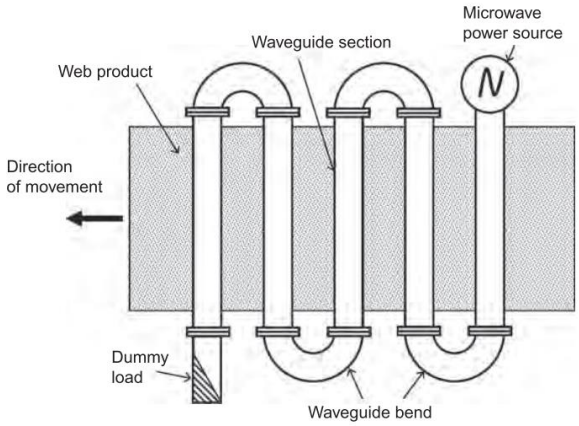


Figure 2.35 Microwave serpentine travelling wave applicator sketch after [43].

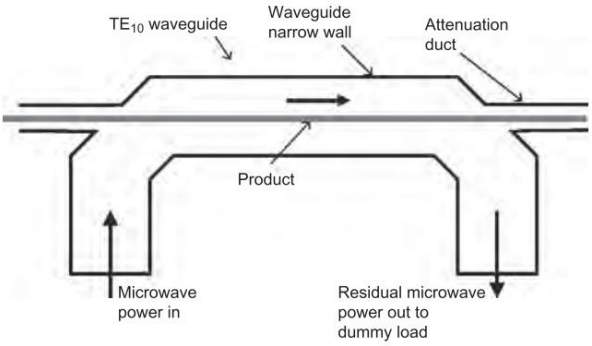


Figure 2.36 Rectangular waveguide section travelling wave applicator after [43].

2.16.2.3 Open-ended transmission lines

This type of applicator consists in an open-ended transmission line that heats the product through interaction with fringing fields coming from the line [43].

Open-ended applicators are an alternative for treating materials that cannot be surrounded by a structure and where only a partial treatment is needed [152]. This technology is regularly used in applications such as diathermy or hyperthermia, microwave ablation and for material sensing and probing [43], [153], [154]. One application where their use has been significantly explored is the selective demolition of concrete [152]. Industrial conveyorised

systems with open-ended applicators have also been investigated [155], but to the author's knowledge, no commercial solutions are based on this type of technology.

Chapter 3 High-temperature microwave applications

Well established commercial applications have been developed in industries including rubber, pharmaceutics, paper and food processing [156]. These systems operate below 250°C in what can be called low-temperature microwave processing. High-temperature microwave processing has shown significant prospects at laboratory scale, for its use in waste treatment, pyrometallurgy and advanced materials sintering. Nevertheless, practical solutions are still far from common or economically viable [13], [62], [64], [65], [82], [157].

This chapter reviews recent developments in major high-temperature microwave processes covering waste treatment, ferrous pyrometallurgy and advanced material sintering, pinpointing technical setups, advantages, limitations and critical issues. A discussion is made regarding prospects for scaling-up. Finally, general conclusions are drawn, and research lines are proposed which may contribute to narrow the gap between promising theoretical and lab-scale research and actual industrial solutions.

3.1 Waste treatment

Microwave waste treatment solutions are mostly pyrolysis-based, which is a thermal degradation process in an oxygen deprived environment comprising carbonisation and thermal decomposition. The process converts the raw materials into solid, liquid and gas products [158]. The use of microwaves for pyrolysis had been reported for a broad range of feedstocks including several types of waste biomass, oil, coals, tyres and plastics. Its commercial and environmental prospects have led to significant research over the last years. It promises a fast, energy-efficient way to achieve waste remediation, with the recovery of commercially valuable products in the form of chemicals or fuels, without the environmental drawbacks of conventional techniques [13]–[15], [157], [159]–[163].

In this section, recent microwave pyrolysis of plastics, automotive industry and biomass wastes research is reviewed, to give an insight into the current state of development and to identify the most pressing issues related to scale-up. For reference, a list of calorific values (high heating values HHV (MJ/kg)) of selected commercial fuels is shown in Table 3.1.

Table 3.1 Commercial fuels calorific value or high heating values (HHV) [164]**.**

Fuel	HHV (MJ/kg)
Gaseous fuels	
Natural gas	52.225
Hydrogen	142.18
Still gas	50.951
Liquid fuels	
Gasoline	46.536
Diesel	45.766
Ethanol	29.847
Solid fuels	
Petroleum coke	31.308
Bituminous coal	27.267
Forest residue	16.473

3.1.1 Waste plastics

Plastic wastes are a significant and growing environmental concern. It has been estimated that 6,300 metric tons of waste plastics had been generated as of 2015, of which only 9% had been recycled, 12% incinerated and 79% accumulated in landfills, and if current trends continue, around 12,000 metric tons of plastic waste will be in landfills by 2050 [165]. Pyrolysis can be a practical alternative for waste remediation and energy recovery; however, its actual economic benefits remain unclear [13]. Plastic destruction is still mainly done through incineration with or without energy recovery [13], [165].

Microwave-pyrolysis technology may be able to provide fast, efficient, and uniform heating with product yields of better quality than conventional pyrolysis on plastic waste processing. Such advantages have promoted significant research in recent years [13], [14], [98], [121], [157], [166]–[168]. Recent reviews on conventional pyrolysis of plastics are available in [169], [170].

Researchers have focused in exploring microwave pyrolysis of common waste plastics such as High-density (HDPE) [98], [117], [121], [166], [167] and Low-density (LDPE) [121], [171], [172] Polyethylenes, Polypropylene (PP) [121], [167] and Polystyrene (PS) [173]–[177]. However, studies with closer to reality feedstocks are scarce (i.e. in similar forms to waste that is being put into landfills). Ludlow-Palafox and Chase [166] revealed the prospects of microwaves to process toothpaste packaging (polyethylene/aluminium laminates). Undri et al. [178] reported the recovery of fuel from polluted multilayer beverage packaging (paper/polyethylene/aluminium). Aishwarya and Nangarthody [168] used a mixture of plastic that simulates the configuration of real plastic waste streams rejected from industrial sorting plants and household plastic wastes. Rosi et al. [179] studied the use of a mixture of various plastics from electric and electronic waste equipment as feedstock.

Very similar reactor setups have been used, comprising modified multimode ovens with one to four magnetrons operating at 2.45 GHz with maximum powers of less than 6 kW [121], [166]–[168], [173]–[177]. Condensation stages are used for retaining liquid yields and gas bags for capturing and sampling incondensable gaseous yields. Nitrogen flows are typically used as carrier gas to drive out the products and to provide an inert and oxygen-free environment (e.g. Figure 3.1).

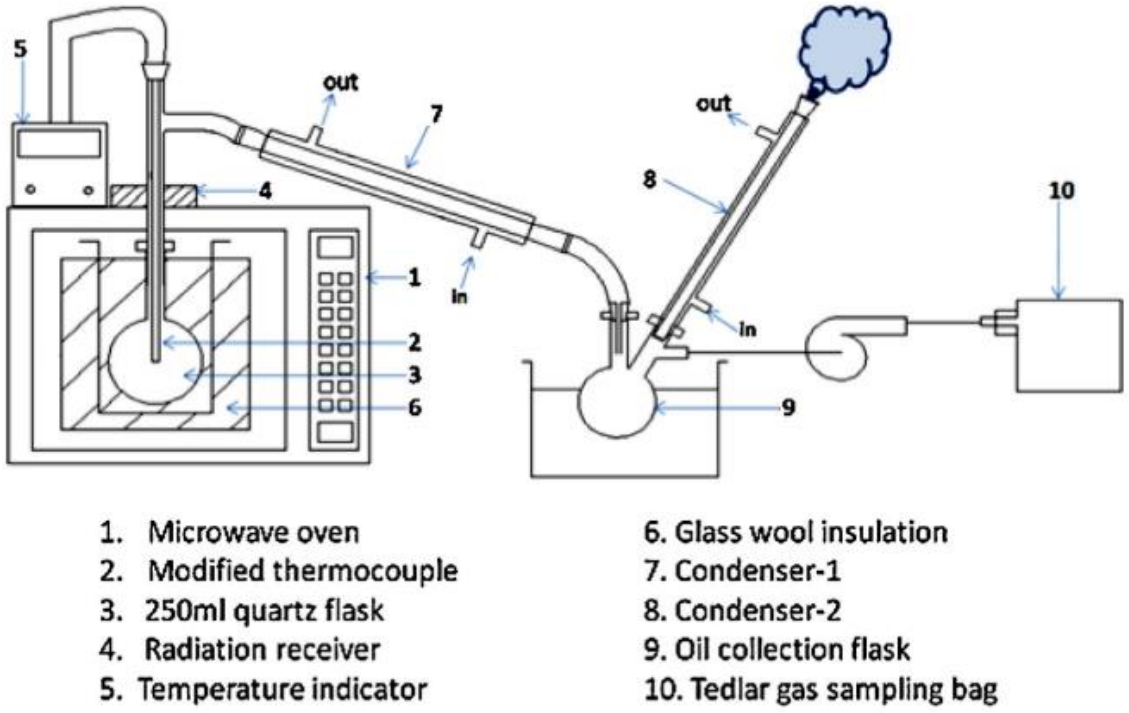


Figure 3.1 Typical microwave polymer processing system example, reproduced from [121]**.**

Different reactor types are reported by Russel et al. [98] which used a cylindrical multimode reactor and Khaghanikavkani et al. [117] in the form of a cylindrical coaxial cavity reactor. All these works are limited to batch operation with samples of no more than 500 g in a batch. Recently, a system for depolymerisation of PET at a 12.5 kg/h has been proposed based on material movement by a metallic Archimedean screw within a transparent glass tube (Figure 3.2), with a power distribution network to improve treatment uniformity which is critical for an effective process at such scale [180].

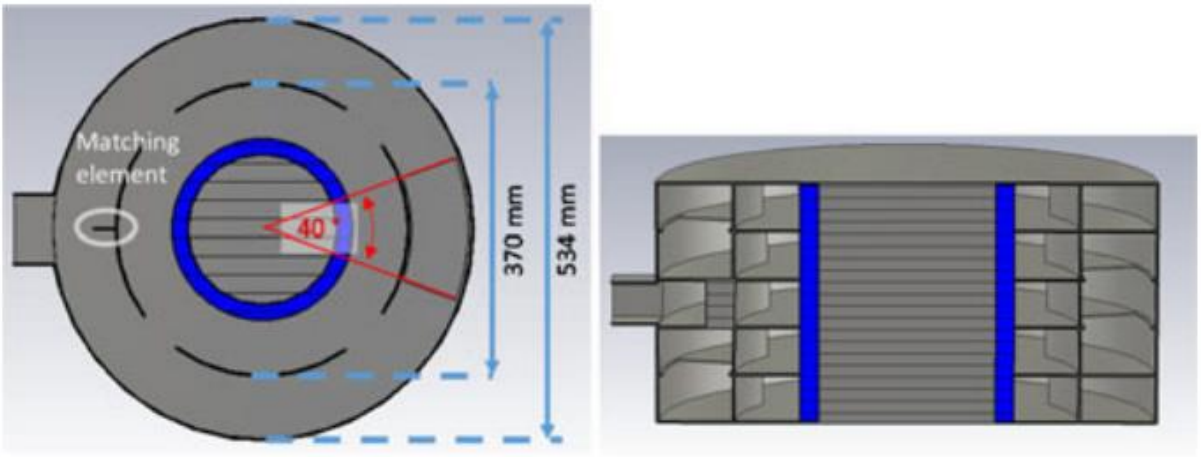


Figure 3.2 PET depolimerization applicator sketch for 12.5 kg/h throughput. WR430 waveguide feeding an external cylinder with internal slotted cylinder, reproduced from [180].

For temperature monitoring, thermocouples or infrared thermometers are used to sense the overall reactor temperatures or to sense the susceptor bed. Nonetheless, accurately measuring the product temperature during microwave treatment seems to be extremely challenging. Suriapparao and Vinu [121] used a modified insulated thermocouple and measured the temperature of the pyrolysing mixtures directly during the microwave source off cycles.

Most waste polymers are microwave-transparent. Thus, indirect heating is the most common treatment strategy. The highly microwave-transparent waste plastics are mixed with different microwave absorbent materials (i.e. susceptors). Microwaves heat the susceptor, which is usually a carbonaceous material, which then heats the actual plastic target by thermal conduction. Susceptors have been used mixed directly with the products [117], [121], [167], [177] or in the form of heating beds [98], [166]. Susceptors can interact with the products, other than as a heating element, to serve as catalysts, which may be used to tailor the chemical composition of the yields to some extent [98], [121]. The use of other catalysts during the process have also been reported, to obtain a more refined product directly [172], [177].

Alternatively, iron grids, and aluminium and copper coils, have also been used as microwave heating elements, instead of carbonaceous susceptors [173]–[175].

Analysing product yields under different process conditions such as power, temperature, nitrogen flows and the use of different susceptor materials in various proportions has been the focus of most of the works above. Wide variability in yields is reported depending on such factors; however, at optimal conditions, microwave pyrolysis experiments tend to result in oils with close to commercial properties. A selection of reported yields is summarised in Table 3.2. To the author knowledge, no studies on the field have seriously analysed energetic needs nor the influence of susceptors on process efficiency neither its economic viability.

Table 3.2 Selected product yields from microwave waste plastic pyrolysis, all with MW operation at a frequency of 2.45 GHz. Solid/Liquid/Gas (%wt) yield and oil high heating value (HHV).

Susceptor	S/L/G (%wt)[a]	Oil HHV (MJ/kg)	Ref
High-Density Polyethylene (HDPE)			
Coke bed	0.0/81.0/19.0	-	[166]
Coke bed	0.0/42.0/58.0	-	[98]
Activated carbon bed	6.0/41.0/53.0	-	[98]
Carbon	-/62.0/-	-	[117]
SiC	-/34.7/-	-	[117]
Tyre	31.3/47.9/20.7	42±4	[167]
Carbon	0.4/83.9/15.7	47±5	[167]
Low-Density Polyethylene (LDPE)			
Zeolite	2.3/32.6/65.1	-	[171]
Graphite	0.8/46.5/52.7	41.65	[121]
Zeolite + activated carbon	2.9/28.1/69.0	-	[172]
Polypropylene (PP)			
Tyre	29.4/58.9/11.7	46±5	[167]
Carbon	12.0/74.7/13.3	38±4	[167]
Graphite	1.18/48.16/50.66	44.45	[121]
Activated carbon	0.4/29.8/69.8	36.54	[121]
SiC	1.6/31.9/66.5	37.77	[121]

Aluminum	1.2/45.4/53.4	36.88	[121]
Fly ash	0.7/21.1/78.2	41.35	[121]
Lignin	1.2/41.9/57.0	39.25	[121]
Polystyrene (PS)			
Carbon	9.8/86.5/3.7	41±4	[177]
Iron mesh	5.0/80.0/15.0	-	[173]
Al. coil	3-4/88.0/9-10	-	[175]

3.1.2 Automotive industry wastes

With waste remediation and energy recovery goals in mind, researchers have explored the microwave pyrolysis application to troublesome automotive industry wastes, in particular, end-of-life tyres and used engine oils.

Around one billion end-of-life tyres are produced each year worldwide. Tyres are one of the most heavily recycled products with recovery rates of over 84% in Europe, USA and Japan. Due to the high energetic value and relatively low cost of end-of-life tyres, derived fuels are used to power cement kilns, paper and steel mills, and industrial boilers. Large-scale pyrolysis solutions, although attractive in principle, are not currently economically viable, so most energy recovery processes are incineration based [181].

Nonetheless, investigations were carried out on large-scale microwave pyrolysis. Sharma et al. [182] reported a processing plant by BRC (BRC Environmental 5000 tpy pyrolysis plant, process schematic shown in Figure 3.3). However, BRC reportedly stopped its work on microwave pyrolysis of tyres due to economic disadvantages over conventional methods [13].

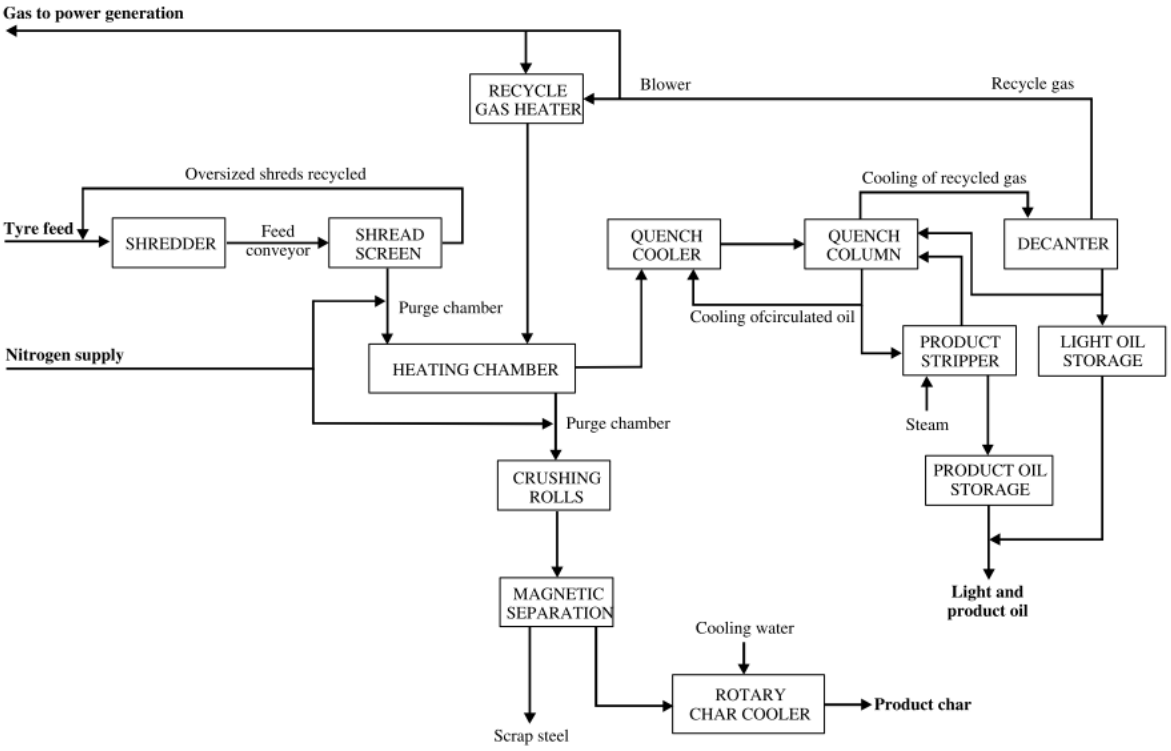


Figure 3.3 Simplified BRC environmental process for pyrolysis of tyres, reproduced from [13]**.**

Research since then has been mostly done on batch setups at laboratory scale using an operating frequency of 2.45 GHz, with systems operating at less than 1kW [122], [183]–[186] and up to 6 kW [187], [188]. These works point to the lack of accurate temperature monitoring as a major obstacle for scaling up of the process, as controlling the reactions becomes increasingly complex. A direct measurement approach was reported by Song et al. [122]. It is based on interrupting microwaves, inserting a thermocouple into the sample centre and measuring the temperature, removing it and restarting the microwaves.Tyres are readily susceptible to microwaves and have been processed with both direct heating [122], [183]–[185], [187], [188] and using activated carbon as complementary susceptor [184], [186]. Investigations have reported rich bio-oils yields with close to commercial fuel properties with gross calorific values ranging from 40 to 48 [MJ/kg]; some selected results are summarised in Table 3.3. There seems to be a lack of techno-economical and energy consumption focused studies.

Table 3.3 Selected product yields from microwave end-of-life tyre pyrolysis, all with MW operation at a frequency of 2.45 GHz. Solid/Liquid/Gas (%wt) yield and high heating value (HHV).

Susceptor	S/L/G (%wt0	S/L/G HHV (MJ/kg)	Ref
-	40.6/43.2/16.3	36±4/48±5/49	[187]
Activated carbon	48.5/20.6/30.9	-/40.4/-	[184]
Activated carbon	-/54.39/-	-/43.7/-	[186]
-	41/50/9	-/-/-	[185]

Used engine oils are a hazardous material which poses a significant environmental concern that can result in pollution of waters if disposed of inappropriately. Currently, the disposal of such wastes is widely regulated. Re-refining strategies are being used for remediation and value recovery from the collected waste oils; however, it is a rather complex process [189]. Current methods for oil treatment and recovery with a focus on pyrolysis were reviewed by Lam et al. [190].

Most published works on microwave pyrolysis of waste automotive oils were carried out by Lam et al. [191]–[195]. They explored various operational parameters and how they affect product yields. The system used is based on a modified catering microwave oven with a maximum power of 5 kW using four magnetrons and an agitation system with a coke bed as a susceptor, as the oils are a poor microwave absorber. The system can operate continuously at 5 kg/h of input waste oils and is schematised in Figure 3.4.

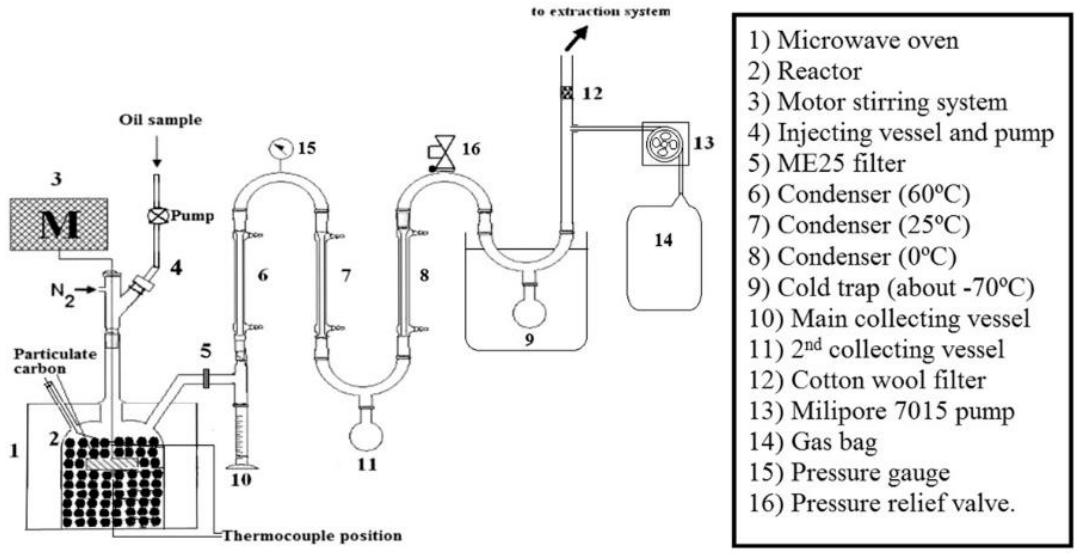


Figure 3.4 Lam et al. oil pyrolysis system schematic, reproduced from [194]**.**

Abo-Dief et al. [196] replicated some of their work in a similar setup operating at 6 kW, supporting most of their findings. Best liquid yields were achieved on temperatures ranging 550 °C - 600 °C [194], [196]. Budianto et al. [197] studied the effects of power, irradiation time, and the use of different susceptors (wood char and coconut shell char), showing better efficiency with higher-powers and with the coconut shell char. Low-temperature (~400 °C) pyrolysis without the use of susceptor agents were proven to be able to produce similar product characteristics as in other works [198].

Significant yields of liquid hydrocarbon oils can be obtained ranging 70-88 %wt and HHV ranging 38.72 to 46.4 MJ/kg [192], [196], [198], which can be treated and used as an energy source or industrial feedstock, showing potential for creating commercially valuable products. Still, no feasibility studies have been carried out.

3.1.3 Biomass

The search for alternatives to fossil fuels has stimulated a high demand for energy efficient conversion technologies from renewable sources. Waste biomasses are an attractive feedstock due to constant generation and that useful products with high energetic value can be extracted via pyrolysis from them, including bio-oils and production gas (syngas). Energy-

intensive pre-conditioning, including drying [199] and grinding [200] are significantly reduced in microwave-pyrolysis, allowing the use of relatively large and untreated feedstocks with the subsequent cost-reduction versus conventional techniques. Recent reviews were published on conventional pyrolysis of woody biomass [201] and microwave-pyrolysis of lignocellulosic biomass [163]. Microwaves have also been studied for their use in refining processes for the production of biodiesel [17]; however, being a low-temperature process, the topic is out of the scope of this review.

A large variety of feedstocks were investigated including larch wood blocks [200], sawdust [202], [203], wood pellets and chips [27], [120], ground sycamore and pine [204], [205], sewage sludge [206]–[208], coffee hull pellets [209], straw bale [210], cotton stalk [211], corn stover [203], [212], [213], rice straw [203], microalgae [214]–[216], macro-algae [217], etc.

Most setups operate at 2.45 GHz including waveguide traveling systems of up to 1 kW [206], [207], [209], [216], [217], single-mode cavities of up to 6 kW [27], [120], and multi-mode cavities [202], [203], [206], [207], [214]–[217].

Potentially scalable concepts were studied including a rotary kiln, conveyor belt, rotating ceramic disc [5], [218], fluidised bed [5], [204], [205], [212], and an auger reactor [5]. The need to operate in a continuous mode with a robust material transport technique, high power densities, uniform heating, low volatiles residence times and avoiding susceptor additives were regarded as critical for scaling-up [5].

From these, only the rotary disc approach seems to have reach significant scale. Their conceptual continuous plant schematic of the plant is shown in Figure 3.5. Nonetheless, according to their final report they manage to produce a prototype batch system with a relatively small footprint able to fit within two 20 feet shipping containers. Major issues included the

cracking of the ceramic plates; material handling issues, rendering the system unable to operate continuously; Lack of integration of monitoring and control systems, limiting process regulation ability; and the lack of validation and process repeatability analysis [219].

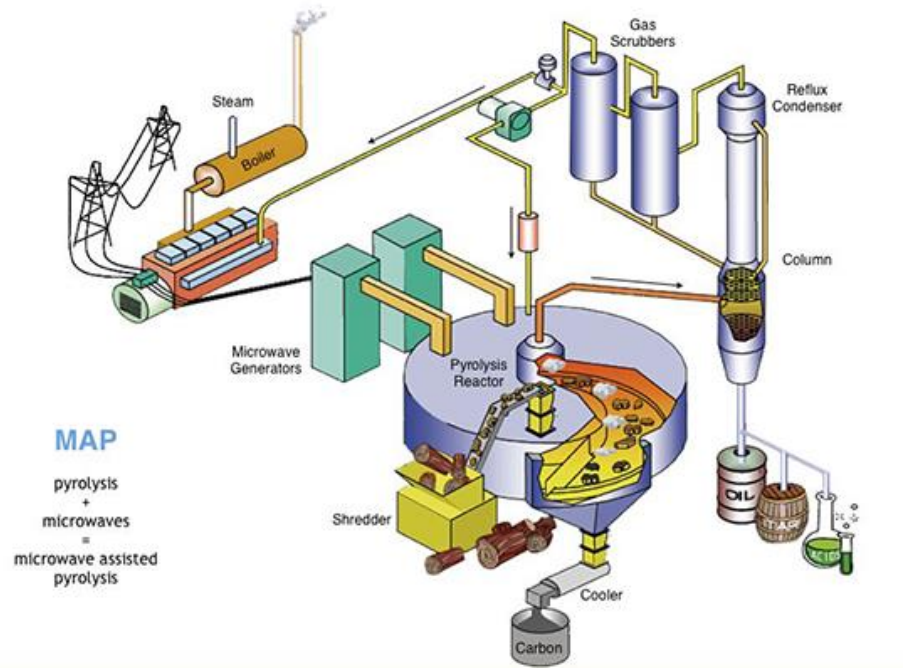


Figure 3.5 Microwave assisted pyrolysis plant conceptual sketch, reproduced from [220]**.**

Large-scale experimental works are scarce. Lin et al [208] investigated the pyrolysis of sewage sludge in a system with twelve 2.45 GHz magnetrons of 800 W for a batch pre-dried product load of 3.5 kg. Microwave pyrolysis of larch wood cylinder samples of up to 300 mm × 300 mm was carried out by Miura et al. [200] with powers of up to 3 kW. Zhao et al. [210] used a batch system with up to 29 kg samples to study the microwave pyrolysis of straw bale in a multimode cavity fed with twenty magnetrons for a total power of 18 kW. A kilo-scale 3 kW cylindrical reactor system was proposed for microwave pyrolysis of corn-stalk pellets [213]. Temperature measurements solutions are mostly based on the use of thermocouples or infrared pyrometers, showing the same issues mentioned above for other pyrolysis systems.

Two major heating strategies can be identified: the use of susceptors [202], [206], [207], [209], [211], [214]–[217] and the direct microwave heating [27], [120], [200], [203]–[205], [210]. The authors have opted to one or the other depending in both the feedstock properties as well as the desired products yields.

Higher temperatures, and thus higher microwave powers, favour gasification over bio-oil production. Absorbent char additives tend to favour gas yields, promoting the generation of local hotspots [120]. Moreover, microwave pyrolysis tends to produce higher syngas yields over conventional pyrolysis. This makes indirect susceptor-based microwave heating an attractive alternative for gasification [202], [206], [207], [209], [211], [212], [214]–[217]. Different additives can lead to significantly different yields, used susceptors include chars [206], [207], [209], [214], [216], [217], activated carbon, CaO and SiC [215], acid and metal salts [211] and charcoal beds [202]. However, the energy consumption per unit of biomass is higher for large susceptor to biomass ratios [214], which will have a direct influence on the commercial feasibility of large-scale solutions and such effect is not usually addressed in most published works.

Regarding the production of quality bio-oils, a direct microwave processing has been reported to produce better liquid yields [27], [120], [203], [210]. Char products have received far less attention, but can be commercially valuable, either from direct production or as a by-product of bio-oil and syngas production [221].

Thorough knowledge of the electromagnetic properties of the feedstock is essential for applicator design. Usually, the cavity perturbation technique is used for dielectric characterisation at high-temperatures. This method allows real-time dielectric properties data gathering during pyrolysis at different temperatures. The system usually comprises a resistive heating furnace and a cylindrical TM_{0n0} resonant cavity [28], [29], [204], [205]. Beneroso et al.

[222] applied a so-called inverse technique in which numerical optimisation was used to calculate the electromagnetic properties of sample material from scattering parameters measured with the sample inside of a waveguide system.

Several authors have provided support for the usefulness of simulations in system optimisation. Li et al. [223] carried out mathematical simulations of a rectangular cavity for wood treatment to optimise the system. Salema et al. [224] simulated the heating behaviour of a biomass bed under multimode microwave treatment using COMSOL showing similar hot-spot locations with experiments suggesting that it can be used to optimise the heating uniformity. Gadkari et al. [225] carried out numerical investigations of microwave-assisted pyrolysis of lignin using COMSOL, which proved to be useful in assessing the effect of different process parameters. Beneroso et al. [5] used COMSOL for evaluating several applicator concepts. Adam et al. [204], [205] used COMSOL for system design.

Tabulated data on product yields and properties including calorific values for various experimental works, can be found in the following papers [10], [163], [221], [226]. Although, much more work has been published compared to the other pyrolysis applications, in particular with the intent to design large scale solutions, the lack of energy-efficiency and techno-economic feasibility studies on the topic makes scaling-up prospects an uncertainty.

3.1.4 Discussion of microwave waste-treatment processes

The advantages of microwave-pyrolysis include fast uniform heating, selective heating, ability to treat large-sized feedstocks, and treatment of non-homogeneous wastes. Furthermore, better yield qualities, energy efficiency and eventually cost savings versus conventional pyrolysis. At first glance, this technology sounds like a practical way to waste remediation with value recovery. However, few commercial solutions have been developed, and such implementations lack any substantial support in the open literature. The lack of information on economic and energetic evaluation and comparative studies versus conventional alternatives,

in addition to measurement and control limitations seem to have hindered any serious attempt to develop large-scale solutions.

Systems are typically modified commercial ovens, with poorly defined field distributions and low-intensity electric fields, and only recent efforts have been made by using more sophisticated applicators and metrology techniques. Large-scale implementations would require continuous or semi-continuous processing to reach significant throughputs, and thus, would need a robust and durable applicator with adequate thermal insulation and material handling capabilities. This is far from a trivial solution, as the microwave-pyrolysis must deal with a multiplicity of factors and material variability during processing which imply that lab-scale–solutions for batch processing are not readily translatable to large-scale systems. A multidisciplinary design effort should be made with an emphasis on solving critical aspects, including

- Hot spots generation and thermal runaway.
- Penetration depth critical reduction.
- Treatment uniformity, field stirring and muti-feeding.
- Safety and electromagnetic compatibility (EMC) compliance and microwave leakage suppression.
- Materials and hardware for continuous operation in harsh conditions.
- Process control according to product properties changes.
- Pressurization.
- Gas handling.
- Maintenance and cleaning.

Regarding heating strategies, microwave processing with susceptors seems like a promising approach for syngas production and for treating highly transparent feedstocks.

However, care should be put in susceptor selection and dimension to achieve the required yields at economical energy inputs. From an energy consumption point of view, more plausible scale-up processes are likely the ones that use a direct microwave heating strategy. However, not every feedstock is readily treatable by microwaves. Combining microwave and conventional heating should be investigated in depth, as this seems to be a major gap in the literature which may provide a practical way for scaling-up.

3.2 Ferrous Pyrometallurgy

Microwave usage in mineral and metallurgical processes have been widely investigated in the last years. Several works on drying, comminution and leaching processes were published [148], [149], [227]–[231]. However, due to the relatively low temperature of such applications, they are not in the scope of this review.

High-temperature metallurgical processes lie within the field of pyrometallurgy, which groups extractive and refining thermal techniques applicable to ores and concentrates. Ferrous-pyrometallurgy, and notably the reduction of iron oxides have received significant attention due to their commercial prospects [65]. Another related application that has shown promise is the microwave production of coke [82], which is one of the main feedstocks of the siderurgical industry. Limited research has also been carried out in oxidation, dephosphorization, recycling and remediation of metallurgical wastes. Among non-ferrous metals, most publications are for copper, gold and titanium metallurgy [65].

In this section, advances in microwave-material interaction characterisation, microwave coke-making and the microwave-assisted reduction of iron ores are briefly reviewed with a special focus on technical implementations and prospects.

3.2.1 Microwave-material properties

Until recently, most microwave-material characterisation efforts were focused solely on electrical permittivity measurements, as dipole polarisation was regarded as the major loss mechanism in microwave heating. However, magnetic properties have significant relevance in ferrous metallurgy [123], [124], [232]–[242].

Iron carrying ores are found in nature in the form of oxides, carbonates and sulphates. The most relevant ores are Hematite (Fe_2O_3), Magnetite (Fe_3O_4) and Goethite ($Fe_2O_3H_2O$), due to large economically minable deposits [243]. Selected works on the electromagnetic characterisation of materials involved in ferrous metallurgy are presented in Table 3.4. Out of cited references, the dielectric loss seems to govern $Fe_{0.925}O$ and Fe_2O_3 heating, while the magnetic loss is predominant in heating Fe_3O_4 up to its Curie point, around 577 ºC, after which the magnetic loss drops sharply to near to zero values. A considerable increase in both real permittivity and dielectric losses are observed over 450 ºC for all these ores.

Table 3.4 Ferrous metallurgy microwave material studies.

Material	Data	Temp (deg C)	Frequency (GHz)	Technique	Ref
Fe0.925O	ε_r	21-1,100	0.915 and 2.45	Cavity pert.	[244]
	ε_r	24-1,085	2.45	Cavity pert.	[245]
Fe1-x	ε_r, μ_r	Room	0.2-13.5	Coaxial line	[246]
α-Fe_2O_3	ε_r, μ_r	Room	0.2-13.5	Coaxial line	[246]
Fe_2O_3	ε_r, μ_r	24-1,000	0.915 and 2.45	Cavity pert.	[247]
	ε_r, μ_r	24-982	2.45	Cavity pert.	[245]
Fe_3O_4	ε_r, μ_r	Room	0.2-13.5	Coaxial line	[248]
	ε_r, μ_r	24-1,000	0.915 and 2.45	Cavity pert.	[81]
	ε_r, μ_r	25-575	0.2-13.5	Coaxial line	[249]
	ε_r, μ_r	24-880	2.45	Cavity pert.	[245]
	Heating rates	0-800	2.45	-	[250]
SiO2	ε_r, μ_r	Room	0.2-13.5	Coaxial line	[248]
Graphite	ε_r	Room	1-12.4	Coaxial/WG line	[251]

Carbon black	ε_r	Room	1-12.4	Coaxial/WG line	[251]
Coal powders	ε_r	Room	1-12.4	Coaxial/WG line	[251]
B. Coal	ε_r	24-900	0.915 and 2.45	Cavity pert.	[28]
Bitumite	ε_r	24-864	2.45	Cavity pert.	[245]
Lignite	ε_r	21-1,000	0.915 and 2.45	Cavity pert.	[83]
Various (carb)	tan(δ)	Room	2.45	-	[97]
Various (carb)	ε_r, tan(δ)	-	-	-	[82]
Various	Heating rates	-	-	-	[252]

Coals are susceptible to microwave heating at low temperatures, mostly due to humidity contents. However, when dry, they typically become microwave transparent. After thermal decomposition begins (over 400 ºC), the release of volatiles and the start of carbonisation processes results in sudden conductivity growth, with the subsequent rise in real permittivity and dielectric losses. The permittivity levels can vary widely for different coals, making characterisation measurements paramount [82].

Conveniently, materials used in ferrous metallurgy are susceptible to microwaves in the ISM frequency bands of 915 MHz and 2,450 MHz, making those frequencies good candidates for the development of industrial applications. Due to the extreme susceptibility of some of these materials, in particular for high-temperatures, penetration depth is a big concern for developing mid to large-scale processing solutions.

3.2.2 Coke-making

Coke is the product of coal carbonisation, a process in which coal feedstocks are heated to temperatures as high as 1,300 ºC, in cycles that can range from 15 to 30 hours. It is typically used for metal smelting, in particular in the production of iron and steel on blast furnaces [253].

This section gives a glimpse of recent developments and the potential of the microwave-based coke-making process.

Fast microwave coke-making was first reported by Lester et al. in a multimode 8 kW system with processing times of around 70 min [254]. The products showed similar properties to conventional coke, in significantly less time, and using feedstocks that are not suitable for traditional coke-making. Experiments disclosed by Binner et al. [85] support these advantages. The authors used a multimode cylindrical cavity, applying microwaves with powers ranging from 750 W to 4,500 W and application times from 15 to 120 minutes. The most significant challenges for the process were identified as the higher energy needs compared to conventional coke-making, and the rapidly changing microwave-material properties with a sudden reduction of penetration depths, the chance of occurrence of thermal runaway, and the need to operate in a high-temperature environment with products at over 1,000 °C. In both works, no temperature measurement was done.

Usually, microwave coke-making relies on the rapid heating of the moisture within the carbon matrix to reach 300 ºC, where its conductivity begins to rise becoming susceptible to microwaves and thus, starts to self-heat. Then, it continues to heat up in accelerated fashion due to a sharp increase in the absorption properties, as mentioned above. This fast enhancement of the absorption makes penetration depth a big concern in microwave coke-making with the inherent uniformity and thermal runaway issues at high-temperatures [82].

Coetzer and Rossouw [255] explored the use of additives in microwave coke making. Chrome and manganese ores and their respective ferro-alloys are deemed as suitable susceptors. Coke formation was completed in 2 to 3 hours reaching up to 1,100 ºC. A batch microwave oven with four magnetrons operating at 915 MHz was used, with a total installed power of 16 kW, treating 5 kg to 7 kg samples. N_2 was used to prevent flammable volatiles accumulation.

K-type ungrounded thermocouples were used for temperature sensing. Ansoft HFSS was used to simulate electric fields distributions to assess treatment uniformity. The authors comment that thermal runaway can be an advantage as it can accelerate the process; however, it can interfere with the coke formation and produce damages to the furnace lining. Their work supports the view that the main issue is the considerable variability of the dielectric loss and penetration depth with temperature, making the process hard to control.

The use of numerical simulations can be useful to understand details on microwave-material interaction as suggested by Hong et al. in [256]. Multi-physics simulations were carried out, showing good agreement with experimental observations, and reporting that valuable insight on the influence of varying different parameters on the process can be obtained, which can be helpful in further optimisation efforts.

Microwave-coal interactions knowledge is the basis for the development of a microwave coke-making system. Different coals possess widely different properties, so measurement of the actual materials to be used is key [82]. Peng et al. [83] carried out the dielectric characterisation of low-rank coals at 915 MHz and 2,450 MHz up to 1000 ºC. Penetration depths changes with temperature are reported, suggesting it can be practical to reduce the operating frequency when penetration depths drop to improve treatment uniformity. The potential of using variable frequency for large-scale microwave heating is discussed. Various other works on coal characterisation were cited in the previous section.

At small-scale, microwave coke-making seems to be plausible and with two significant advantages, rapid processing and the ability to use low-grade coal feedstock, which can result in the revalorisation of natural resources. However, energy consumption differences versus conventional processes have hindered the motivation for developing large-scale systems. To date, no commercial solution has been found on a significant scale. Most equipment used are

based on modified commercial microwave ovens used in batch or low-volume single-mode laboratory systems. Techno-economical evaluations are non-existent in the open literature to the author's knowledge and are urgently needed to assess the real feasibility of the process.

Key issues identified are the large energy requirements, rapid change of electromagnetic properties diminishing the microwaves penetration ability at higher temperatures, and the occurrence of thermal runaway. Moreover, large-scale implementations are likely to be of continuous nature to produce relevant throughputs. These should be able to handle substantial material volumes with inherent material transport; heat-loss and insulation; volatiles handling; high-power; safety; and reliability concerns, all under extremely harsh environments.

Due to large variations in the material properties during processing, multistage systems are a promising concept to research, with different stages providing the most effective treatment to the product at the particular stage, using different powers, frequencies or applicator geometries. However, material property changes might prove to be too fast and of heterogeneous occurrence for such implementations. Hybrid heating that combines microwaves with conventional techniques should also be evaluated, as the current literature has ignored this type of approach. These sophisticated processing techniques, developed in a multidisciplinary approach, plus the ever-maturing know-how in handling microwave processing and the use of advanced tools such as multi-physics simulations can eventually provide a technological step-change needed for scaling-up. The focus should be put into reducing the energy consumption difference versus conventional methods and in providing technical feasibility for high throughputs.

3.2.3 Iron ore reduction

The reduction of iron ores employing microwave radiation had been the subject of several studies in recent years, as a supplementary technology in iron and steel-making

processes. Efforts have been made in the reduction of iron ore pellets [96], [123], [124], [257]–[264] and powder mixtures [77], [78], [95], [265]–[271].

Typical iron and steel making comprise several steps. First, the production of concentrate through mining, crushing and milling, flotation and concentration (Other beneficiation processes such gravity concentration, water washing and magnetic separation are also used) [243]. Secondly, agglomeration, mostly by pelletising in travelling-grates, or shaft-furnaces, or grate-kilns [243]. Finally, the pellets are mixed with coke and limestone as a fluxing agent and fed to either a blast furnace or to a directly reducing system (DRI) and then to an arc furnace [243]. DRI can be done with carbon pre-mixed within the pellets rather than purely on natural gas for fast self-reduction [272].

The main issue with conventional pellet reducing is the inability to heat the pellet core fast enough to fuel the gasification of carbon to CO to serve as reducing agent. Microwaves, due to their volumetric heating properties can overcome this limitation, allowing a practical way for high metallisation, and also to speed up the reactions [96]. These conclusions, along with lower reduction temperatures have been supported by several authors [96], [123], [124], [259]–[266]; Nonetheless, the unreacted core problem cannot always be avoided using microwaves [258]. The pellet compositions, size, and arrangements within the reactor should be carefully planned and tested to achieve the desired levels of reduction. Efforts have been made to even tailor the pellet structure to optimise the microwave penetration by creating core-shell iron ore-biochar pellets [272].

Different reductant agents have been tried either as a pellet component or in powdered mixtures. Charcoal [77], [259], [264], [266], coke [77], [96], [124], [257], [259], [266], graphite [77], and even waste plastics, biochar and biomass [267], [272], [273]. Charcoal versus coke comparison suggests the use of charcoal results in faster reactions and higher temperatures

[259], [266]. The use of fluxing agents for better slag separation [96] and other additives such as cement to increase microwave absorption and reaction rates have also been reported [259]. The reducing agents are typically microwave absorbent materials, so they provide a double function of reductant and microwave susceptor which can lead to localised reduction zones within the pellet structure [260].

Atmospheric control is key in the reducing process, in particular, the reduced oxygen to avoid re-oxidation. Inert atmospheres based on nitrogen [250], [260], [262], [268]–[270], [274] and argon [123], [124], [259], [267], [275] are typically used, and a few carbon monoxide rich atmospheres have also been used [263], [265]. No comparative studies in this respect have been found.

Rigs range from modified over the shelf microwaves ovens with atmosphere controlled reaction vessels [96], [259], [267], to varying specific geometries such as cylindrical [263], [264], cylindrical with two conic trapezoids [78], pentagonal [260], [261], [268], [269] and hexagonal [77], [270] shapes. Single-mode setups have also been reported [95], [123], [124], with the particular use such systems to study the separated effects of the electric and magnetic fields on the reduction process. Operation frequencies are generally 2,450 MHz and 915 MHz.

Large-scale implementations are scarce. Nagata et al. [274] proposed a concept for large-scale microwave steel making furnaces based on a horizontal flow system with a rotary kiln. A reverberator furnace was studied using numerical simulations for field distribution evaluation [276]. The development of a bench-scale prototype for direct steel-making combining microwave, electric arc and exothermal heating was commented in [277]. Patent claims for concepts as continuous rotary hearth furnace, a rotary kiln, a linear conveyor and vertical shaft furnace for use in microwave reduction of iron oxides were made by the same authors [278].

Temperature measurements are mostly reliant on pyrometers [77], [78], [95], [123], [124], [258], [261], [268]–[270], with the limitation of only surface temperature measurements. The use of thermocouples has also been reported [96], [250], [258], [259], [262], [265], [266], [275]. Standish et al. [96], [265], [266] reported on measurements done by turning off microwaves and quickly inserting a sheathed chromel-alumel thermocouple into the composite sample through a small hole in the crucible wall. Aguilar et al. [258] dealt with accuracy issues of such a technique, and used a strategy based on the different observable phases (solid or molten) and estimated a range of temperatures based on material properties, complemented with the use of optical pyrometers. Jermolovicius et al. [123] comment how the lack of actual energy balance in previous works hindered research, proposing the control of incident and reflected powers, along with mass and temperature measurements. Thermal insulation was deemed as critical with up to 99 % of the energy loss in non-insulated experiments. The use of full thermal insulation in microwave reduction processes can result in significantly higher final temperatures [259].

The reviewed literature suggest that microwave-based reduction of iron oxides seems to occur at lower temperatures, faster and more efficiently than conventional methods. The cold-core problem can be solved by microwave-volumetric heating, which allows almost complete metallisation in laboratory setups. The economics of the process remains uncertain.

Attempts have been made to develop large-scale solutions but are mostly conceptual propositions. Experimental results are yet to be seen. Commercial patents of large continuous systems do exist; however, to the best of the author's knowledge, none of such concepts has been publicly implemented.

There seems to be a long way to go to develop large-scale systems. Large-scale implementations would require continuous or semi-continuous processing to reach significant

throughputs, and thus, would need robust and durable furnaces with adequate thermal insulation, microwave choking, atmospheric control and product handling capabilities. A multidisciplinary design effort should be made with the goals to control critical processing aspects such as hot spots; penetration depth; thermal runaway; arcing; treatment uniformity; safety and EMC regulations compliance; durability for operation in harsh conditions; efficient processing according to fast product properties evolution; pressurisation; toxic gas handling; maintenance and cleaning. The investigation of optimal pellet composition and shapes for microwave processing, as well as techno-economic feasibility studies, are needed to advance further. The use of hybrid and staged systems should also be explored to design scalable solutions.

3.3 Sintering of advanced materials

Sintering is the process in which powdered materials are pressed and heat treated at high-temperatures (below the melting point) to form a solid product. This technique is commonly used in both ceramic and powder metallurgy, using gas or electric furnaces. Demand for finer micro-structures and better physical and mechanical properties have promoted microwave-sintering research, as early results have shown such advantages [8]. Moreover, microwave technology can have the upper hand regarding processing times and energy consumption [93]. Reduction of treatment times of up to 90 % and energy consumption of up to 80%, with finer grain size, higher density, enhanced corrosion resistance and better strength products can be achieved in both ceramic and metallic powder sintering [279].

The prospects for microwave ceramic sintering applications have been widely researched and it is arguably the most developed high-temperature microwave processing technology with several works being published each year. Moreover, since 1999, research has significantly expanded to cover powder metallurgy and compound materials sintering [280]. In this section an overview of the microwave sintering process for ceramic and powder metallurgy

is presented, with attention to technical implementations and the prospects to develop large-scale solutions.

3.3.1 Microwave ceramic sintering

Microwave ceramic sintering presents some significant advantages over traditional sintering techniques. However, most technical implementations rely on conventional thermal treatments, in particular because of the lack of large-scale solutions [140], [279], [281].

The fast heating provided by microwaves is desirable for the sintering of advanced ceramics to avoid overgrowth of grain size, which can deteriorate mechanical properties significantly. This, plus the enhancement of efficiency, reduction of processing times and improvement of treatment uniformity, are the primary advantages that fuel microwave sintering research [181].

Microwave sintering of several ceramics including alumina, zirconia, PZT, BT, BMT, BZT, ceramic glasses, bio-ceramics, and ferrites, have been studied, reporting, among others, successful sintering with improvements on reaction and diffusion kinetics, better product properties, faster processing, and lower sintering temperatures versus conventional methods. The use of hybrid heating or microwave susceptors has been deemed as critical in most of these applications [21], [62], [281].

The relevance of the use of hybrid heating and susceptor assisted heating is further reinforced in several works compiled by Bhattacharya and Yahaya et al. [66], [282]. These suggest that with an adequate susceptor selection, shaping and positioning, uniformity can be enhanced significantly, as well as reducing thermal runaway, processing times and energy consumption. The control over the balance between power and time, or temperature and time, with suitable susceptors, can result in highly dense and homogeneous microstructures [63]. Susceptors used are silicon carbide, carbon, and magnetite.

The challenge in this type of sintering is to create a controlled environment to bring the ceramic parts to an adequate temperature where it becomes susceptible to microwaves. This can be done by preheating by conventional methods or by using susceptors. Furnace and susceptor design and placement can lead to an enhanced heat treatment which can improve yields and product properties [140].

Hot spots, thermal runaway, and repeatability are critical issues in the microwave sintering process, several modelling efforts to predict such events have been carried out with limited success [21]. Thorough knowledge and detailed data on the dielectric properties of the materials involved in conjunction with advanced multi-physics simulations have shown promising results in predicting thermal runaway in zirconia processing [283]. Rybakov et al. [284] reviewed modelling and simulation efforts in the sintering process, highlighting the trend of using multi-physics simulations combining electromagnetic and thermal solution and coupling with sintering models. This approach can make it possible to predict and optimise density distributions and shrinkage of the sintered products.

Implementations to date have been small lab-scale batch systems [140], with temperature monitoring based mostly on infrared pyrometers. Commercial batch systems are available for low-volume throughput applications such as sintering of zirconia-based dental restorations [285]. A prototype continuous operating kiln was reported, in the form of a pusher system with controlled atmospheres [279], but beside this, few if any large-scale systems are available to produce significant research. Continuous microwave processing can provide higher energy savings, lower equipment costs, faster production and better yields [140].

3.3.2 Powder metallurgy

Various metal powders have proved to be quite good microwave absorbents allowing direct microwave-based sintering [286]. Enhanced properties [7], extreme energy savings of up to 96 % and reduction in processing times of up to 90 % over conventional sintering have been

reported [280]. Even bulk metals, when preheated to certain temperatures can exhibit good absorbing qualities [62]. With the use of hybrid and susceptor-based techniques, new applications have been developed including melting, brazing, annealing, joining, cladding and casting [7], [64], [66], [280].

Microwave sintering of commercial metal powders was reported in [286], [287]. Iron and steel, copper, aluminium, nickel, molybdenum, cobalt, tungsten, tungsten carbide and tin, and their alloys were used successfully. Several types of products including toothed gears were created. Various products have been investigated, among others powdered copper steel [288], lower dielectric constant Ni-Zn ferrites [289], metal green parts [290], refractory metals like W, Mo, Re, W-Cu, W-Ni-Cu and W-Ni-Fe [291], [292]. Tabulated information on sixty microwave sintering works was compiled recently by Mishra and Sharma [280], covering investigations on pure metal, metal alloys and metal composite powders. Reducing processing times and energy, as well as comparable or even superior mechanical properties are the most commonly found advantages over conventional sintering.

Microwave powder metallurgy laboratory setups generally operate at 2.45 GHz in both single [232], [233], [235], [236], [241], [290], [293] and multi-mode [289], [290], [294] systems, with powers ranging 1 kW to 6 kW in controlled atmospheres. Temperature measurements are based on optical and infrared pyrometers and in some cases sheathed thermocouples.

Although microwave heating of powdered metals, in particular for sintering, has been broadly used, there is still lack of understanding of the fundamentals behind it. Much of the experimental work has been carried out to clarify such interactions. The relevance of magnetic losses in microwave heating of metal samples was reported in early research on the topic, giving significant relevance to the induction of eddy currents [235]–[237]. In these works, the samples

were treated in a single-mode rectangular cavity with a variable short circuit allowing the shift of the position of the electric and magnetic field maximum amplitude, to match the location of the samples and to assess the nature of the effects independently. Cao et al. [232], [233], [241], [242] support the importance on heating of the magnetic fields, based on experiments in a similar E-H field separation setup for heating PZT, gold thin films, and silicon substrates. To the author's knowledge, the only work on the relevance of the polarisation of the fields concerning the sample that has been published is [232], revealing that sample surfaces perpendicular to the magnetic fields are those more efficiently heated.

Various attempts to develop a theoretical model have been made. Luo et al. [238] attribute the loss mechanism mostly to eddy currents or magnetic induction, with good agreement with experimental observations, but with severe limitations at high-temperatures. Rybakov et al. [239] propose a formulation for conductive particles surrounded by insulating oxide layers. Empirical observations for silicon, iron and copper powder compacts were carried out validating the proposed theoretical model to some extent. Mishra et al. [240] also suggested a model for microwave heating of particulate metals, predicting temperature variations with time during sintering, and assessing the effect of powder size, emissivity and susceptor heating on the heating rates. The model is validated experimentally observing thermal profiles of tin, copper, and w-alloy compacts in a 2.45 GHz multi-mode microwave furnace. A formulation based on plane wave normal incidence is presented by Peng et al. [234], calculations show that the magnetic loss can be up to four times larger than the dielectric loss for the heating of ferrites. However, the model was not directly contrasted with experimental results other than qualitatively.

Localized focusing phenomena, in particular where particles touch (i.e. sintering neck), with high electric fields, led to the generation of micro-discharges during sintering, which results in the acceleration of the process [7], [290]. Field focusing behaviour, for the magnetic

field, was numerically studied using Ansoft HFSS [295] where a set of 49 particles of aluminium was subjected to a 2.45 GHz at 3 kW in a TE_{103} rectangular resonator. Based on the concept of E-H field separation, the particles were placed in a magnetic field maximum. Their results showed micro-focusing of magnetic fields in the sintering neck, which may explain the acceleration of sintering rates. This effect decreases gradually with the advance of the sintering progress as the neck grows and is more significant for particles in the outside parts of the group, slowing down the sintering rates. Although practical to better comprehend the microwave-material interactions, micro-scale behaviours are rather complex or computationally prohibitive to use straightforwardly in large-scale simulations.

3.3.3 Discussion of microwave sintering of materials

Despite successful processing and advantages widely reported in the literature, microwave sintering systems are mostly limited to small volume batch production and laboratory-scale setups. Solutions primarily rely on modified commercial microwave ovens or over the shelf equipment with powers of less than 6 kW, and a typical operating frequency of 2.45 GHz, with some laboratory single-mode applicators [21], [62], [66], [282].

Much work is still needed to reach a full commercial scale. Sophisticated high-temperature applicator technology with adequate control over the process and repeatability, applying advanced techniques such as hybrid heating in a continuous process is needed. Among the critical reasons that have hindered such development are: the need for a profound knowledge of microwave-material interactions; process dependence on the material ability to absorb microwaves and its rapid change during processing; heating uniformity issues leading to hot spots, thermal runaway and arcing; need for sophisticated insulation; poor repeatability and product quality consistency due to the system dependence of a multiplicity of factors, and the lack of control over those; lack of practical high-temperature and microwave friendly sensing and monitoring equipment; robustness of continuous processing system able to sustain

operation under harsh conditions, complying with leakage and safety regulations, and ability to process large enough volumes to meet industry standards.

Research lines that can help narrow the gap to scale-up are the accurate microwave-material interaction characterisation; numerically-assisted process optimisation with multi-physics codes; variable processing parameters such as operational frequencies, powers and applicator geometries; pulsed microwaves to allow heat redistribution; hybrid heating; optimal sample shape and size; susceptor selection and shaping. All in the context of the development of a continuous system.

3.4 Conclusions

Applications in which fast volumetric or selective heating is needed is where microwave-material processing thrives.

Most problems with high-temperature microwave processes seem to be common across industries. Authors' conclusions point to the need for a thorough understanding of microwave and material interactions and detailed characterisation of its properties variations under different process states. Thus, precise measuring and predictive methods are paramount. The need of specially designed applicators and microwave systems for each particular process is highlighted in literature, accounting for aspects of the different process and material conditions such as material volume, material flow, field uniformity and distribution, field or material stirring, power density, temperature distribution, penetration depth, thermal runaway and arcing. Furthermore, systems should be robust and safe for continuous operation under harsh environments, using proper construction materials, microwave leakage suppression, thermal insulation, gas handling and atmospheric control. Also, these systems should implement methods for waste and contamination management, metrology, matching and control of the process that ensure efficiency and adequate process conditions.

The study of techno-economic implications, including material and equipment deterioration, energy costs and production volumes are virtually non-existent.

All these considerations make the development of high-temperature microwave systems for industrial-scale a highly complex engineering challenge. Due to the diversity of parts involved in the process, the design effort should take a multidisciplinary approach with a holistic view of the problem. Advanced computer modelling solutions can be an essential tool in both achieving a deep understanding of the variables and complexities of the process and for the design and optimization of applicator structures and dimensioning of hardware requirements. The use of sophisticated heating strategies, such as hybrid and multistage systems, needs to be explored further. Hybrid systems present a notorious knowledge gap in all fields of application. Careful selection of material size, shape and positioning, as well as applicator geometries and the ability to operate continuously are critical for large-scale implementations.

Chapter 4 Methods, materials and modelling framework

In this chapter the measurement methodologies and materials are detailed. The modelling framework is set and validated against a set of experimental measurement examples. This sets the foundation for the design work, measurements, and analysis performed in the following chapters.

First, the measurement and characterisation of applicator structures are laid out, including scattering parameters, quality factor, power measurements and thermal imaging. Second, the used dielectric measurement methodologies are explained, including cavity perturbation and transmission line techniques. Third, selected materials used for design and/or validation purposes are presented, showing their measured dielectric properties (FOAMGLAS®T4, quartz powder, Ecoal50 charcoal briquettes and copper ore). The properties of auxiliary materials used for sample positioning, furnishing and structural support are also characterised. Fourth, a general framework for modelling and simulation using COMSOL Multiphysics is proposed and validated experimentally with several examples.

4.1 Measurement of scattering parameters

This parameters are used for both dielectric characterisation and cavity design validation. The measurement of these parameters is done using a vector network analyser (VNA). Calibration at the measurement planes is carried out to de-embed the influence of the measurement system from the properties of the device under test (DUT). Unless otherwise specified in the specific section, all scattering parameter measurements were made by calibrating the VNA using either a Thru-Reflect-Line (TRL) or a Short-Short-Load-Thru (SSLT) method for waveguide ports, and a Short-Open-Load-Thru (SOLT) for coaxial ports [296]. Once the ports are calibrated, they are connected to the corresponding ports of the DUT to perform scattering parameter measurements.

The VNA sweep a signal of varying frequency. Then, it will separate incident, reflected and transmitted waves. The detected signals are used to calculate the respective ratios associated with the scattering parameters, including magnitude and phase information. The VNA can switch the signal source port, allowing for the direct measurement of various ports parameters simultaneously, depending on the number of available ports. The configuration of the instrument depends on the model and on the particularities of the device to be tested and needed resolution.

4.2 Measurement of Q-factor

The quality factor serves as basis for dielectric measurements in cavity perturbation systems and for validation and performance evaluation of resonant applicators. Resonant frequency, coupling coefficient and the quality factor of a cavity can be obtained with the transmission, reflection and transient decay [297], of which the most practical and straightforward for waveguide-based cavities are arguably transmission and reflection type. Classical equipment used to perform Q-factor measurements have mainly been replaced by network analysers that allow a fast frequency swept and measurement of scattering parameters [298]. Direct measurement results in the loaded quality factor (Q_L), which includes line and coupling losses. Determination of unloaded quality factor (Q_0) requires the knowledge of the coupling coefficient (g) to the external circuit. Then, it can be calculated as [298]

$$Q_0 = (1 + g)Q_L \tag{4.1}$$

In this work, two types of Q-factor measurement were used, two-port transmission for dielectric characterisation in resonant cavities, and one-port reflection measurements for applicator characterisation.

4.2.1 Two-port measurement of Q-factor

Q_L can be determined using a VNA to measure the transmission scattering parameter $|S_{21}|$. By determining the resonance frequency f_0 and the half-power frequency points where $|S_{21}|$ has dropped 3 dB from its value at resonance (Figure 4.1). This frequency range $\Delta f = f_2 - f_1$ allows for the calculation of the loaded quality factor as [2]

$$Q_L = \frac{f_0}{f_2 - f_1} \tag{4.2}$$

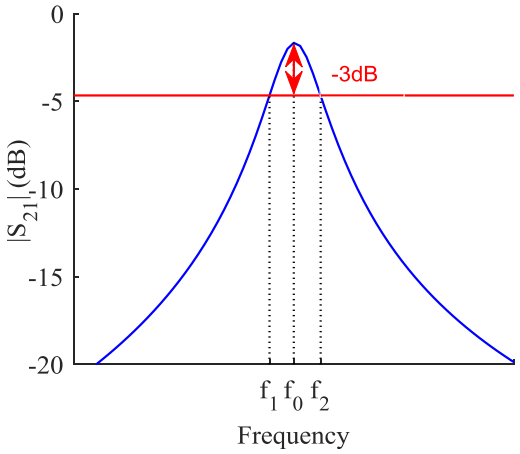


Figure 4.1 Example transmission coefficient of an iris passband filter with a small dielectric insert.

Then, the coupling coefficient can be calculated at resonance, if the coupling ports are symmetrical, as [298]

$$g = \frac{|S_{21}(f_0)|}{1 - |S_{21}(f_0)|} \tag{4.3}$$

where, $|S_{21}(f_0)|$ is the linear magnitude of the transmission coefficient at the resonant frequency. These two quantities (equation (4.2) and (4.3)) can be replaced in equation (4.1) to calculate Q_0 as

$$Q_0 = \left(\frac{1}{1 - |S_{21}(f_0)|}\right)\frac{f_0}{f_2 - f_1} \tag{4.4}$$

The accuracy of such measurement can be hampered when the coupling is relatively high with $|S_{21}(f_0)|$ approaching unity, so the measurements should be performed away from a critical coupling.

4.2.2 One-port measurement of Q-factor

The most common scenario in microwave heating is having one port available, which will be used for delivering energy to the system. In such a case, reflection measurements should be used. Details of such methods and its use with other equipment can be found elsewhere [2], [12], [298]. In this section a simple methodology is adapted from [12], [298]–[300] to measure Q_0 based on VNA reflection coefficient and $VSWR$ near the resonance frequency is detailed.

The reflection scattering parameter S_{11} (i.e. the reflection coefficient Γ) is measured in a frequency span around the resonance with a VNA. The voltage standing wave ratio ($VSWR$) is then calculated from it, as

$$VSWR = \frac{1 + |S_{11}|}{1 - |S_{11}|} \tag{4.5}$$

At resonance, the $VSWR$ is minimum and the coupling factor will be given by

$$g = \begin{cases} VSWR(f_0) & \text{if over-coupled} \\ 1/VSWR(f_0) & \text{if under-coupled} \\ & \text{if critically coupled both are equal} \end{cases} \tag{4.6}$$

The coupling can be inspected by plotting the reflection coefficient in the Smith-chart plot (Figure 4.2). The diameter of the circle normalised to the diameter of the chart will determine the coupling factor as

$$g = \frac{1}{\frac{d_c}{d} - 1} \tag{4.7}$$

If the circle diameter is half the chart diameter, the cavity is critically coupled (e.g. green line Figure 4.2), if it is smaller is under-coupled (e.g. blue line Figure 4.2), and if it is larger is over-coupled (e.g. red line Figure 4.2). The accuracy of measurement will greatly depend on the number of points measured. Therefore, to provide good accuracy without unnecessary excessive data, the VNA span should be centred in the resonant frequency reduced to just enough to show an almost complete resonance circle in Smith chart mode, as this is enough for Q-factor estimation. In this work most, measurements were performed at 1,001 points for spans of less than 50 MHz and calibration were performed for the same settings.

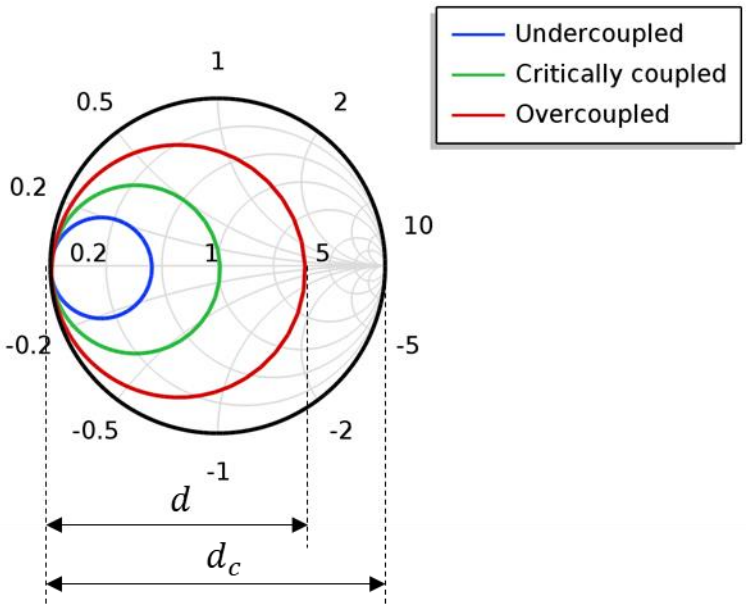


Figure 4.2 Smith chart plot of three example of resonant cavities. Under-coupled (blue line), critically coupled (green line), and over-coupled (red line).

If the network presents significant coupling losses, these cannot be ignored from the coupling coefficient calculation. In such case, the resonant circle will be detached from the smith-chart perimeter, and an auxiliary circle tangential to both the Smith chart and resonance circle needs to be used to determine the coupling factor correctly (Figure 4.3). Then, it can be calculated as

$$g = \frac{1}{\frac{d_{aux}}{d} - 1} \tag{4.8}$$

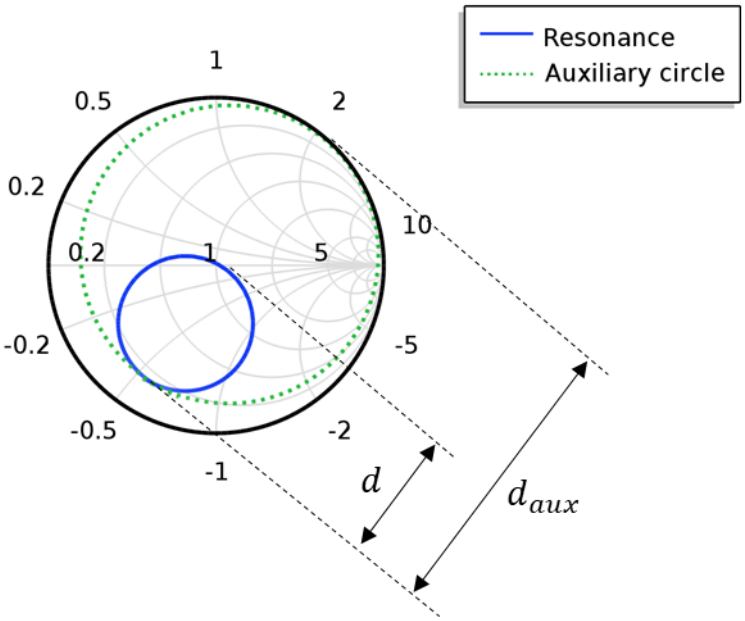


Figure 4.3 Auxiliary circle for smith-chart calculation of coupling factor, with lossy coupling structure.

The measured data were fitted and post-processed using MATLAB.

The behaviour of a resonant cavity can be modelled as an equivalent RLC resonator if observed from the detuned short position, which is the plane at which the impedance looking into the coupler and cavity has a frequency response like the one of a parallel RLC circuit. Considering the generic system illustrated in Figure 4.4 a basic circuital model as the one in Figure 4.5 can be constructed.

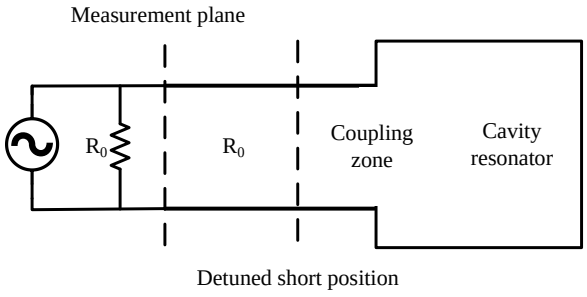


Figure 4.4 Generic representation of a microwave resonant cavity system.

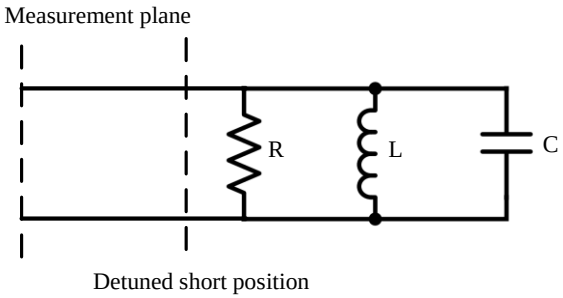


Figure 4.5 Circuital model representation as parallel RLC circuit, of a generic microwave resonant cavity system.

The coupling coefficient relates to the quality factors as $g = Q_0/Q_{ext}$, and, from the circuital approximation can be defined simply as $g = R/R_0$.

The S_{11} data requires to be calibrated in order to be referenced to the detuned short position as

$$S_{11}^{cal}(f) = S_{11}^{meas}(f)e^{j2\pi f t_{delay}}$$

This can be done by ensuring that

$$S_{11}^{cal}(f_0) = Re\left(S_{11}^{meas}(f_0)e^{j2\pi f_0 t_{delay}}\right)$$

And that $S_{11}^{cal}(f)$ approach a short circuit when departing from the resonant frequency.

This is illustrated in the Smith chart in Figure 4.6.

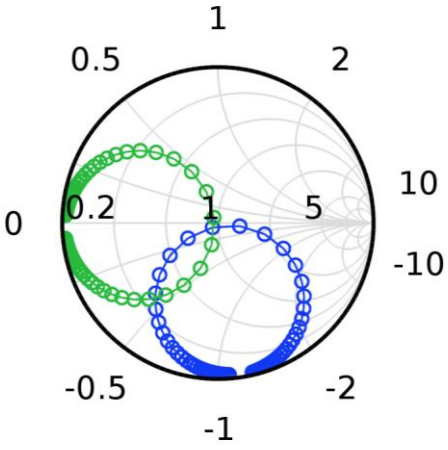


Figure 4.6 Representation of a resonator resonant circle from a measurement plane (blue circles) and a calibrated to the detuned short port position with an adequate delay (green circles).

The half-power points occur when the resistance is equal to the reactance, given the equivalence to an RLC circuit as the impedance is reduced by $1/\sqrt{2}$. . The VSWR at half power points for the empty quality factors is given by

$$VSWR_{hp} = \frac{2 + g^2 + \sqrt{4 + g^2}}{2g} \tag{4.9}$$

The frequency band covered by these points and the measured resonant frequency can be used to obtain $Q_0 = f_0/(f_6 - f_5)$. This points and the ones that can be used to calculate the other quality factors are shown in the Smith chart in Figure 4.7. The calculation can be done directly on a network analyser by the use of the Smith chart representation identifying these frequency points. Q_0 is calculated from the difference between f_5 and f_6 points in the resonant circle which comply with the condition that $Re\{Z\} = Im\{Z\}$. Q_{ext} from the difference between f_3 and f_4 points in the resonant circle which are in $Z = \pm j$. Q_L from the difference between f_1 and f_2 that shows minimum imaginary part of S_{11}, $|Im\{S_{11}\}| \rightarrow max$.

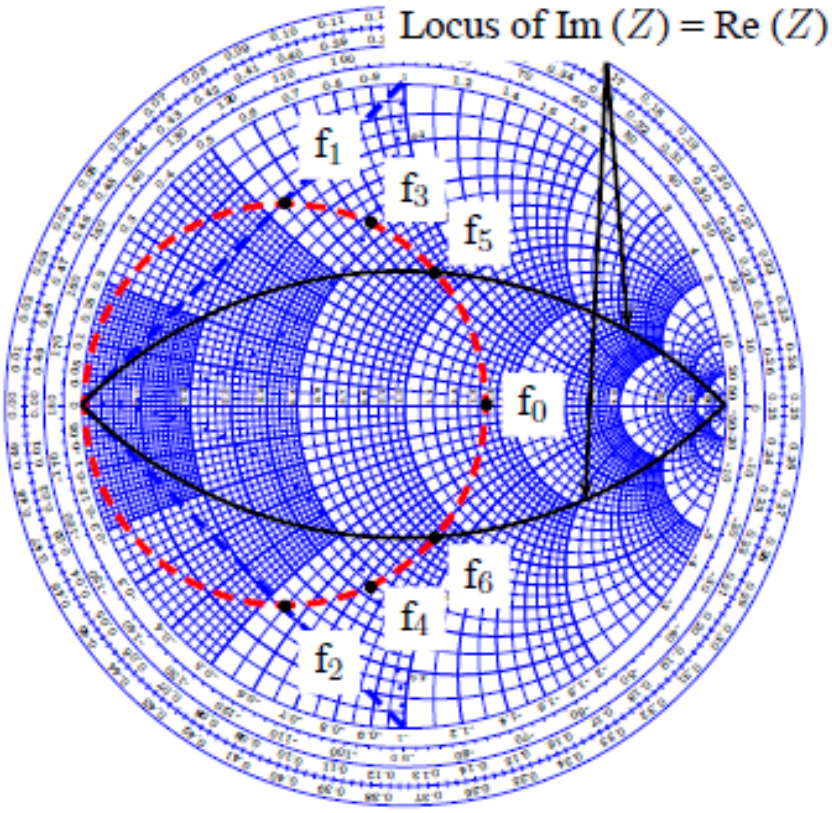


Figure 4.7 Smith chart representation of the half power frequency points for the calculation of the different quality factors, reproduced from [300].

4.3 Power measurements

Direct power measurements and associated metrics including average power loss density, power uniformity index and power conversion efficiency, presented below, are used to evaluate the performance of the different applicator designs.

4.3.1 Direct power measurements

During microwave treatment, a useful parameter to monitor is the absorbed and reflected power. The power variation gives insight into the material evolution and allows to act during processing to improve efficiency. Two techniques were employed for power measurements during heating. The use of directional couples with Agilent U2000A power sensors [301], and the use of an automatic three stub tuner with an integrated six point measurement device which allows to measure frequency, and reflection coefficient phase and amplitude [302].

4.3.2 Average power loss density

The average power density in a volume V can be defined as [303]

$$P_{davg} = \frac{1}{V}\int_V P_d dV \tag{4.10}$$

where P_d is the power density. This quantity gives insight to the attainable power density on the bulk of the material. This quantity cannot be easily established experimentally, unless the majority of the absorbed power is expected to be dissipated in the product (e.g. for relativly high loss materials treated in low-loss walls systems with transparent furniture), a rough estimation can be performed as the ratio of dissipated power to sample volume. An alternative metric is to define the power density versus product mass rather than volume, which can be more practical for processing engineering estimations.

In practice, approximate experimental limits to the operational power can be projected based on the common apparition of arcing for certain power density at certain product states;

however, this strongly depends on the applicator configuration, and therefore should be tested in detail upon scaling operations.

4.3.3 Power uniformity index

To assess the treatment uniformity within a volume the Power Uniformity Index (PUI) is defined, averaging the power density data spread and normalising to the average power density as [303]

$$PUI = \frac{\int_V \sqrt{\left(P_d - P_{davg}\right)^2} dV}{V\, P_{davg}} \tag{4.11}$$

The minimum achievable PUI is zero for a totally uniform power density throughout the product (i.e. the power density evaluated in each point of the volume is equal). Due to the impossibility to asses such quantity experimentally, this metric is used to evaluate simulation results.

4.3.4 Power conversion efficiency

The power conversion efficiency is a measure of the part of the power that is actually being absorbed by the sample. This can be estimated by measuring the unloaded quality factor with an empty cavity (Q_{0empty}) and with the sample inside of the cavity ($Q_{0filled}$) as [67].

$$P_c = 100 \times \left(1 - \frac{Q_{0filled}}{Q_{0empty}}\right) \tag{4.12}$$

4.4 Dielectric measurement methodology

In this section the methodologies used for dielectric characterisation are described. This to cover the objective of characterising the different testing materials proposed for design and performance analysis of the designed applicator solutions.

4.4.1 Cavity perturbation technique

The system comprises an electric tube furnace and a two-port cylindrical copper TM_{0m0} resonant cavity connected to an HP 8753 vector network analyser, as shown in Figure 4.8.

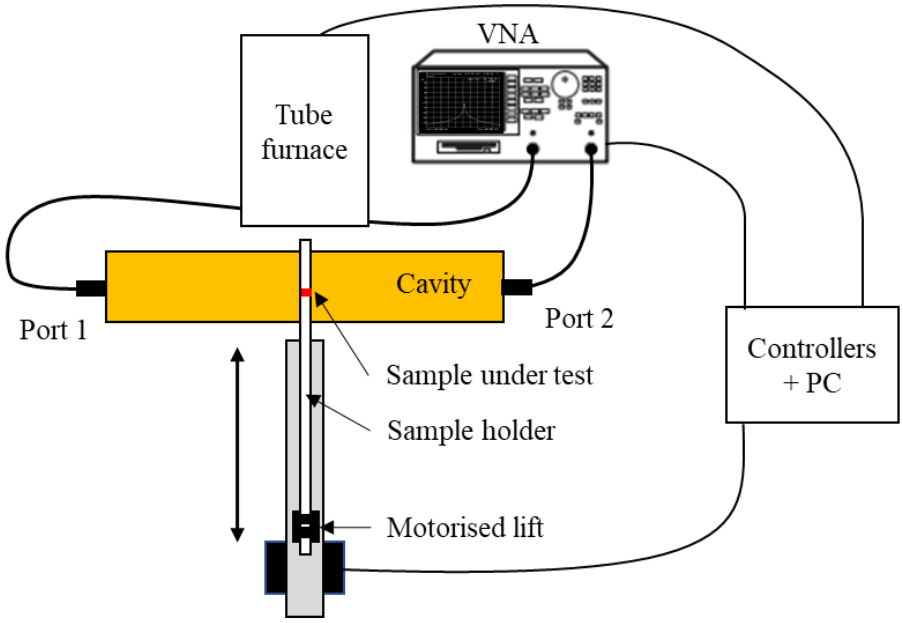


Figure 4.8 Schematic representation the cavity perturbation measurement rig.

The cavity was designed to allow several resonant modes near ISM frequencies of interest with a diameter of 578 mm and 58 mm height. The empty cavity resonance frequencies used in this setup are 395 MHz, 910 MHz, 1,429 MHz, 1,949 MHz, 2,470 MHz and 2,989 MHz, for TM_{0n0} with $n = 1, 2, 3, 4, 5\ and\ 6$, which corresponding electric field distributions illustrated in Figure 4.9.

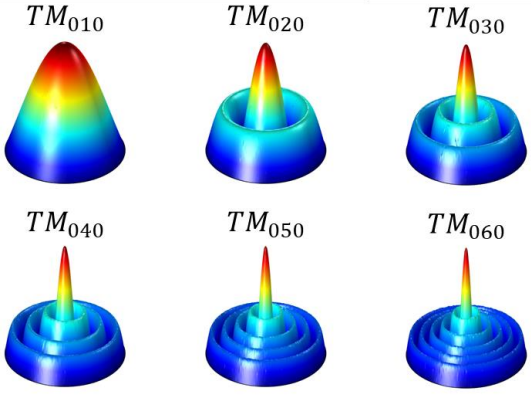


Figure 4.9 Electric field distribution of resonant modes of the cavity for dielectric measurements.

Quartz tubes of internal diameters from 2 mm to 4 mm with ceramic wool plugs (its dielectric properties can be found in [304]) are used as a sample holder. The influence of the sample holder is calibrated out by measuring the empty cavity quality factor and resonance frequency in the presence of the empty holder.

The sample is heated up in the tube furnace, which, after reaching the set temperature for a fixed time is rapidly moved to the resonant cavity with an automated step-motor. The shift of resonant frequency and change of quality factor are measured in transmission mode from the two cavity ports (see section 4.2.1) allowing the determination of the dielectric constant and the dielectric loss factor as [305]

$$\varepsilon' = 1 + 2J_1^2(X_{l,m})\left(\frac{V_c}{V_s}\right)\left(\frac{f_0 - f_s}{f_0}\right) \tag{4.13}$$

$$\varepsilon'' = J_1^2(X_{l,m})\left(\frac{V_c}{V_s}\right)\left(\frac{1}{Q_s} - \frac{1}{Q_0}\right) \tag{4.14}$$

Where J_1 is the first order of Bessel function, $X_{l,m}$ is the root of the first order Bessel function. V_0 and V_s are the volumes of the empty and loaded cavity, f_0 and f_s are the resonant frequencies of the empty and loaded cavity, and Q_0 and Q_s are the quality factors of the empty and filled cavity. Tabulated values of the Bessel function roots can be found in Appendix A. A further modification was incorporated by the author to provide inert dielectric measurements by flowing nitrogen through the quartz sample holder. Detailed discussion on how this relations are obtained can be found in [47], where the theory behind the use of shorter than the cavity height samples is developed, by calculating an effective depolarizing factor.

Among sources of error, sample volume estimation, contamination of sample holder, calibration, and inherent inaccuracies of the technique due to large perturbation of the fields when measuring materials with high dielectric constant and loss factor are the most significant. For relatively large complex permittivity materials, the use of small samples is suggested to

improve measurement accuracy effectively [305]. For high-temperature measurements, the variation of the sample volume during heating, contamination of the tube, and the inherent heat loss in the transition from the furnace to the cavity and between measurements at different frequencies can be significant. The heat loss error can be reduced by measuring one frequency at a time, leaving less than 5 seconds for the sample to cool. Nonetheless, this introduces an inherent uncertainty in the accuracy of the results. Alternative methods based on in-situ monitoring have been recently start to gain attention [306].

The aforementioned methodology along with measurement results were published by the author of this work for nutshell char biomass [307].

4.4.2 Transmission line technique

Three different waveguide two-port waveguide systems have been used in this work for ISM 2,450 and 915 MHz measurements. A WR340 running the NNI algorithm was designed and implemented for granular materials. Existent WR430 and WR975 based systems with a selection of NWR, IPF and other commercial algorithms were also used. Only room temperature measurements were made on these systems.

4.4.2.1 WR340 system

A two-port waveguide setup for measuring the bulk dielectric properties of granulated materials at room temperature was developed. The system comprises an Agilent E5071C VNA with both ports connected to opposing ends of a waveguide transmission line. Standards were custom fabricated to allow an accurate and fast TRL calibration at sample holder reference planes [308]. The sample holder consists of a $\lambda_g/4 = 43.3$ mm waveguide section with expanded polystyrene windows. Before each measurement, the sample holder is filled with the material under test and sealed with polystyrene windows. The windows influence, although generally negligibly, is compensated by de-embedding [309]. The measured scattering

parameters are converted into complex permittivity values using code written by the author implementing the NNI algorithm.

The system design and code were validated by measurement of well-known polymers, PTFE and Nylon66, contrasting measured data with literature at 2.45 GHz, with results shown in Table 4.1.

Table 4.1 Dielectric constant and loss tangent measured at 2.45 GHz vs literature [24] for Nylon66 and Teflon - average of twelve measurements.

	Nylon66		PTFE	
Parameter	Literature	Measured	Literature	Measured
ε_r'	2.98	2.94	2.08	2.08
$\tan\delta$	0.0145	0.0139	0.00029	0.00048

4.4.2.2 WR430 and WR975 systems

In these two systems, an Agilent E5701C network analyser is used. Both have sample holder cells fitted with PEEK windows. The influence of the windows is eliminated by de-embedding in the post-processing software for the calculation of permittivity values, by using its dimensions and properties. The permittivity can be calculated either by NWR, IPF or fast transmission algorithms. For magnetic materials, only NWR can be used.

4.5 Thermal pattern using infrared imaging

Thermal measurement were required in order to validate the simulation results of the different developed prototyes.

Infrared radiometry measures surface temperature by interpreting the infrared radiation intensity seen by the camera. A NEC H2640 infrared thermal camera was used in post-treatment thermal imaging. This camera allows recording the temperature of each pixel in a 640 × 480 resolution with a field of view of 21.7° (Horizontal) x 16.4° (Vertical). It covers a temperature range from -40 °C to 500 °C, with a minimum focusing range of 30 cm [310]. Images are

computer monitored using Radiometric Complete® software for data acquisition and post-processing.

The principle of operation is based on the measurement of radiated power in the infrared spectrum (NEC H2640 spectral range from 8 μm to 13 μm) and estimation of temperature. According to Stefan-Boltzmann Law, these quantities are related as [311]

$$P = e\sigma A(T^4 - T_C^4) \tag{4.15}$$

Where P is the net radiated power, e is the material emissivity, A is the radiating area, T is the radiator temperature, and $\sigma = 5.6703 \times 10^8\ \mathrm{W/(m^2K^4)}$ is the Stefan-Boltzmann constant.

Up to the camera operational range of 500 °C, practically all body radiation falls within the infrared range [312]. The emissivity coefficient indicates the radiation from a grey body as a fraction of the ideal black body ($e = 1$) and needs to be set on the camera for accurate measurement. Tabulated values for different material surfaces can be found elsewhere [313]–[315].

The camera is fixed to a position in an adjustable frame or tripod, with positioning according to the size of the product to be imaged in respect to the camera field of view. This distance should be calculated to frame the whole sample. A chart created to aid the positioning of the camera respective to sample size is given in Figure 4.10. The camera is focused on the target, and the appropriate emissivity coefficient should set according to the material surface characteristics.

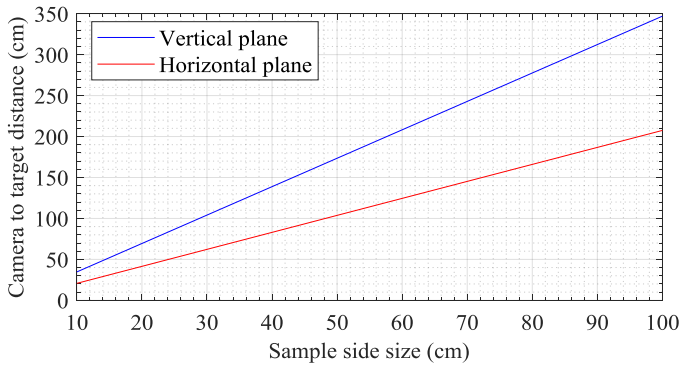
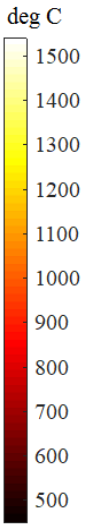


Figure 4.10 NEC H2640 Thermal camera minimum distance from target depending on sample size.

In some high-temperature experiments, estimation of the heat map was carried out using an optical camera. An approximate estimation of the temperature range can be done based on surface colour comparison (for incandescent bodies). For example, a scale used for estimation of the temperature range of an incandescent material is shown in table Table 4.2.

Table 4.2 Incandescent body temperature estimation based on colour for ultra-high temperature materials adapted from [316]

Colour	Temperature range (°C)
Lowest visible red	475
Lowest visible red to dark red	475-650
Dark red to cherry red	650-750
Cherry red to bright cherry red	750-815
Bright cherry red to orange	815-900
Orange to yellow	900-1090
Yellow to light yellow	1090-1315
Light yellow to white	1315-1540
White to dazzling white	≥1540



4.6 Test materials

Several materials were needed in order to perform validation and performance analysis on the developed prototypes.

Three sample materials were selected as the basis for experimental validation of computational models to cover a broad range of properties, given their relative dielectric stability and ease of handling. FOAMGLAS®T4, quartz powder and charcoal briquettes, all were measured up to 400 °C. Copper ore samples were also used for design and testing purposes in other chapters. Some auxiliary materials used for thermal insulation or sample positioning included Alumina, Boron Nitride and Firebricks. In this section a brief summary of their measured characteristics is given.

4.6.1 FOAMGLAS® T4

This material was selected as the primary test material for validation of numerical models. It was chosen due to its easiness to cut to shape, zero hygroscopicity, non-combustibility, thermal and dimensional stability, chemical resistance [317], and due to its stable microwave properties, which are almost constant up to 350 °C. Its complex permittivity temperature dependency was measured using the cavity perturbation technique (CPT) (see section 4.4.1) up to 650 °C (Figure 4.11). WR430 waveguide transmission measurements (see section 4.4.2.2) using NWR were done at room temperature with an average complex permittivity of $\varepsilon_r = 1.29 - j0.77$ (room temperature $\tan\delta \approx 0.6$). Both measurements were carried at the same material density of 0.115 g/cm^3 (solid cut-outs from commercial presentation).

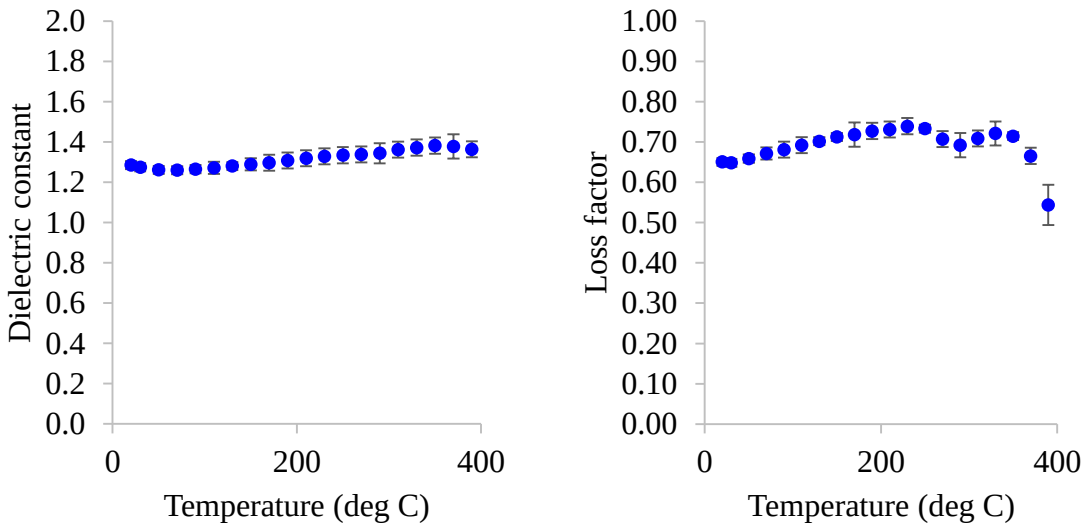


Figure 4.11 Dielectric constant and loss factor versus temperature up to 400 °C of FOAMGLAS® T4 measured by CPT at 2,470 MHz at a packing density of 0.115 g/cm^3 – Average of three measurements.

4.6.2 Quartz powder

Quartz powder samples (70 µm - 300 µm)from 99.9950 % purity pebbles' subjected to microwave pre-treatment and magnetic separation, as had been published by the author in [318] (feedstock used for stage four tests in cited reference) was selected as test material as they provide a good representative of low-loss material with stable microwave response up to 400 °C. The average dielectric constant and loss factor measured by CPT at 1.16 g/cm^3 from room temperature to 400 °C at 2.47 GHz are shown in Figure 4.12. The material dielectric constant exhibited a relatively stable response in the whole measured range and its considerably transparent with a room temperature loss tangent of 0.005.

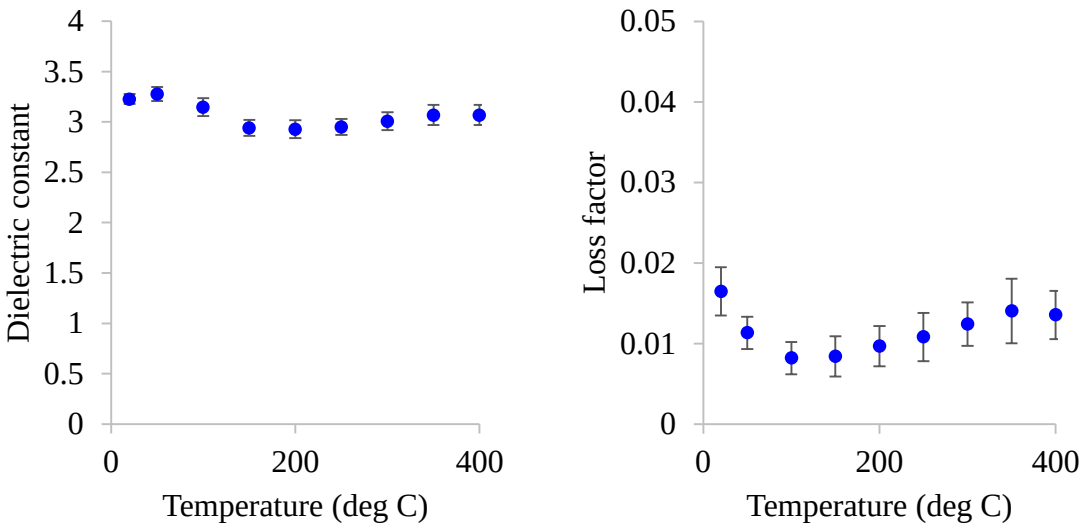


Figure 4.12 Dielectric constant and loss factor versus temperature up to 400 °C of Quartz powder measured by CPT at 2,470 MHz at a packing density of 1.16 g/cm^3 – average of three measurements.

4.6.3 Ecoal50 coal briquettes

Commercial briquettes composed of 50% Anthracite and 50% renewables [319] were used (Figure 4.13(a)), given that they represent materials with intermediate loss with stable dielectric properties up to 400 °C. The product showed an average density of 1 g/cm^3. Cut-outs revealed a heterogeneous particle distribution and size within each briquette as noticeable in Figure 4.13(c). As some product particles are of similar size (> 4 mm) to the needed for dielectric testing using CPT (see section 4.4.1), solid pieces from it would constitute a bad representation of the bulk; moreover, machining to such sizes proved to be unpractical. Therefore, pulverised samples were made for dielectric characterisation (Figure 4.13(d)).

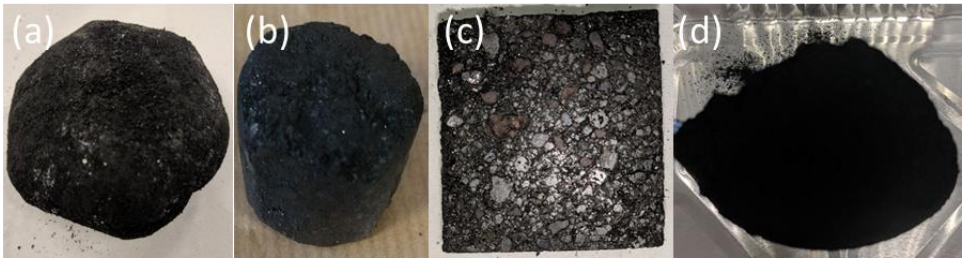


Figure 4.13 Charcoal briquettes (a) commercial shape, (b) cylindrical cut-out for microwave tests, (c) cross-cut, and (d) pulverised.

The complex permittivity measurement of up to 400 °C of charcoal briquette powders was made at 2.47 GHz using CPT (see section 4.4.1), with average packing densities close to the product at 1 g/cm^3. Two type of samples were produced: Pulverised and stored in sealed bags, labelled as normal; pre-dried for 24 h at 105 °C before measurement (left to cool at ambient for 15 minutes before measurements), labelled as pre-dried.

The average dielectric constant of normal and pre-dried samples is shown in Figure 4.12. Up to 400 °C, the pre-dried sample is virtually constant. The normal sample permittivity is higher due to moisture content, as measurements taken after 100 °C (150 °C and onwards) starts to show the same behaviour as the normal sample. This trend is mirrored in the loss factor results. At room temperature, the normal sample shows a loss tangent of $\tan\delta = 0.15$ and the pre-dried sample of $\tan\delta = 0.016$.

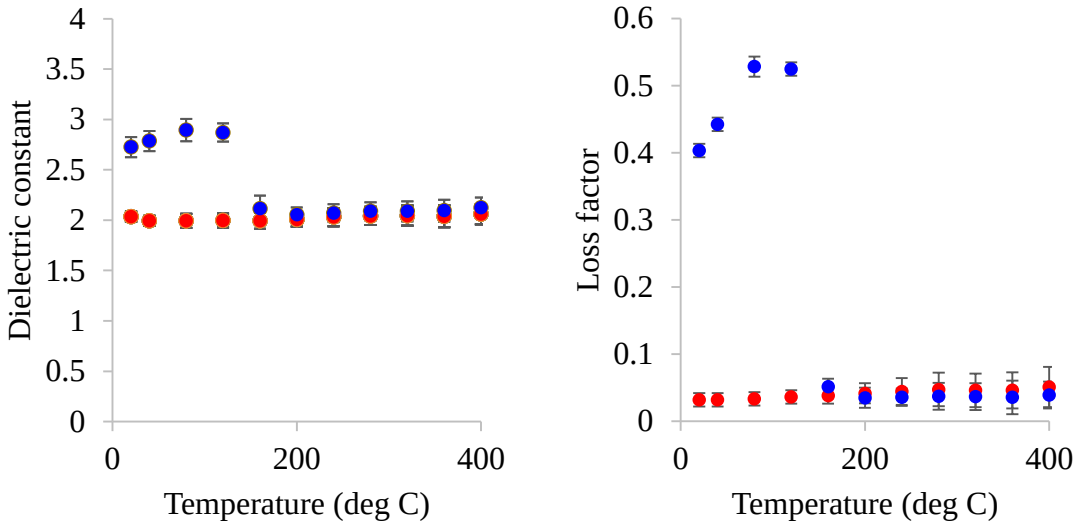


Figure 4.14 Dielectric constant and loss factor versus temperature up to 400 °C of charcoal briquette powder measured by CPT at 2,470 MHz at a packing density of 1 g/cm3, normal (blue circles) and pre-dried (red circles) – average of three measurements.

4.6.4 Copper ore

Copper bearing ores with a high mineralisation grading of 2 % copper (determined by assays performed by Andina) were measured at room temperature using the transmission line technique (WR340 system), as it allowed accurate measurement of medium loss materials [40]–

[42] in a similar presentation as the expected during processing (i.e. similar packing density and grain size). These showed a dielectric constant of 3.16 ± 0.05 and a loss tangent of 0.038 ± 0.003 at a packing density of 1,400 kg/m^3, for grains in the 2 mm – 4 mm range, average from twelve measurements. All samples were taken from a single probing site on Andina copper mine in Chile.

4.6.5 Sample support and holder materials

Firebrick crucible material (72 % Alumina – grade 30 [320]) were previously characterised in [304], showing a room temperature $\varepsilon_r = 3.02 - j0.006$. Almath alumina crucible material was measured by CPT at room temperature showing $\varepsilon_r = 8.9 - j0.004$. Boron-nitride crucible material properties were extrapolated from the data available in [321] $\varepsilon_r = 3.9 - j0.0003$.

4.6.6 Metals

The metallic materials used in this work included copper, aluminium, brass, stainless steel and Inconel. Magnetic permeability and conductivity values are shown in Table 4.3.

Table 4.3 Relative magnetic permeability and conductivity of metals

Material	μ_r	σ (S/m)	Reference
Copper	1	5.85×10^7	[322]
Aluminium	1	3.77×10^7	[323]
Brass	1	1.67×10^7	[323]
Stainless steel	1.05	1.45×10^6	[322]–[324]
Inconel	1	7.7×10^5	[322]

4.7 Electromagnetic simulation general framework

A simulation framework adequate for microwave heating applicator design was needed in order to support the design and evaluation of the prototypes by using full-wave

electromagnetic simulation. In this section a framework is proposed and validating considering some example systems.

For complicated structures with varying arrangement of loads, field equations can be difficult or practically impossible to solve analytically, making computer modelling a fundamental tool for the design and investigation of microwave heating systems [3]. Moreover, simulations can provide insight into the microwave-material interaction, helping to identify the influence of aspects such as material properties, dimensions, power, heating rates, and sample positioning, [325].

Several full-wave numerical techniques can be used to study microwave heating applications, such as frequency domain finite element method (FEM), finite difference time Domain (FDTD), finite integration technique (FIT), transmission line matrix (TLM), and the method of moments (MoM) [3], [325]–[330]. Commercial packages that integrate computer-aided design with full-wave electromagnetic are available.

In this work, most design and simulations were carried out using COMSOL Multiphysics, which is based on FEM [330]. Cross-platform result validations, and some specific optimisation tasks where performed using CST Microwave, based on FIT [329].

4.7.1 COMSOL simulation framework

The simulation module suitability in COMSOL for solving electromagnetic problems efficiently depends mostly on the problem geometry size as detailed in Figure 4.15.

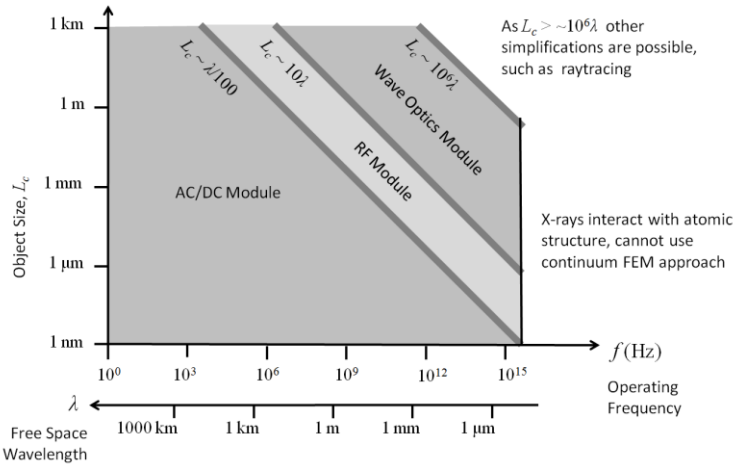


Figure 4.15 COMSOL suggested solver module according to electrical size after [331]

In this work, simulated geometries fit within the range of the Radio-Frequency (RF) module. Therefore it was selected as a simulation platform. The electromagnetic wave equation in differential form is solved in the frequency domain, following [332]

$$\nabla \times \frac{1}{\mu_r}(\nabla \times \mathrm{E}) - \omega^2 \varepsilon_0 \mu 0 \left(\varepsilon_r - \frac{j\sigma}{\omega \varepsilon_0}\right) E = 0 \qquad (4.16)$$

The models are discretised by a FEM mesh. Three problem dependent factors drive the necessary mesh resolution: geometrical (e.g., small features require finer mesh to represent), skin effects (i.e. field variation due to losses) and wavelength in the medium. As a rule of thumb, a good compromise between mesh density and accuracy doing volume meshing is to use five elements per wavelength [332]. In this work, a basic starting mesh was set with a maximum element size of $\lambda/5$, with λ being the wavelength inside of the material (i.e. $\lambda = \lambda_0/\sqrt{\varepsilon_r'}$), for the entire simulation domain, with a $\lambda/10$ maximum element size within the sample volume. Further refinement was carried in a problem-specific basis.

To illustrate the effect of the meshing density on accuracy, a TE_{101} rectangular resonator with aluminium walls was simulated and compared with the analytical values for different maximum mesh element size (Table 4.4). Walls were treated as an impedance boundary, and the cavity dimensions were set as $a = 70$ mm and $b = 35$ mm and length $d = 100$ mm. The

resonant frequency can be calculated from equation (2.61) for a TE_{101} mode as $f_0 = 2.614$ GHz. The analytical TE_{101} expression for the quality factor is given by [36]

$$Q_0 = \frac{\pi}{2R_s}\sqrt{\frac{\mu}{\varepsilon}}\left[\frac{b(a^2+d^2)^{\frac{3}{2}}}{ad(a^2+d^2)+2b(a^3+d^3)}\right] = 11{,}481.57 \tag{4.17}$$

Table 4.4 Aluminium rectangular resonator of 70 mm x 35 mm x 100 mm simulated at different meshing densities compared to analytical values.

Maximum mesh element size	$f0$ (analytical=2.614) (GHz)	Q_0 (analytical=11,482)
$\lambda/2$	2.623	11,320
$\lambda/3$	2.616	11,423
$\lambda/4$	2.614	11,459
$\lambda/5$	2.614	11,472
$\lambda/6$	2.614	11,459
$\lambda/7$	2.614	11,478
$\lambda/8$	2.614	11,479
$\lambda/9$	2,614	11,480
$\lambda/10$	2.614	11,481

A general-purpose error check procedure was used, consisting in increasing the mesh density and analysing the difference of a parameter of interest against a fixed error tolerance. This was done as a general reduction of the maximum mesh element by a factor of 1.5 and comparing the scattering parameter relative error. Error estimation based in $|S_{11}|$ variability was carried taking an error of less than 1 % as acceptable to stop further mesh refinement. If in excess of this threshold, the mesh was refined further with strategies depending on the specific problem (e.g. global refinement, local refinement, others).

$$Error(\%) = \left|\frac{|S_{11}|_{ref} - |S_{11}|_{original}}{|S_{11}|_{ref}}\right| \times 100 \tag{4.18}$$

Once the desired mesh quality is reached, small changes can be confidently simulated under roughly similar meshing conditions without much loss in accuracy. There is a direct compromise between mesh size and time and memory requirements. In cases, the use of a coarser grid for initial analysis and optimisation is desired, and detailed refinement can be used at a later stage, closer to prototype manufacturing.

Mesh quality analysis was performed considering that a minimum element quality of 0.1 is an indicator of a good mesh that will converge easily. Few low-quality elements can be generally acceptable if located in not critical areas. Common geometric entities that lead to poor quality elements are large aspect ratios, thin and small edges and faces, and high-curvature surfaces; hence, meshing might not be as straightforward and locally examining the mesh quality and enhance it manually might be necessary.

For models with a considerable number of low-quality elements that cannot be avoided, the convergence of iterative solvers is unlikely, making direct solvers the only option. However, these solvers can be memory intensive for large problems, and might require the use of high-performance computing facilities.

All the dielectrics in this work were modelled as isotropic dielectric media with bulk properties based on measurements. Metallic surfaces were treated as impedance boundaries, as the skin depth is significantly smaller than any metallisation in the system; thus, an approximation considering that the currents are only superficial can be made. This assumption is accurate where $L/\delta > 10$ [332], being L the metallisation dimension and δ the skin depth, which can be calculated as [36]

$$\delta = \sqrt{\frac{1}{\pi f \mu_0 \mu_r \sigma}} \tag{4.19}$$

For the metals considered in this work, the skin depths are in the order of a few micrometres as shown in Table 4.5, calculated using the material properties from Table 4.3. As every metallisation of the studied structures are of at least a millimetre thick, it largely surpasses the approximation accuracy threshold. For example, the worst case of Inconel result in a skin depth of 11.59 μm, so the critical minimal feature size for the approximation to hold would be of 0.12 mm.

Table 4.5 Skin depth of some metallic materials at 2.45 GHz

Material	$\delta\ (\mu m)$
Inconel	11.59
Stainless steel	8.24
Brass	2.49
Aluminium	1.66
Copper	1.33

Validations were carried out to assess the suitability of the proposed simulation framework considering the approach to meshing and modelling previously detailed, in the context of microwave heating cavities. Three materials were tested in a single-mode system for validation:

- The high-loss FOAMGLAS®T4 ($\tan\delta \approx 0.6$).
- Medium-loss charcoal briquettes ($\tan\delta \approx 0.15$).
- Low-loss quartz powder ($\tan\delta \approx 0.005$).

Heating experiments were carried out for the charcoal briquettes and quartz powder to assess the similarity of thermal profiles with simulated power density profiles and thermal simulations.

Furthermore, for validation of the framework for larger multi-mode systems, the simulated power density profiles were qualitatively compared against thermal profile measurements of heating experiments using FOAMGLAS®T4 in a multi-mode system.

4.7.2 Single-mode resonant cavity validation

A rectangular WR430 TE_{10n} applicator was selected to carry out the initial experimental work due to its flexibility to test different configurations and integrated material handling and monitoring port. A schematic drawing of the system is shown in Figure 4.16.

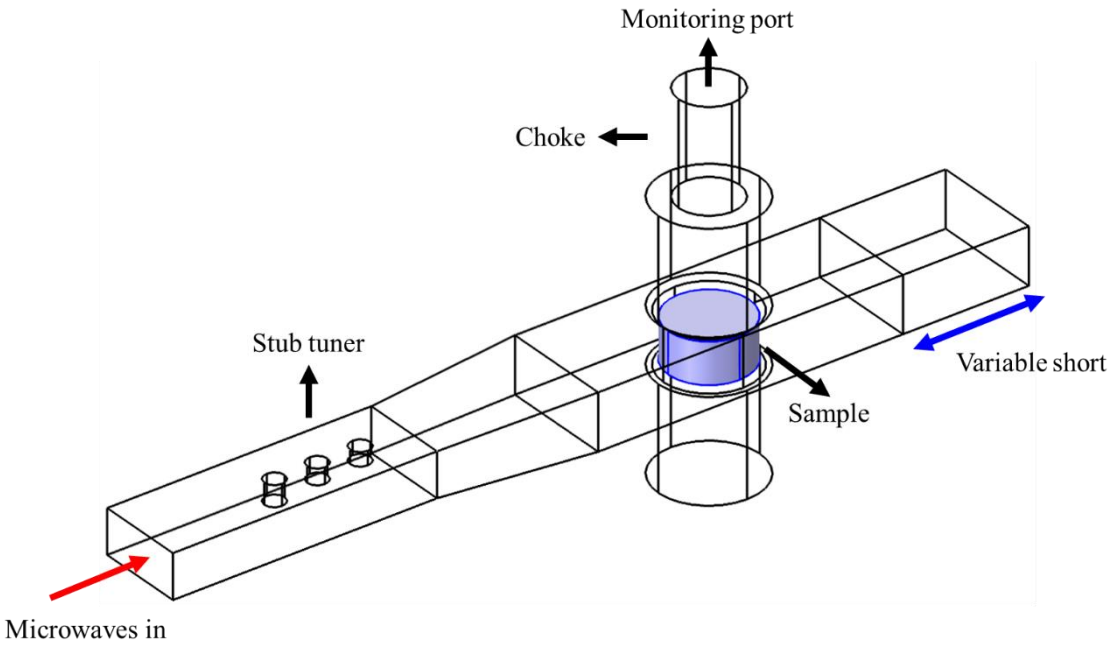


Figure 4.16 WR430 TE_{10n} applicator with 82 mm diameter extension tube, and 25 mm diameter choking section, for monitoring.

The setup consists of a WR430 267 mm long applicator with material handling tubes cut on the top and bottom of it, of 82 mm diameter, being the upper one 117 mm tall (up to the choke) and the bottom one 37 mm (closed). A variable short circuit with a length of travel ranging 60 mm to 170 mm, able to provide more than $\lambda_g/2$ of travel. On the other end, a 347 mm long WR430 manual triple stub tuner was used, with 20 mm stubs separated approximately $3\lambda_g/4 \approx 111$ mm from each other.

For heating experiments, the manual tuner is replaced by an automatic three stub tuner connected to the applicator using a 200 mm WR430 to WR340 tapered transition as shown in Figure 4.16. A Sairem 2 kW generator was used to provide the microwave energy for heating experiments carried out at 2,450 MHz [333], and an IR thermal camera or optical camera was set for thermal imaging of sample surfaces.

4.7.2.1 FOAMGLAS©T4

Sample cylinders of 25 mm x 25 mm were cut for cavity characterisation. Firebrick crucibles of 64 mm diameter and 35 mm were cut to hold the sample in place. The sliding short and triple-stub were adjusted to achieve resonance at 2.45 GHz. The same short position (~82 mm) was set in the computational model and tuned by numerical optimisation using a combination of Monte Carlo and Nelder-Mead optimisation methods implemented by COMSOL [330] to achieve a similar coupling degree as seen experimentally.

The reflection coefficient magnitude graphs (Figure 4.17) shows a slightly broader experimental resonance profile. The resonance circles are shown in the impedance Smith chart (Figure 4.18) with excellent agreement, with their location shifted due to the difference in phase reference between measurement and simulations (i.e. a length of transmission line). These were used for calculation of the experimental and simulated quality factor reaching values of 309 and 313 respectively.

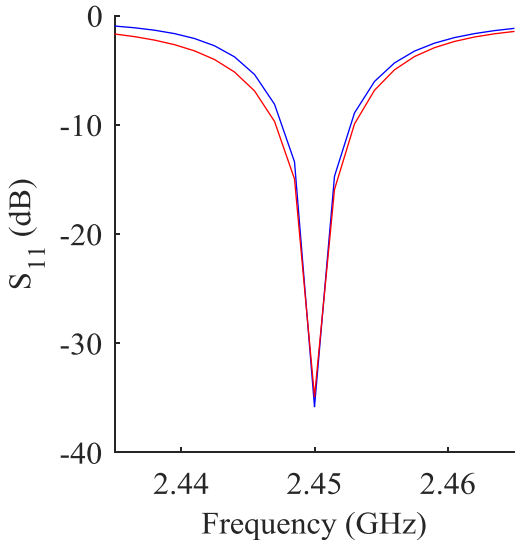


Figure 4.17 Simulated (blue line) and experimental (red line) S_{11} (dB). Single-mode loaded with FOAMGLAS®T4 sample.

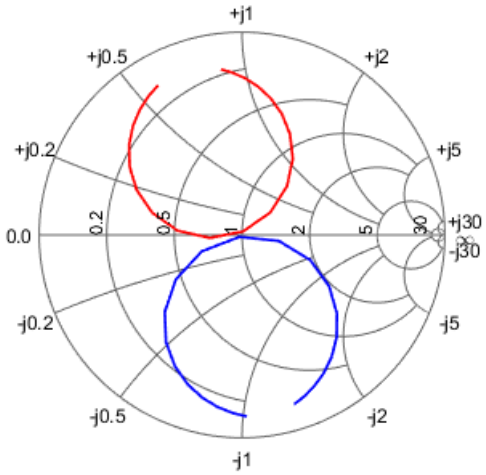


Figure 4.18 Simulated (blue line) and experimental (red line) impedance plot Smith chart. Single-mode loaded with FOAMGLAS®T4 sample.

4.7.2.2 Quartz powder

A 100 g quartz powder cylindrical sample of 58 mm diameter and 32.7 mm height was set in an alumina crucible for cavity characterisation. The sliding short and triple-stub were adjusted to achieve resonance at 2.45 GHz. The same short position was set in the computational model and virtually tuned by numerical optimisation using a combination of Monte Carlo and Nelder-Mead optimisation implemented by COMSOL [330] to achieve a similar coupling degree as seen experimentally.

The reflection coefficient magnitude and impedance Smith chart plots are shown in Figure 4.19 and Figure 4.20 with experimental and simulated quality factors of 3,169 and 3,019 respectively, which are in excellent agreement with each other.

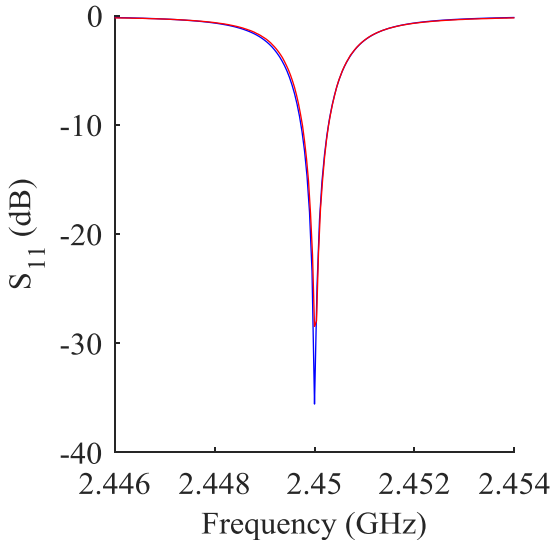


Figure 4.19 Simulated (blue line) and experimental (red line) S11 (dB). Single-mode loaded with quartz powder sample.

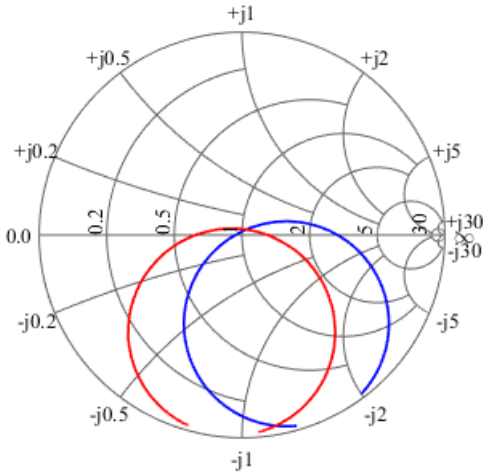


Figure 4.20 Simulated (blue line) and experimental (red line) impedance plot Smith chart. Single-mode loaded with quartz powder sample.

The cavity was used for experiments of high-power density and high-temperature selective heating of quartz powder to enhance impurity removal by leaching. A slightly different configuration was used incorporating a longer material handling tube and choke to allow to be able to visualise the whole sample, as well as the use of a 5 mm thick boron nitride crucible. Results of this study were published in [318].

Due to the low-loss of the sample material at room temperature tuning can be challenging, as the cavity presents a relatively large quality factor. Therefore, a continuous wave low-ripple (<1 %) switch mode power generator [333] was needed to allow for a minimum frequency spread and efficient matching. An automatic triple stub tuner and a sliding short circuit were used to tune the cavity during experiments. A circulator is fitted on the output of the magnetron head which allows protection of the generator and avoid frequency pulling effects. Power measurements during processing resulted in excellent matching at 1.1 kW, whereas at powers of less than 600 W the system struggled to provide a good match via auto-

tuning due to frequency spread, as can be seen in the experimental power log shown in Figure 4.21.

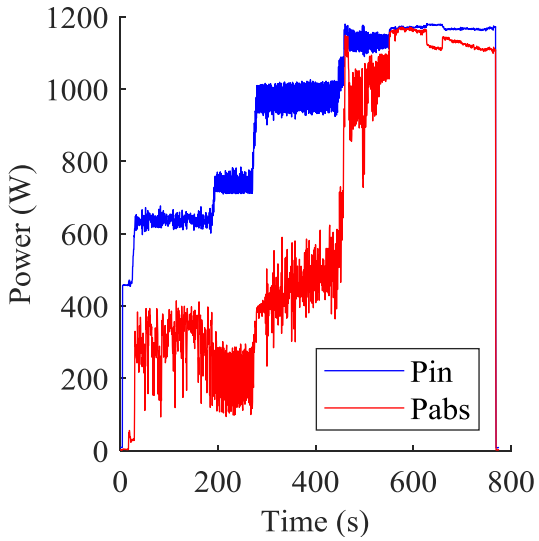


Figure 4.21 Power input (blue line) power absorbed (red line) during quartz powder treatment.

4.7.2.3 Results

Simulations of the heating setup showed a quality factor of 3,593 with product power uniformity index of $PUI = 0.56$ and an average power loss density of $P_{davg} = 1.14 \times 10^7\ \mathrm{W/m^3}$. If all power is assumed to be dissipated in the product, a rough experimental estimation gives a $P_{davg} = 1.27 \times 10^7\ \mathrm{W/m^3}$, which is close to the simulation value.

As the sample was treated for a relatively long time (~14 min), the temperature profile would not constitute a good direct representation of the power loss density distribution on its surface. For obtaining a corresponding profile, the heat transfer problem needs to be considered. The lack of knowledge of the actual thermal properties of the materials involved prevented the realisation of accurate multiphysics simulations.

For a qualitative comparison, heat-transfer coupled simulations were carried out using thermal properties of similar materials found in the literature. The sample using quartz sand properties of $k = 0.4\ \mathrm{W/(mK)}$ and $C_p = 1{,}250\ \mathrm{J/(KgK)}$) from [334]. Crucible properties of

$k = 2\ \mathrm{W/(mK)}$ and $C_p = 2{,}000\ \mathrm{J/(KgK)}$ from [321], [335]. The properties were assumed as isotropic.

For simplicity, the stepped power experimental run was simulated as a fixed power of 635 W for the same total energy as in experiments. Free convective heat flux (heat transfer coefficient $h = 5\ \mathrm{W/(m^2K)}$ [336]) and diffuse radiation with an emissivity of 0.8 were assumed at the boundaries. Figure 4.22 shows the simulated thermal profile (a) with a colour scale based on Table 4.2 and a photography of the top of the sample after treatment [318] (b), with a good agreement between each other. The power loss density at the top surface shown in Figure 4.22(c) also exhibit two distinguishable hot-spots as present in the thermal distributions.

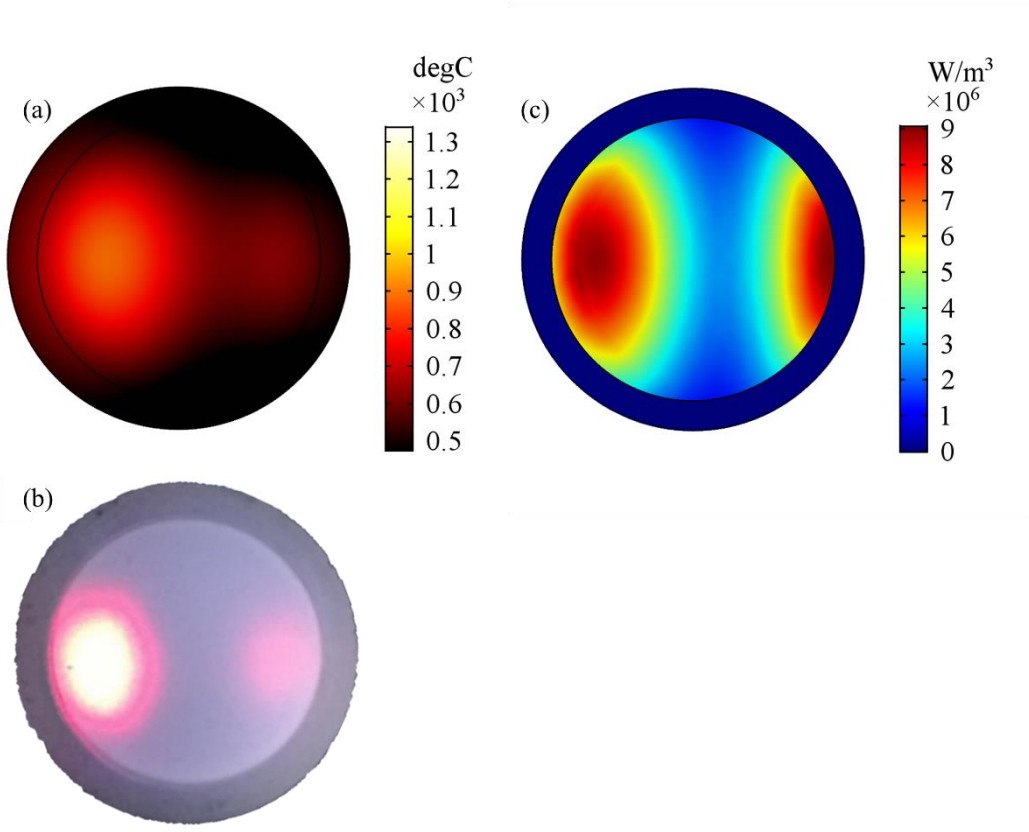


Figure 4.22 Simulated temperature distribution (a), photography after quartz heating experiment (b) and simulated power loss density distribution (c) at the top surface.

4.7.2.4 Charcoal briquette

A charcoal briquette sample of 32 mm × 19 mm was cut-out (Figure 4.13(b)). The size was determined due to machining capabilities and to allow retaining sample integrity. Reflection coefficient magnitude and impedance Smith chart plots are shown in Figure 4.23 and Figure 4.24, with measured and simulated quality factor of 1,038 and 933 respectively. Good agreement is seen between measurement and simulations, although less accurate than previous examples, most likely attributable to the lower accuracy of dielectric measurement (CPT technique on a medium loss sample).

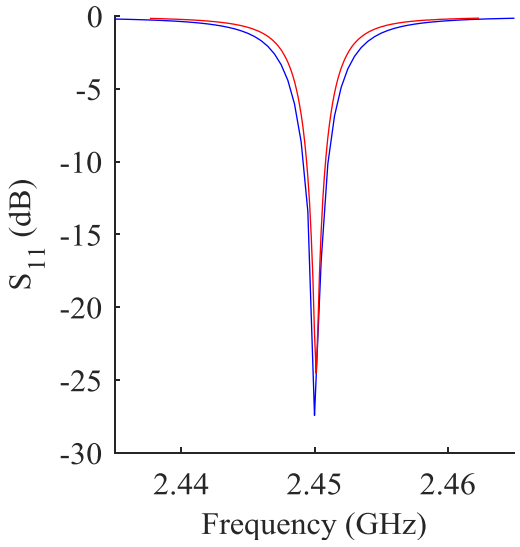


Figure 4.23 Simulated (blue line) and experimental (red line) S11 (dB). Single-mode loaded with charcoal briquette sample.

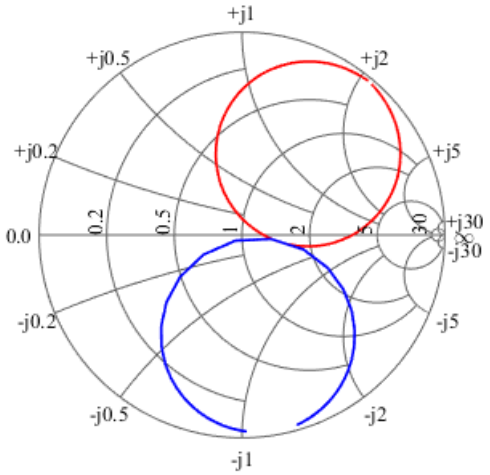


Figure 4.24 Simulated (blue line) and experimental (red line) impedance plot Smith chart. Single-mode loaded with charcoal briquette powder sample.

A charcoal briquette cylinder sample of 30 mm × 27.5 mm was treated with an average of 83 W power and a residence time of 5 min, in an arbitrary short-circuit position. The temperature distribution in the sample surface alongside with the simulated power loss density distribution is shown in Figure 4.25. The experimental temperature distribution provided a good approximation of the power loss density distribution seen in simulations.

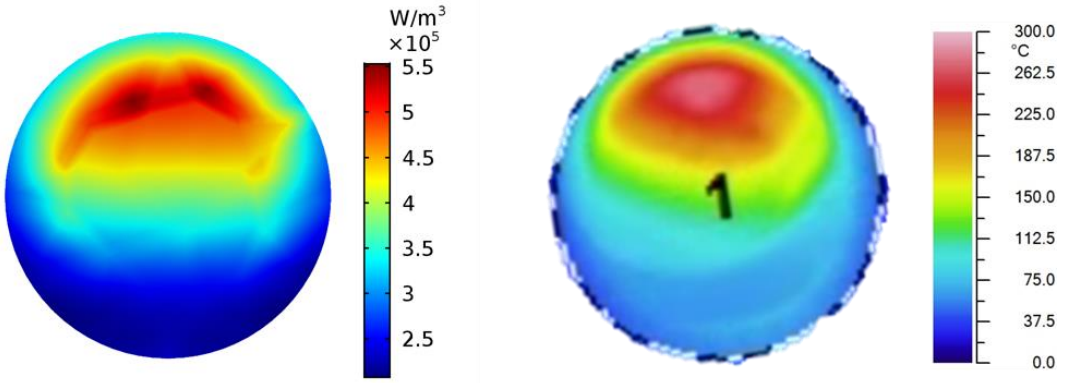


Figure 4.25 Simulated power loss density (W/m^3) and experimental temperature distribution (°C) of a 5min run at 83W at the top surface of the sample.

4.7.3 Multimode cavity validation

A two-port controlled atmosphere hybrid heating furnace was designed and fabricated supporting conventional heating up to 1,000 °C. The cavity geometry is sketched in Figure 4.26.

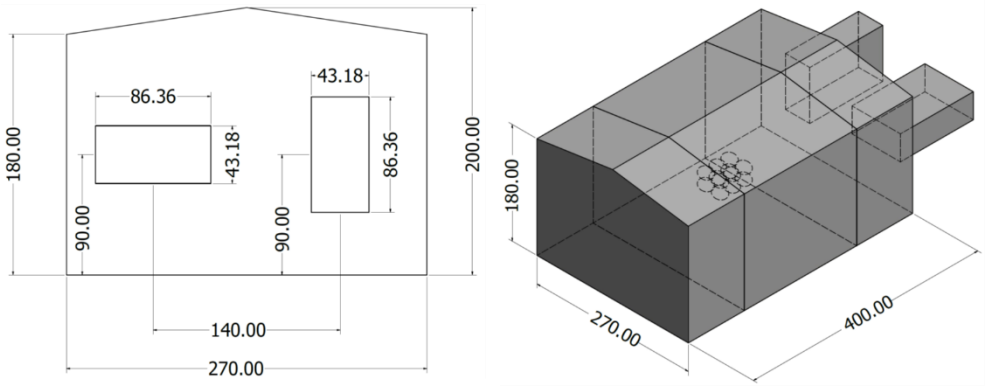


Figure 4.26 Multimode system sketch

Heating experiments were carried out on a FOAMGLAS®T4 400 mm × 270 mm × 24 mm tile at different positions within the cavity using a Sairem 2 kW generator to provide the microwave energy [333] connected to the horizontal port (vertical port was short-circuited). Comparison between the experimental temperature profiles and power loss density distributions

are shown in Figure 4.27, Figure 4.28, Figure 4.29 and Figure 4.30, with qualitative agreement between experiment and simulations.

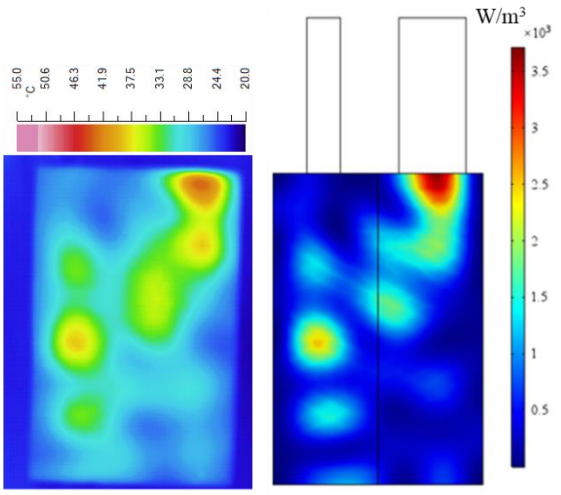


Figure 4.27 Experimental thermal image and simulation of power loss density at the surface of a FOAMGLAS®T4 tile, heated in the floor of the multimode cavity.

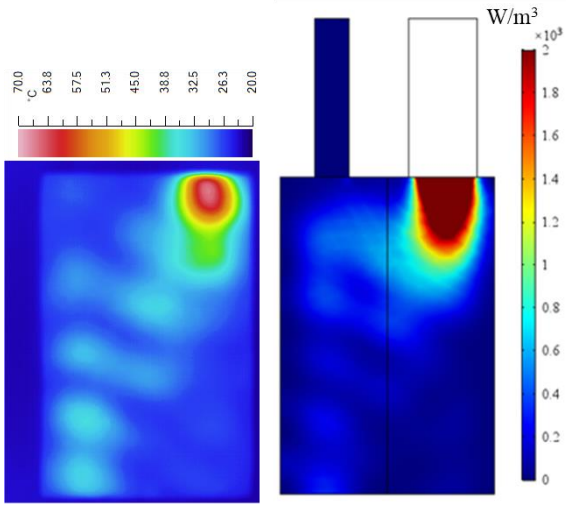


Figure 4.28 Experimental thermal image and simulated of power loss density at the surface of a FOAMGLAS®T4 tile, heated 39 mm from the floor of the multimode cavity.

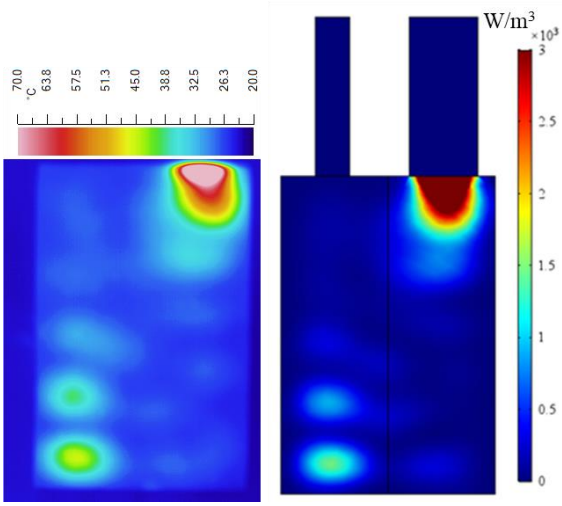


Figure 4.29 Experimental thermal image and simulated power loss density distribution at the surface of a FOAMGLAS®T4 tile, heated 66 mm from the floor of the multimode cavity.

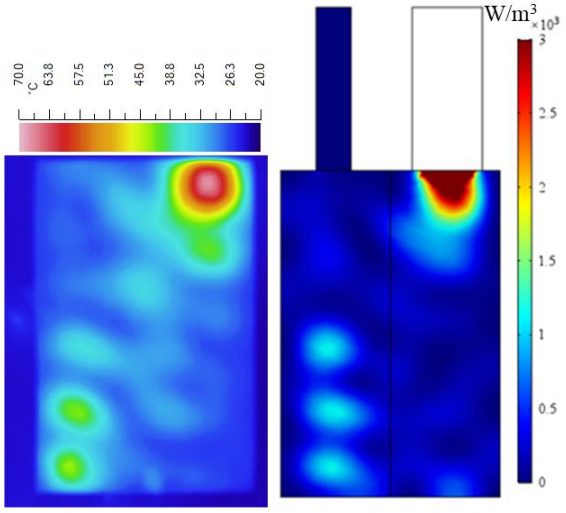


Figure 4.30 Experimental thermal image and simulated power loss density distribution at the surface of a FOAMGLAS®T4 tile, heated 93 mm from the floor of the multimode cavity

This system was designed with two ports perpendicular to each other and carefully positioned to excite two set of different modes keeping a low cross-coupling between both

ports. This allowed for effective treatment uniformity enhancement versus single-port setups. The system is currently being used to carry out high-temperature (up to 1000 °C conventional heating) hybrid heating experiments.

4.7.4 Electromagnetic simulation framework conclusions

The presented results validate the proposed simulation framework as a practical approach for modelling microwave heating systems, with coupling and heating patterns accurately predicted. Therefore, the framework was used as the basis for the design and analysis of microwave heating applicators in the following Chapters.

4.8 Summary

The microwave measurement methodologies, dielectric properties characterisation techniques and thermal imaging measurement procedures used throughout the thesis were detailed. A framework for the electromagnetic modelling of microwave heating systems was proposed and validated experimentally by network measurements and thermal imaging, using a variety of materials in both a single-mode and a multimode system. The validations support the modelling approach for its use as design tool in the subsequent chapters.

Chapter 5 Applicator for liquids and fine powders

Industrial microwave processes where the product exhibits a low penetration depth can be limited to relatively low processing volumes to meet the treatment uniformity requirements [120]. On the other hand, relatively microwave transparent materials need to be exposed to high field intensities in order to be heated effectively [3], [19] without using microwave susceptive additives. Applications such as the treatment of waste engine oils, plastic waste streams, quartz powders, mineral ores and the sintering of various ceramics match these processing requirements (see Chapter 3 and section 5.1).

Single-mode microwave cavities can deliver high field intensities to small volume loads. This technology is mostly suitable for the processing of liquids, filamentary and fine powder materials, due to its inherent limitations regarding product size [3]. This type of resonator has been used extensively in a broad range of applications including telecommunication systems, particle accelerators, material characterisation systems and, to a lesser extent, in material processing [2], [43]. Reported uses for selected material processes were reviewed in Chapter 3, with most solutions relying on rectangular and circular cross section cavities as the ones shown in Figure 5.1. These geometries have been widely studied and fundamental analysis, design guidelines, and details of its use for material processing systems can be found elsewhere [1]–[3], [12], [19], [22], [36], [43].

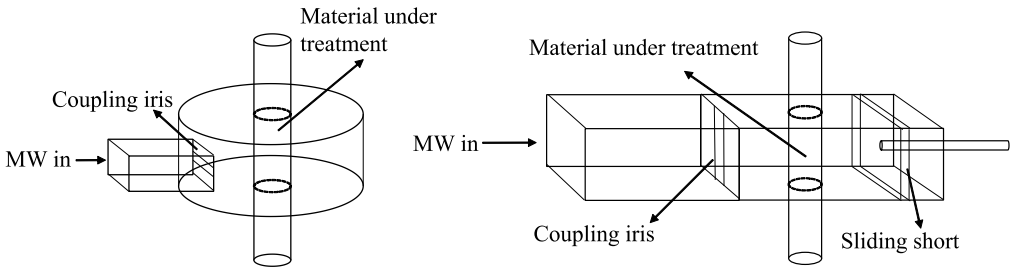


Figure 5.1 Sketch of typical circular and rectangular single-mode applicators.

The electric field maximum positions on a rectangular cavities TE modes are dependent on the material properties. Adjustment using a sliding short is a commonly used technique to

reposition the electric field on the product zone [12]. Circular cavities TM modes are mostly attractive due to the relatively fixed nature of its field distribution and concentrated field [3]. In particular, the TM_{010} mode can be an excellent alternative for treating small loads at its centre and can be particularly useful in microwave flow chemistry [143]. However, for larger loads, the cavity size can become unpractically small in order to keep the desired resonant frequency and can even surpass the practical limit (i.e. cavity size smaller than product load). This call for the use higher order modes such as e.g. TM_{110} or TM_{210}; however, circular cavities exhibit mode degeneracy (i.e. modes sharing the same resonant frequency) and modal polarisation dependency and splitting due to geometrical symmetry (i.e. degenerate modes of the same shape orthogonally polarised), which can lead to the excitation of undesired modes [22], [337]. Diverse strategies can be used to minimise the likelihood of unwanted mode excitation, for example, the use of wire meshes or inserts [337], grooves with lossy loads [338], [339], and surface slits [43]. TM_{0n0} modes with $n > 1$ go to the other extreme, requiring considerably large structures and showing a sharp decrease in electric fields from the centre [22].

In this chapter, a solution is proposed that diminishes both problematics, an elliptical cross-section cavity resonator. Such geometry may allow for a relatively fixed field distribution (i.e. small displacement due to dielectric properties changes) without modal degeneracy nor polarisation mode splitting for low order modes, in the same fashion as the correspondent elliptical waveguide [340], [341].

First, some applications in which the technology could be used are identified and discussed. Second, the fundamentals of elliptical cavities for material processing are reviewed. Third, an example modal analysis is given to provide insight on cavity behaviour and design charts are provided. Fourth, a general design methodology is proposed and assessed by the design of an applicator for an example product. Numerical simulations are cross-checked by two different modelling methods and are verified by experimental measurements. The

prototype performance is evaluated against initially established design requirements to assess the design methodology suitability. Finally, a discussion on its large-scale implementation is given for some selected applications.

5.1 Potential applications

A detailed review of research works can be found in Chapter 3. Among the reviewed applications, the elliptical cavity might provide practical means for developing solutions for the treatment several products. Some of these processes details are discussed next.

5.1.1 Waste engine oil treatment

Research of processing of waste oils has shown that similar to commercial fuels product properties can be obtained by microwave treatment, with the use of susceptors [191]–[195], [197]; however, the use of susceptors in microwave processing generally result in a loss of process efficiency [5], [214]. The use of high power density single-mode cavities could provide a means to avoid the use of susceptors and has not been explored in the literature for this particular product.

Common contamination present on waste lubricant oils leads to considerably better microwave absorptive properties than fresh oils, which are relatively poor microwave absorbers [194], [197]. Over 1 GHz, only soot and water contaminants affect the oil permittivity significantly [342], [343]. According to [344], fresh lubricating oils typically exhibit loss tangents of around 0.01, while heavy contaminated oil loss tangents can be close to 0.1, with dielectric constants ranging from 2.25 to 2.45. Reported complex permittivity measurements of waste transformer oil, showed near to $\varepsilon_r = 2.2 - j0.08$ for 433 MHz, $\varepsilon_r = 2.4 - j0.16$ for 915 MHz, and $\varepsilon_r = 2.25 - j0.08$ for 2.45 GHz [345]. Oils dielectric constant usually remain roughly constant whereas its loss factor tends to increase with temperature, which can be attributed to the respective increase of molecular mobility [346].

The liquid presentation could make it suitable to be pumped through a processing system, as in [347]; however, the handling of hot oils, gaseous and solids by-products can be a significant engineering challenge which might require the operation at elevated pressures and temperatures throughout the system.

5.1.2 Waste plastic pyrolysis and depolymerization

Most plastic waste can be hard to treat with microwaves directly due to their relative microwave transparency. Therefore, research has been focused on the use of susceptors for indirect heating, similar to waste engine oil studies [13], [14], [98], [121], [157], [166]–[168]. Investigators generally deal with pyrolysis of plastics of specific composition; however, the accurate sorting of waste streams by specific polymer type might not be viable for recycling purposes [348]. Non-readily recyclable domestic plastic waste streams in the United Kingdom are roughly composed as shown inTable 5.1. The dielectric constants of different plastics are usually confined between 2 to 5, whereas loss factors can go from less than 0.0004 up to 0.15 [24], [25], [349]. At the time of writing, no information of dielectric properties for temperatures where plastics began to decompose could be found in the literature.

Table 5.1 UK domestic plastic waste stream general composition after [348]

Polymer type	Composition (%)
Polyethylene (PE)	38.5
Polypropylene (PP)	22.2
Polyethylene terephthalate (PET)	15.3
Polyvinyl chloride (PVC)	3.5
Polystyrene (PS)	4
Contamination	16.5

Generally, the plastic feedstock is shredded to small flakes; nonetheless, the combination with pre-heating could allow for an extruded presentation or even a liquid stream pumpable flow to through the system in a similar fashion as suggested for waste engine oils.

This pre-heating could also improve the microwave absorption characteristics of the waste stream leading to more efficient heating.

5.1.3 Ceramic sintering

Fast heating rates are usually desirable in most ceramic sintering processes to prevent grain overgrowth [281]. Microwave sintering of ceramics can provide unique product properties [63], desirable for the production of high-value parts. Due to the relative transparency of some ceramics to microwaves, conventional pre-heating and the use of susceptors are a common strategy to achieve good quality products [63], [140]. Single-mode systems could allow for a more streamlined process, being able to provide uniform heating for the whole processing range and eventually better product quality; although it would be limited to small parts only.

5.1.4 Quartz powder fracture and purification

The development of high purity silica alternative production routes is required to cover future expected demands, one of which can rely on the microwave selective heating and fracture of its microfluidic inclusions, as we explored in [318]. However, quartz powders can be considerably microwave-transparent (e.g. measured feedstock permittivity of $\varepsilon_r = 3.2 - j0.016$), making them challenging to treat.

High-power densities could allow for improved selective heating of the impurities at fast rates, which may contribute to improve leaching and impurity removal. Initial experimental tests on a single mode rectangular cavity have been performed as summarised in Chapter 4 and described in [318], for processing a product previously treated, trying to target residual impurities; however, it yield no further contamination reduction. The use of an elliptical resonator could overcome the limitations of the used system, improving treatment uniformity and allowing to achieve considerably higher power densities, which could increase the effectiveness of the leaching and therefore contamination reduction.

5.1.5 Mineral ore treatment

High-power densities and short residence times to take advantage of the heating selectivity of microwaves are considered necessary to provide comminution of ores improvement at economical energy inputs [227], [229], [350], [351]. Although in principle suitable for a single-mode based approach; material handling limitations can make it unfeasible for production scales, as the particle size would be limited due to applicator size. Nonetheless, recent works have proven that significant throughputs can be achieved with relatively large particle sizes using single-mode applicator technologies for the treatment of ores [148], [149].

5.1.6 Discussion on potential applications

All these applications require considerably higher electric fields than would be found in a multimode cavity in order to exploit selective heating or to overcome their low microwave absorption properties without the use of additives that may reduce process efficiency severely. Such conditions are hard if not impossible to meet with conventional multimode microwave cavities. An elliptical resonator could provide a focused field within a well-defined treatment zone without significant distortion due to modal overlapping, enabling the direct treatment of these materials.

Although at laboratory scale it could provide a means for proof of concept and valuable research; large-scale implementations can be severely limited given production throughputs. This reduces its usefulness in industrial settings for products that can be conveniently conveyed continuously through small tubes, such as pumpable liquids, or to produce high-value products.

5.2 Elliptical cavities

The possibility of taking advantage of the properties of transverse magnetic modes on elliptical waveguides for microwave material processing was first pointed out by Kretzschmar [340], [352]. These structures can exhibit distinct high electric fields with zones of varying size

and position. One can be used to input the microwave energy and others to set the material to be treated as illustrated in Figure 5.2.

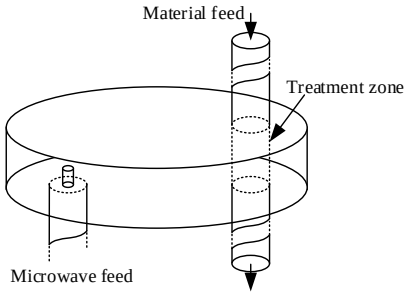


Figure 5.2 Sketch of elliptical cylinder applicator.

Most of the practical aspects were not discussed until the numerical investigations performed in [341]. Recently, elliptical-cylinder applicators have been used for studying low power chemical reactions [353], [354]. Well-defined and relatively fixed-field distributions, with high electric field concentrations, non-degenerated low order modes, no mode splitting or polarisation rotation under slight deformations are among the elliptical geometry advantages [12], [340], [341], [352]. The fixed nature of the resonant modes can guarantee, to some extent, repeatability, mostly requiring control over matching conditions [353].

The usage of transverse magnetic modes of an elliptical waveguide can be attractive for material processing applications [340]. The succession of modes in elliptical waveguides is a function of its eccentricity [355], which can be calculated as

$$e = \sqrt{1 - \left(\frac{b}{a}\right)^2} \tag{5.1}$$

Being a the semi-major and b the semi-minor axis.

Elliptical waveguides modes can be examined analytically by solving the Mathieu's functions [355]–[357]; however, its solution is computationally intensive. Alternatively, other numerical methods have been used for modal analysis [358], [359]. The use of these methods cannot be applied straightforwardly to loaded cavities. This makes more general-purpose

numerical methods key to study such structures and is, therefore, the approach taken in this work.

5.3 Modal analysis and design charts

An eigenmode analysis on an example elliptical cavity of eccentricity of 0.7, semi-major axis $a = 110$ mm and height $h = 50$ mm was done using COMSOL. The resonant frequencies for the first 31 modes are listed in Table 5.2. The first twelve TM modes electric field distributions are graphed in Figure 5.3 and Figure 5.4. There is a variety of mode naming conventions, mostly based on Mathieu's solutions. In this work, for simplicity, the naming convention is based on the sequence of apparition from low to high resonant frequencies in this example cavity ($e = 0.7, a = 110$ mm, $h = 50$ mm). All these modes present a uniform vertical field distribution, with a variety of maximum field spots arrangements which make them interesting for the treatment of a cylindrical column of material uniformly.

Table 5.2 Resonant frequencies in (GHz) for the first 31 modes of an elliptical cylinder cavity $a = 110$ mm $h = 50$ mm and an $e = 0.7$.

#	TM	TE	#	TM	TE
1	1.2672	3.1047	10	3.6373	3.7041
2	1.8462	3.1932	11	3.6898	3.8738
3	2.1754	3.2547	12	3.8069	3.9906
4	2.4532	3.3286	13	4.0713	4.0065
5	2.6989	3.3966	14	4.1791	4.0122
6	3.0709	3.5208	15		4.034
7	3.1216	3.6333	16		4.2918
8	3.2459	3.6745	17		4.3029
9	3.6373	3.675			

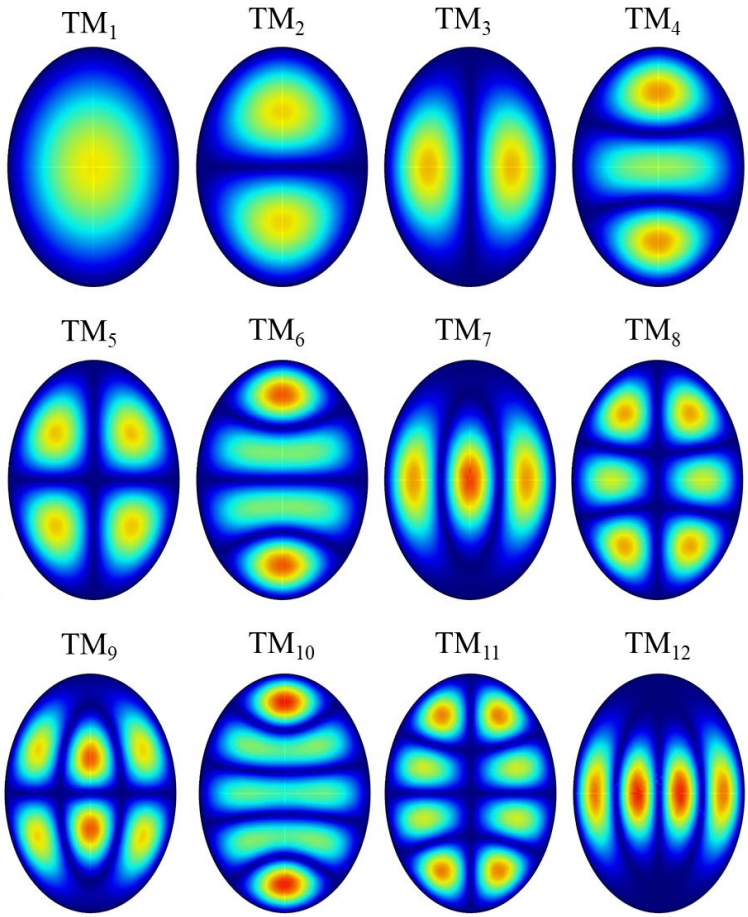


Figure 5.3 First 12 TM modes of an elliptical cylinder cavity $D_2 = 220$ mm $h = 50$ mm and an $ecc = 0.7$.

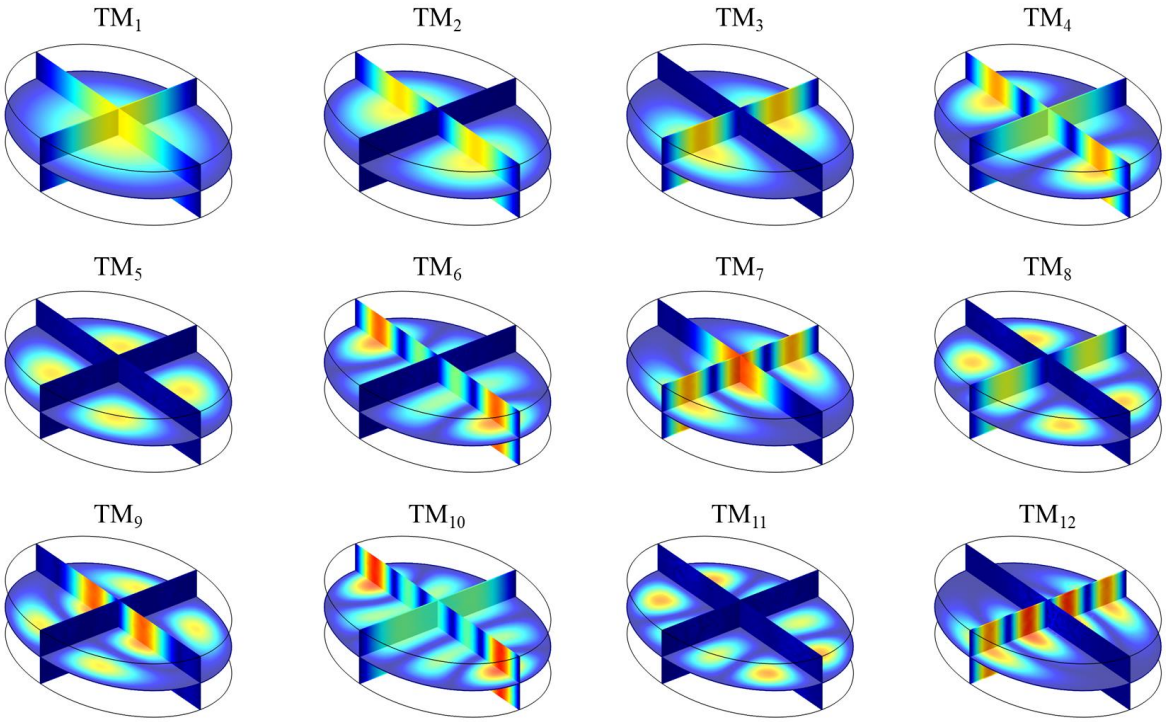


Figure 5.4 First 12 TM modes of an elliptical cylinder cavity $D_2 = 220$ mm $h = 50$ mm and an $ecc = 0.7$, cross-planes.

A chart of cut-off wavelength normalised to the semi-major axis size versus eccentricities ranging 0.5 to 0.9 was prepared for the first five TM modes of an elliptical waveguide, based on the fitting polynomials published in [355] and [341]. The resonant frequency of these modes is independent of cavity height.

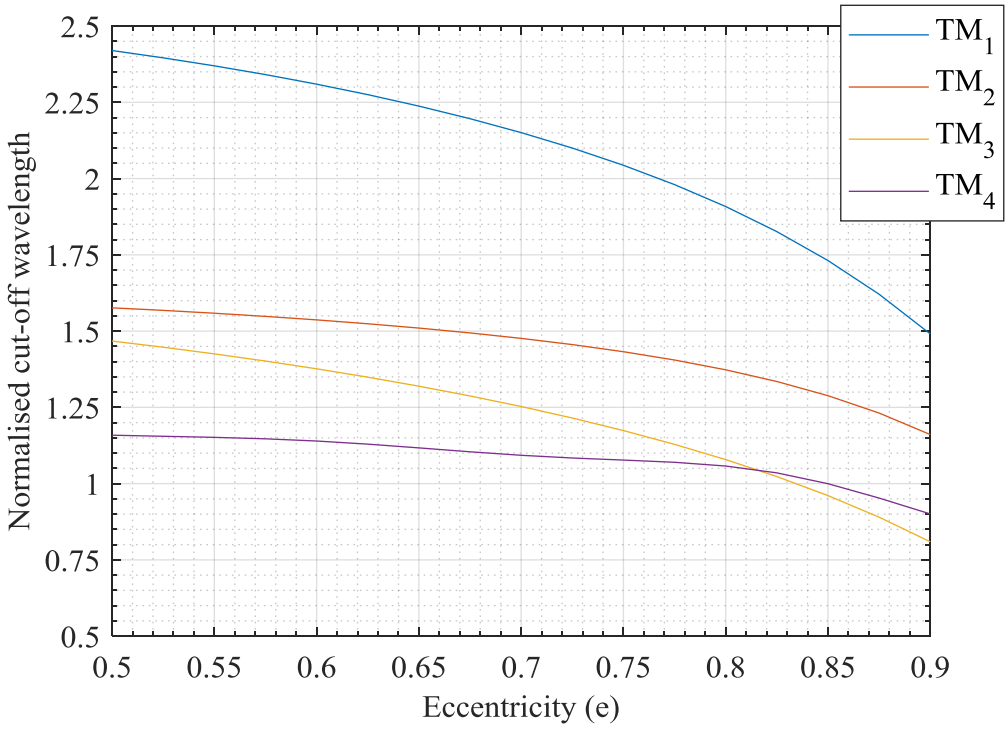


Figure 5.5 Normalised cut-off wavelength (λ_c/a) of five TM modes of an elliptical cylinder cavity waveguide adapted from the polynomials published in [355] **and** [341]**.**

For a frequency of interest, a design chart can be plotted to estimate empty cavity size as a function of the eccentricity or one semi-axis. In Figure 5.6, Figure 5.7 and Figure 5.8, design charts for the ISM bands 2,450 MHz, 915 MHz and 433 MHz are shown respectively. The use of different frequencies results in a considerable change of cavity size, as evident from the design charts, which provide the ability to treat larger loads at lower operational frequencies.

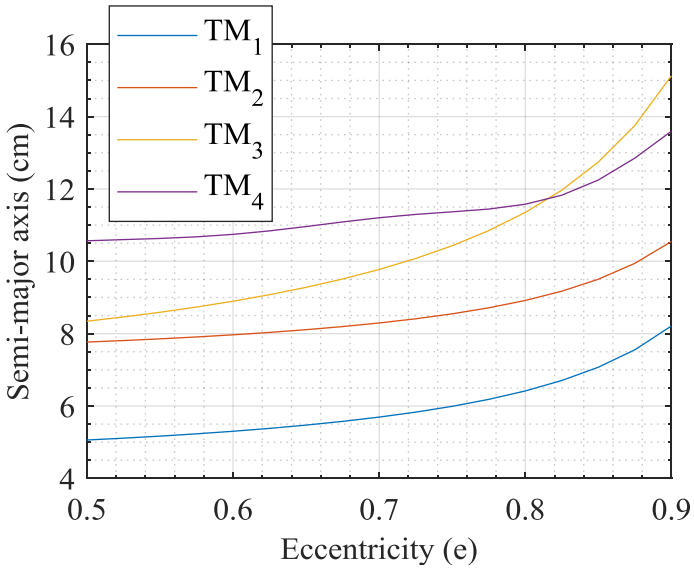


Figure 5.6 Design chart for the empty elliptical cavity, first four modes, at 2,450 MHz

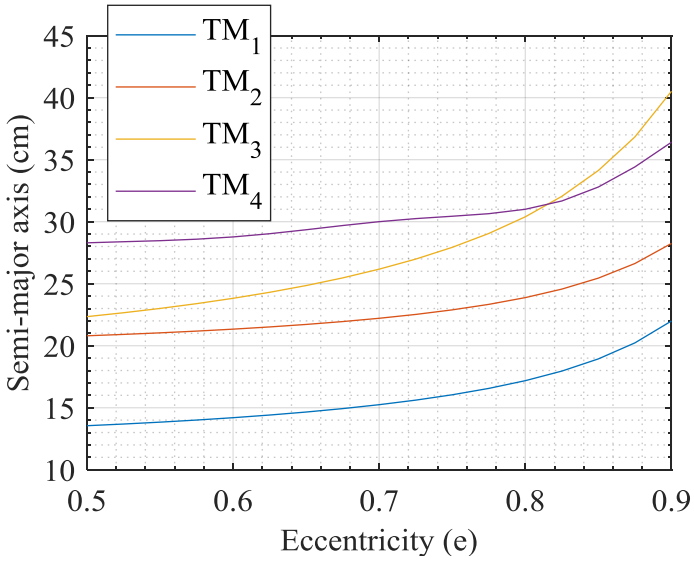


Figure 5.7 Design chart for the empty elliptical cavity, first four modes, at 915 MHz

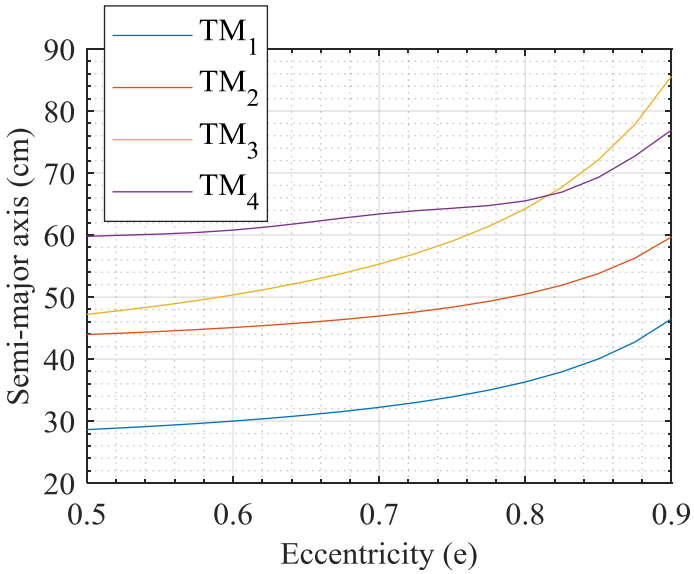


Figure 5.8 Design chart for the empty elliptical cavity, first four modes, at 433 MHz

5.4 Cavity design methodology and case study

5.4.1 Design requirements for a case study

A system able to provide a high average bulk power density on a consistent, repeatable fashion was required for small-scale laboratory testing of microwave treatment of ores. Specific targets were set to be considerably above average power densities seen in the literature, pushing the boundaries of practical limitations, and to provide good treatment homogeneity.

The basis of designed specified an average power density on the bulk of the sample able to reach on the order of $\sim 3.5 \times 10^8$ W/m^3 (orders of magnitude higher in susceptible phases). Power uniformity index limit was set to be less than 0.18, which is the equivalent of a half-power density decay from centre to side of a cylinder sample uniformly treated in the vertical coordinate of an ideal circular resonator TM_{010} decay profile as illustrated in Figure 5.9.

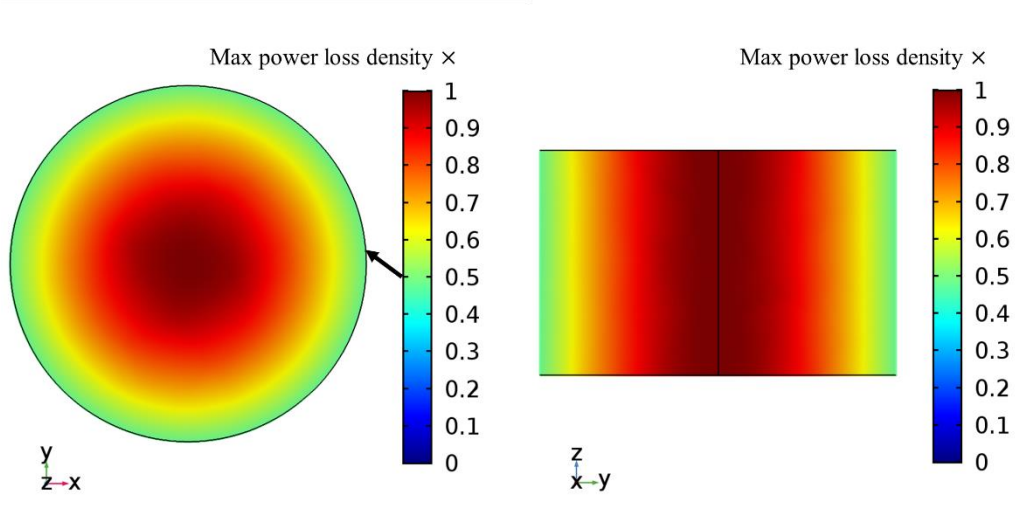


Figure 5.9 Normalised power loss density of a sample with a PUI = 0.18, uniformly treated in the vertical coordinate.

Moreover, a maximum energy dosage on the order of 3 kW/t with conversion power ratio of at least 95 % (i.e. part of the accepted power absorbed in the product) was requiered.

As a reference point, the study made in [148] worked at an average power density in the bulk of $\sim 6.6 \times 10^6$ W/m^3 and a PUI of 0.64 (0.27 using two complementary applicators in series).

The ISM band 2.45 GHz was selected to produce a prototype for validation and proof of concept. The available equipment worked at a typical frequency of 2.46 GHz; thus, the presented designs were realised for this frequency. To achieve such high power density level and good repeatability circular TM and elliptical TM applicators were initially considered.

5.4.2 Microwave properties characterisation

The resonant behaviour of a cavity is dependent on the material dielectric properties, and its knowledge is essential for its design [43]. The ores comprise different mineral phases. Some phases are transparent to microwaves while others readily absorb them. For a short microwave exposure only the small selectively heated phases will vary in temperature significantly, while the bulk will remain mostly unchanged [360]; hence, the material bulk properties are likely to remain stable. This makes bulk room temperature (i.e. ~20 °C) the parameter of interest for cavity sizing. The measured properties can be found in Chapter 4.

5.4.3 Material feeding

Three parameters were considered as drivers for the material bulk size selection from a microwave point of view. The achievable power loss density due to the available generator power, the ability to operate self-choked (i.e. not allowing the microwaves to propagate further), and the required treatment uniformity levels.

The maximum generator power was 6 kW, which operating at maximum on ideal conditions (i.e. all power absorbed by the product) would be able to treat 17 cm^3 of material at the required average power density of 3.5×10^8 W/m^3. However, conversion efficiency should also be taken into account. At an assumed 95 % efficiency, the maximum treatable volume is reduced to 16 cm^3.

The feeding tube can be considered as a dielectrically filled circular waveguide. The cut-off frequency of the dominant dielectric-filled circular waveguide is given by

$$a = \frac{1.841}{2\pi f_c \sqrt{\mu\varepsilon}} \tag{5.2}$$

As the waveguide acts as a high-pass filter, a given set of material properties and dimensions will prevent propagation through the tube, avoiding the need for additional choking structures. The material feed tube size was constrained to a maximum diameter $D = 2a$ that allow it to act as a self-choking microwave element. This allows optimal containment of the radiation, maintaining the treatment uniformity and providing a practical way to transport the material avoiding the use of choking structures [67]. A graph of the maximum diameter for self-choking versus dielectric constant for the main ISM frequencies is shown in Figure 5.10. Estimations for some of the considered applications are presented in Table 5.3.

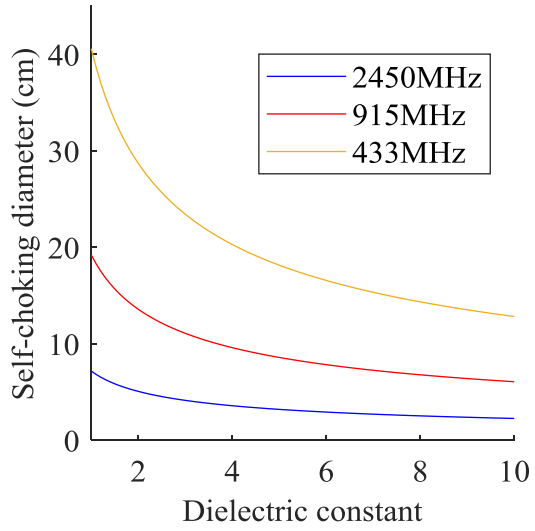


Figure 5.10 Maximum diameter for self-choking behaviour at ISM frequencies 2,450 MHz (blue line), 915 MHz (red line) and 433 MHz (yellow line) for different dielectric constant materials.

Table 5.3 Estimated maximum diameter for self-choking behaviour of a feeding tube for different applications.

	Dielectric constant typical range	Ref.	Diameter (cm) – 2.45GHz	Diameter (cm) – 915 MHz	Diameter (cm) – 433 MHz
Waste oils	2-2.5	[67], [342]–[346]	4.5 – 5.1	12.0 – 13.7	25.5 – 28.9
Waste plastics	2-5	[24], [25],	3.2 – 5.1	8.6 – 13.7	18.1 – 28.9

		[349]			
Ceramics powders	3-8	[24], [25], [361]	2.5 – 4.1	6.7 – 11.0	14.1 – 23.2
Quartz powder	2.9-3.3	Measured	4.0 – 4.2	10.7 – 11.2	22.6 – 23.8

For the copper ores a diameter of $D \approx 40$ mm results in a cut-off frequency of 2.46 GHz.

The attenuation due to mode evanescence (below cut-off frequency) for the dominant mode can be calculated evaluating the propagation constant in such conditions, resulting in the following expression for attenuation per centimetre of tube length

$$\alpha\left[\frac{dB}{cm}\right] = \frac{1}{100} Re\left[2\pi\sqrt{\mu\varepsilon}\sqrt{\left(\frac{1.841}{2\pi a\sqrt{\mu\varepsilon}}\right)^2 - f^2}\right]\frac{20}{\ln 10} \tag{5.3}$$

The real part operator on the expression nullify the phase constant in over cut-off operation cases. The attenuation for a variety of filling materials is plotted in Figure 5.11 for 2.45 GHz and in Figure 5.12 for 915 MHz, illustrating tube length for different attenuation requirements under different operating conditions.

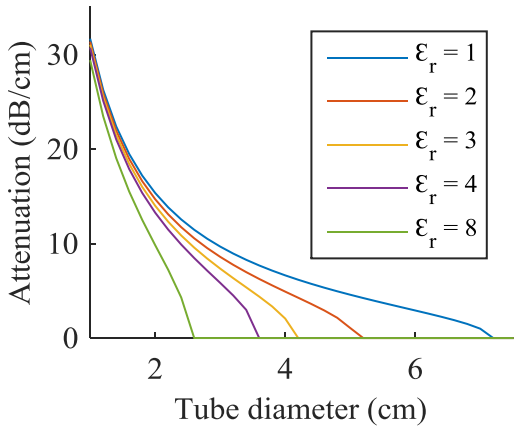


Figure 5.11 Below cut-off attenuation per centimetre versus tube diameter for 2,450 MHz, with different dielectric filling material.

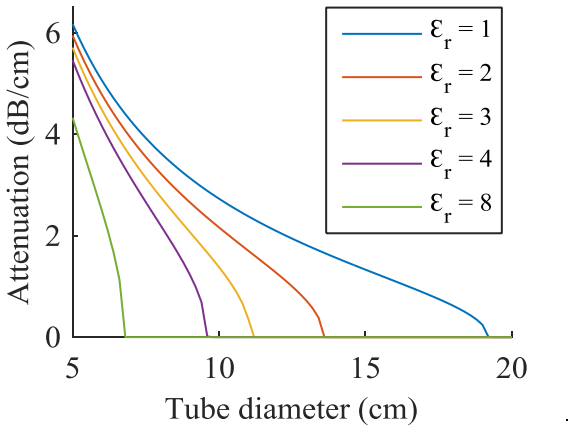


Figure 5.12 Below cut-off attenuation per centimetre versus tube diameter for 915 MHz, with different dielectric filling material.

If the material to treat has a higher dielectric constant, smaller tubes would be needed to act as self-choking structures as evident from Figure 5.10. Other approaches are the use of reflective and absorbing chokes or the use of long enough tubes that allow the fields to decay by product absorption [12]. An example of reflective multi-mode cylindrical choke design for 915 MHz is given in section 5.4.11.6 for a 16.1 cm aperture tube diameter.

For the basis of design, the choking behaviour revealed to not be the limiting factor for the sample diameter. A study performed on the behaviour of a TM_{010} circular cavity, summarised in Appendix B, had shown that a diameter of 20 mm was needed to achieve the desired treatment uniformity (PUI < 0.18), and a roughly similar behaviour could be expected from an elliptical cylinder cavity. An initial 20 mm sample diameter was therefore selected as a starting design point.

5.4.4 TM elliptical cylinder cavity

The geometry and size govern the resonant frequency and, in particular, the eccentricity plays a significant role in the relative order of the modes and how separated in frequency they are [340], separation needed to ensure stable operation in the designated mode (i.e. not possible to couple power efficiently to any other mode). A TM mode with at least two well-defined high-intensity focus spots was desired to ease the microwave coupling in one end and the product loading in the other, e.g. for TM_2 or TM_4 (Figure 5.3 and Figure 5.4) the feeding and product load would be located close to the maximum spots in the major axis, similar to the sketch in Figure 5.2.

Cavity size can become close to the load size for low order modes, which results in fabrication complexity as can be implied from the design chart shown in Figure 5.6. This aspect gets worse upon sample loading, as the effective electrical size of the cavity increase, and the physical size of the cavity needs to be reduced to keep the original resonant frequency whereas higher order modes can result in massive and bulky cavities for treating a comparatively small

sample volume. The TM_2 and TM_4 modes (Figure 5.3 and Figure 5.4) were considered as practical candidates in the middle size range.

5.4.4.1 Empty TM_2 cavity

An initial design approximation was made by using the design chart in Figure 5.6 for an eccentricity of 0.7, resulting in a $a = 83.0$ mm and $b = 59.2$ mm. An initial height of 50 mm was selected considering the theoretical maximum height of 51 mm to achieve the desired power density within the sample for a 20 mm diameter load (with all power absorbed in the product). This height should prevent the possibility of overlapping modes, in a similar fashion as discussed for circular cavities (see Appendix B). The height should not affect the resonant frequency nor the achievable quality factor and PUI, as seen in circular cavities. All these aspects are analysed next.

Eigenmode analysis showed a resonant frequency of 2.45 GHz with the desired field pattern shape (Figure 5.13 and Figure 5.14), with maximum electric fields at ± 37.9 mm with a 3 dB width of 40.3 mm and an empty quality factor of 17,756 (aluminium walls).

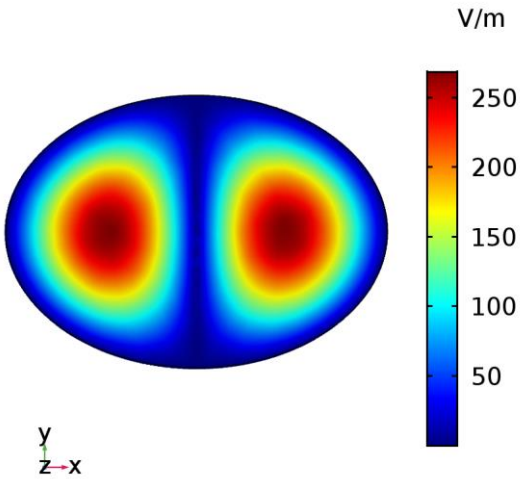


Figure 5.13 TM_2 mode electric field distribution in central cut-plane. Empty $e \approx 0.7, a = 83$ mm, $b = 59.2$ mm cavity.

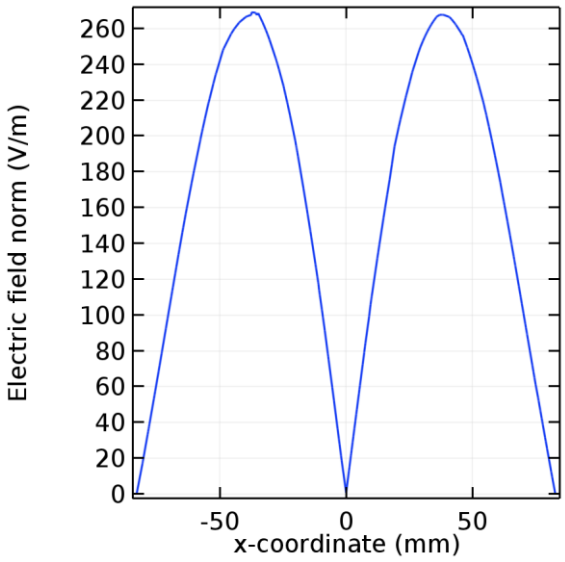


Figure 5.14 TM_2 mode electric field distribution along the major axis. Empty $e \approx 0.7, a = 83$ mm, $b = 59.2$ mm cavity.

5.4.4.2 Empty TM_4 cavity

The same approach used for TM_2 was used. A design approximation was made by using the design chart in Figure 5.6 for an eccentricity of 0.7, resulting in a $a = 112$ mm and $b = 80$ mm. Same height was considered (50 mm). Eigenmode analysis on the structure showed a resonant frequency of 2.41 GHz with the desired field pattern shape (Figure 5.15), with maximum electric fields at ± 70 mm from its centre with an additional maximum in the centre (Figure 5.16). A 3 dB width of 39.19 mm and an empty quality factor of 20,015 were observed.

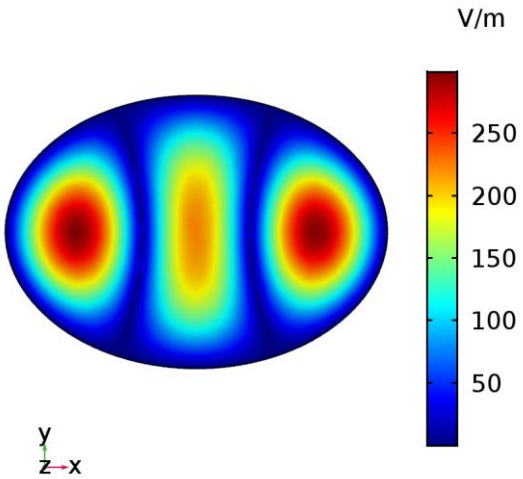


Figure 5.15 TM_4 mode electric field distribution in central cut-plane. Empty $e \approx 0.7, a = 112$ mm, $b = 80$ mm cavity.

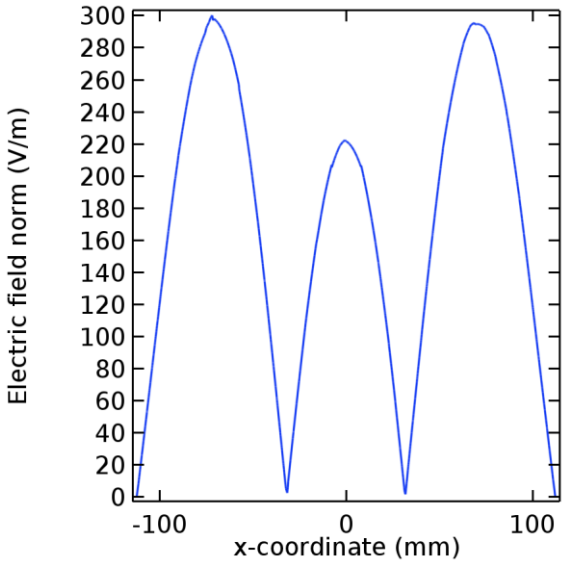


Figure 5.16 TM_4 mode electric field distribution along the major axis. Empty $e \approx 0.7, a = 112$ mm, $b = 80$ mm cavity.

5.4.4.3 Loaded resonant elliptical cavities

Simulations models were adjusted considering the load and PTFE tube, to provide resonance near 2.46 GHz, following the procedure is given in Figure 5.17. Eigenmode analysis of the estimated empty cavity (from charts/analytical estimation) was carried out, and maximum electric field positions were located. Then, the product was positioned coincident to this maximum electric field and an eigenmode analysis is performed again assessing the resonance frequency, electric field position and modal frequency separation. The sample position is shifted towards the new maximum (if displaced significantly) and the cavity size and eccentricity are adjusted towards resonant frequency (smaller cavity result in higher resonance frequency) and modal separation (eccentricity dependant) targets. This cycle is repeated until the resultant cavity resonates at the design frequency, with the specified modal separation and with the sample positioned at the electric field maximum within the specified tolerances.

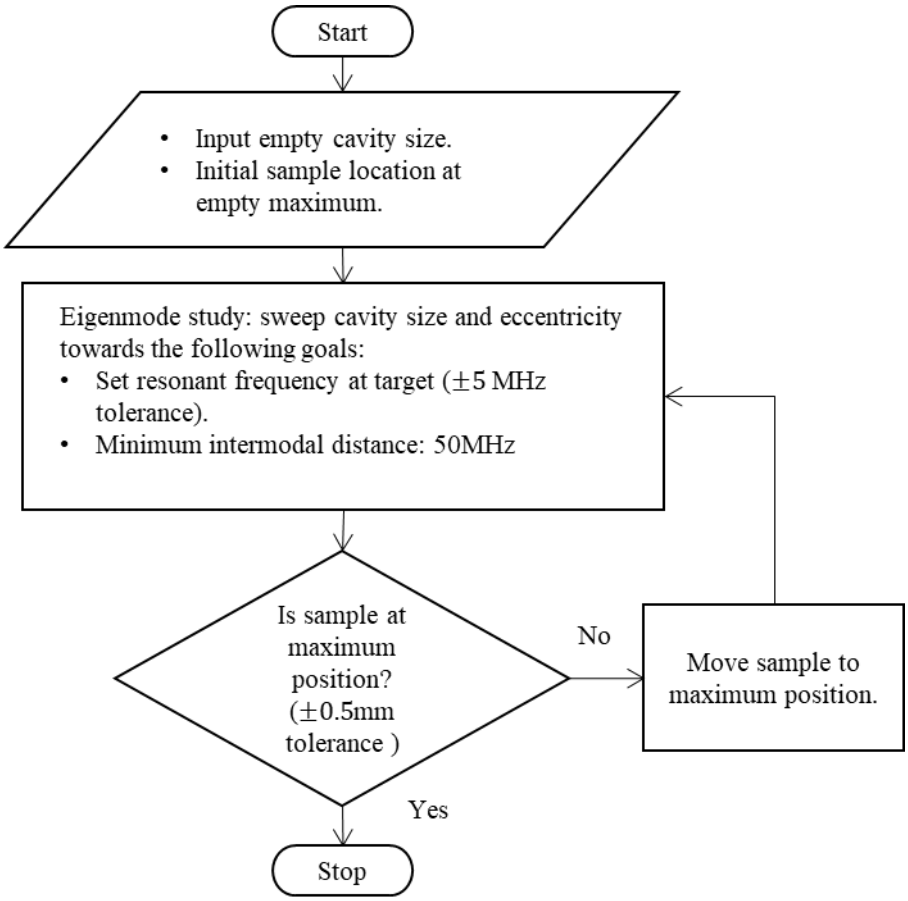


Figure 5.17 Loaded cavity size and load positioning adjustment procedure summary.

The resultant cavities electric field distributions at the major axis are shown in Figure 5.18, with the product load position marked as dash lines. The horizontal and vertical cut-plane distributions are shown in Figure 5.19 and Figure 5.20 for TM_2, and Figure 5.21 and Figure 5.22 for TM_4. Both cavities exhibit a similar performance with practically the same power uniformity index and power conversion efficiency and a slightly different quality factor. The cavity dimensions and performance parameters are summarised in Table 5.4.

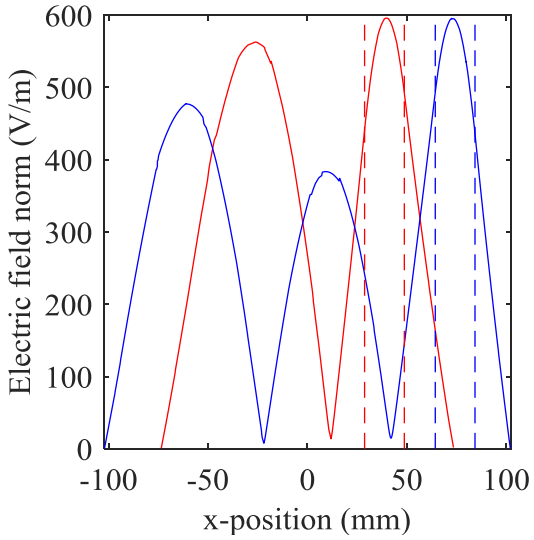


Figure 5.18 Electric field distribution at the vertical middle cut plane, TM_2 cavity (red line), TM_4 cavity (blue line). The dashed lines represent the sample boundaries.

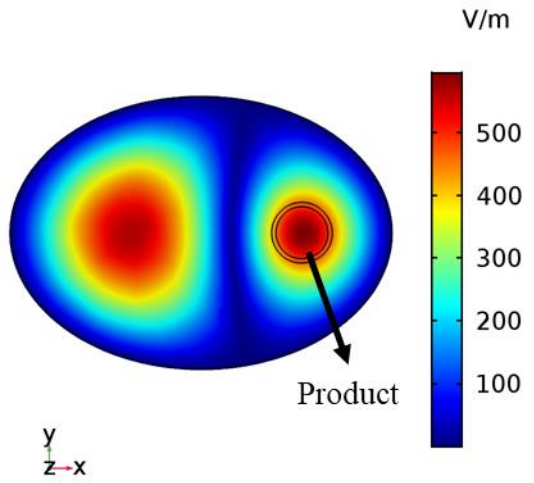


Figure 5.19 TM_2 Electric field distribution at the horizontal middle cut plane. Loaded cavity with $e \approx 0.7, a \approx 73.6$ mm, $b \approx 52.5$ mm, load at 38.8 mm from the centre.

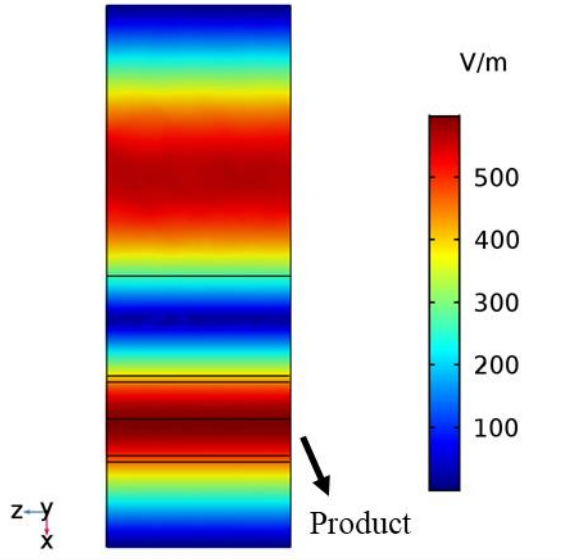


Figure 5.20 TM_2 Electric field distribution at the vertical middle cut plane. Loaded cavity with $e \approx 0.7, a \approx 73.6$ mm, $b \approx 52.5$ mm, load at 38.8 mm from the centre.

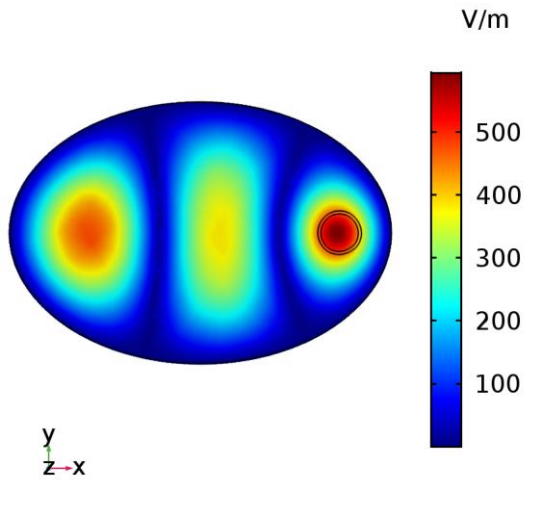


Figure 5.21 TM_4 Electric field distribution at the horizontal middle cut plane. Loaded cavity with $e \approx 0.73, a \approx 102$ mm, $b \approx 70$ mm, load at 74.4 mm from the centre.

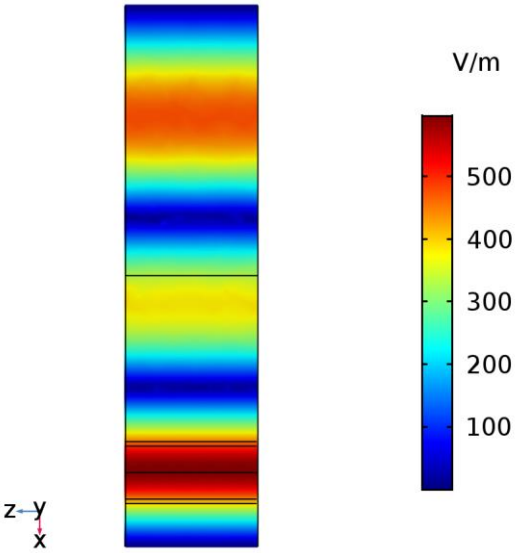


Figure 5.22 TM_4 Electric field distribution at the vertical middle cut plane. Loaded cavity with $e \approx 0.73, a \approx 102$ mm, $b \approx 70$ mm, load at 74.4 mm from the centre.

Table 5.4 Properties of TM_2 and TM_4 elliptical cavities loaded with product.

	e	a	b	f_0	Q_0	Peff (%)	PUI
TM_2	0.7	73.6	52.5	2,455.5	101	99.4	0.115
TM_4	0.73	102.1	70	2,462.8	121	99.4	0.117

Several heights from 20 to 140 were tested to confirm that the resonance frequency, quality factor and power uniformity index remain the same with its change (Table 5.4), with the small difference due to numerical accuracy.

Table 5.5 Properties of TM_2 and TM_4 elliptical cavities loaded with product for varying heights (d).

	TM_2			TM_4		
d(mm)	Frequency (Hz)	Q0	PUI	Frequency (Hz)	Q0	PUI
20	2455451169	100.3	0.115	2462745053	120.3	0.117
40	2455455961	100.7	0.115	2462752479	121.0	0.117
60	2455467573	100.8	0.115	2462756838	121.2	0.117
80	2455484298	100.9	0.115	2462765090	121.3	0.117

100	2455489361	101.0	0.115	2462771270	121.3	0.117
120	2455500231	101.0	0.115	2462773466	121.4	0.117
140	2455491380	101.0	0.115	2462776302	121.4	0.117

5.4.5 Cavity selection

Performance-wise, the circular TM_{010} (Appendix B), and elliptical TM_2 and TM_4 exhibit similar behaviour, with PUI of 0.11, 0.12 and 0.12 respectively and over 99 % of power conversion efficiency. A larger difference is seen regarding the quality factor with 44, 101 and 121 respectively. Quality factors below 450 usually require only basic tuning adjustments, whereas higher values, notoriously in the thousands require the use of automatic tuners or more active control strategies [12]. Cavities with quality factors of less than 25 usually do not require intervention after initial setup [12]. Nonetheless, for highly variable load properties the use of active tuning might be needed to compensate for frequency shifts and sharp changes of loss and hence quality factor. When compared to a rectangular applicator (WR340 TE_{103} Appendix E), the elliptical applicator showed higher field intensities within the sample and, therefore, power loss density; a higher empty quality factor and consequent better power conversion efficiency; and less sensitivity of the position of the maximum field with change of sample permittivity, with similar performance uniformity-wise.

The similar performance left the decision making to manufacturing and flexibility aspects. The circular cavity was discarded as it only provided 2 cm clearance space between tube and cavity and being considerably smaller than a standard WR340 waveguide, making microwave feeding by either waveguide or using probes complex to manufacture and risky, given the intended high-power operation. The TM_4 cavity provided considerably more space for fitting the microwave feeding structure as well as room for the addition of insulation and other ancillary equipment if needed, at roughly the same performance as the TM_2. Moreover, the TM_4 mode gives additional flexibility as it can treat double the product at the same time by

feeding the cavity from the central high field zone and fitting two treatment zones in the other two, if required. Therefore, it was decided to fabricate a prototype based on the elliptical TM_4 cavity.

5.4.6 The microwave feeding

The excitation of the TM_4 mode can be done via a waveguide with an iris aperture or using a coaxial probe. A waveguide fitted in the opposite side of the product fitted with its broadside in line with top and bottom of the cavity as shown in Figure 5.23 will provide vertical polarisation, magnetically coupling with the cavity. Similarly, a monopole in the bottom or top of the cavity (Figure 5.24) could also provide the needed excitation. Alternatively, a central monopole could excite the required mode and would allow the symmetrical treatment of two simultaneous loads as shown in Figure 5.25.

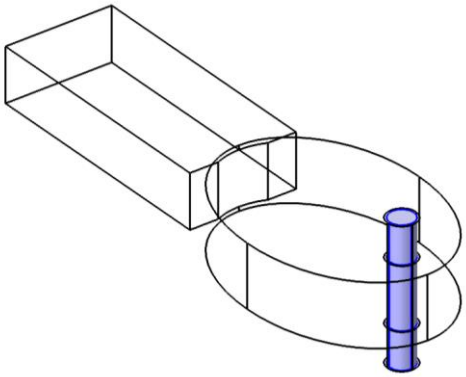


Figure 5.23 Sketch of waveguide feeding of the elliptical cavity.

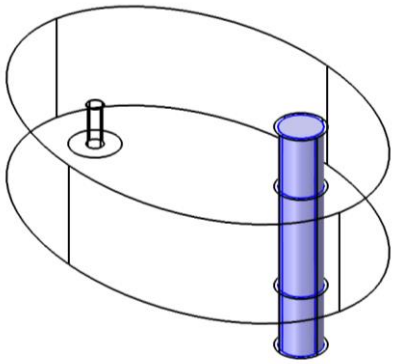


Figure 5.24 Sketch of monopole (i.e. coaxial) feeding of the elliptical cavity.

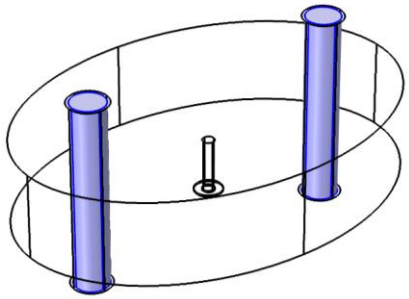


Figure 5.25 Sketch of monopole (i.e. coaxial) feeding of an elliptical cavity with two loads.

For this prototype, a coaxial feeding was selected, as the cavity was going to be machined from a solid aluminium block, leaving a relatively thick wall (see Figure 5.30). This made the manufacturing of the needed cavity-waveguide interface complicated. Modular construction could allow replacing the coaxial for a second load with the shift of the feeding to the cavity centre as in Figure 5.25, increasing its flexibility. Nonetheless, for comparison, numerical analysis on a waveguide-fed cavity was carried out.

5.4.6.1 Waveguide-fed system

The feeding tube extensions were incorporated into the model. A WR340 waveguide was used to feed the cavity via a coupling iris, which size was adjusted via simulations to keep resonance at 2.46 GHz. This resulted in a quality factor of 162 and a PUI of 0.17.

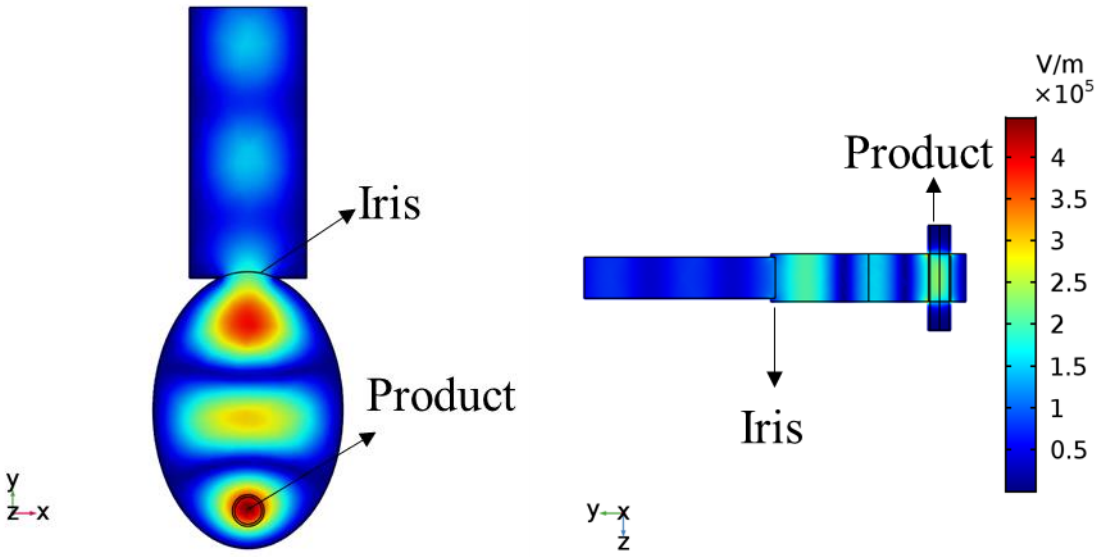
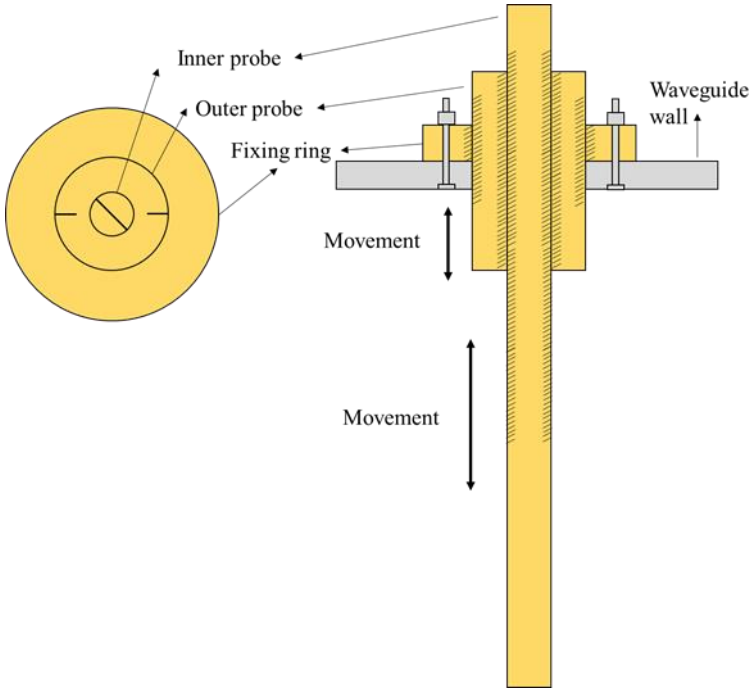


Figure 5.26 Electric field distribution in the horizontal middle cut-plane for the waveguide-fed elliptical cavity.

Figure 5.27 Electric field distribution in the vertical middle cut-plane for the waveguide-fed elliptical cavity.

5.4.6.2 Coaxial probe

The probe was designed for 50 Ω to allow interchange with standard connectors for testing purposes. An 8.7 mm internal and 20 mm external conductor diameter, equivalent to the standard EIA RF (10s of kW to MW [362]) RS-225 50 Ω 7/8" (military standard M-24044/1) was used. The probe was designed with two interior adjustable lengths, named as inner and outer probes. Their length can be adjusted externally for impedance matching purposes, as illustrated in Figure 5.28. A picture of the built probe is shown in Figure 5.29.



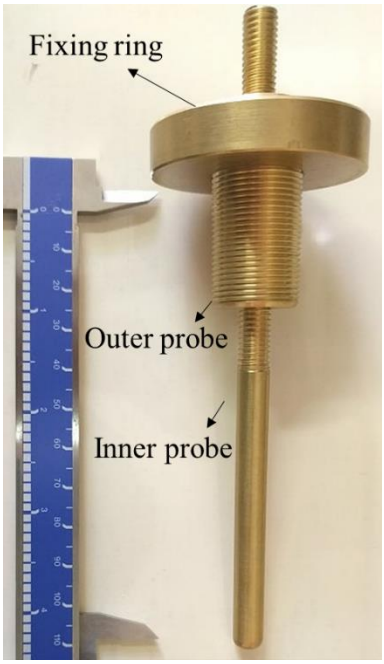


Figure 5.28 Adjustable grounded coaxial probe sketch.

Figure 5.29 Fabricated adjustable grounded coaxial probe.

The volume of the inner probe inside the cavity effectively reduce the cavity size and therefore increase its resonant frequency — nonetheless, the degrees of freedom of probe adjustment allow to move the resonance to the specified operational frequency. The concept

was checked using simulations and experimentally by fabricating a rudimentary probe and cavity prototype prior to fabrication.

5.4.7 Resonant cavity

The cavity was machined from an aluminium block in a CNC Datron M8. A picture of the fabricated prototype is shown in Figure 5.30.

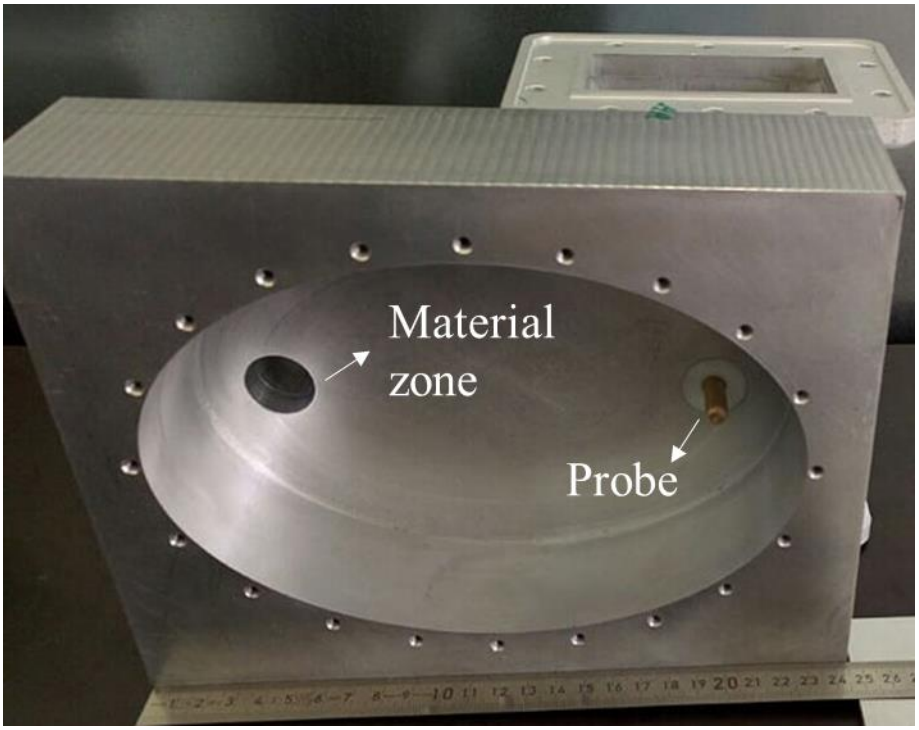


Figure 5.30 Picture of the internal part of the prototype.

5.4.8 System schematic drawing

Dimensions of the fabricated prototype can be found in Figure 5.31 with associated Table 5.6.

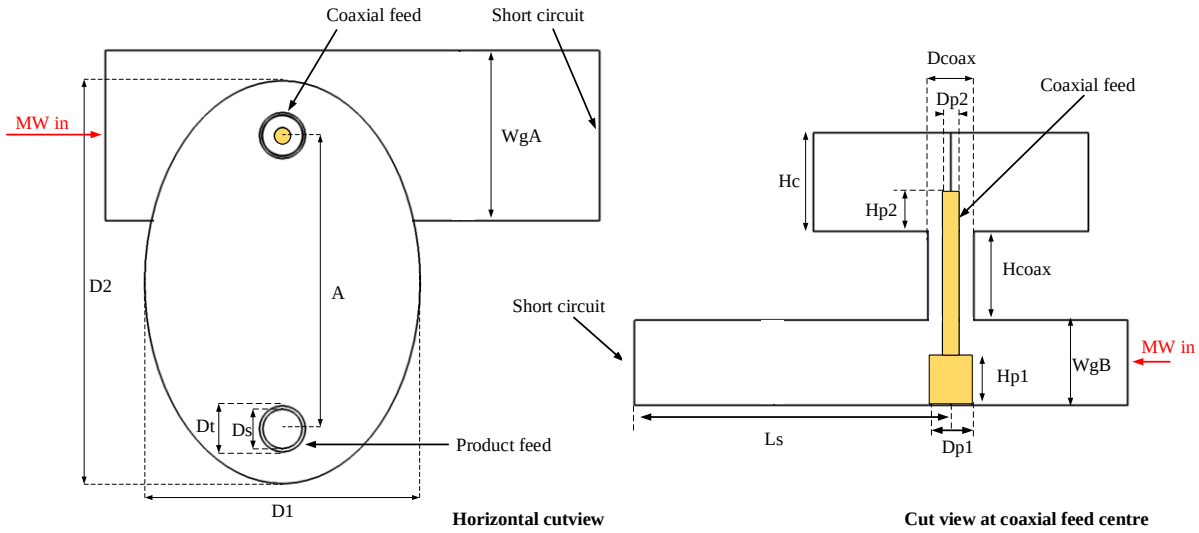


Figure 5.31 Schematic of fabricated prototype elliptical cylinder applicator with main dimensions.

Table 5.6 Dimensions of prototype elliptical cylinder applicator

Dimension	Abreviation	Value (mm)
Cavity elliptical major diameter	D2	204.28
Cavity elliptical minor diameter	D1	140.00
Product feed tube external diameter	Dt	23.40
Product feed tube internal diameter (i.e. sample external diameter)	Ds	20.00
Coaxial to product feed distance (centre to centre)	A	148.77
Waveguide broad side size	WgA	86.36
Waveguide narrow side size	WgB	43.18
Distance from short circuit to probe	Ls	161.18
Probe coupling section height	Hp1	25.00
Probe coupling section diameter	Dp1	21.00
Probe penetration section height	Hp2	20.00
Probe penetration section diameter	Dp2	7.94
Coaxial section height	Hcoax	45
Coaxial section diameter	Dcoax	23.4
Cavity height	Hc	50

5.4.9 Results and model validation

CST microwave time domain FIT simulations with hexahedral meshing [329] and frequency domain FEM simulations on COMSOL with tetrahedral meshing [330] were carried

out for analysis in parallel for cross-validation, incorporating the effects of the feeding probe and material feeding tubes. The comparison of results from simulations using different techniques can add significant confidence to their validity and is a popular approach for validation of electromagnetic models [363].

The electric field distribution is shown in Figure 5.32 (CST) and Figure 5.33 (COMSOL), and power loss density plots shown in Figure 5.34 (CST) and Figure 5.35 (COMSOL) reveals relatively uniform distribution across the sample with an estimated PUI of 0.17 in both cases, which is the same as the obtained for the waveguide fed simulation (see section 5.4.6.1). The same average power loss density in the bulk of 3.5×10^8 W/m^3 is seen in all simulations for a 6 kW input power.

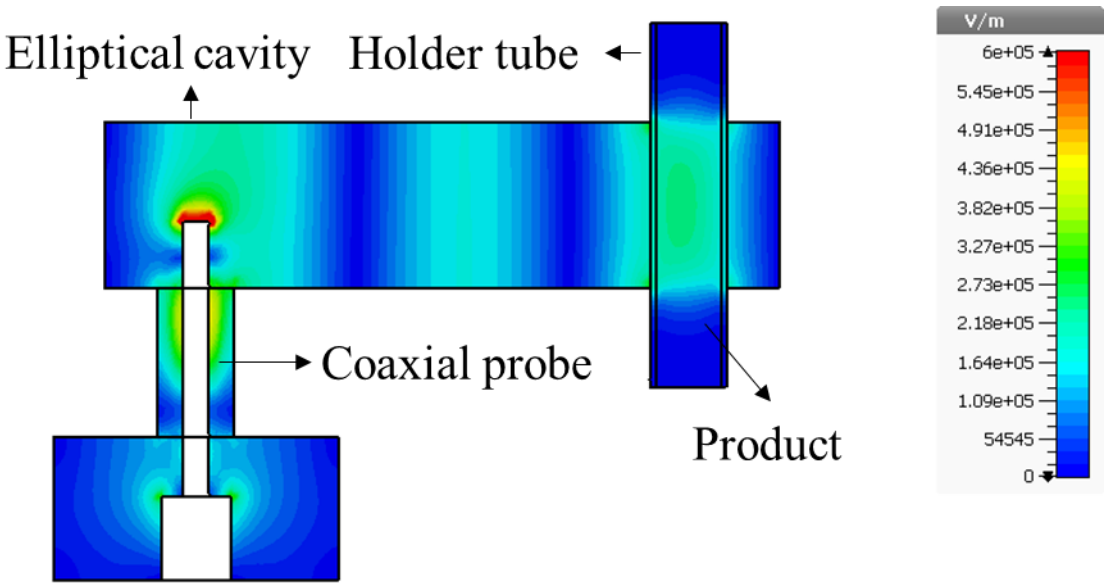


Figure 5.32 Electric field distribution (V/m) simulated by CST Microwave at 2.46 GHz.

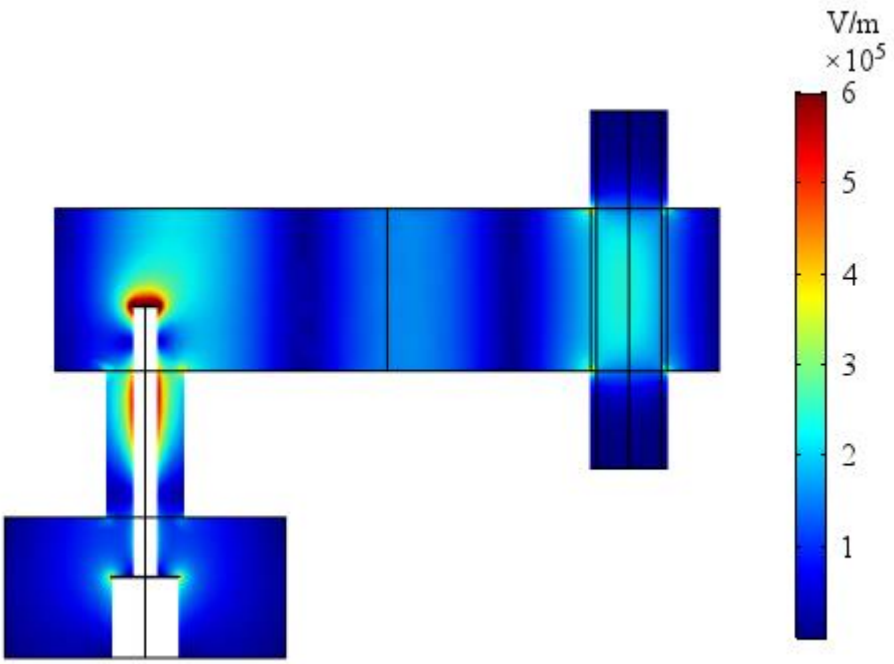


Figure 5.33 Electric field distribution simulation (V/m) simulated by COMSOL at 2.46 GHz.

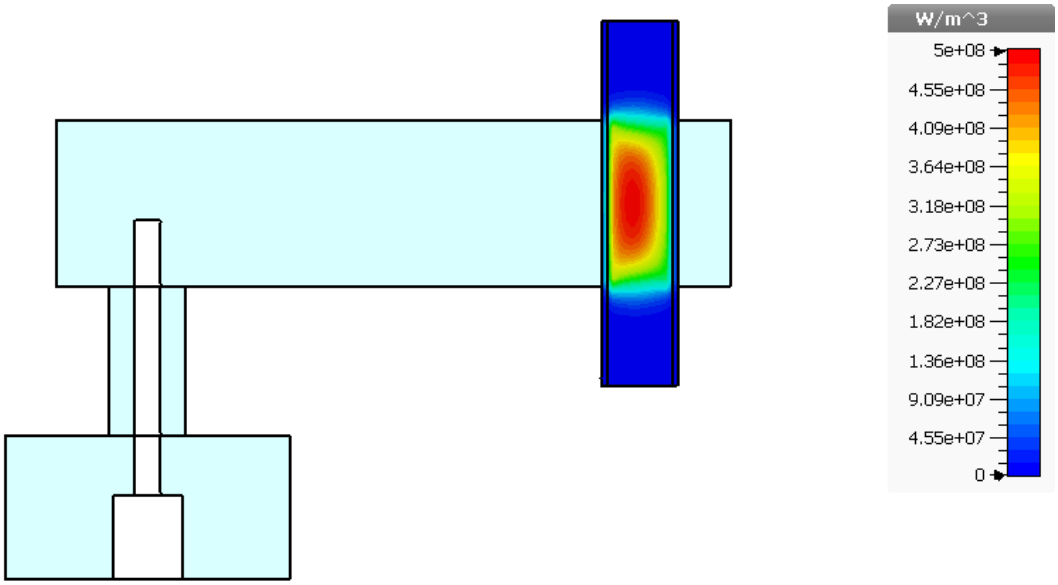


Figure 5.34 Power loss density simulation (W/m3) simulated by CST at 2.46 GHz.

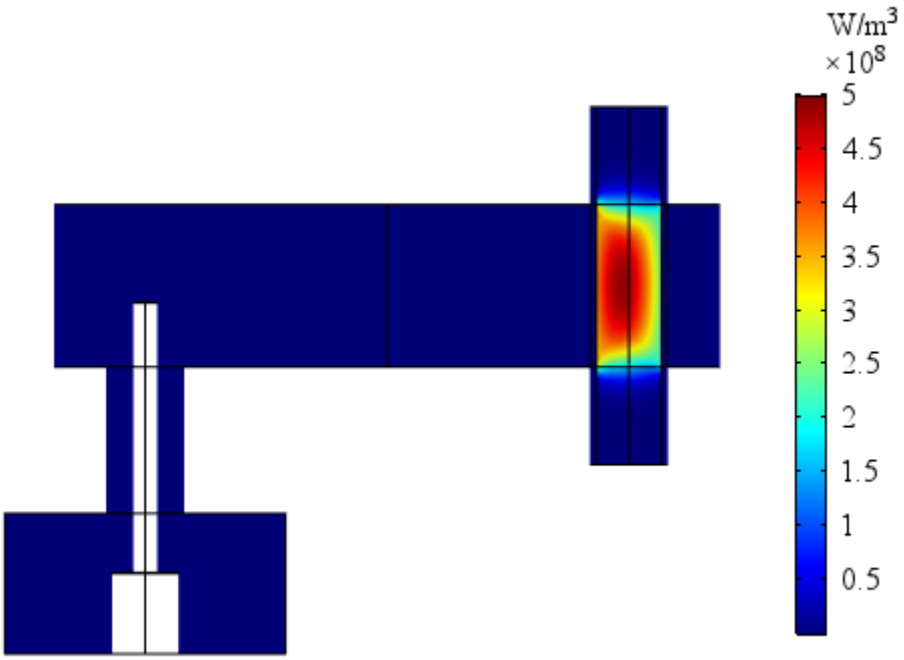


Figure 5.35 Power loss density simulation (W/m^3) simulated by COMSOL at 2.46 GHz.

An EN5071C network analyser was used to measure the reflection coefficient and quality factor. Simulated and measured reflection coefficient magnitude are shown in Figure 5.36. A reflection coefficient -10 dB bandwidth of 8 MHz was measured, whereas both simulated bandwidths were of 9 MHz. The measured quality factor was 233, whereas the simulated quality factors were and 198 and 196 for COMSOL and CST respectively. While the waveguide fed system exhibited a lower value at 165. These values, all well below 450, are considered relatively easy to match and would only require basic tuning adjustments without sophisticated control [12].

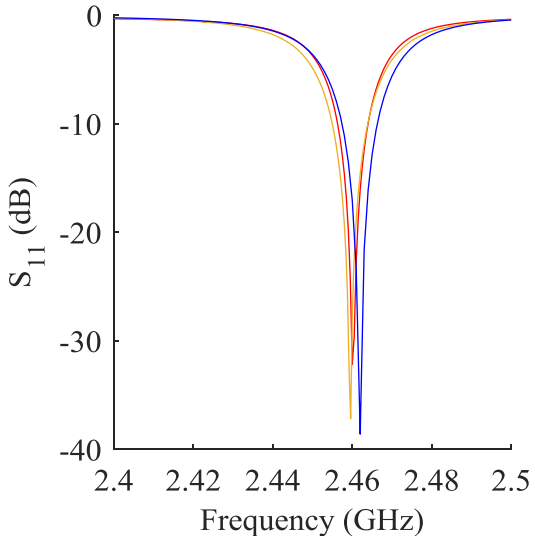


Figure 5.36 Reflection scattering parameter S11 (dB) experimental measurement (red line), COMSOL simulation (blue line) and CST simulation (yellow line).

The difference in quality factor between simulations is negligible, and the measurement deviation is small considering that it falls within the material properties standard deviation range (e.g. changing the simulated loss factor from 0.12 to 0.11, a simulated quality factor of 244 is observed simulated in COMSOL). Furthermore, the permittivity measurement packing density (~1,400 kg/m^3) is slightly higher than the product presented in the processing tube (due to space constraint). This results in an effectively lower loss factor in the tube, which could result in a higher quality factor measurement. Conversion efficiencies of 99 % were obtained for all cases. The results are summarised in Table 5.7.

Table 5.7 Measured and simulated results for TM_4 elliptical cavity with a 2 mm - 4 mm ore load.

	S_{11} -10 dB bandwidth (MHz)	Q_0	Power conversion efficiency (%)	PUI	Average power loss density
Measured	8	233	99	-	3.5
CST	9	196	99	0.17	3.5
COMSOL	9	198	99	0.17	3.5

The discussed simulation results and measurements present excellent agreement, which serves as validation of the models. The design methodology is also proven valid as all the design

goals were met. This provides confidence to apply the design and modelling to evaluate other possible materials and therefore discuss its applicability in various applications.

5.4.10 Heating system

The generator output frequency spectrum needs to match with the applicator bandwidth to make the energy transfer efficient [364], this is illustrated in Figure 5.37.

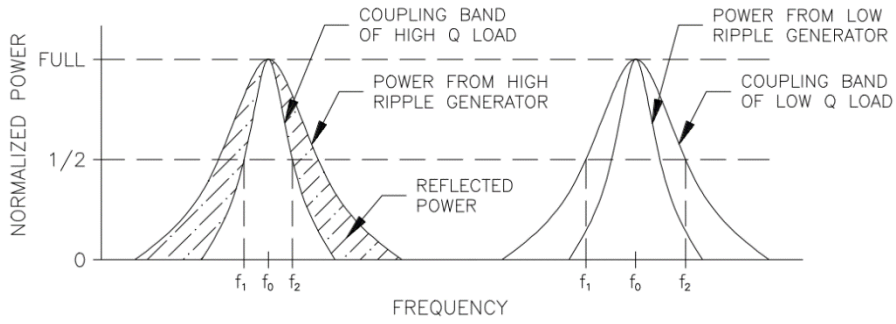


Figure 5.37 Generator output versus applicator frequency bands after [364].

This matching process, commonly called tuning, can be a challenge that requires the use of generators with narrow output spectrum (e.g. low-ripple continuous wave, solid state) [3], [364] in particular for low-loss products. Controlled tuning components such as automatic tuners and motorised short-circuit plungers can be used [12], [19]. Solid state generators can also provide automatic tuning by frequency adjustment [365], [366]. Generator output spread is frequency modulated in proportion to the ripple of the power supply (see magnetron pushing figure in the magnetron datasheet). Commercially available high-power low-ripple systems with a switching-mode power supply can provide signals with less than 1 % ripple, and solid-state ones less than 0.2 % [333], [365]–[367]. To illustrate this effect, magnetron typical output frequency spectrums powered by different power supplies are shown in Figure 5.38.

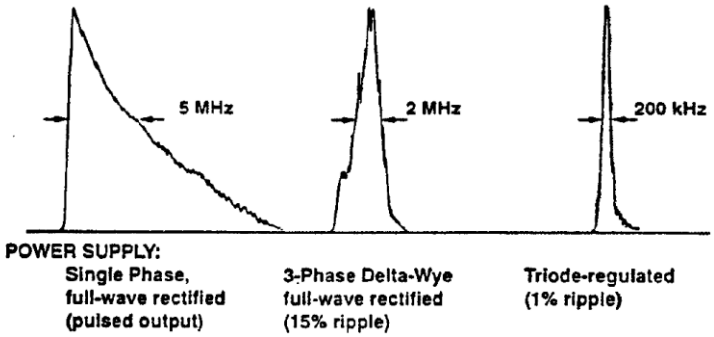


Figure 5.38 Typical magnetron output spectrum for different types of power supplies, reproduced from [368]

Moreover, the magnetron output frequency and spectrum vary as a function of the power level, being narrower at the maximum rate as the ripple generally has a fixed peak-to-peak amplitude regardless of the output power (i.e. relative variability increase with the decrease of output power). The output generator frequency grows with power [368]. Therefore, operation at a fixed maximum power can improve reliability. The magnetron output frequency also changes with the matching (see magnetron frequency pulling figure in the datasheet) and can be reduced by using a circulator, as the mismatch seen by the magnetron is reduced by it.

The generator system comprises a low ripple switch-mode power supply and magnetron head for operation in continuous wave (CW). The Muegge MX6000D-110KL power supply has a ripple of less than 5% at maximum power with an expected output spectrum half power bandwidth on the order 230 kHz. The magnetron head was isolated by a circulator and water load reducing most frequency pulling effects. A chiller and a pump were used to regulate cooling water temperature and flow in a closed cooling circuit. A manual triple stub was used as the main tuning mechanism to adjust to different loads. Directional couplers and power meters were fitted to monitor power reflection during operation.

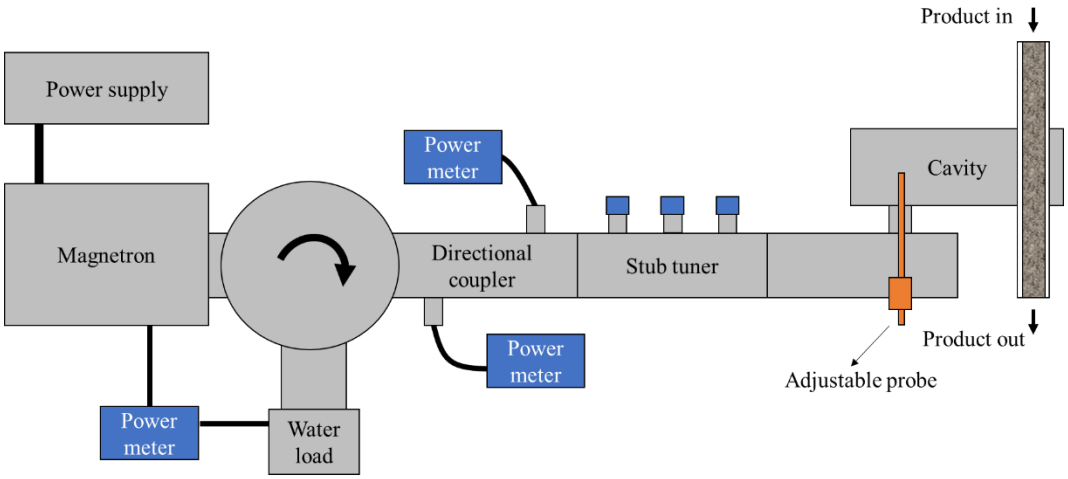


Figure 5.39 Heating system. Cooling circuit omitted, and cavity orientation rotated for clarity.

The system is being used for processing of small grain (<4 mm) ores in batch mode. Within the tested materials, at least 90 % absorption was achieved consistently in each run without retuning and over 99 % if tuned for the sample.

5.4.11 System scale-up

Direct paths for system scaling are the parallelisation of processing lines and the reduction of operating frequency. Assuming similar dielectric properties in each band, which is supported by the similarity of properties seen in the literature for similar materials at 915 MHz [148], the treatment volume can be increased ~19 times by reducing the operating frequency to 915 MHz (volumetric scale factor given by the frequency ratio of $\times (f_{original}/f_{new})^3$); hence increasing the effective throughput by the same factor. This would require a 100 kW generator to provide a similar degree of power density, which is covered within the commercial range. The throughput of the system depends on the process residence time. Residence times at full power of around 50 ms are considered as the initial target, resulting in a required column speed of ~1 m/s to achieve an energy dose near 3 kWh/t. This would result in a 1.6 tonne per hour throughput. Assuming successful proof of concept at 2,450 MHz, further scale-up stages were considered at a lower frequency. The equivalent scaled alternative at a lower 915 MHz that provide similar treatment conditions is presented in Table 5.8. However, material handling

could be the limiting factor due to small product diameter; therefore, estimations were carried out as a first pass feasibility of the proposed operational parameters.

Table 5.8 Frequency scale-up first-pass estimation for elliptical applicator prototype.

Frequency (MHz)	Treatment zone			Column speed (m/s)	Input power (kW)	Energy (kWh/t)	Throughput (t/h)
	Height (mm)	Diameter (mm)	Volume (cm3)				
2450	50.0	20.0	15.7	1	6.0	3.16	1.6
915	133.9	53.6	302.13	2.7	115.2	3.16	30.5

5.4.11.1 Material handling approach

A practical material handling technique needs to be adopted that is compatible with industrial scaling-up. Two alternatives were considered, free-fall of the particles and a bottom fed control packed load.

The free-fall approach was attractive mostly due to its inherent simplicity. However, it can result in a low packing density which would reduce conversion efficiency and the ability to match the microwaves to the load in a stable fashion by increasing the cavity quality factor. Discrete element method particle flow simulations using EDEM [369] were carried out, with details in Appendix C, revealing a 274 kg/m^3 average packing density after release from a steep conical hopper to a 20 mm diameter tube. The permittivity of granular and powder materials can be estimated at a bulk density based on the measured permittivity at another bulk density based on the Landau – Lifshitz – Looyenga (LLL) equation as [370]

$$\varepsilon_b = \left[\left((\varepsilon_a)^{\frac{1}{3}} - 1\right)\frac{\rho_b}{\rho_a} + 1\right]^3 \tag{5.4}$$

where ε_a is the complex permittivity measured at a bulk density ρ_a and ε_b is the mixture at a different density ρ_b. This gives an estimated complex permittivity of $\varepsilon_r = 1.3 - j0.013$. After

adjustment of the probe for tuning the system at 2.46 GHz, a power conversion efficiency of 94 % and a quality factor of 1,215 is observed; thus, the use of automatic tuning and frequency tracking equipment would be required [12], [368].

Using a controlled feeder, as illustrated in Figure 5.40, a tightly packed load can be achieved, easing the microwave matching and allowing to control the residence time by regulating the bottom-feeding speed. An example of a commercial bottom feeder system is shown in Figure 5.41

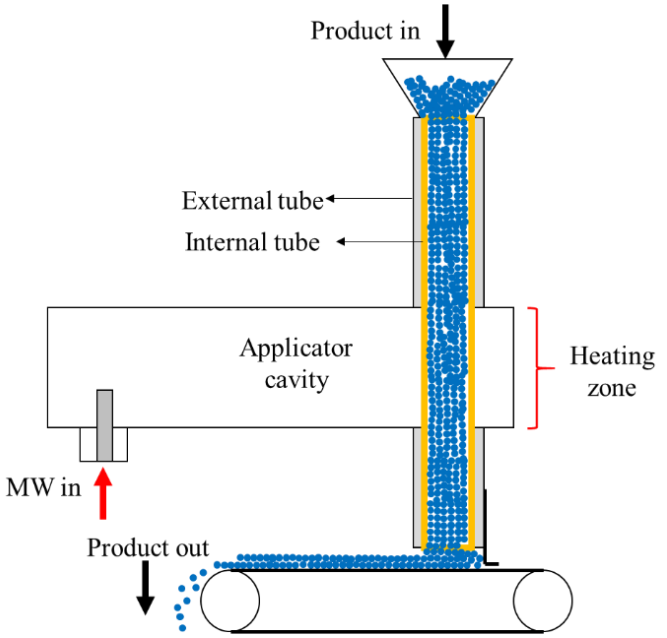


Figure 5.40 Controlled feeder concept sketch for material handling for elliptical cylinder applicator



Figure 5.41 Merrick 970N weight belt feeder from [371]**.**

As the internal tube will be continuously subjected to abrasion and microwave energy, a microwave transparent and mechanically resistant ceramic is needed. Hexagonal boron-nitride makes an excellent candidate with these characteristics [115] with notorious wear resistance, chemical inertness, and also behaves as a solid lubricant with friction coefficients which can be even lower than PTFE and Graphite [372].

5.4.11.2 Outlet size, particle size and hopper diameter

A hopper feeder discharge capability should be in excess of the required throughput to be able to provide enough stream of product continuously. A schematic of a conical hopper is shown in Figure 5.42. The major parameters affecting the discharge are analysed next.

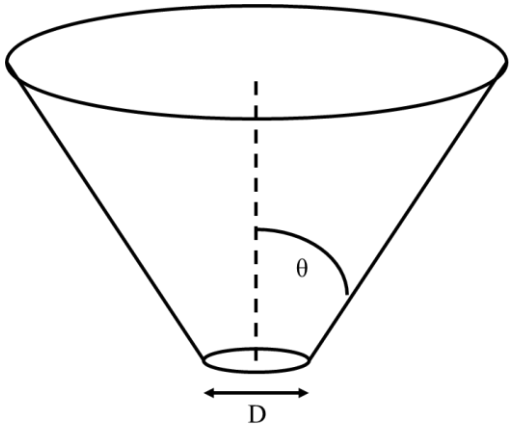


Figure 5.42 Conical hopper schematic, being D the outlet diameter and θ the semi-included angle.

The outlet diameter should be large enough to allow for continuous operation without clogging. The critical outlet to particle diameter ratio is considered to be 4 [373]; however, flow irregularities or intermittent behaviour can be seen in the range of 4-6, depending on the shape of the particle [373]. The discharge rate typically increases with the decrease in particle size and can be considered independent of hopper diameter if it is at least 2.5 the outlet diameter [373].

A particle size of up to 3.3 mm was set as a maximum limit for a 20 mm outlet to comply with the discussed limitation. Under the same criteria, a particle size limit of a maximum of 9

mm resulted for the 915 MHz system. Hoppers with diameters of at least 2.5 times the outlet diameter were considered.

5.4.11.3 Filling height

The pressure at the bottom of a hopper can be constant if the height is larger than the hopper diameter, and the hopper diameter is at least 2.5 times the outlet diameter [373].

5.4.11.4 Discharge rate estimation

Several empirical discharge rate models can be used to predict the discharge rates of granular materials from conical hoppers with circular apertures [373]–[375]. The following equations were used as an initial estimation

$$W = \frac{\pi}{4} D^2 \rho_b \sqrt{\frac{Dg}{4\tan(\theta)}} \qquad \text{Ref. [375]} \quad (5.5)$$

$$W = 0.16 D^{2.5} \rho_s \sqrt{g} \left(\frac{D}{d} - 3\right)^{0.3} f(\theta)(Z-5)^{-0.5}$$

$$f(\theta) = (\tan\theta)^{-0.35} \text{ if } \theta < 90 - \alpha$$

$$f(\theta) = (\tan(90-\alpha))^{-0.35} \text{ if } \theta \geq 90 - \alpha \qquad \text{Ref. [374]} \quad (5.6)$$

where

W: discharge rate
D: outlet diameter
d: particle diameter
g: gravitational acceleration 9.807m/s2
ρ_b: bulk density
ρ_s: particle density
θ: hopper semi included angle

α: angle of repose
Z: shape factor. For spherical particles Z=6 [376]

Estimated properties values are given in Table 5.9. The estimated discharge rates using both equations are plotted in Figure 5.43, considering spherical particles. An extremely steep angle of 1.5° for a 1.6 t/h discharge rate was calculated from equation (5.6). More sophisticated hopper design using inserts can provide a practical workaround in which only a small part consists of a regular conical hopper while the rest can be much wider, saving height [377]. Nevertheless, a reduction of the operation throughput to around 1 t/h was applied, resulting in a basic conical hopper with θ =5.9° by equation (5.6).

Table 5.9 Product properties for the estimation of discharge rates – unreferenced values comes from initial sizing and measurements.

Parameter	Value	Ref	Material from [378]
D	20mm		-*
d	3mm		4/8mm
ρ_s	2,500kg/m3		2,400 kg/m3
ρ_b	1,400kg/m3		1320 kg/m3
ϕ_i	38-45.9°	[379]	45°
Z	6	[376]	6**
α	30-44°	[380]	29°***

**Different geometry*

***Particle spherical approximation*

****Calculated from reported coefficient of static friction as* $atan(\mu) = \alpha$

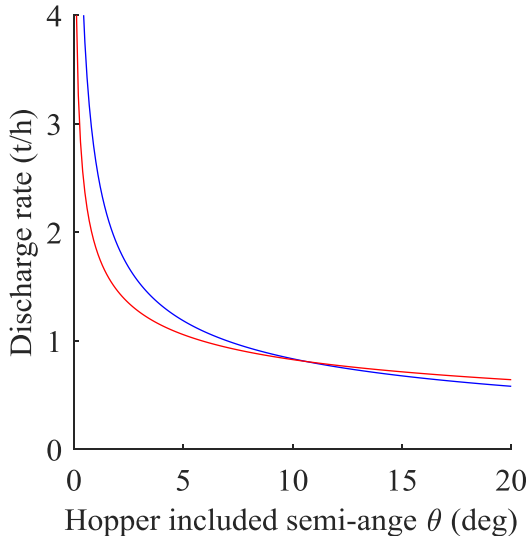


Figure 5.43 Estimated conical hopper discharge rate calculated from equation (5.5) (blue line) and equation (5.6) (red line).

At 1 t/h, the product would receive almost double the energy dose (column speed reduced by almost half). To keep the energy levels, a drop of power, an increase of applicator height or sample diameter would be needed, at the expense of reducing the power density and uniformity. The new estimated operational values and estimated maximum particle sizes are shown in Table 5.10, considering a drop in power and average power density to half (~1.8×10^8 W/m^3).

Table 5.10 Second-pass estimation for elliptical applicator prototype.

Frequency (MHz)	Treatment zone			Particle size (mm)	Column speed (m/s)	Input power (kW)	Energy (kWh/t)	Throughput (t/h)
	Height (mm)	Diameter (mm)	Volume (cm3)					
2450	50.0	20.0	15.7	<3	0.63	3.0	3.0	1
915	133.9	53.6	302.13	<9	1.67	57.6	3.0	19

An initial hopper size of 20 mm outlet diameter, 130.8 mm top diameter and 540 mm length, with a semi included angle of $\theta = 5.9°$ for a 1 t/h according to equation (5.6) was analysed by discrete element method simulations using EDEM software [369], to check the design discharge rate for a particle size of 3 mm in Appendix C. Model calibration was derived

from calibration valuesbased on the ones used in [378], due to the similarity on particle type and setup as seen in Table 5.9. Accurate modelling would require experimental characterisation for model calibration; nonetheless, the basic simulations are in general agreement with the expected results by the used empirical models, showing the need for an even steeper hopper. This suggest that using such a small opening is not likely a suitable alternative for working with the desired particle size.

5.4.11.5 915 MHz material handling considerations

Equation (5.6) was plotted for the estimated particle size (9 mm) and outlet diameter (53.6 mm) for the 915 MHz implementation. An even steeper hopper semi included angle is needed for the estimated 19 t/h at 1.4°. An applicator redesign is suggested to allow for a more sensible diameter. At larger diameters, the treatment uniformity will drop significantly as previously discussed. Therefore, an alternative to keep a similar uniformity while allowing for much bigger material diameters was devised in the use of applicators in series with the high-field zone slightly off-set in a complementary way, an illustration of this concept is shown in Figure 5.45.

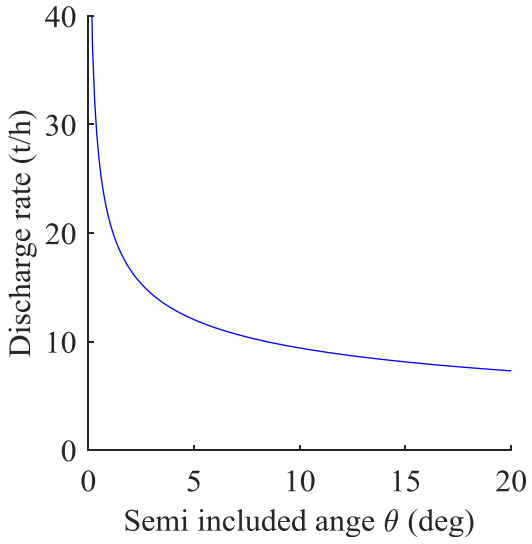


Figure 5.44 Estimated conical hopper discharge rate for a 9 mm particle size and 53.6 mm outlet diameter, calculated from equation (5.6)

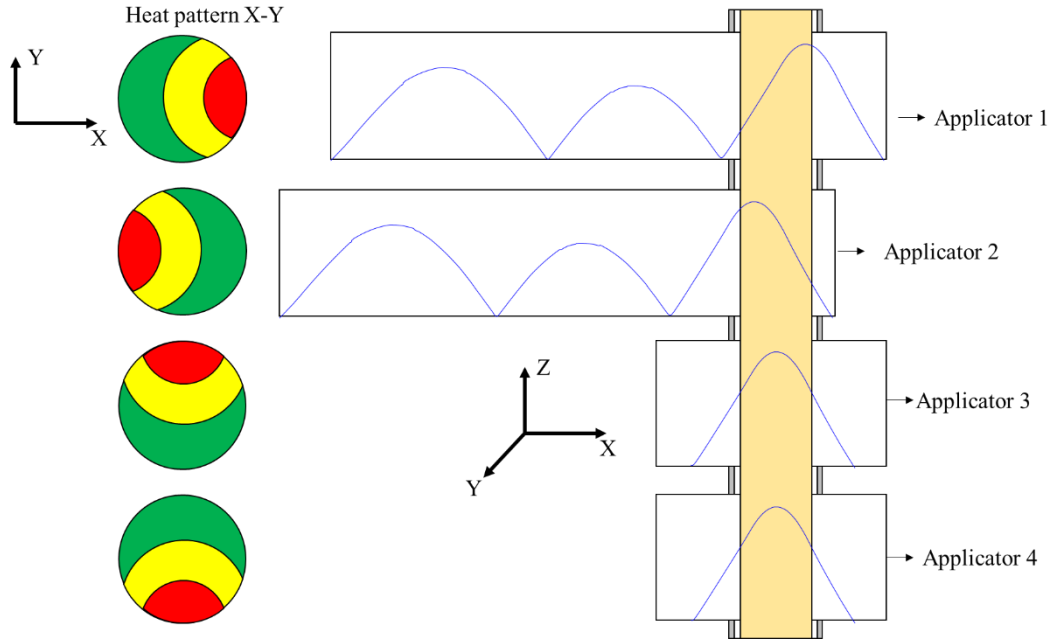


Figure 5.45 Large diameter product through series of off centred applicators conceptual sketch.

For example, considering diameter three times higher at 161mm; a maximum particle size could be of up to 27 mm. Let us consider particles of 25.4 mm (i.e. one inch), giving possible discharge rates on the order of 130 t/h for a hopper semi included angle of 15°, as seen in Figure 5.46. Due to the larger size, the microwave propagation through the tube should be considered. Choking elements are therefore required to ensure the microwave containment and to keep the power densities high [19], [148].

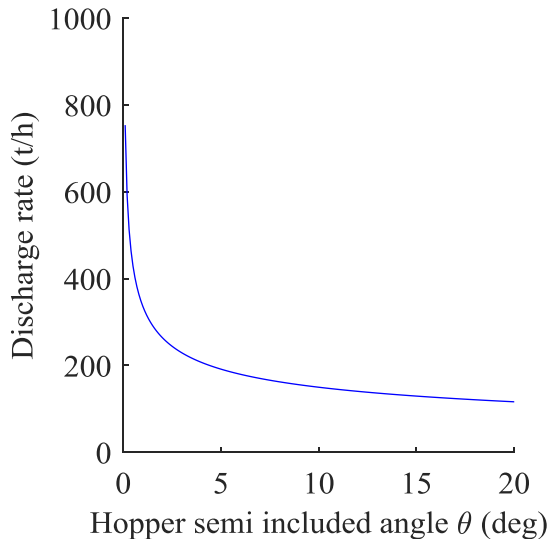


Figure 5.46 Estimated conical hopper discharge rate for a 25.4 mm particle size and 161 mm outlet diameter, calculated from equation (5.6)

5.4.11.6 Cylindrical choke example design

The material transporting tube can be considered as a dielectrically-filled waveguide. Under the assumption that the filling is uniform with $\varepsilon_r' = 3.16$ the possible transmitted modes were studied. Only modes TE_{11} and TM_{01} are propagating modes with cut off frequencies of 613 and 802 MHz. The higher order modes are evanescent (i.e. rapidly decay within the guide), with the following mode cut off frequency being over 1 GHz.

The choke structure needs to be capable of blocking both modes. The use of corrugations can provide filtering by means of resonation [72]. A set of five concentric corrugations were designed to provide over 30 dB band rejection for both modes. Three corrugations separated by $\lambda_{g-TE_{11}}/2$ and two separated by $\lambda_{g-TM_{01}}/2$. The corrugation diameters were optimised numerically to achieve the required rejection, with two different diameters, 290 mm for the rings separated in $\lambda_{g-TE_{11}}/2$ and 262 mm for the rings separated by $\lambda_{g-TM_{01}}/2$, as illustrated in Figure 5.47. Materials were considered as lossless to only evaluate the introduced reflection choking, as in reality the material will also provide an additional mean for power dissipation along the tube. The scattering parameters for both modes are shown in Figure 5.48, Figure 5.49, Figure 5.50, and Figure 5.51. The electric field distribution at 915 MHz for both modes is shown in Figure 5.52 and Figure 5.53.

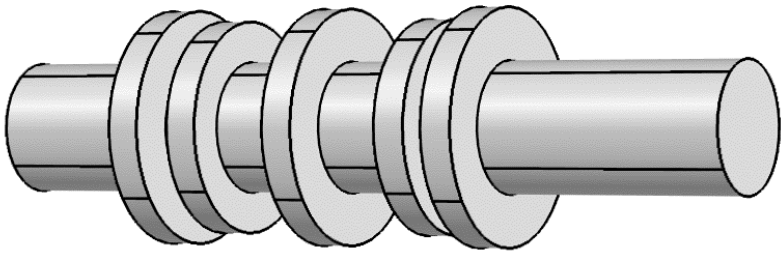


Figure 5.47 Choke structure based on resonating corrugations.

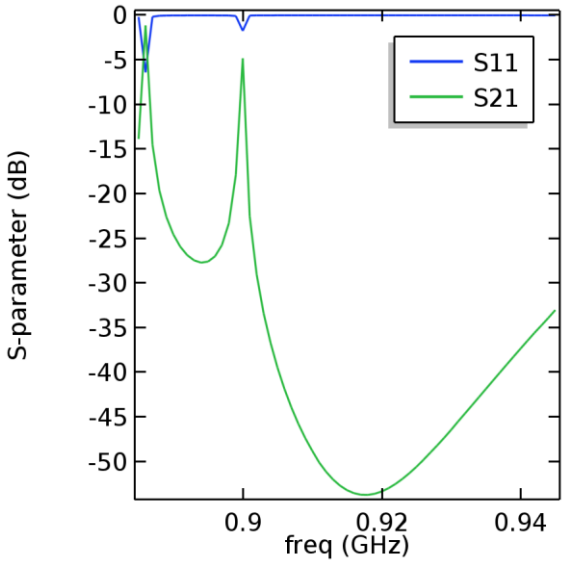


Figure 5.48 Choke scattering parameters – TE_{11} to TE_{11}.

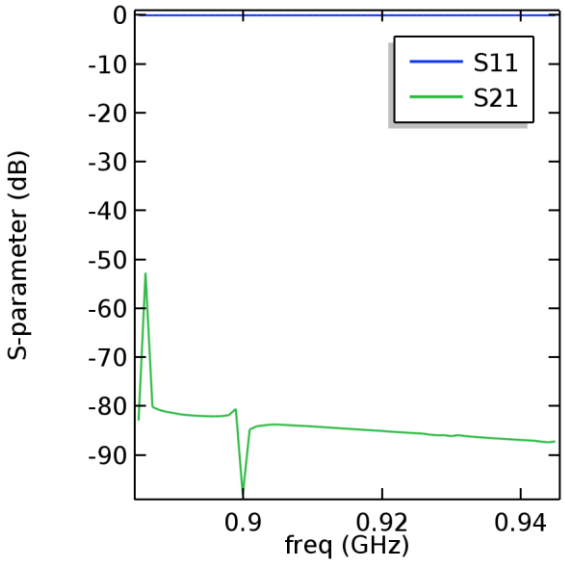


Figure 5.49 Choke scattering parameters – TM_{01} to TM_{01}.

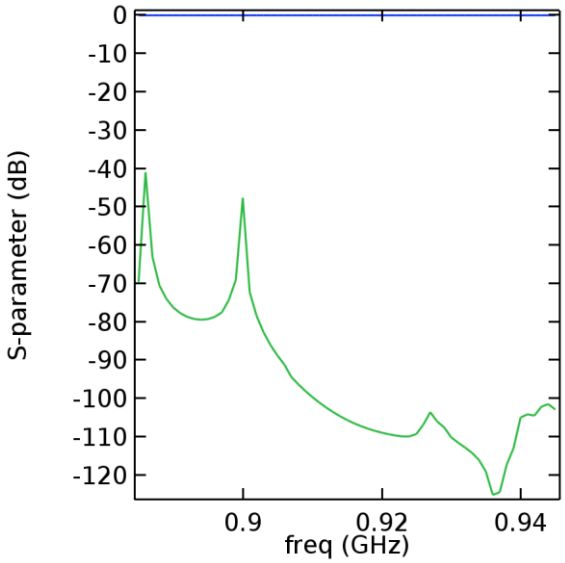


Figure 5.50 Choke scattering parameters – TE_{11} to TM_{01}.

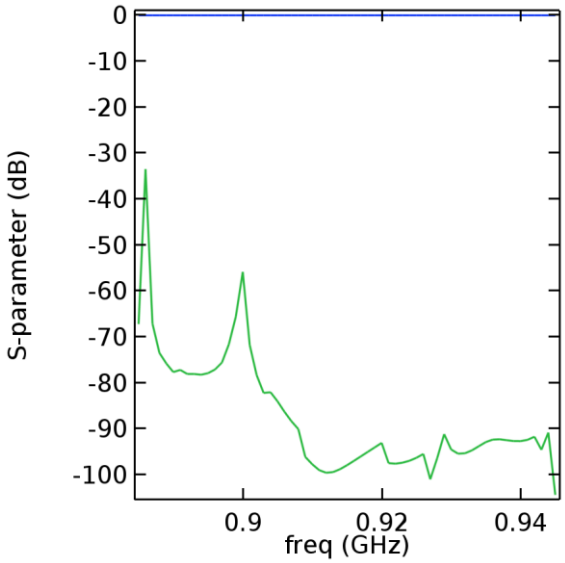


Figure 5.51 Choke scattering parameters – TM_{01} to TE_{11}.

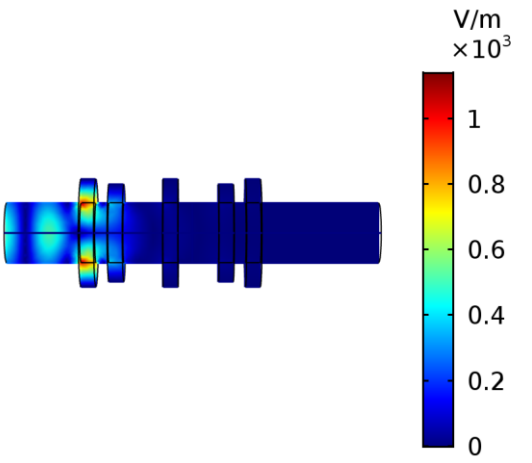


Figure 5.52 Choke electric field distribution at 915MHz for a TE11 excitation.

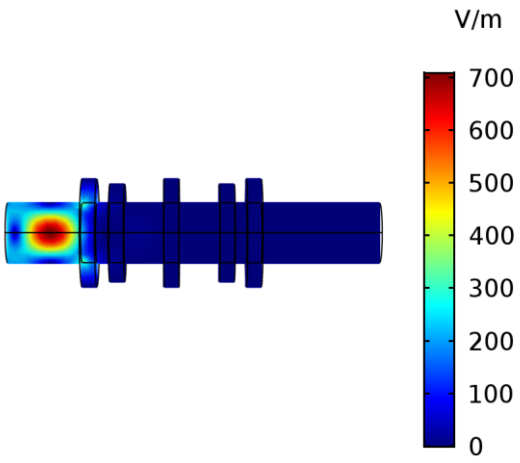


Figure 5.53 Choke electric field at 915MHz for a TM01 excitation.

5.4.11.7 Discussion

Although the technology serves as an effective laboratory testing rig for high power density experiments, material handling issues make it not likely suitable for ore processing at a large scale due to the intrinsic particle size limitations and low effective throughputs. An alternative was suggested based on the use of offset applicators in series with cylindrical multi-mode chokes, which reduces material handling limitations considerably; nonetheless, such concept has not been proved yet. It is believed that this technology is better suited for the treatment of liquids or fine particles.

5.5 Conclusions

The fundamental operation of TM elliptical cavities was described. A design methodology was proposed and validated experimentally. Results showed that such a device could effectively provide elevated power densities and uniform, reliable and repeatable treatment. The identified usage scope is to serve as a suitable replacement to circular cross-section cavities for operation in higher order modes without mode degeneracy. Simulation results for a prototype were validated by cross-platform simulation and experimentally by using

copper ores as test material with good correlation between measurement and simulations, showing a difference of 1 MHz in -10 dB bandwidths, and a quality factor of 198 and 233 for simulation and experimental measurement respectively.

The possible use on a variety of applications and scaling approaches were discussed. The concept is flexible for several applications and can be scalable by means of parallelisation and frequency reduction; however, effective throughputs are considerably limited due to load size limitations. Its use is more promising in continuous flow microwave chemistry applications such as the processing of waste oils and plastics. The characterisation of microwave properties of these materials at expected processing states is critical to develop the technology further and to envisage practical ways for implementation.

Chapter 6 Applicator for granular products

The most common issues that have been reported by researchers as an obstacle to the implementation of high-temperature microwave processing systems are the lack of solutions that can overcome typical poor treatment uniformities, increasing product dielectric properties during processing, the need of robust material transport techniques and structural materials compatible with microwave processing [5], [82]. Techniques for field homogenisation that require moving parts for material handling or stirring fields may not be easily implemented in high-temperature systems and which are appropriate for use in a microwave applicator. These issues are common when processing materials that can become highly microwave-susceptible such as carbonaceous materials, metal powders and iron oxides that can suddenly present extremely low penetration depths and high localised heating rates (Chapter 3).

When dealing with materials in granular presentations between a 1 to 20-millimetre particles sizes, a plausible solution to the treatment uniformity problem is the use of fluidised bed technologies. This could provide a practical way to effectively mix the product without interfering with the microwave heating process and can be robustly operated up to high temperatures (industrial fluidised beds can operate in wide ranges of temperatures of over 1,000 °C [381], [382]) in which the use of mechanical means of mixing with moving parts such as stirrers, turntables, conveyor belts can be unpractical [3], [12], [43]. This also can help to reduce the challenge of dealing with changing dielectric properties, hotspot and arcing occurrence.

The use of microwave heating could also reduce heat transfer limitations in the processing of low thermal conductivity products, a common issue in several fluidised bed applications [84], by providing fast volumetric heating, which could allow for processing of larger particles [205]. Furthermore, this in turn maximises mass transfer as the microwaves elevate the particle temperature and the high velocity gases rapidly move the diffused gas from the particle surface. The combination of heating techniques (i.e. hybrid heating) can open the

scope to a broad range of applications by pre-conditioning the product to a state where microwave heating can be highly efficient, as discussed in Chapter 3.

Microwave fluidised beds have been investigated in the literature with major emphasis in drying applications, especially foodstuffs, due to the excellent mixing provided by the fluidisation in combination with the fast and efficient drying due to microwave heating [383]–[390]. Other applications which have been explored included chemical reactions using metal powders [391], metal ores and concentrates [392], [393] and recently, pyrolysis of biomasses [204], [205], [394].

Most systems described in the above-mentioned literature are multi-mode microwave cavities, mostly modified domestic ovens, with a microwave transparent glass column acting as fluidised bed reactor. Due to the fragility of the used reactor tubes for processes were the apparition of char particles and microwave absorbent by-products than can easily stick to its walls (e.g. pyrolysis), could result in tube overheating and failure [395]. Exemptions are the use of waveguides/ducts [383], [384], [396] and setups in which the fluidised reactor itself acts as microwave cavity [392], [397], [398], which in principle could provide a more robust operation. A summary of the characteristics of the scientific referenced works is shown in Table 6.1.

Table 6.1 Summary of microwave fluidised beds in the scientific literature.

Description	Reactor size		Frequency (GHz)	MW Power (W)	Product load	Temperature	Ref
	Diameter	Height					
Pyrex tube/Domestic oven	100 mm	220 mm	2.45	540	Potato	60 °C	[386]
Pyrex tube/Domestic oven	60 mm	250 mm	2.45	900	55 g soybeans	60 °C	[399]
Pyrex tube/Domestic oven	100 mm	350 mm	2.45	300	90 g apple cubes	70 °C	[388]
Unspecified material	90 mm	600 mm	2.45	500	103 g Soybean	140 °C	[389]

tube/domestic oven		(389 mm)			kernels		
Unspecified glass tube/domestic oven	100 mm	300 mm	2.45	700	200 g carrot slices	60 °C	[390]
Silica tubing	150 mm	N/A	2.45	700	Few grams metal powders	1,000 °C	[391]
Quartz tube/domestic oven	100 mm	150 mm	2.45	450	Palm biomass	237 °C	[394]
Quartz tube/multimode cavity	50 mm	200 mm	2.45	5,000	70 g sycamore biomass	400 ° C	[204], [205]
Circular waveguide cavity of unspecified material.	120 mm	N/A	2.45	2,000	7.5 kg SiC beads	144 °C	[396]

In this chapter, a novel hybrid fluidised bed convection-microwave heating system is proposed, combining a proven flexible and scalable fluidised bed technology with innovative microwave feeding techniques in a way that could allow a practical way to scale-up to industrial production levels in continuous processes based on the operation in 915/896 MHz frequency band.

The proposed concept could provide far superior heat and mass transfer with improved gas-solid reactions due to higher contact surface in comparison with other treatment technologies for granular products such as rotary kilns or shaft furnaces, and alternative fluidising techniques [400] which can result in much faster/intense reactions [401]. Moreover, the fluidisation regime has lower particulate carry-over and relative insensitivity to physical attributes of the particles (i.e. shape, geometry and size) compared with common fluidisation methods [401], [402], with the added improvement given by microwave volumetric heating for the processing of relatively large particles [395]. The low thermal inertia of the microwave

operation makes the stop and start of the process much easier, and the concept could allow for a robust construction that can withstand continuous operation under harsh conditions as the system has no moving parts and is manufactured from stainless steel.

To the author knowledge, the batch prototype system developed in this work is of considerably higher capacity than any published microwave fluidised bed system at the time of writing with over half a kilo per batch, and the expected full size system will have around a 5 kilo loading capacity with continuous material feeding with expected throughputs of over the tonne per hour mark for some applications.

6.1 Potential applications

6.1.1 Fast/flash pyrolysis of waste biomass and coals

Fast pyrolysis occurs for fast heating rates in temperatures ranging from 500 to 550 °C with short exposure times of a few seconds where the primary product yield is the liquid fraction [84]. Fluidised beds are particularly attractive for fast pyrolysis processes due to its high heat transfer between the heated gas and the particles due to the large contact surface [403]. In order to achieve high enough heat transfer for fast pyrolysis, the particle size is usually limited to particles of less than 3 mm, given the low thermal conductivity of biomass [84], [404]. Coals exhibit slightly higher thermal conductivities but are still low with around an order of magnitude less than most rocks [405], [406].

This issue constitutes an opportunity to incorporate the use of microwaves, which may be able to overcome such limitation by providing another path for high heating rates from within the particles in the form of volumetric heating. Moreover, the fast nature of the process (i.e. residence times of a few seconds) could also help to limit the reduction of efficiency due to heat loss from particle to gas.

During microwave pyrolysis, the fast increase of the dielectric properties had hindered most attempts to scale up, as sudden penetration depth issues at high temperatures appear. This usually leads to uneven treatment, localised hotspot and regular occurrence of thermal runaway. Such events, in combination with the use of fragile construction materials, in particular glass reactors and delicate gas distributors which can be easily fouled by pyrolysis by-products, have resulted in common system failure [395] (e.g. microwave coupling to glass walls and eventual breaking). These issues can be reduced considerably due to the fluidisation particle separation and thorough mixing provided by a fluidised bed, improving the treatment homogeneity and reducing the likelihood of thermal runaway due to hotspots. Nonetheless, in microwave fluidised systems the use of glass reactors still poses a significant risk of failure, due to the ease of having products stuck to the walls that can eventually lead to destructive events by overheating, making the materials of construction of the reactor a critical design feature for such applications.

Microwave fluidised bed systems have been employed, using microwaves as the only heat source, for oil production from palm biomass with the aid of char as microwave susceptor [394], and susceptor-less pyrolysis of sycamore biomass [204], [205]. The use of higher power densities is discussed in the latter as able to provide shorter residence times and hence, lower heat losses from the particles and reduced energy consumption. As concluded from the literature review in Chapter 3, the use of susceptor additives in microwave pyrolysis leads to indirect and inefficient heat transfer based processing of the product, this would be accentuated in a fluidised system where the susceptor and product would not be in intimate contact with each other making it unpractical and likely to be un-economic.

6.1.2 Direct reduction of iron ore

The direct reduction of iron ore (DRI) of lump ore or pellets can be carried out in a variety of systems including shaft furnaces, rotary hearth and retorts [407]. In Chapter 3, the

possibilities and advantages of microwave-assisted reduction were reviewed. A fluidised bed would allow processing low-cost fines using gas as a reducing agent, avoiding the need for sintering or pelletising [407], [408]. This process was initially hindered due to the increase in cohesiveness during metallisation (i.e. particle sticking to each other) [409], [410]; however, the use of a combination of hydrogen and carbon monoxide fluidising gas diminished the cohesiveness of the particles due to carbon precipitation in their surface [411]. Current fluidised bed DRI technologies include FINMET®, Circored®, FINEX® and HIsmelt® and their main characteristics are summarised in [408].

The use of microwaves could allow to rapidly reach high metallisation temperatures as the iron exhibit excellent microwave absorption properties, without exposing the reactor to such temperatures. This can result in a reduction of requirements and costs for structural material and ancillary equipment for gas conditioning. Moreover, as seen in Chapter 3, microwaves can provide high metallisation levels at considerably less time than regular means, which combined with the excellent material mixing provided by the fluidised bed reactor could lead to an efficient and fast DRI.

The only works the author found in the literature that discuss the use a fluidised bed microwave system for processing ores are the following patents [392], [393], although not related to the reduction of iron oxides.

6.2 Reactor design

The reactor design has been a joint work with Torftech©, as an evolution of the Torbed Compact Bed Reactor (CBR) technology [412] for integrated hybrid convective and microwave heating. A shallow bed of particles is suspended by jets of the process gas stream that is forced through stationary angled blades at high velocity, which in conjunction with the central cone allows the gas to provide a product toroidal motion as illustrated in Figure 6.1

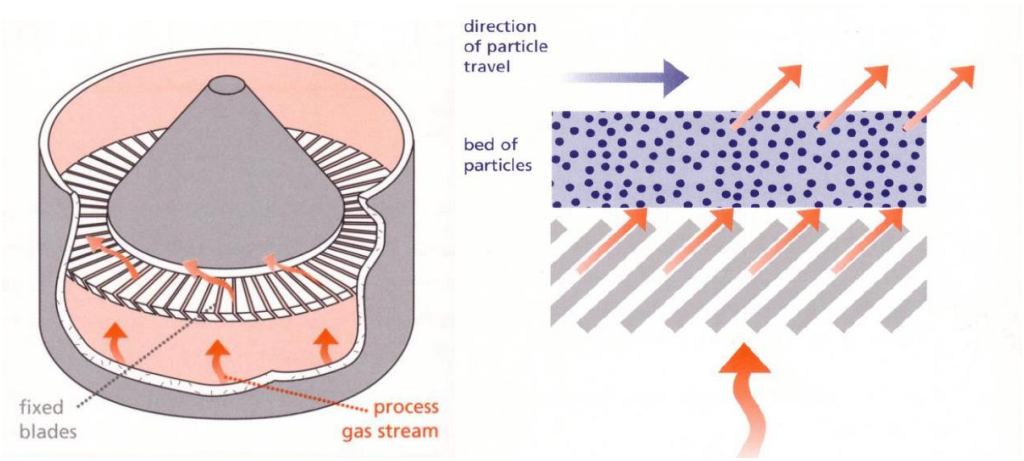


Figure 6.1 Torbed CBR operation principles sketch after [412]**.**

The CBR reactor design can provide an efficient heat transfer, less need to grade feedstock carefully, a simple way for recycling of the process gas stream and flexibility to handle different materials by process gas optimisation [412]. This type of reactor has been used successfully at commercial scales in several industries in both batch and continuous processes, including mineral, metallurgical, chemical and foods [412]. Advantages over conventional fluidised bed reactors include smaller reactor size; improved particle movement and more thorough processing; enhanced heat and mass transfer; low pressure drop in the gas distributor; flexible operation (i.e. for different product shapes and sizes); process intensification due to difference between solid and gas velocities; reduced particle carry over [401], [402], [412].

From a microwave integration perspective, the Torbed CBR provides a relatively dense and stable bed [401] that moves horizontally, making it suitable for a relatively stable microwave coupling. The metallic cavity construction with an internal cone could allow for the setup of resonant modes that could be used effectively for microwave heating a bed near the bottom of the cavity with a relatively uniform power distribution, provided that the bed can be positioned in a suitable area, which can be in principle possible thanks to the Torbed CBR bed position flexibility (gas flow adjustable bed height positioning) [401]. Upon scaling up, the bed can retain a roughly similar transverse shape mostly increasing the toroid major diameter;

therefore, if a suitable scalable microwave feeding strategy is used, the general behaviour could remain similar. Moreover, the thorough and fast mixing of the bed could help minimising the creation of hotspots and thermal runaway.

In conventional fluidised beds based on long columns with vertical flows, achieving a uniform power spread can be challenging, in particular when scaling up as the reactor becomes larger. Currents strategies to achieve this rely in setting some form of transverse uniformity along the column and rely on the vertical mixing of the feedstock as in [204], [205]; however, such strategy is in principle unpractical for large diameter columns, where penetration depth issues can be significant.

The technology developed in this chapter could provide a means to develop a highly scalable system with reduced likelihood of undesired hot-spots and thermal runaway events, good robustness and treatment uniformities, with a broad range of applications for different sized feedstocks.

6.2.1 Reactor geometry

Torbed CBR reactors are characterised by a triangular cross section toroidal bedformed between internal cone and the external wall of the reactor, covering roughly 95% of the blade distributor [401]. Considering the blade sizes used by Torftech, a 1,000 mm reactor should be able to handle around 10 litres of load, given the expected bed shape, whereas for a tenfold product scale-down to 1 litre would require the use of a 400 mm diameter reactor.

The bed density can be considerably high, as for example for regular spherical particles a void fraction of 0.39 can be achieved [413], which come close to what is expected from a poured random packing model for spherical particles [414].

The throughput of the system depends on product bed density and expected residence times, and whether a continuous or batch operation is used. For example, for a 30 second

residence time and a relatively low-density material such as some woody biomass (for this example with a rough estimation of a 0.5 g/cm^3 bed density) the 400 mm could result in a 60 kg/h throughput, whereas the 1,000 mm one could result in a 600 kg/h.

Several design concepts were developed for operation at 2,450 MHz and a prototype was fabricated and tested to validate the design approach and provide proof of concept before the commissioning of a full scale 915 MHz system. As a basis for design, the 2,450 MHz system should be able to handle up to 6 kW of power (15 kW desirable), which is approximately equivalent, power density wise, to a 100 kW system in a 915 MHz system (assuming a volumetric escalation proportional to the wavelength change).

A 400 mm diameter Torbed CBR reactor was chosen as size for the 2,450 MHz, as preliminary simulations showed plausibly usable resonant modes and given its ability to handle a one litre load in batch operation which is significantly higher than current microwave fluidised systems. A schematic of its main parts can be seen in Figure 6.2. The reactor geometry was adjusted to produce a resonant behaviour near the operational frequency with high electric fields in the zone were the product bed is expected to be.

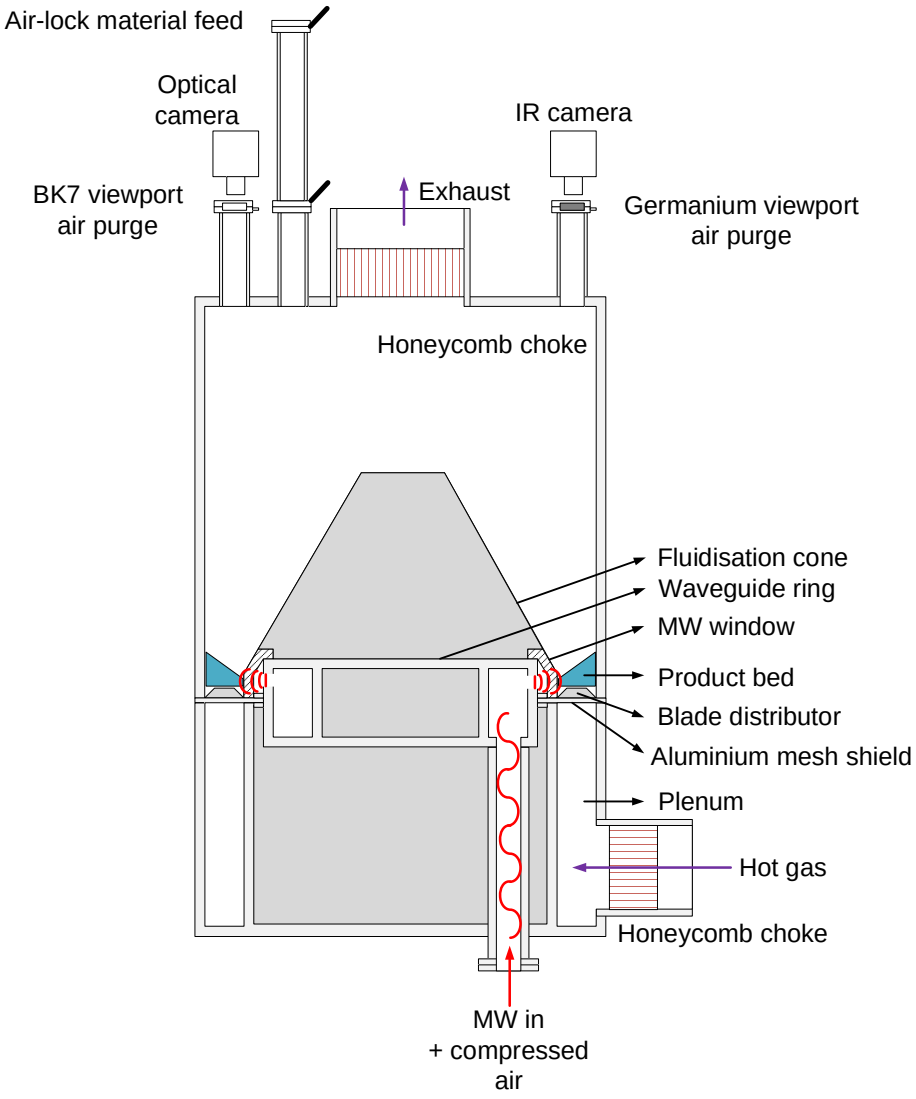


Figure 6.2 Torbed T400 CBR schematic.

The external reactor diameter, product bed shape and position were fixed, and an initial conductive central cone was set in the cavity centre. It was assumed that both blades and exhaust elements behaved as conductive plates for simplicity. The cone was truncated to produce a more compact reactor chamber of 400 mm height. Slight dimensional adjustment of the cone, detailed in the general schematic shown in Figure 6.3, allowed for the set of resonant modes with high electric fields near the blades for an empty cavity. The electric field distribution of such modes,

obtained by eigenfrequency analysis, are shown in Figure 6.4 and Figure 6.5, where the bottom plane of the plot is a middle cut of the expected bed position.

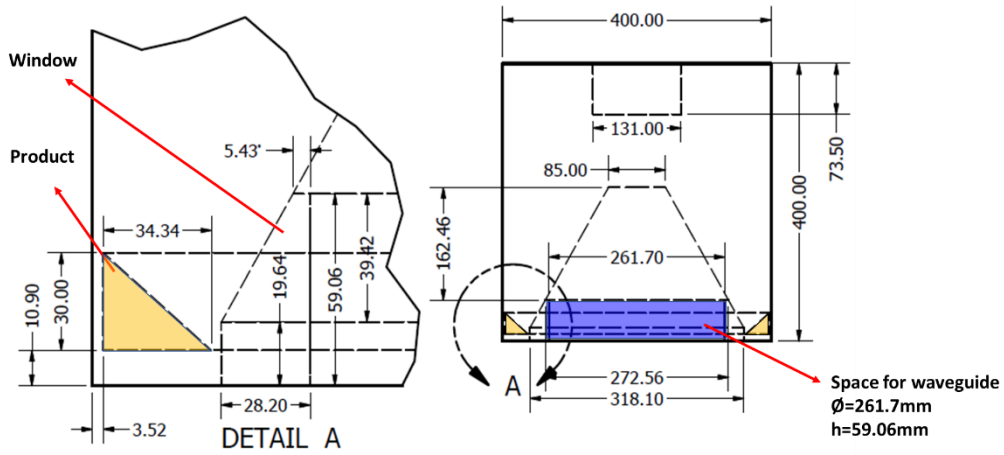


Figure 6.3 Reactor general dimensions and a typical bed geometry.

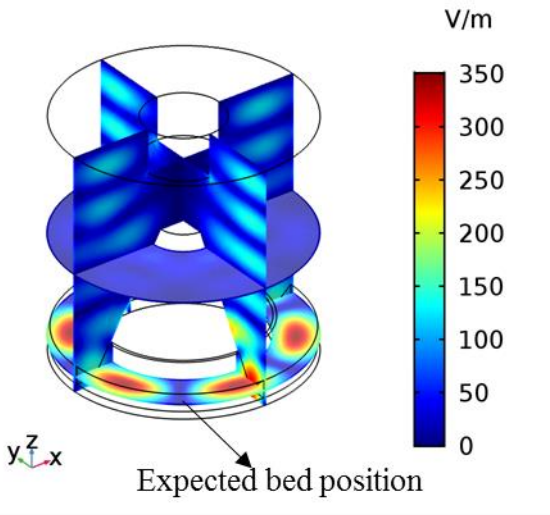


Figure 6.4 Central cut planes electric field distribution resonant mode at 2,449 MHz for empty cavity (only one polarisation shown). XY cut-plane at expected bed position centre (~26 mm from base).

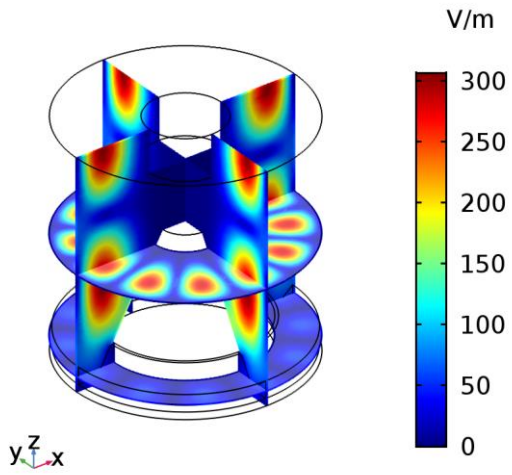
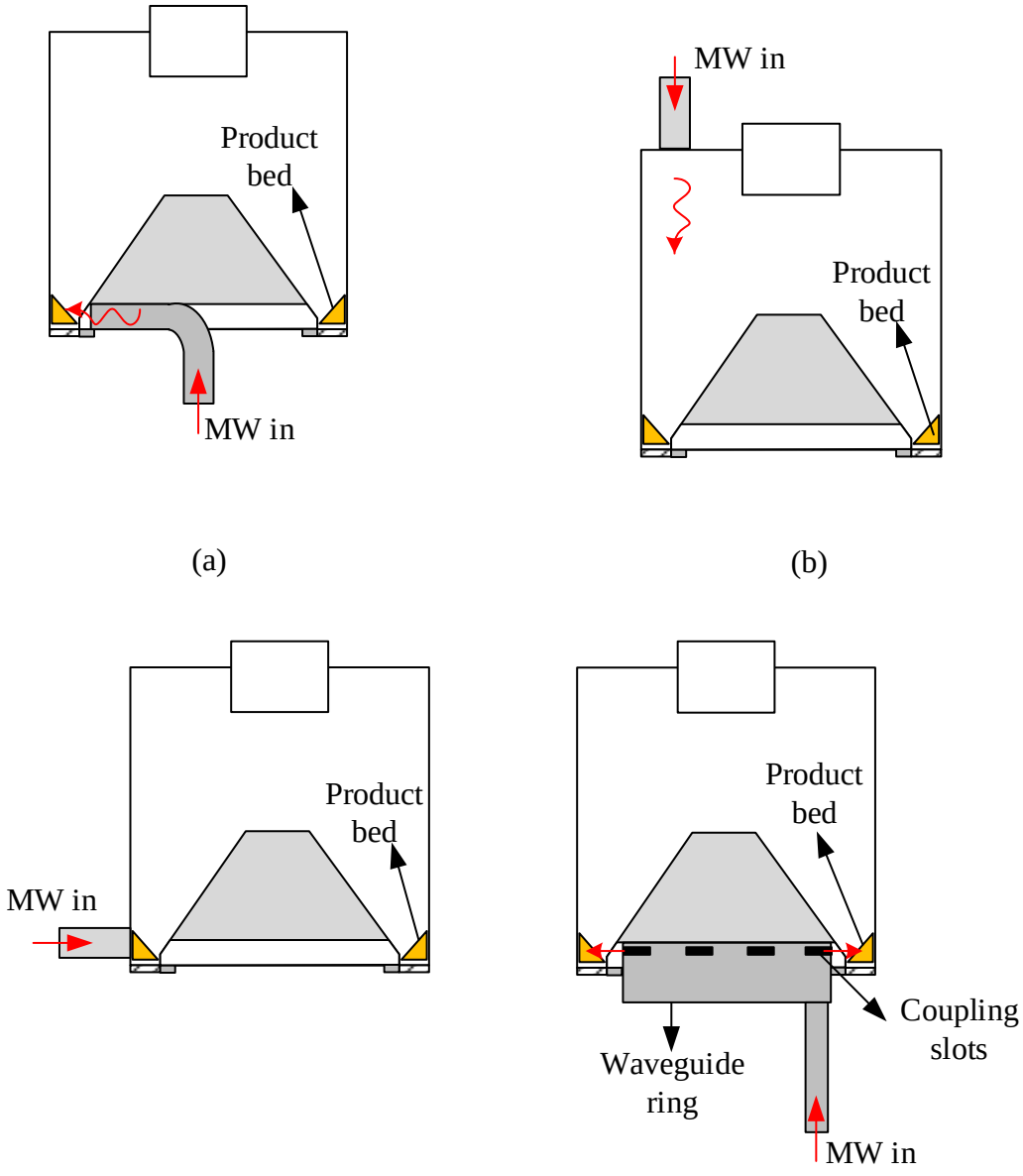


Figure 6.5 Central cut planes electric field distribution for polarisation rotated modes resonant at 2,458 MHz for empty cavity (only one polarisation shown). Additional XY cut-plane at expected bed position centre (~26 mm from base).

6.2.2 Microwave feeding

Several possible microwave feeding arrangements were considered to excite the desired resonant behaviour. First, a waveguide feeding the cavity from the inner cone (Figure 6.6(a)). Second, a waveguide feeding the cavity from its lid (Figure 6.6(b)). Third, a waveguide feeding the cavity from its wall, near the bed (Figure 6.6(c)). Fourth, a broad wall slotted waveguide ring feeding from the internal cone (Figure 6.6(d)). Fifth, a narrow wall slotted waveguide ring feeding from the internal cone ((Figure 6.6(e))). Finally, a slotted waveguide ring feeding from the cavity wall (Figure 6.6(f)).



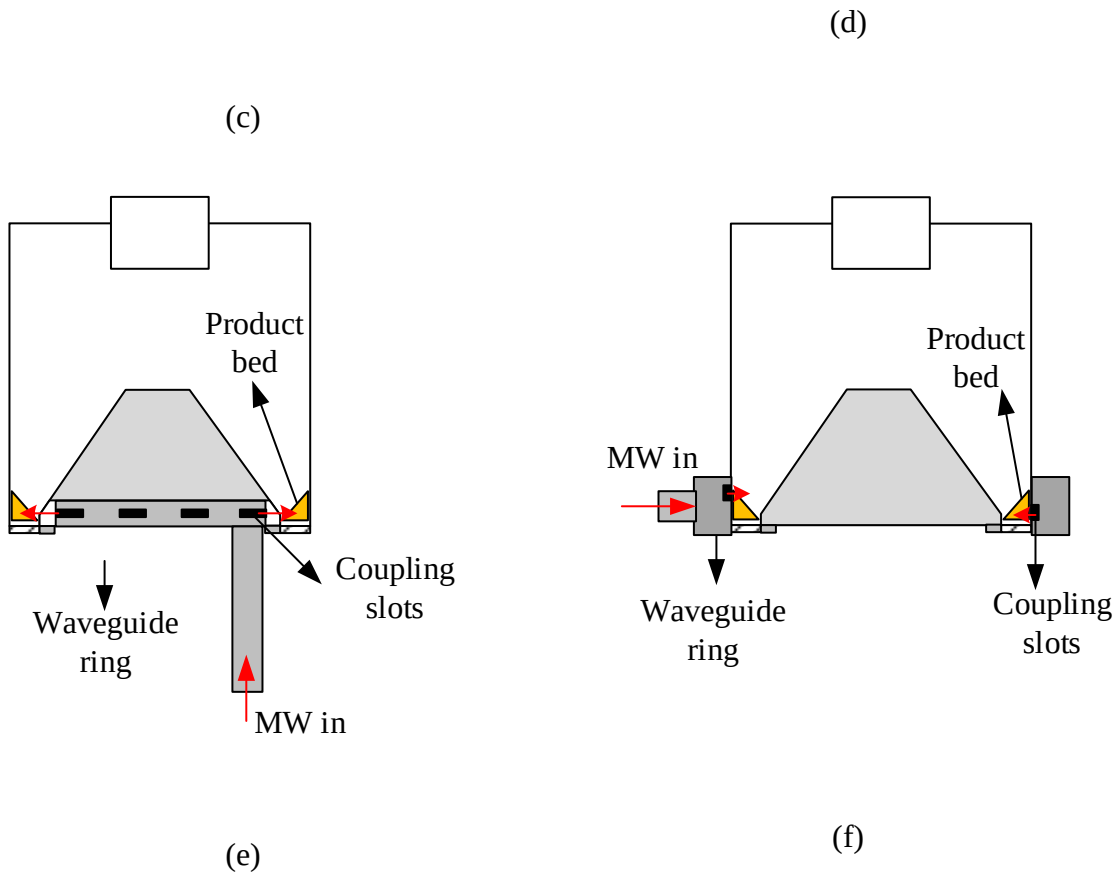


Figure 6.6 Schematic of different feeding arrangement for Torbed T400 CBRMW reactor. (a) Waveguide through central cone, (b) waveguide from lid, (c) waveguide through reactor wall, (d) broad wall slotted waveguide ring through central cone, (e) narrow wall slotted waveguide ring through central cone, (f) slotted waveguide ring through reactor wall.

The reactor bed toroidal motion makes the bed to constantly collision with the external reactor wall while the central cone rarely contacts the product. Therefore, microwave feeding through the external wall was discarded due to the likelihood of wear and contamination of the needed microwave windows for long-term operation ((Figure 6.6(c)) and (Figure 6.6(f))).

Microwave feeding through the central cone was deemed as attractive for its ability to provide a close to the product microwave feeding zone without exposing sensitive parts, as the microwave windows, to mechanical wear and contamination. A mechanism to deliver the energy to the load efficiently and being conformal to the conical structure was needed in order not to disrupt the gas flow and bed fluidisation.

In this work, the investigated possible feeding arrangements are presented, including direct waveguide feeding and two type of slotted waveguide designs. Such concepts are conformal to a conically shaped refractory microwave window (firebrick, modelled as $\varepsilon_r = 3 - j0.001$), which acts as a gas barrier, thermal insulation and contamination protection of the microwave components, and retain the normal fluidised operation of the CBR reactor by not altering the internal geometry.

6.2.3 Open waveguide radiation alternatives

6.2.3.1 Cone feed

A TE_{10} rectangular waveguide with an open end will radiate in the same near-field polarisation as the waveguide. Due to the initial spatial constraints imposed by the reactor size suggested by Torftech, the feeding waveguide is in principle limited to a horizontal alignment in order to the whole waveguide aperture to fit within the reactor limits (i.e. maximum 59 mm of space, whereas a WR340 waveguide internal dimensions are 86.36 mm x 43.18 mm). This configuration allows for the use of a small conical window directly in front of the waveguide. A sketch of this concept is shown in Figure 6.7.

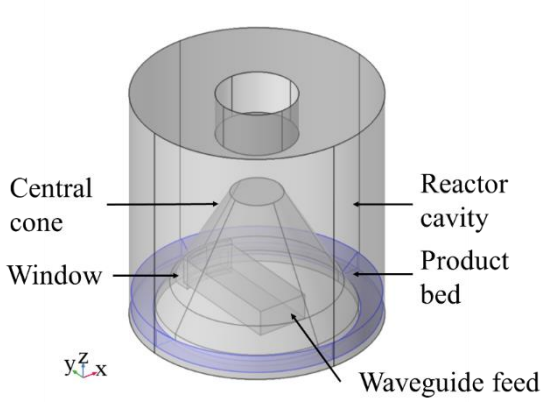
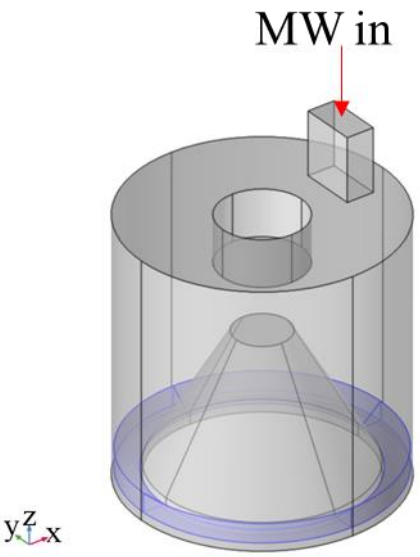


Figure 6.7 Cone waveguide fed reactor sketch.

Such a feeding arrangement should be able to couple magnetically to the cavity providing a mostly vertical polarisation, which should readily excite one of the discussed resonant modes.

6.2.3.2 Lid feed

For feeding with a waveguide from the lid, two polarisations could be used by placing the waveguide oriented in different directions as shown in Figure 6.8 and Figure 6.9. The waveguide could be tapered to improve coupling to the cavity, if needed (e.g. horn feeding).



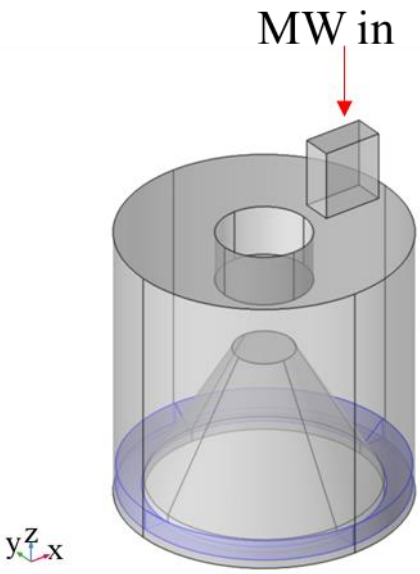


Figure 6.8 Lid waveguide fed reactor sketch 1. **Figure 6.9 Lid waveguide fed reactor sketch 2.**

6.2.4 Waveguide slot radiation

Slotted waveguides are commonly used as antenna arrays [415]–[420]. The slots interrupt the current flow, forcing it to go around it, making them radiate as the equivalent half-wave dipole. Broad wall slot antennas result in a vertically polarised, whereas narrow wall slot in a horizontally polarised field in the far-field region [420]. Slots can also be used to couple the fields from a waveguide to a product or a cavity for material processing in a controlled fashion [3], [12], [19]. Such coupling structure could be used to couple microwaves to the cavity.

To effectively radiate, the slot longer side needs to be aligned perpendicularly to the current polarization to interrupt its flow effectively. The surface currents on a rectangular

waveguide operating in TE_{10} are shown in Figure 6.10 for the broad wall and Figure 6.11 for the narrow wall. An overlay of possible positions for radiating and non-radiating slots are shown to illustrate their interaction with the surface current. In the travelling wave regime, the current maximum moves with the wave, whereas in a standing wave regime the maximums become fixed and spaced from each other by $\lambda_g/2$. The surface current and respective electric field for two slots on the broad-side of a TE_{10} are shown in Figure 6.12, showing how a slot in the middle of the broad-side does not radiate significantly, whereas an off-centred slot does.

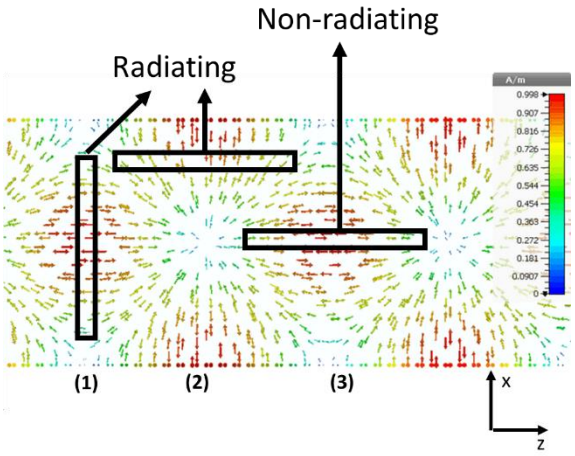


Figure 6.10 TE_{10} rectangular waveguide surface current on its broad-side. Overlay of possible positions for radiating and non-radiating slots.

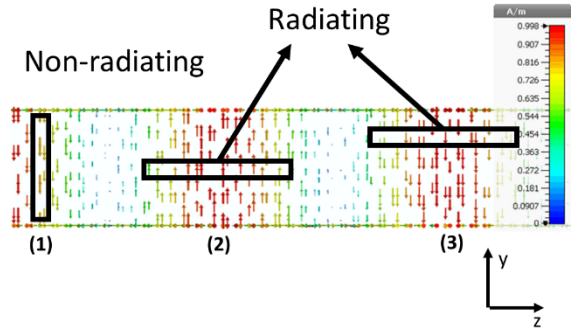


Figure 6.11 TE_{10} rectangular waveguide surface current on its narrow-side. Overlay of possible positions for radiating and non-radiating slots.

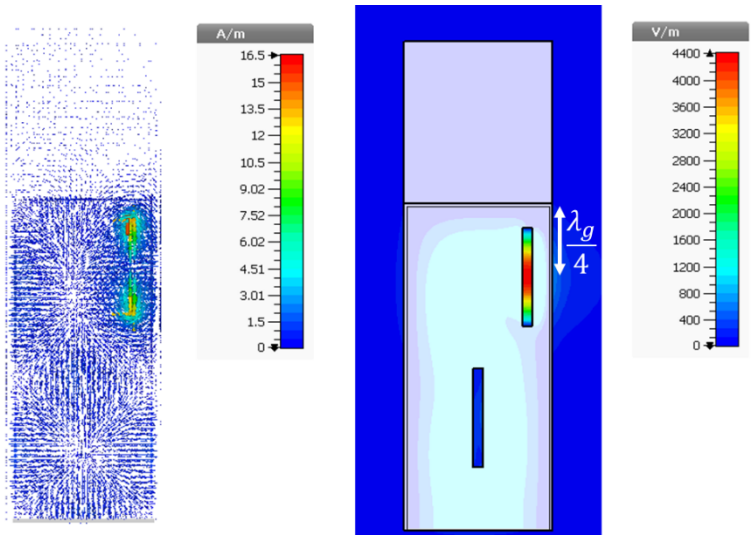


Figure 6.12 TE_{10} rectangular waveguide surface current and electric field distribution on its broad-side with two slots, one in the middle and one shifted to one side.

The slot resonant length that behave as complementary of a half-way dipole is around $\lambda_0/2$, which in practice considering a finite slot width of around $0.035\lambda_0$ is typically $L_c \approx 0.4625\lambda_0$ [419], [421].

As discussed above, only limited space was available to feed the microwaves through the central cone, with a maximum of 261.7 mm diameter and 50.9 mm height. Therefore, two options were considered that could be conveniently fitted within such limitations: narrow wall radiating slots with arbitrary vertical positioning (ring height of 43.13 mm), and broad wall radiating slots located in the upper region of the ring (ring height of 86.36 mm). These arrangements are sketched in Figure 6.6(d) and (e).

6.2.4.1 Slot power handling and slot width

The average power handling limits are commonly associated to heating effects, while peak powers limits operation due to possible arcing. A single slot maximum power due to arcing limits can be obtained modifying the expression given in [416] as

$$P_{max}[W] = \frac{4R_d E_{arc}^2 w^2}{Z_0^2} \tag{7}$$

Where P_{max} is the maximum power handling by a slot, $R_d = 73.2\,\Omega$ is the complementary resonant dipole radiation resistance, considering half free space wavelength

slots, $E_{arc} = 30{,}000$ V/cm is the air dielectric strength, w is the slot width in cm, and $Z_0 = 120\pi\ \Omega$ is the open space impedance. The maximum slot power handling versus slot width at room temperature is plotted in Figure 6.13.

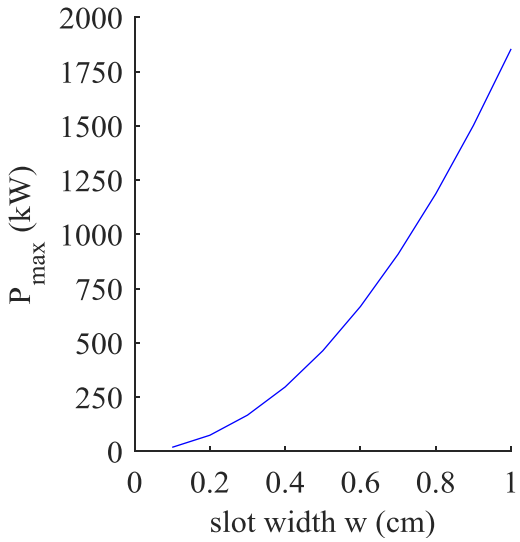


Figure 6.13 Maximum slot power handling according to slot width at room temperature air.

As mentioned in section 2.14.2, Paschen's law dictates that gases dielectric strength decay with temperature rise and care should be taken in considering expected gas temperatures and pressure to estimate arc-free operation. Generally, the power handling is approximately proportional to the square of the air density ($\sim 1/T$ at constant pressure). The use of pressurised solutions and gas barriers should be considered in extreme operation cases.

To approximate the power handling at different gas densities the following relation is introduced (under the assumption of a constant pressure)

$$E_{arc-1} = \frac{\rho_1 E_{arc-0}}{\rho_0} = \frac{(1/T_1)E_{arc-0}}{(1/T_0)} = \frac{T_0 E_{arc-0}}{T_1} \qquad (8)$$

Such dependency to temperature has been confirmed by Uhm et al. studies in cylindrical electrodes [422]. The effect of temperature on the maximum power handling of a slot is illustrated in Figure 6.14

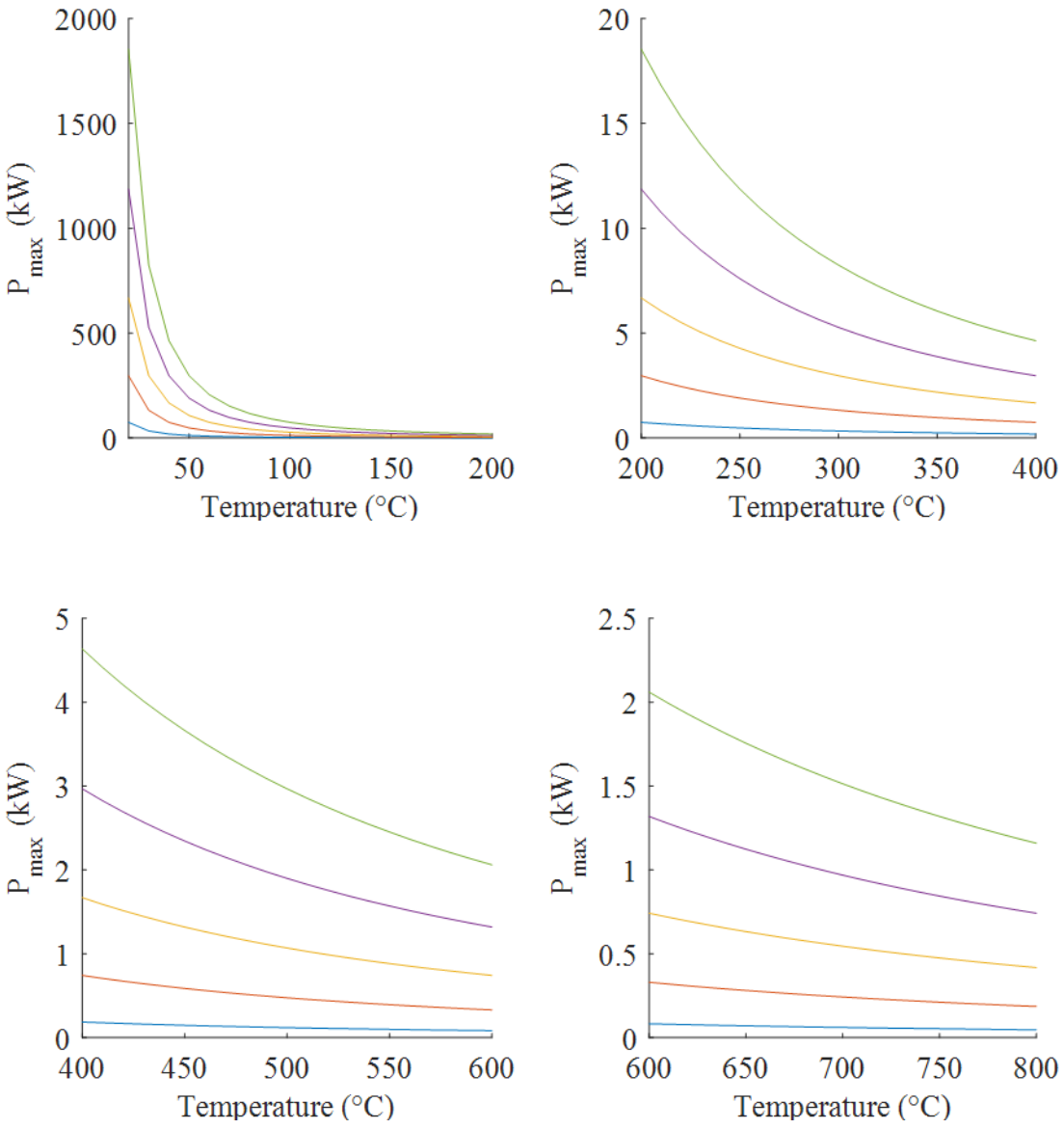


Figure 6.14 Maximum slot peak power handling versus air temperature for various slot widths. 2 mm (blue line), 4 mm (red line), 6 mm (yellow line), 8 mm (purple line), and 10 mm (green line).

Evidently, the gas temperature around the slots is critical in its power handling ability. This makes reasonable to pursue the use of some form of insulation from hot gases inside the reactor. It is evident that the use of wider slots leads to better power handling. The slot width should be selected to be able to handle the power stated in the basis of design as desirable. For the initial planned prototype, gas temperature is not expected to exceed 250 °C. A safety margin of 2 times the power was selected. Therefore, for a six-slot setup, each slot should be able to handle 2.5 kW, which for the safety margin would be 5 kW, which following the charts result

in a 6 mm slot. This width was selected as a design start; however, is likely that the slot waveguide system will have a larger number of slots, in principle varying this threshold estimations.

The frequency bandwidth can be increased by reducing waveguide wall thickness and increasing slot width, reducing waveguide cross-section size and by putting the slots the furthest possible from the centre line in case of broad wall slots [423].

6.2.4.2 Narrow wall feed design

For the narrow-wall design, an E tee splitter feeding the ring result in a virtual short circuit in the opposite end (i.e. an electric field minimum). As the splitter arms are in counterphase, as illustrated in Figure 6.15, the waves of each arm have the same amplitude and travel the same electrical length and therefore add destructively in the end (as they meet at counter phase), virtually behaving as a short circuit. The splitter needs to be slightly tapered to fit due to the ring curvature reducing the broad side size upon connecting to the ring.

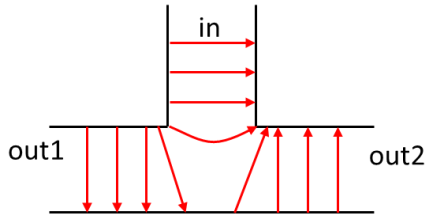


Figure 6.15 E tee splitter electric field behaviour, arm outputs in opposite phase.

Given the virtual short circuit at one end, the next maximum electric field will appear at a quarter of the guided wavelength. As the waveguide is bent in a ring shape, this distance would need to be measured at the internal circumference (average between inner and outer wall diameter). Given the space limitation in the cone and waveguide wall thicknesses of 2 mm, a 260 mm outer ring diameter was used. This resulted in an internal circumference of radius 86.82 mm. As the guided wavelength is 173.62 mm (TE_{10} mode on a WR340 waveguide), the quarter wavelength being the arc length that represents the distance between the virtual short and the

first slot will be $\lambda_g/4 = 43.4$ mm, equivalent to an angular separation of $\theta = (\lambda_g/4)/R_{in}[rad] \approx 29°$ at the centre of the waveguide ring.

This was confirmed by simulating the waveguide ring, shown in Figure 6.16, which also shows that the maximum positioning appears at 29° from the virtual short and at $2 \times 29° = 58°$ from each other, equivalent to a half guided-wavelength distance on a straight short-circuited waveguide.

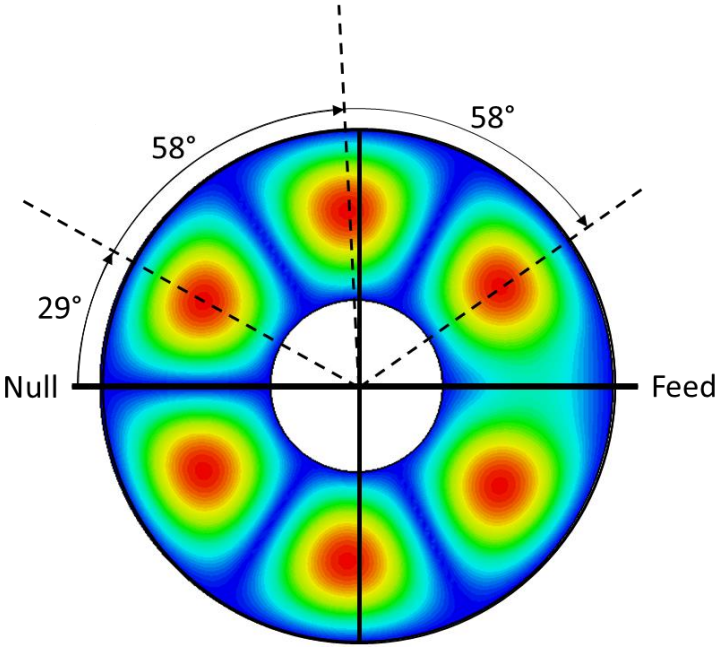


Figure 6.16 Electric field distribution within the waveguide ring designed for narrow wall slot feeding.

The resonant slot length is $L_c \approx 0.4625\lambda_0 = 56.63$ mm for a typically used slot width for antenna arrays of $0.035\lambda_0 \approx 6$ mm, which coincides with the estimated slot width able to handle the desired power [419], [421], [424].

As the vertical current distribution in the narrow wall is uniform, the coupling is unaffected by the vertical location of the slot in relation to the waveguide. However, the slot position does affect the coupling behaviour with respect to the cavity. The vertical location of the slot was fixed at the ring centre, and the whole ring position was swept parametrically to assess the best location regarding power coupling for a product load in the middle of the

working parameter range ($\varepsilon_r = 4.5 - j0.5$), resulting in a slot positioned immediately below the load (around 1 mm from the bed bottom).

6.2.4.3 Broad wall slot design

For the broad wall design, an H tee splitter was used, in which case the output arms of the splitter are in phase (Figure 6.17), creating an electric field maximum in the opposite to the splitter as the waves meets in phase and add constructively. In this case, the narrow size needs to be tapered to fit due to the tight curvature of the ring.

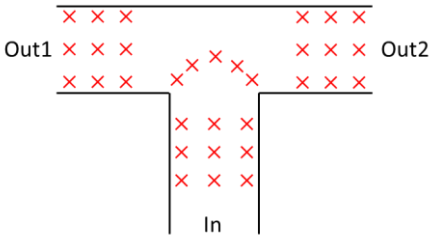


Figure 6.17 H tee splitter electric field behaviour, arm outputs in phase.

Given the next maximum at the opposite end of the feed, the subsequent maximums are separated by half guided wavelength. As the waveguide is bent in a ring shape, this distance would need to be measured at the internal circumference of radius 108.41 mm (average between inner and outer wall diameter). As the guided wavelength is 173.62 mm, the quarter wavelength being the arc length that represents the distance between the virtual short and the first slot will be $R\theta = \lambda_g/4 \rightarrow \theta \approx 23°$

This is confirmed by simulating the waveguide ring, shown in Figure 6.16, confirming the maximum positioning spaced at $2\theta = 46°$ from each other, equivalent to a half guided-wavelength distance on a straight short-circuited waveguide. An eight maximum is located at the feeding point, as a superposition of two slightly displaced maximums coming from each arm.

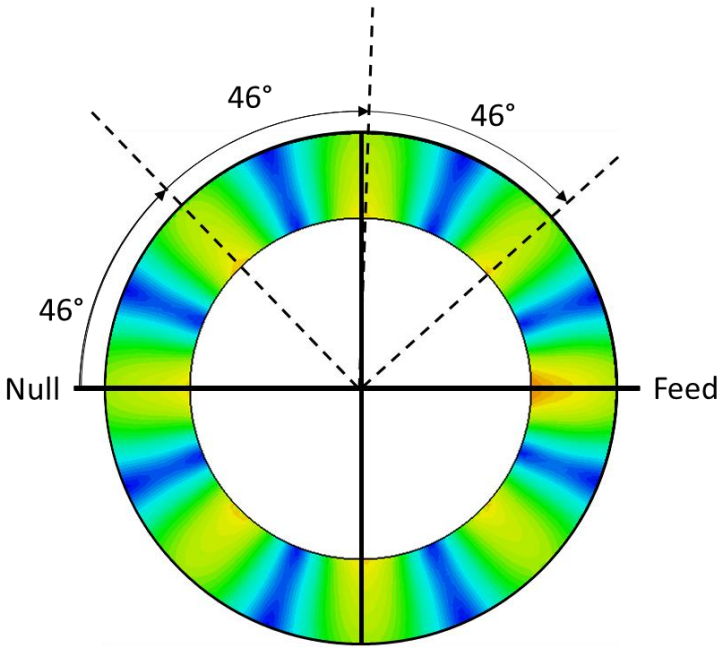


Figure 6.18 Electric field distribution within the waveguide ring designed for broad wall slot feeding.

As the vertical current distribution in the broad wall is non-uniform, the coupling is dependent on the vertical location of the slot in relation to the waveguide. The further from the centre, the larger the coupling. In antenna arrays, subsequent slots are generally interleaved in opposite positions in reference to the centre-line to minimise the horizontally polarised component in the far-field [420], this, however, is not a requirement for heating purposes. The vertical location of the slot, in the upper end of the waveguide due to space limitations, and the ring position in respect to the reactor were swept parametrically to locate the best setting regarding power coupling for a product load in the middle of the working parameter range ($\varepsilon_r = 4.5 - j0.5$), resulting in slots positioned in front of the upper part of the load (2 mm from the bed top).

6.3 Microwave fluidised bed concepts simulation results

6.3.1 Waveguide fed

Feeding the cavity using a waveguide from the lid (in either polarisation) and from the inner cone prove to be a bad strategy for treatment of low loss materials, such as for example Vermiculite (i.e. $\varepsilon_r = 1.5 - j0.05$). These configurations showed conversion efficiencies ranging from only 20% in the worst case up to 65% in the best case. Such levels of conversion

efficiency were deemed to be unpractical. To illustrate this, results for the configuration with a waveguide feeding through the central cone are shown in this section.

First, the reflection coefficient magnitude with a bed with a dielectric constant of 1.5, 4.5 and 7.5 for loss factors ranging 0.05 to 4.5 are shown in Figure 6.19, Figure 6.20 and Figure 6.21. This complex permittivity values were chosen to analyse the behaviour for a variety of bed types that might be used in this system, covering a range from relatively low loss such as biomass at low temperatures to relatively high loss such as hot carbonaceous materials like carbonising biomass, coals or iron ores.

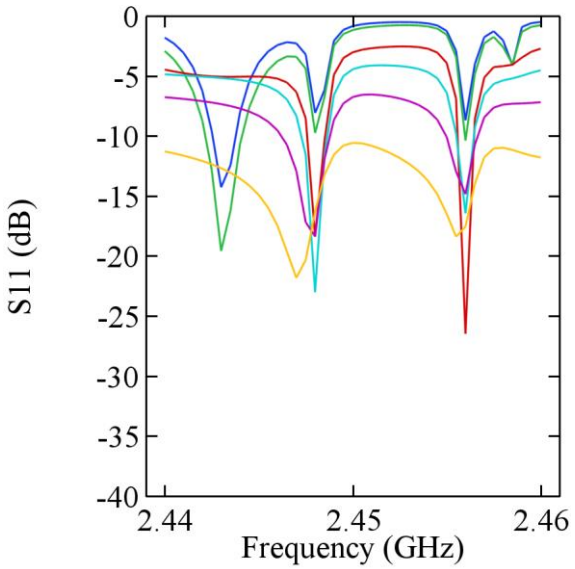


Figure 6.19 Reflection coefficient magnitude of a waveguide fed reactor with a product bed with a dielectric constant of 1.5 and loss factor of 0.05 (blue line), 0.1 (green line), 0.5 (red line), 1 (cyan line), 2 (purple line) and 4.5 (yellow line).

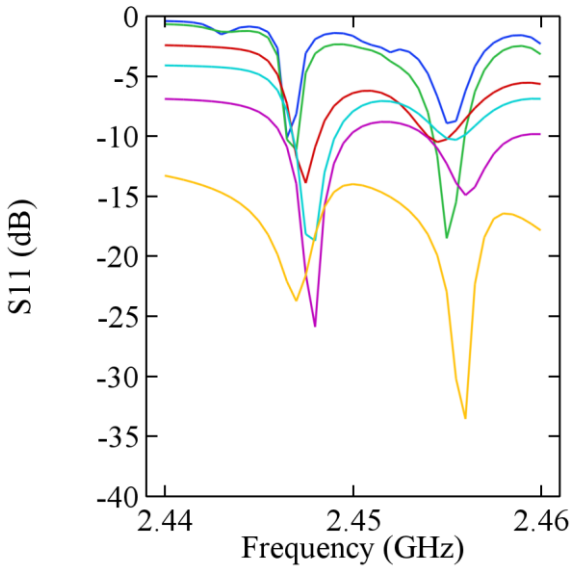


Figure 6.20 Reflection coefficient magnitude of a waveguide fed reactor with a product bed with a dielectric constant of 4.5 and loss factor of 0.05 (blue line), 0.1 (green line), 0.5 (red line), 1 (cyan line), 2 (purple line) and 4.5 (yellow line).

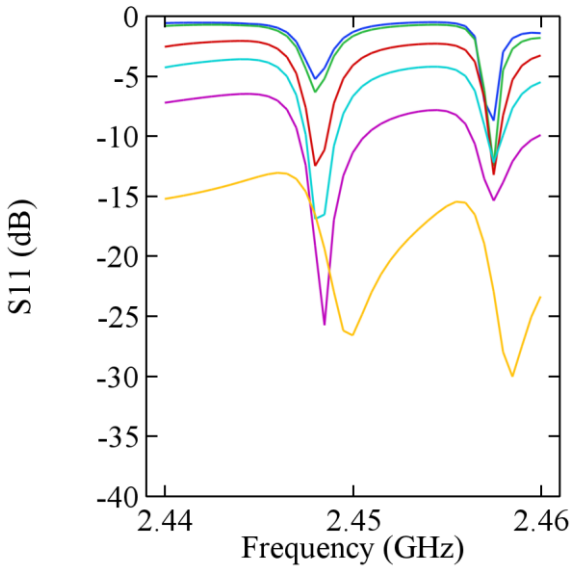


Figure 6.21 Reflection coefficient magnitude of a waveguide fed reactor with a product bed with a dielectric constant of 7.5 and loss factor of 0.05 (blue line), 0.1 (green line), 0.5 (red line), 1 (cyan line), 2 (purple line) and 4.5 (yellow line).

Evidently, the feeding approach is able to excite a resonant behaviour, as two distinct resonances can be observed close to the central operating frequency of 2.45 GHz for all cases. An obvious broadening of the resonances as well as general decrease of the reflection coefficient in the whole band follows the increase of the loss factor. It can be seen that the behaviour is fairly stable regardless of the change of dielectric constant, an attractive characteristic from a processing perspective.

For gaining deeper insight on the behaviour of the sysem under operational conditions, two tuned cases were examined. For $\varepsilon_r = 1.5 - j0.05$ representing low loss materials such as

crude vermiculite or dry biomass. And $\varepsilon_r = 4.26 - j1.48$, representing higher loss carbonacius materials at carbonisation temperatures, in this particular example, Anthracite coal (appendix D). The tuning was performed by a capacitive iris positioned in the feeding waveguide line, to represent a similar behaviour as expected during opertion in tuned conditions, and an input microwave power of 6 kW was used for simulations.

The low loss case reflection coefficient magnitude is shown in Figure 6.22, exhibiting a relatively large quality factor of 4,140, with a very sharp resonance. Such a significant quality factor imply the need for low ripple microwave generators and fast automatic tuning and frequency tracking techniques to maintain resonance during processing [12], [425]. This also results in a low power conversion efficiency, in part due to the stainless steel construction, at only 43.1 %, with around 56.1 % being dissipated in the walls and around 0.8 % in the refractory window. As initially discussed, this was considered an excesive waste of energy for heating applications; thus, such system was deemed as not likely to be practical for low loss materials.

Furthermore, the electric field and power loss density distributions shown in Figure 6.23 and Figure 6.24 reveal a clear preferential heating zone right in front of the waveguide aperture, with a secondary heating zone in the opposite side with less than half the power loss density maximum level. An average power loss density of 4.3×10^6 W/m^3 is dissipated within the load with a PUI of 0.80. This behaviour might not be desirable in some applications, especially for operation at elevated powers where it may lead to overheating and thermal runaway events, as most of the power dissipation in concentrated in a small volume. This also results in an increased likelihood of arcing in the vicinity of this area.

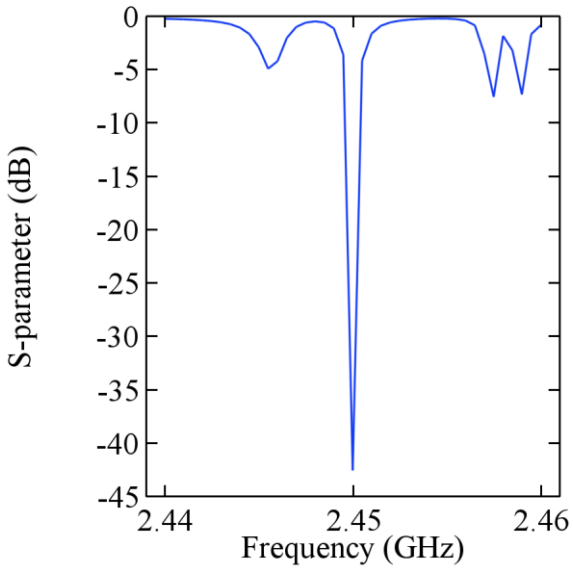


Figure 6.22 Reflection coefficient magnitude of a waveguide fed reactor with a product bed with a dielectric constant of 1.5 and loss factor of 0.05, tuned for 2.45 GHz.

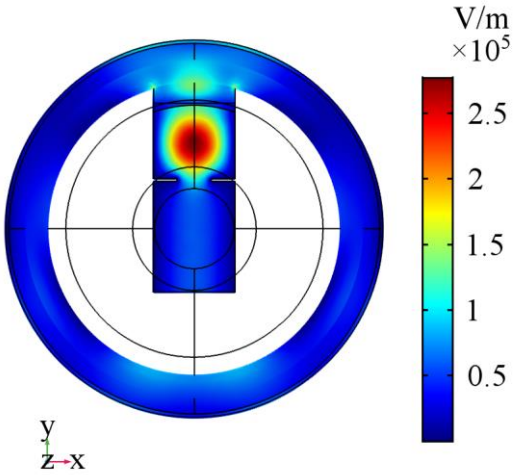


Figure 6.23 Electric field distribution of a waveguide fed reactor with a product bed with a dielectric constant of 1.5 and loss factor of 0.05, tuned for 2.45 GHz. XY cut-plane at bed centre.

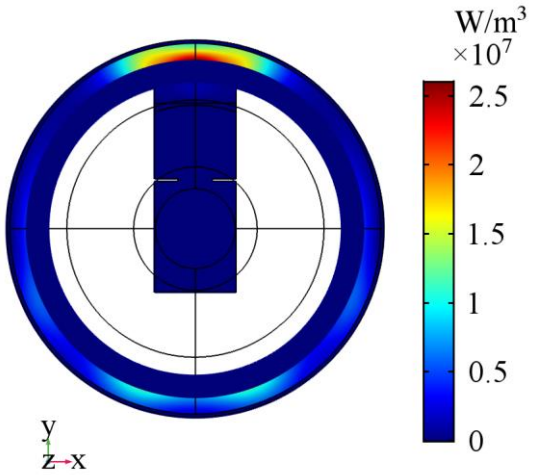


Figure 6.24 Power loss density distribution of a waveguide fed reactor with a product bed with a dielectric constant of 1.5 and loss factor of 0.05, tuned for 2.45 GHz. XY cut-plane at bed centre.

The high loss case reflection coefficient magnitude is shown in Figure 6.25 (green line), exhibiting a quality factor of 356. This would allow operation without the need of a low ripple generator [12], [425]. Moreover, keeping the same tuning conditions, two other material

properties were tested representing a possible broad temperature range of operation between 600 and 1000 °C (blue and red lines), maintaining over 70% of power coupling in the whole generator range without retuning (over 90% around the central frequency). A power conversion efficiency of 95.0% is obtained, with around 4.8% being dissipated in the walls and around 0.2% in the window. The electric field and power loss density distributions are shown in Figure 6.26 and Figure 6.27, showing an even more concentrated preferential heating zone in front of the waveguide aperture. An average power loss density of 9.5×10^6 W/m^3 is dissipated within the load with a PUI of 0.98.

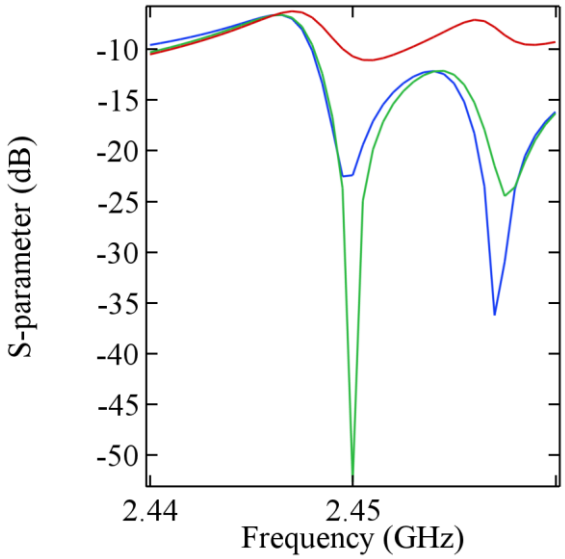


Figure 6.25 Reflection coefficient magnitude of a waveguide fed reactor with a product bed with a complex permittivity of 3.96-j1.23 (blue line), 4.26-j1.48 (green line), and 5.78-j4.99 (red line), tuned for a 4.26-j1.48 load at 2.45 GHz.

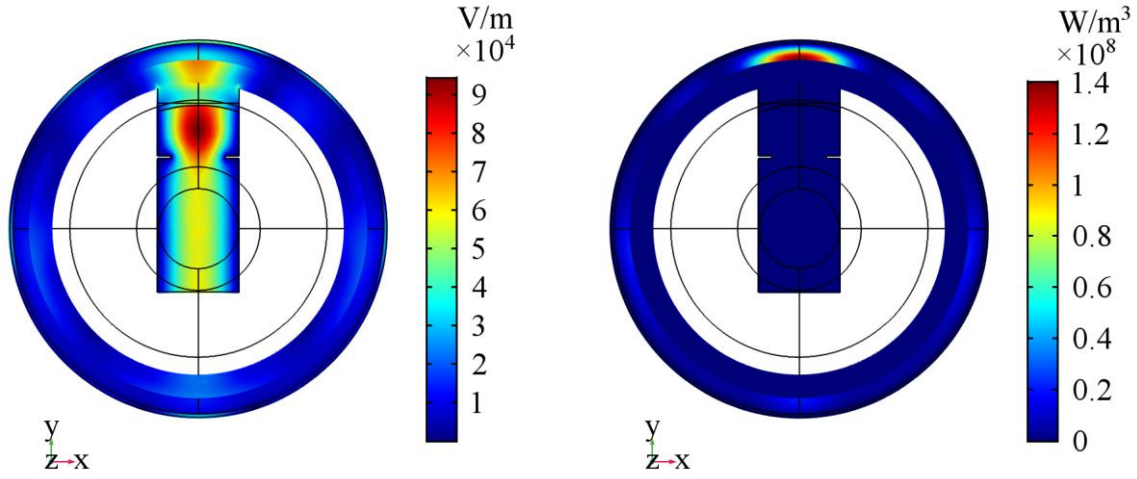


Figure 6.26 Electric field distribution of a waveguide fed reactor with a product bed with a dielectric constant of 4.26 and a loss factor of 1.48, tuned for 2.45 GHz. XY cut-plane at bed centre.

Figure 6.27 Power loss density distribution of a waveguide fed reactor with a product bed with a dielectric constant of 4.26 and a loss factor of 1.48, tuned for 2.45 GHz. XY cut-plane at bed centre.

6.3.2 Narrow wall slot fed

The reflection coefficient magnitude with a bed with a dielectric constant of 1.5, 4.5 and 7.5 for loss factors ranging 0.05 to 4.5 (same range for comparison) are shown in Figure 6.28, Figure 6.29 and Figure 6.30, for the narrow wall slot fed reactor. No distinct resonances can be observed due to the detuning effect introduced by the E tee splitter, as E and H tee splitters require tuning elements to behave as symmetric power splitters [426], [427].

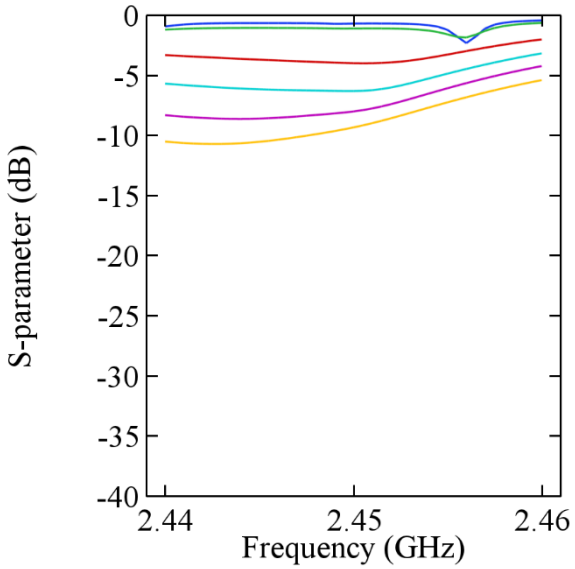


Figure 6.28 Reflection coefficient magnitude of a narrow wall slot fed reactor with a product bed with a dielectric constant of 1.5 and loss factor of 0.05 (blue line), 0.1 (green line), 0.5 (red line), 1 (cyan line), 2 (purple line) and 4.5 (yellow line).

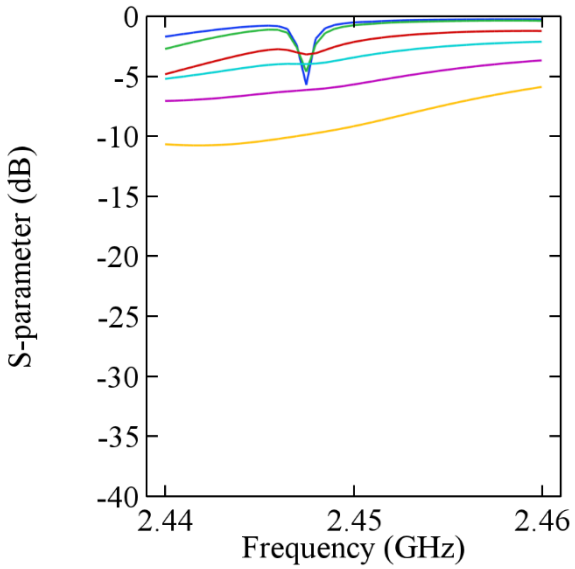


Figure 6.29 Reflection coefficient magnitude of a narrow wall slot fed reactor with a product bed with a dielectric constant of 4.5 and loss factor of 0.05 (blue line), 0.1 (green line), 0.5 (red line), 1 (cyan line), 2 (purple line) and 4.5 (yellow line).

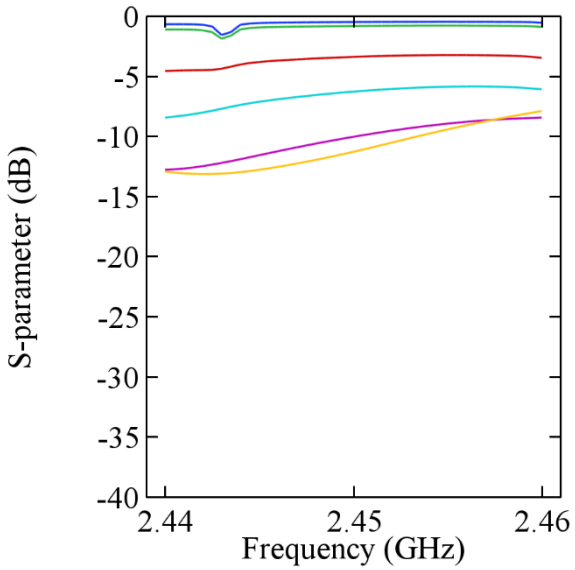


Figure 6.30 Reflection coefficient magnitude of a narrow wall slot fed reactor with a product bed with a dielectric constant of 7.5 and loss factor of 0.05 (blue line), 0.1 (green line), 0.5 (red line), 1 (cyan line), 2 (purple line) and 4.5 (yellow line).

Two tuned cases were investigated with the same type of capacitive tuning iris and 6 kW input power.

For the low loss case, the reflection coefficient magnitude is shown in Figure 6.22, showing a much lower quality factor of 1,672 compared to the waveguide fed case with a significantly broader resonance. Nonetheless, a relatively low ripple microwave generator and automatic tuning techniques are likely needed to maintain resonance during processing [12], [425]. A power conversion efficiency of 71.1 % is observed, with around 14.8 % being

dissipated in the walls and around 14.2 % in the window (much bigger window compared to the waveguide fed case). The electric field and power loss density distributions are shown in Figure 6.23 and Figure 6.24 with various heating zone distributed along the product bed. An average power loss density of 7.0×10^6 W/m^3 is dissipated within the load with a PUI of 0.62. The power is evidently spread more evenly across the treatment zone.

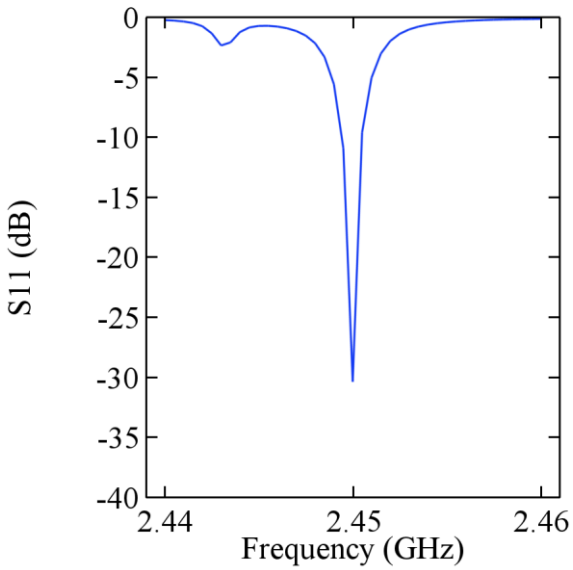


Figure 6.31 Reflection coefficient magnitude of a narrow wall slot fed reactor with a product bed with a dielectric constant of 1.5 and loss factor of 0.05, tuned for 2.45 GHz.

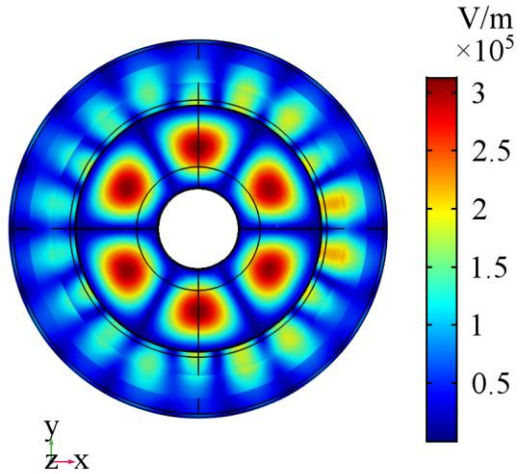


Figure 6.32 Electric field distribution of a narrow wall slot fed reactor with a product bed with a dielectric constant of 1.5 and loss

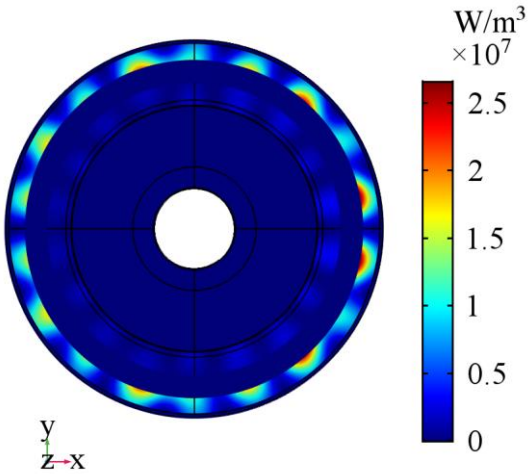


Figure 6.33 Power loss density distribution of a narrow wall slot fed reactor with a product bed with a dielectric constant of 1.5 and loss

factor of 0.05, tuned for 2.45 GHz. XY cut-plane at bed centre.

factor of 0.05, tuned for 2.45 GHz. XY cut-plane at bed centre.

For the high loss case, the reflection coefficient magnitude is shown in Figure 6.34 (green line), with a quality factor of 111. This would allow operation without the need of a low ripple generator [12], [425]. As in the waveguide fed case, two other material properties were tested representing a possible broad temperature range of operation between 600 and 1000 °C (blue and red lines), maintaining over 90 % of power coupling in the whole range without retuning, even covering the whole generator bandwidth ($\pm$10 MHz). This implies that it can likely work stable on the whole temperature range with a single pre-tuning step (i.e. cold tuning). A power conversion efficiency of 98.5 % is obtained, with around 1.0% being dissipated in the walls and around 0.5 % in the window. The electric field and power loss density distributions are shown in Figure 6.26 and Figure 6.27, showing a similar distribution as the low loss case with the same PUI of 0.62 and an average power loss density of 9.9×10^6 W/m^3 is dissipated within the load.

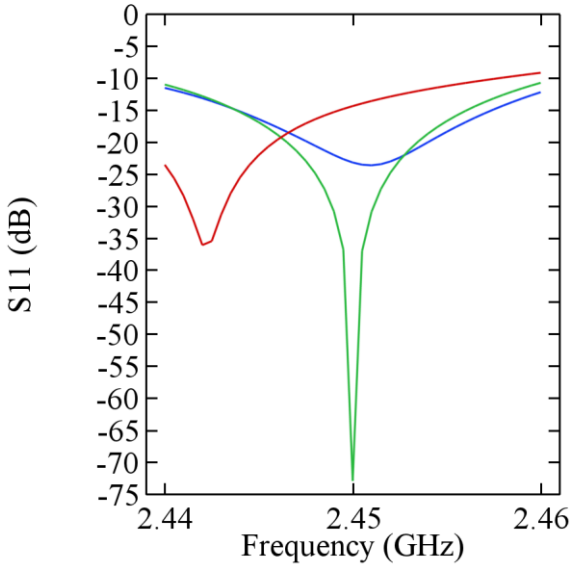


Figure 6.34 Reflection coefficient magnitude of a narrow wall slot fed reactor with a product bed with a complex permittivity of 3.96-j1.23 (blue line), 4.26-j1.48 (green line), and 5.78-j4.99 (red line), tuned for a 4.26-j1.48 load at 2.45 GHz.

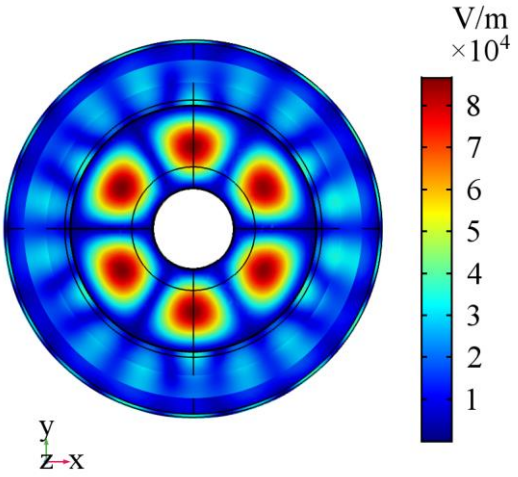


Figure 6.35 Electric field distribution of a narrow wall slot fed reactor with a product bed with a dielectric constant of 4.26 and loss factor of 1.48, tuned for 2.45 GHz. XY cut-plane at bed centre.

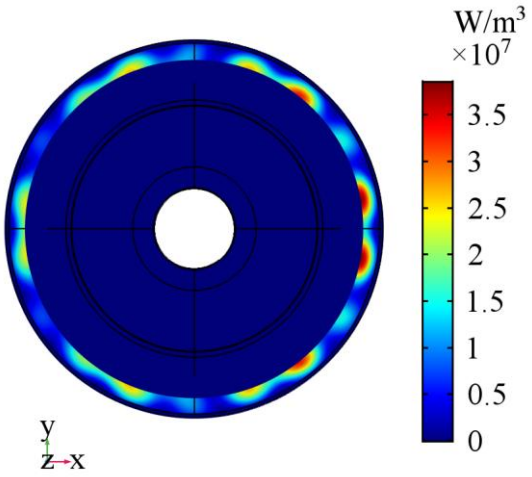


Figure 6.36 Power loss density distribution of a narrow wall slot fed reactor with a product bed with a dielectric constant of 4.26 and loss factor of 1.48, tuned for 2.45 GHz. XY cut-plane at bed centre.

6.3.3 Broad wall slot fed

As in the previous cases, the reflection coefficient magnitude with a bed with a dielectric constant of 1.5, 4.5 and 7.5 for loss factors ranging 0.05 to 4.5 was simulated, with the results shown in Figure 6.37, Figure 6.38 and Figure 6.39, for the broad wall slot fed reactor. No dominant resonant behaviour can be readily observed in the simulated band near the operation frequency.

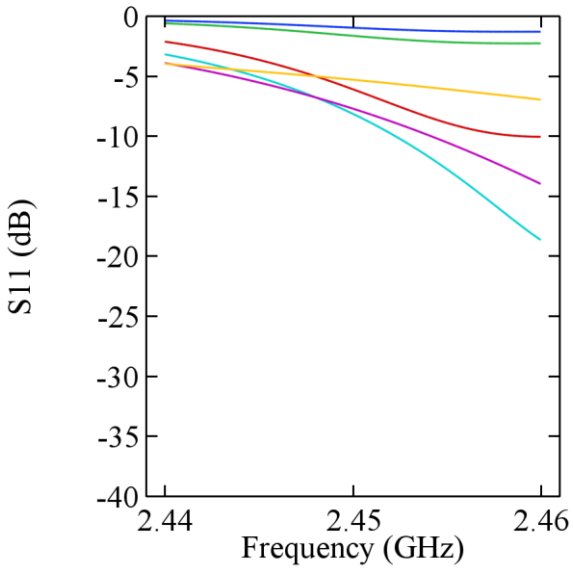


Figure 6.37 Reflection coefficient magnitude of broad wall slot fed reactor with a product bed with a dielectric constant of 1.5 and loss factor of 0.05 (blue line), 0.1 (green line), 0.5 (red line), 1 (cyan line), 2 (purple line) and 4.5 (yellow line).

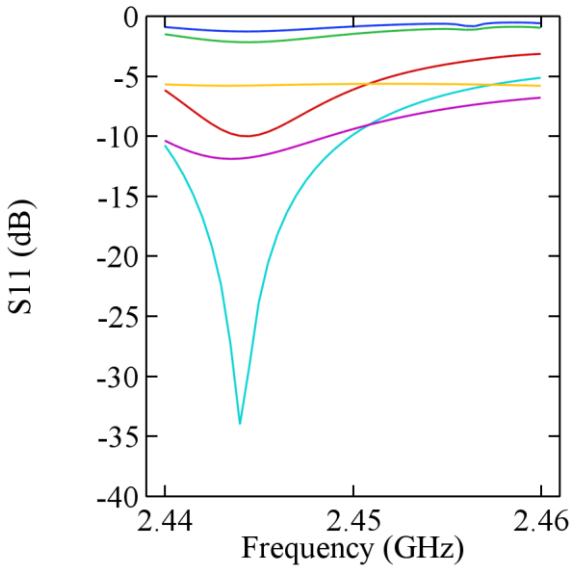


Figure 6.38 Reflection coefficient magnitude of broad wall slot fed reactor with a product bed with a dielectric constant of 4.5 and loss factor of 0.05 (blue line), 0.1 (green line), 0.5 (red line), 1 (cyan line), 2 (purple line) and 4.5 (yellow line).

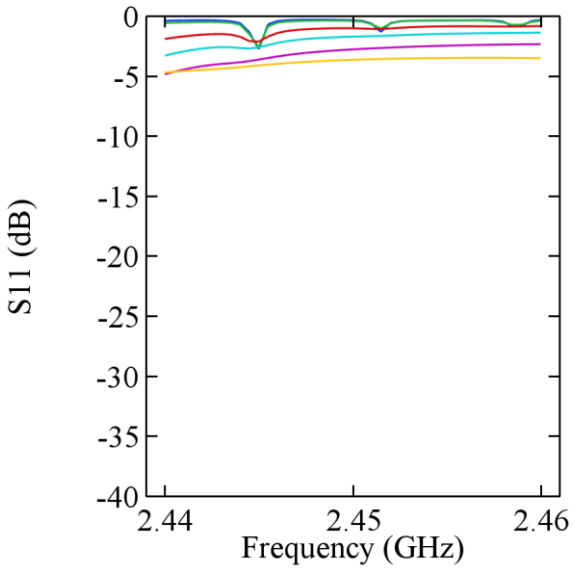


Figure 6.39 Reflection coefficient magnitude of broad wall slot fed reactor with a product bed with a dielectric constant of 7.5 and loss factor of 0.05 (blue line), 0.1 (green line), 0.5 (red line), 1 (cyan line), 2 (purple line) and 4.5 (yellow line).

The same two tuned cases examined for the previous designs were investigated with the same type of capacitive tuning iris and 6 kW input power.

For the low loss case, the reflection coefficient magnitude is shown in Figure 6.40, showing a quality factor of 2,134. A relatively low ripple microwave generator and automatic tuning techniques are possibly needed to maintain resonance during processing [12], [425]. A power conversion efficiency of 73.4 % is observed, with around 18.0 % being dissipated in the walls and around 8.6 % in the window (considerable less power going to the window). The electric field and power loss density distributions are shown in Figure 6.41 and Figure 6.42, with various heating zone distributed along the product bed. An average power loss density of 7.4×10^6 W/m^3 is dissipated within the load with a PUI of 0.71.

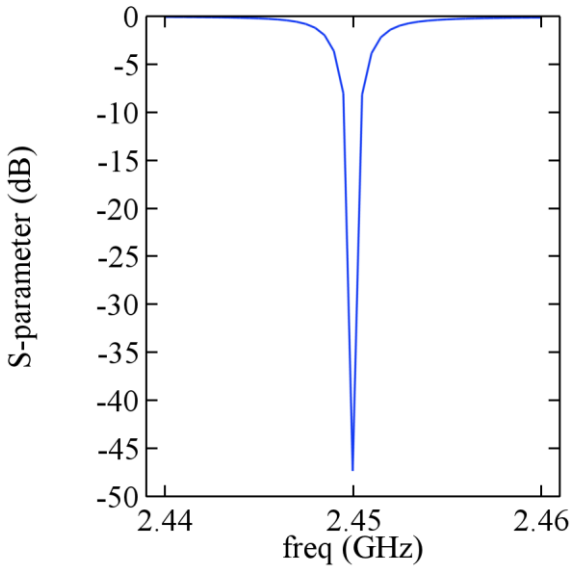


Figure 6.40 Reflection coefficient magnitude of a broad wall fed reactor with a product bed with a dielectric constant of 1.5 and loss factor of 0.05, tuned for 2.45 GHz.

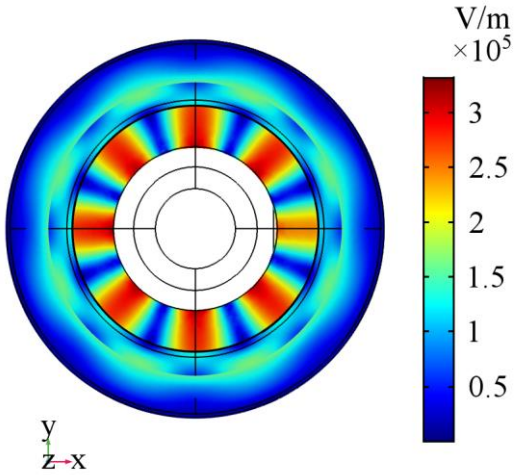


Figure 6.41 Electric field distribution of a broad wall slot fed reactor with a product bed with a dielectric constant of 1.5 and loss factor of 0.05, tuned for 2.45 GHz. XY cut-plane at bed centre.

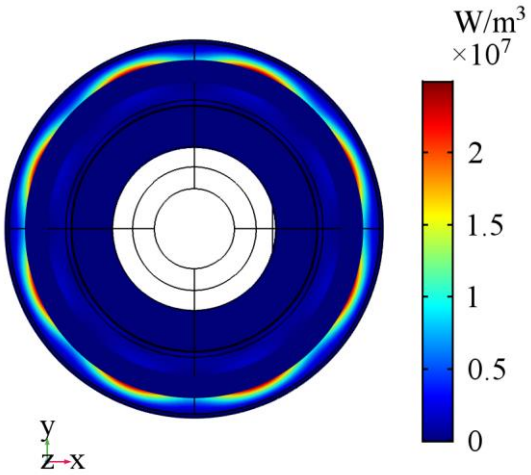


Figure 6.42 Power loss density distribution of a broad wall slot fed reactor with a product bed with a dielectric constant of 1.5 and loss factor of 0.05, tuned for 2.45 GHz. XY cut-plane at bed centre.

For the high loss case, the reflection coefficient magnitude is shown in Figure 6.43 (green line), with a quality factor of 155. This would allow operation without the need of a low ripple generator [12], [425]. As in the previous cases, two other material properties were tested representing a possible broad temperature range of operation between 600 and 1,000 °C (blue

and red lines), maintaining over 70 % of power coupling in the entire generator bandwidth ($\pm$10 MHz). Hot re-tuning is likely needed when approaching the upper-temperature range, to keep coupling power over 90 %. A power conversion efficiency of 98.5 % is obtained, with around 1.3 % being dissipated in the walls and around 0.2 % in the window. The electric field and power loss density distributions are shown in Figure 6.44 and Figure 6.45, showing a distributed field and power density with a PUI of 0.67 and an average power loss density of 9.9×10^6 W/m^3 is dissipated within the load.

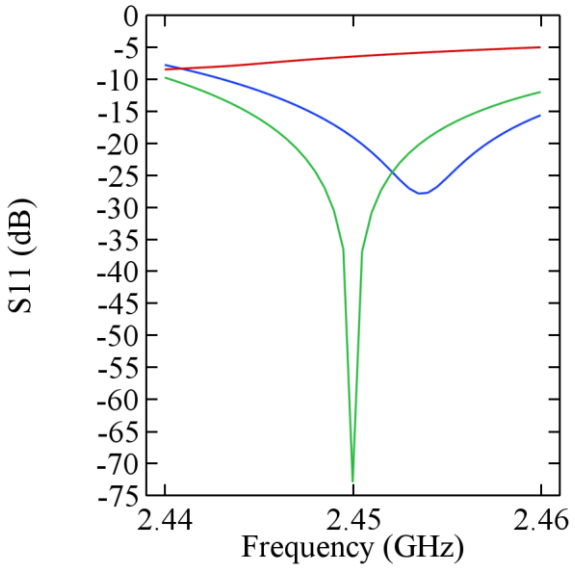


Figure 6.43 Reflection coefficient magnitude of a broad wall fed reactor with a product bed with a complex permittivity of 3.96-j1.23 (blue line), 4.26-j1.48 (green line), and 5.78-j4.99 (red line), tuned for a 4.26-j1.48 load at 2.45 GHz.

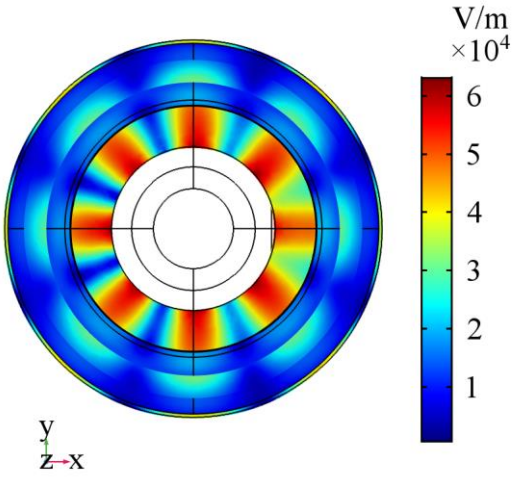


Figure 6.44 Electric field distribution of a broad wall slot fed reactor with a product bed with a dielectric constant of 4.26 and loss factor of 1.48, tuned for 2.45 GHz. XY cut-plane at bed centre.

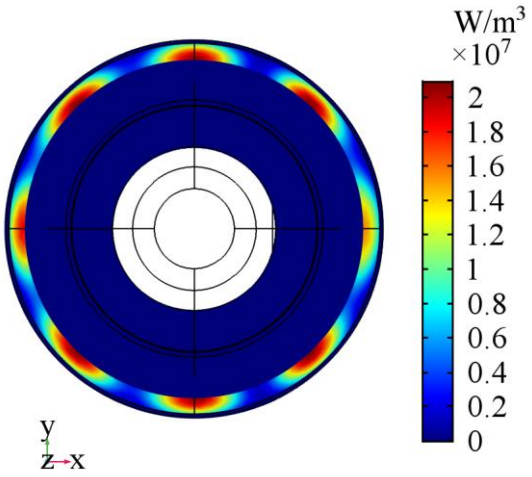


Figure 6.45 Power loss density distribution of a broad wall slot fed reactor with a product bed with a dielectric constant of 4.26 and loss factor of 1.48, tuned for 2.45 GHz. XY cut-plane at bed centre.

6.3.4 Microwave fluidised bed simulations results summary

A summary of the results for the three investigated feeding concepts, the waveguide (WG), narrow wall slot (NWS) and broad wall slot (BWS) fed reactors at 2.45 GHz in tuned conditions for a low loss ($\varepsilon_r = 1.5 - j0.05$) and a high loss ($\varepsilon_r = 4.26 - j1.48$) material is shown in Table 6.2. The narrow slot fed reactor showed a lower quality factor and PUI, whereas the broad wall slot fed reactor showed a better power conversion efficiency. The waveguide fed reactor on the other hand exhibit the worst all around metrics with higher quality factors, lower power conversion efficiencies, higher PUI and lower average power density. Any of the investigated concepts would likely require the use of a low ripple generators and an automatic tuning for low loss materials.

Table 6.2 Summary of results for waveguide (WG), narrow wall slot (NWS) and broad wall slot (BWS) fed reactor at 2.45GHz, for a 6 kW microwave power input.

	$\varepsilon_r = 1.5 - j0.05$			$\varepsilon_r = 4.26 - j1.48$		
Parameter	WG	NWS	BWS	WG_HL	NWS	BWS

Q_0	4,140	1,672	2,134	356	111	155
P_{eff} (%)	43.1	71.1	73.4	95.0	98.5	98.5
P_{win} (%)	0.8	14.2	8.6	0.2	0.5	0.2
P_{wall} (%)	56.1	14.8	18.0	4.8	1.0	1.3
PUI	0.80	0.62	0.71	0.98	0.62	0.67
Qav (W/m^3)	4.3×10^6	7.0×10^6	7.4×10^6	9.5×10^6	9.9×10^6	9.9×10^6

6.4 Microwave fluidised bed prototype design

A prototype based on the broad wall slot waveguide feeding scheme was developed for simulation validation and proof on concept before developing a full-scale system. This concept was selected due to showing the best conversion efficiency for the low loss cases, mostly by reducing the power absorbed by the window.

Several changes were introduced due to practical considerations during fabrication and to improve performance with the required changes. A prototype was fabricated for validation via static testing (no fluidised bed), followed by a functional prototype currently in commissioning stage.

6.4.1 Prototype and validation

The microwave parts of the system were fabricated in aluminium via laser cut and welding. Several bespoke transitions were designed and fabricated also. The original tapered feeding was replaced for a more straightforward interconnection by a WR284 line welded directly to the ring as shown in Figure 6.46. External waveguide ring with an outer diameter of 262 mm and a height of 49.18 mm, and a feeding waveguide line of 550 mm long.

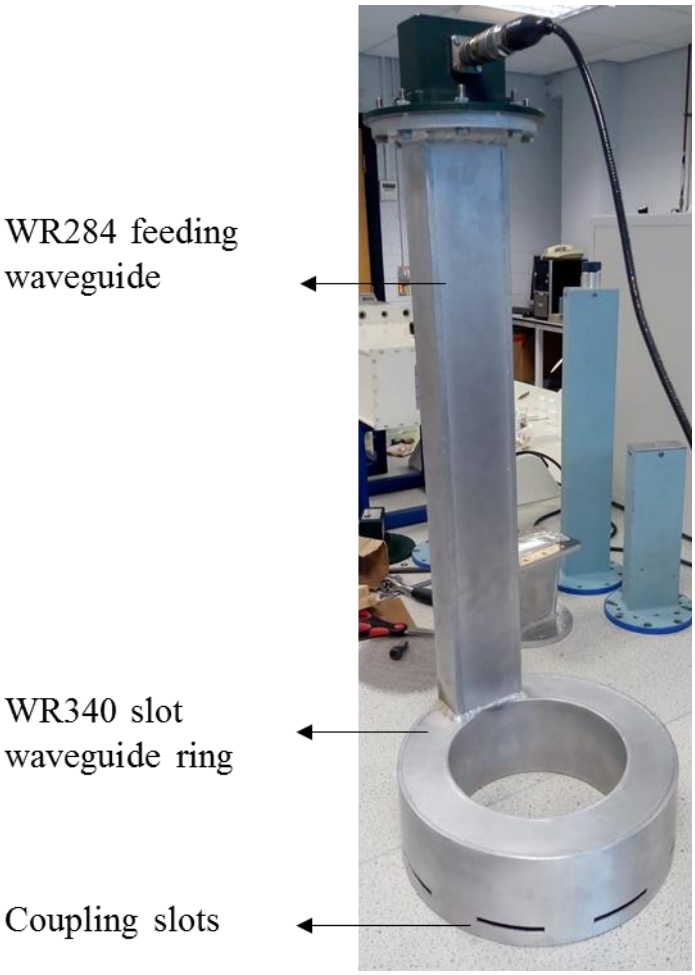


Figure 6.46 Initial prototype waveguide feeding ring.

All cavity internals were fabricated from aluminium sheets and taped sealed using aluminium tape. A FOAMGLAS® piece was cut to the expected shape of a common fluidised bed as shown in Figure 6.45, lifted to position by with six 2 cm x 1 cm strips of alumina wool.

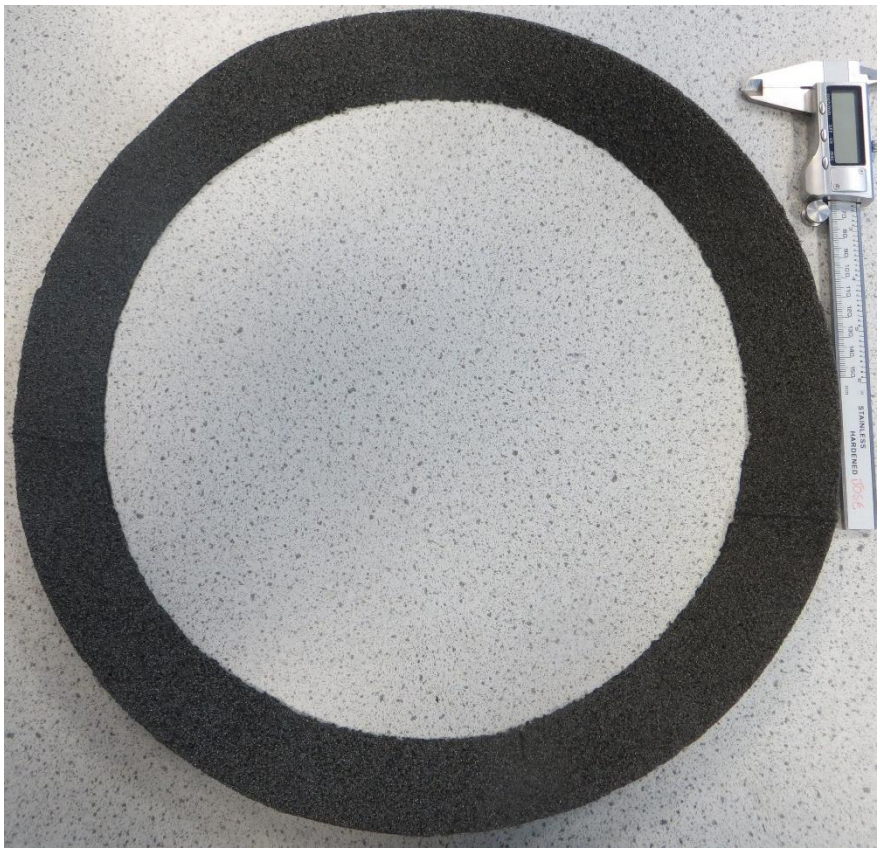


Figure 6.47 FOAMGLAS® static bed triangular profile with 30 mm height and 34 mm width, 395 mm outer diameter, 327 mm internal diameter.

The reflection coefficients were measured and simulated for this material ($\varepsilon_r = 1.29 - j0.77$). The results are shown in Figure 6.48 where the blue line is the experimental and the red line is the simulation results. Both results are in good agreement, showing the same resonance frequency, similar resonance levels and a difference of only 1 MHz in its -10 dB bandwidth (simulation 38 MHz, experimental 37 MHz).

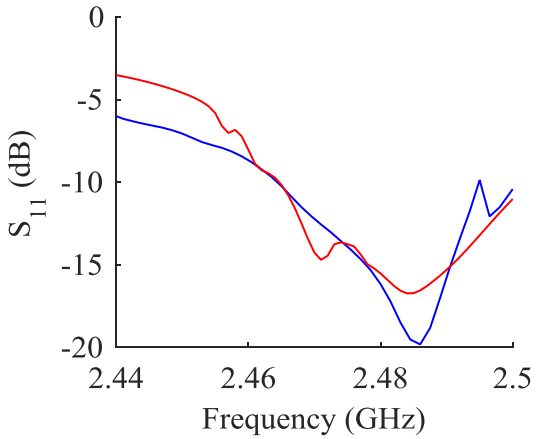


Figure 6.48 Simulation (red line) and measurement (blue line) of initial Torbed T400 CBRMW prototype, with a static FOAMGLAS® load.

A heating experiment was also carried out by heating the FOAMGLAS® load for 10 seconds at 300 W. A comparison between the simulated power loss density and the thermal image after heating can be seen in Figure 6.49, with excellent agreement regarding its heating pattern.

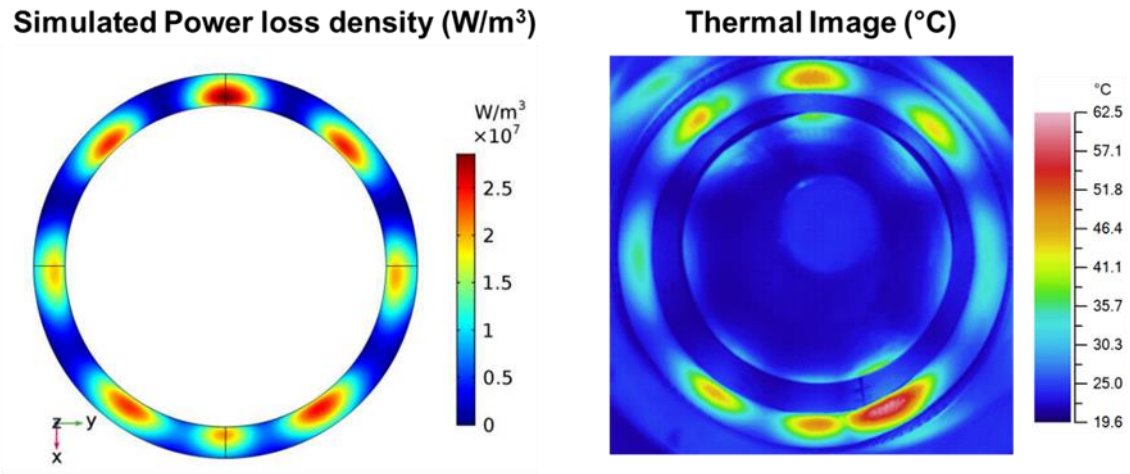


Figure 6.49 Torbed MWCBR400 with PTFE window shell (3 mm) and FOAMGLAS® load – Power loss density simulation vs thermal imaging measurement, for 300 W microwave input for 10 seconds.

6.4.2 T400 CBRMW reactor

The reactor was fabricated in stainless steel with a PTFE window for initial testing (other windows types are currently being manufactured for high temperature operation). The slot vertical positioning was adjusted to provide an improved performance considering a low loss product ($\varepsilon_r = 1.5 - j0.05$). An initial estimation of the performance of the fabricated prototype

was carried out via simulations, which for the low loss case showed a conversion efficiency of 88%, quality factor of 1,065 and a PUI of 0.79. Pictures of the prototype reactor and its internals are shown in Figure 6.50 and Figure 6.51.

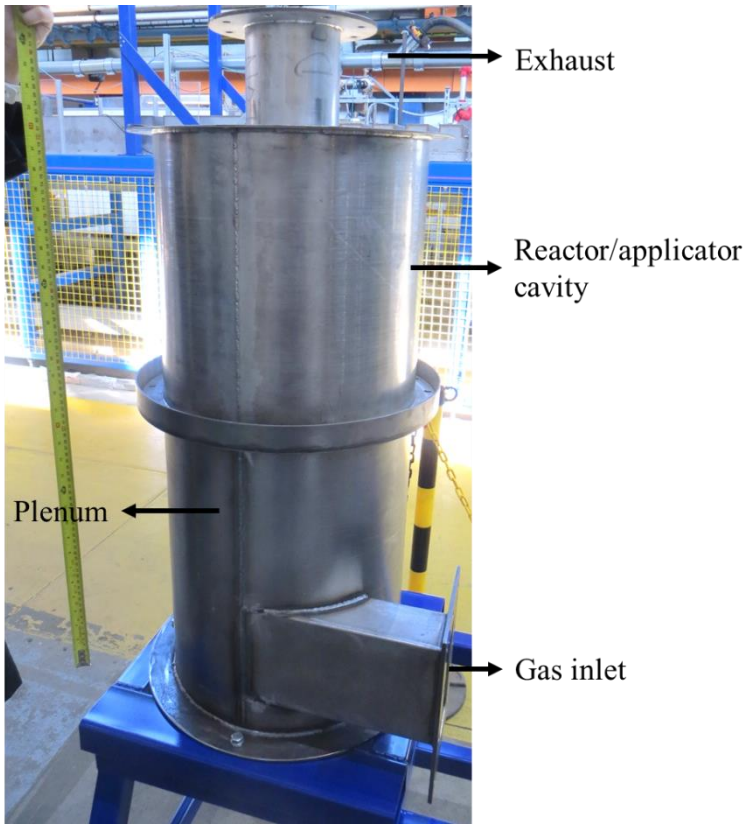


Figure 6.50 Torbed T400 CBRMW prototype external view.

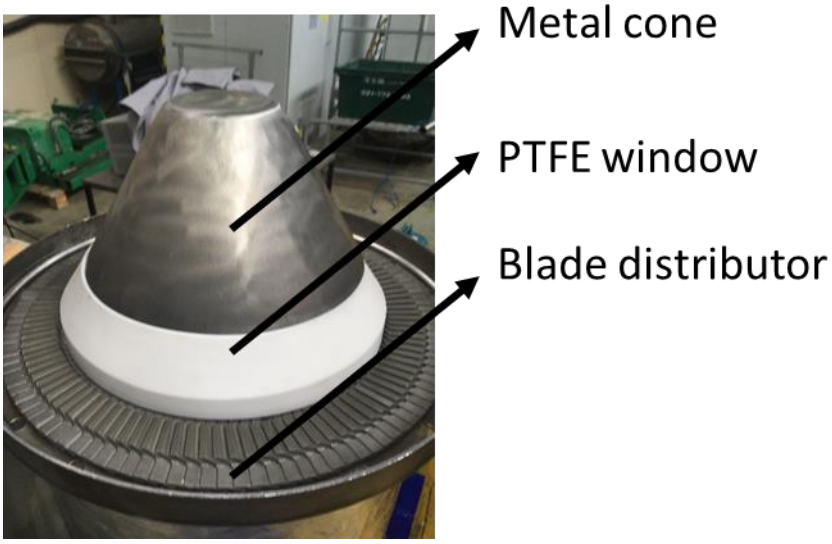


Figure 6.51 Torbed T400 CBRMW prototype internals

Additional ancillary parts were designed for observation and microwave choking purposes. A summary of these follows.

6.4.2.1 Inlet and exhaust choking

Given the size of gas inlet and exhaust, some microwave choking alternative was needed which should avoid limiting the air flow through the system. The use of regular expanded mesh or punctured plates were not possible, as they provide opening areas of no more than 70%. To overcome such problem, a honeycomb air straightener aluminium structure was chosen as choking element, as they provide over 95% open area [428]. The attenuation ability of such structure was tested by measuring the transmission coefficient by using custom rectangular to circular waveguide transitions as seen in Figure 6.52. The honeycomb was set and removed several time at various rotations, showing for an absolute minimum attenuation of 40 dB for the worst case. A tested wire mesh with similar attenuation performance resulted in a 40% open area only. Two layers of honeycomb should be used stacked in orthogonal orientation to minimise polarisations effects [429].

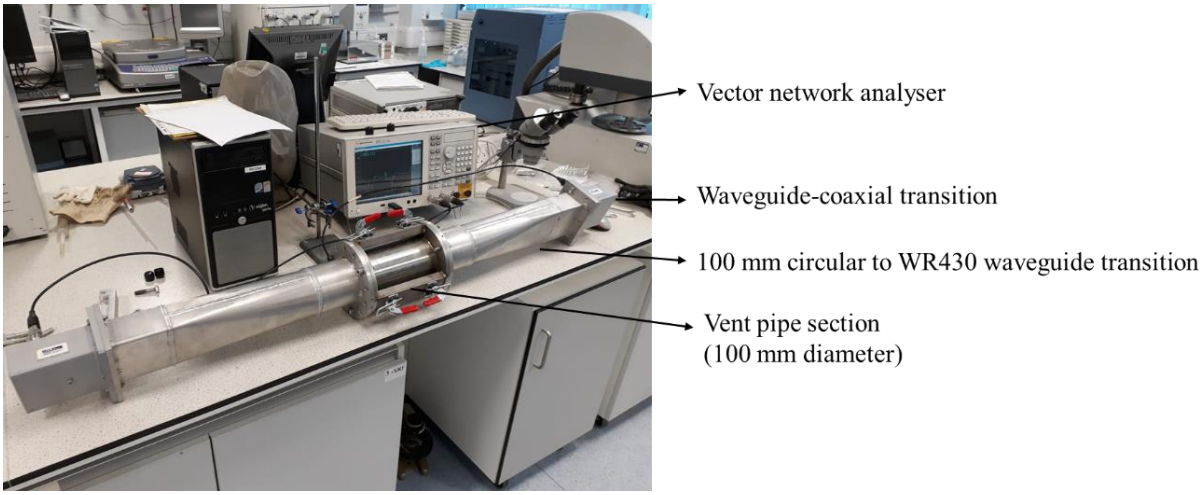


Figure 6.52 Inlet and exhaust choke testing rig

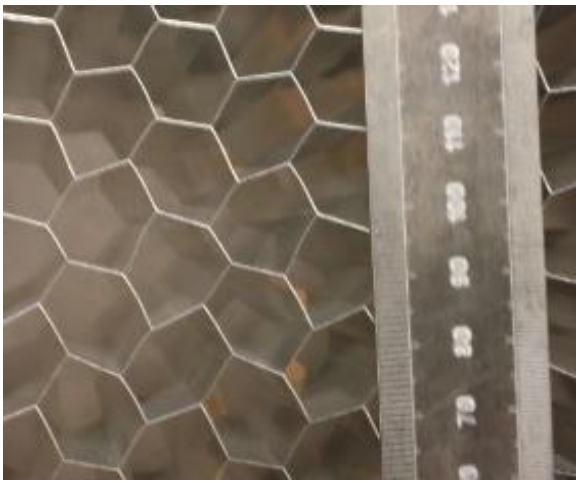


Figure 6.53 Honeycomb structure picture 15 mm x 100 mm cells.

6.4.2.2 Viewing ports

For operational monitoring various feeding ports were designed. These consist on 150 mm long, 40 mm diameter tube sections bolted to the lid with observation windows and gas input port to protect them from processing by products. For such diameter an attenuation of 6.6 dB/cm is achieved (Figure 6.54); hence a total of around 99 dB attenuation for each port, to avoid any possible interaction with the thermal camera's electronics.

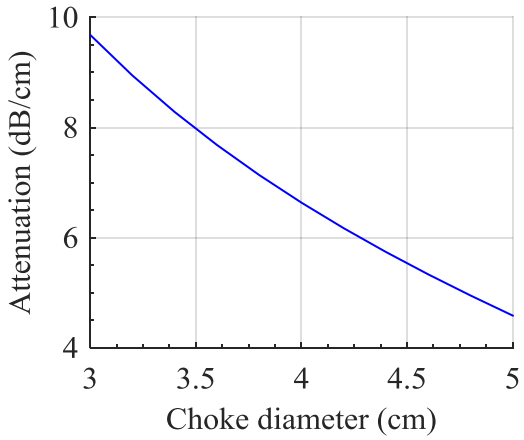


Figure 6.54 Empty tube choke attenuation

The available thermal imaging cameras worked within the 8 µm to 13 µm, in the infrared spectrum; therefore, typical optical window materials were not suitable. A chart of the transmission range of optical materials is shown in Figure 6.55, among which the only compatible candidates were Germanium and Zinc Selenide windows. A germanium window with AR/AR (antireflection coating) was selected and its configuration is shown in Figure 6.56,

and a transmission spectrum. For optical camera observation a borosilicate glass window was employed in a twin viewing port.

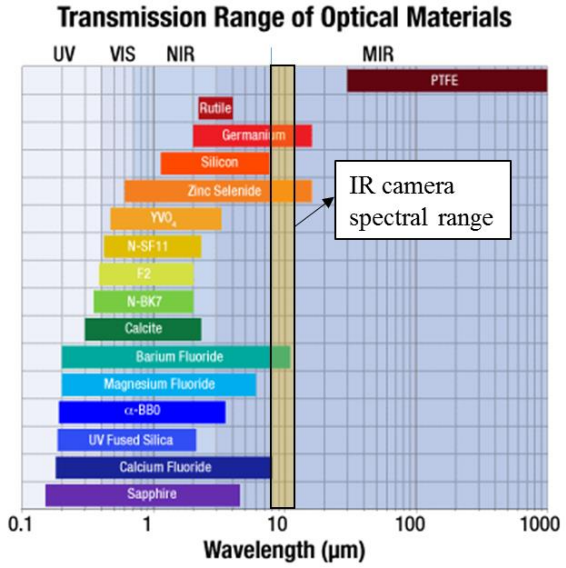


Figure 6.55 Transmission range of optical materials, adapted from [430]

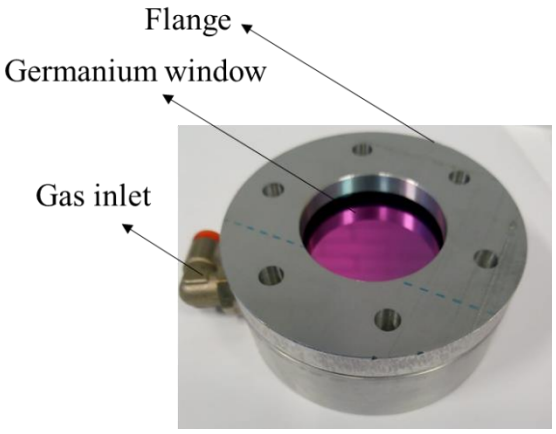


Figure 6.56 IR viewing port configuration – germanium window.

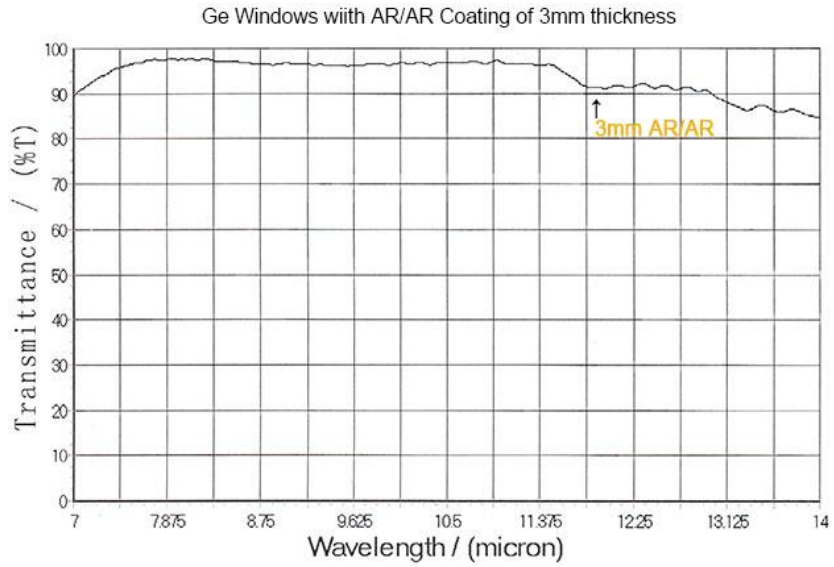
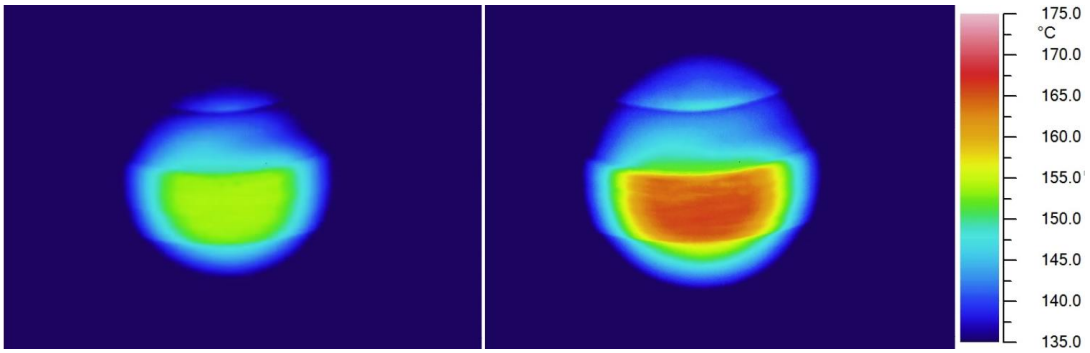


Figure 6.57 Germanium window with AR/AR coating – 3 mm thick, after [431]**.**

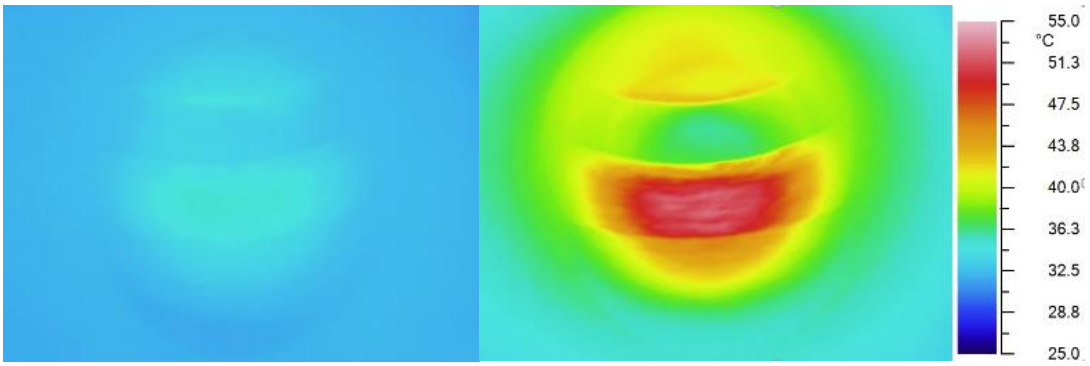
6.4.3 Initial heating trials

A range of heating trials have been performed up to 5 kW. A selection of two tests is shown here, to illustrate the excellent achieved heating uniformity. An hybrid heating test of corn with before and after microwave treatment surface temperature distribution shown in Figure 6.58. A purely microwave heating test of malt, with before and after microwave treatment surface temperature distribution shown in Figure 6.59. Both cases exhibiting an excellent temperature distribution across the bed.



(a) (b)

Figure 6.58 Hybrid heating test on the Torbed MWCBR400 with PTFE window shell (3 mm) and 500 g load of corn –Thermal imaging (a) after convection heating to 150 °C (b) after 2 kW microwave input for 20 seconds (full absorbed power).



(a) (b)

Figure 6.59 Purely microwave heating test on the Torbed MWCBR400 with PTFE window shell (3 mm) and 300 g load of malt –Thermal imaging (a) after convection heating to 150 °C (b) after 2 kW microwave input for 20 seconds (full absorbed power, cold matched).

6.5 Microwave fluidised bed system scale-up

A broad wall slot reactor was designed for 896 MHz as an example of scale-up. At this frequency, the free space wavelength is 334.82 mm. For a standard WR975 waveguide cross section 247.65 x 123.825 mm operating at TE_{10} mode the guided wavelength is 454.36 mm. This led to a 651.3 mm outer and 403.65 mm inner waveguide ring diameter. The space between maximums is therefore approximately 49° and can fit 7 slots. This feeding structure can be used to process material in a 1,000 mm diameter reactor.

It is relevant to notice that the larger the broad-wall (i.e. smaller guided wavelength) and the smaller the narrow-wall (i.e. smaller internal ring diameter), the more maximums and slots can be fitted within the ring. For example, a ring of 284 x 123.825 mm cross-section with the same outer diameter of 651.3 mm will lead to a 45° spacing between maximums and therefore to symmetrically distributed 8 slots along the ring.

The behaviour of a low loss case ($\varepsilon_r = 1.5 - j0.05$) and high loss case (based on Anthracite properties for 600, 800 and 1,000 °C, tuned for 800 °C properties at 915 MHz, see Appendix D) were examined. The reflection coefficient magnitudes are shown in Figure 6.60 and Figure 6.61, and electric field and power loss density distributions are shown in Figure

6.62, Figure 6.63, Figure 6.64, Figure 6.65, considering a commercially available power source of 100 kW showing a better performance than its 2,450 MHz counterpart studied in the previous section, except for a higher PUI, values summarised in Table 6.3.

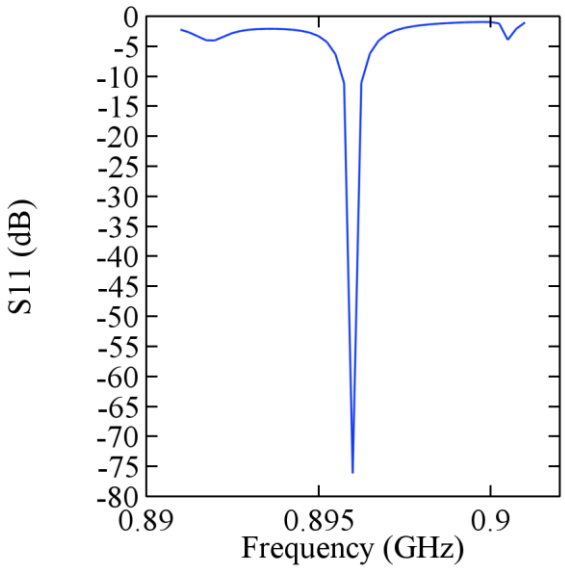


Figure 6.60 Reflection coefficient magnitude of a broad wall fed reactor with a product bed with a complex permittivity of 1.5-j0.05 tuned for 896 MHz.

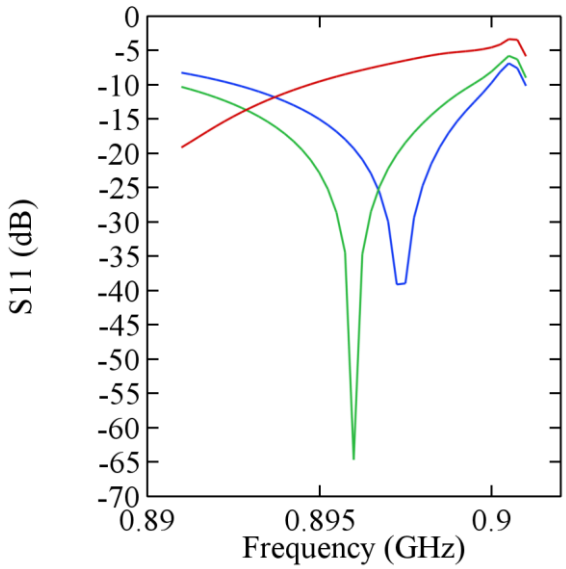


Figure 6.61 Reflection coefficient magnitude of a broad wall fed reactor with a product bed with a complex permittivity of 4.32-j1.86 (blue line), 4.67-j2.26 (green line), and 7.26-j5.64 (red line), tuned for a 4.67-j2.26 load at 896 MHz.

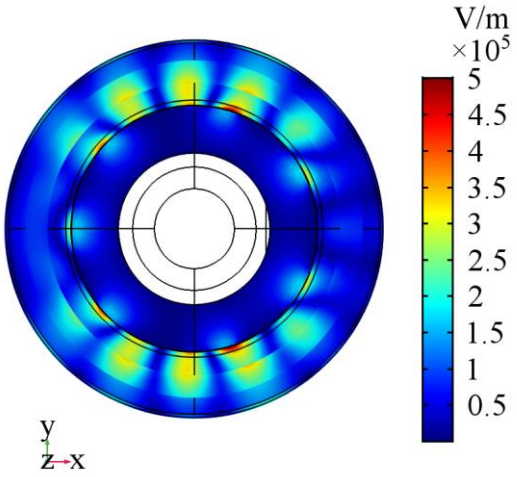


Figure 6.62 Electric field distribution of a broad wall slot fed reactor with a product bed with a dielectric constant of 1.5 and loss factor of 0.05, tuned for 2.45 GHz. XY cut-plane at bed centre.

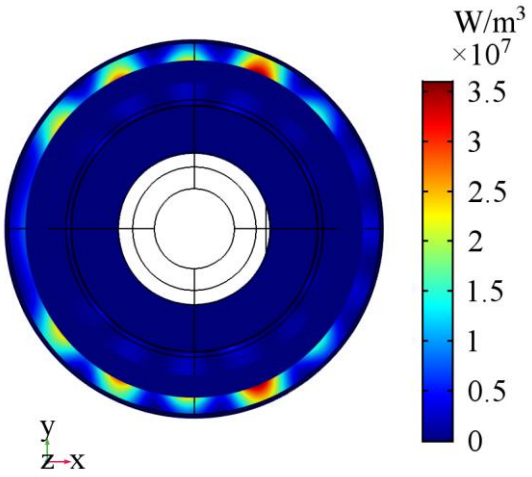


Figure 6.63 Power loss density distribution of a broad wall slot fed reactor with a product bed with a dielectric constant of 1.5 and loss factor of 0.05, tuned for 2.45 GHz. XY cut-plane at bed centre.

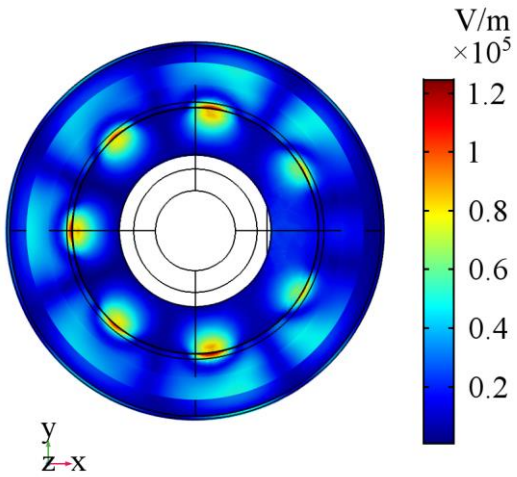


Figure 6.64 Electric field distribution of a broad wall slot fed reactor with a product bed with a dielectric constant of 4.67 and loss factor of 2.26, tuned for 2.45 GHz. XY cut-plane at bed centre.

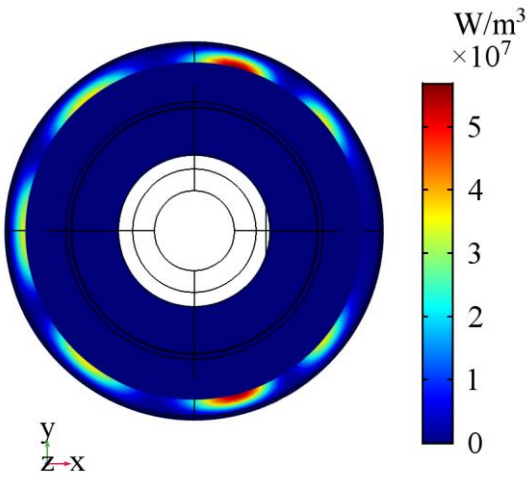


Figure 6.65 Power loss density distribution of a broad wall slot fed reactor with a product bed with a dielectric constant of 4.67 and loss factor of 2.26, tuned for 2.45 GHz. XY cut-plane at bed centre.

Table 6.3 Summary of results for the broad wall slot fed reactor at 896 MHz for a 100 kW microwave power input.

Parameter	$\varepsilon_r = 1.5 - j0.05$	$\varepsilon_r = 4.67 - j2.26$
Q0	1,200	107.1
Peff (%)	81.6	98.8
Pwin (%)	9.0	0.5
Pwall (%)	9.4	0.7
PUI	0.74	0.78
Qav (W/m^3)	8.1×10^6	9.8×10^6

This change in operating frequency and reactor size results in an approximate tenfold throughput increase. The absolute throughput will depend on the material and processing requirements, and specific material handling strategies. For example, as a rough estimate (any process would require thorough research to establish processing parameters), a continuous fast process (e.g. flash pyrolysis) involving a 10 second average residence time at a nominal loading of 5 kg could achieve a maximum throughput of 1.8 t/h.

6.5.1 Effect of bed position variation

Upward bed displacement of 0.5 and 1 cm of the bed were simulated for the $\varepsilon_r = 4.67 - j2.26$ case, to assess the sensitivity to bed position variation. The observed effect is a displacement of the resonance to higher frequencies for a bed positioned higher at approximately 2 MHz/cm.

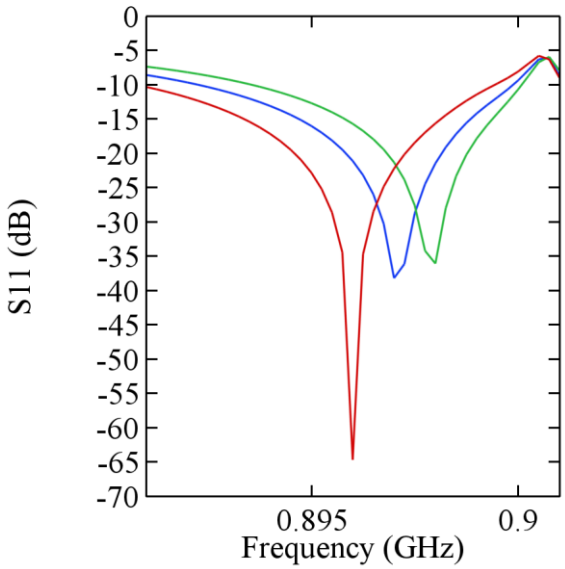


Figure 6.66 Reflection coefficient magnitude for original bed position (red line), shifted upwards by 0.5 cm (blue line) and 1 cm (green line).

6.5.2 The increase of reactor diameter

The system could be scaled further using the same frequency by increasing the reactor diameter and retaining a similar blade size, therefore increasing the waveguide ring and central cone. For example, a broad wall slot fed reactor with an outer waveguide ring diameter of 1,000 mm considering a standard WR975 cross-section results in 12 maximum spots/slots, as the separation between maximums is roughly 30°. The blades, and therefore bed cross section, can remain roughly the same increasing the volume upon toroid diameter increase, requiring an approximate 1,400 mm reactor diameter.

The increase of number of slots redistribute the energy more uniformly within this larger volume; however, slotted waveguide bandwidth is reduced when increasing the number of slots [423]. An alternative approach is the use of a smaller waveguide size, for example, WR770 (195.58 mm x 97.79 mm). This serves to increase the bandwidth by (i) reducing waveguide ring cross section and (ii) reducing the number of slots, as the guided wavelength becomes larger with a maximum separation 41° resulting in 8-9 slots. To achieve a uniform distribution a custom cross section of 189.9 x 97.79 mm results in a 45° spacing with symmetrically distributed 8 slots. The maximum electric field positions for both the 12 slot and uniform 8 slot

waveguide rings are illustrated in Figure 6.67 and Figure 6.68. If a broader frequency response is required, increasing the slot width and using a thin waveguide wall should be considered.

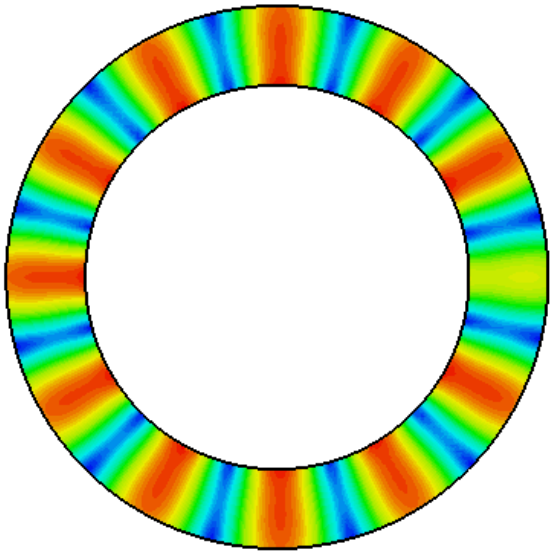


Figure 6.67 Electric field distribution of 1,000 mm waveguide ring with WR975 waveguide cross-section.

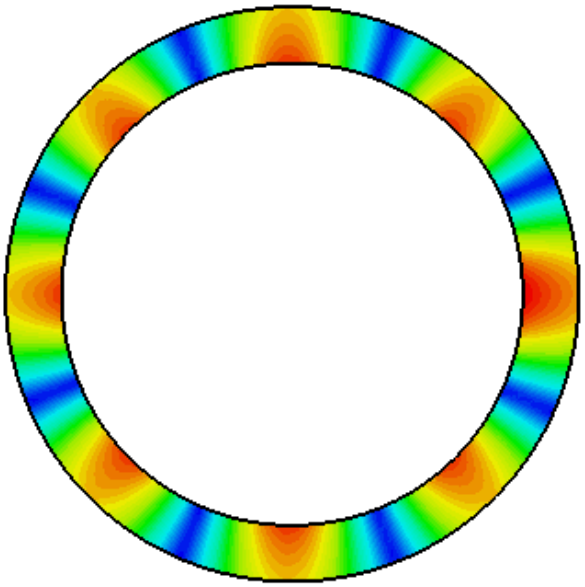


Figure 6.68 Electric field distribution of a 1,000 mm waveguide ring with custom 189.9 x 97.79 mm cross-section.

6.6 Conclusions

A novel hybrid heating convection-microwave fluidised bed reactor was proposed for treatment of a broad range of granular products. Applications such as fast pyrolysis of biomass and coals, and direct reduction of iron ores were discussed and suggested as good candidates to take advantage of the technology characteristics, in particular material mixing, robust materials of construction high gas velocities and therefore mass transfer. Such applications present shortcomings when treated in fluidised beds due to heat conduction limitations, needing pre-conditioning of the feedstock to regular fine particles, whereas in conventional microwave setups typically these processes present poor treatment uniformities due to low penetration depth and lack of effective mixing mechanisms at high-temperatures.

The combination of conventional convection heating by fluidised bed with fast volumetric microwave heating serves to overcome such limitations by providing an effective way to rapidly heat low thermal conduction materials using microwaves, and thoroughly mixing the bed allowing for excellent treatment uniformity.

Among the studied feeding arrangements, the broad wall and narrow wall slot feeding through a window conformal to the central cone delivered distributed energy deposition throughout the product bed effectively, with PUI ranging of 0.71 and 0.62 respectively. For low loss or highly variable dielectric processing during processing, the use of automatic tuning equipment and low ripple generators are likely required as quality factor close to 2,000 are observed. For high loss products the operation is robust even for considerable variation on the load position and properties.

The model was validated experimentally by use of a prototype showing excellent agreement in both resonant frequency and resonance level, with only a 1 MHz difference between experimental and measurement -10 dB bandwidth. The ducting for the operational fluidising prototype is currently under commissioning.

A path for large-scale implementation for continuous operation was proposed based on the use of the 896 MHz band with the possibility to extend the reactor diameter to meet process throughput requirements, for over 1 tonne/hour continuous processing. Initial estimations reveal better performance estimations regarding efficiency and matching. A pilot plant is expected to start commissioning during 2019.

Chapter 7 Applicator for large products

The literature review in Chapter 3 revealed that one of the major obstacles for the implementation of large-scale microwave processes of relatively high temperature (i.e. over 250 °C) is the lack of compatibility of a continuous, high-throughput, flexible, robust and reliable material transport technique to move the material with the microwave applicator system.

In previous chapters, solutions were investigated in the form of an elliptical cylinder resonator and a novel hybrid heating fluidised system. The former was able to treat pumpable liquids and small granular materials of few millimetres by the use of pneumatic conveying or packed beds controlled by a bottom feeder through a robust microwave transparent tubing (see Chapter 5). The latter was able to handle a wide range of granular products of an estimated particle size of 20 mm continuously (see Chapter 6). The temperature capabilities of both systems were mostly limited by the ceramic material used either as a tube for the elliptical applicator or the conical window in the fluidised bed system. For processes which involve large feedstocks with particles larger than 20 mm, and temperatures in excess of 250 °C, a flexible and robust material conveying solution compatible with microwaves is needed.

Industrial material conveying solutions include, among others, gravity flow, pneumatic conveying, vibratory feeders, screw conveyors, and conveyor belts [79], [432]. Of these, conveyor belts are generally regarded as the most adaptable and reliable technology for low-cost transport of bulk materials [433]. They provide flexibility to handle a broad range of bulk materials from fines (e.g. cement powders, grains, flour) to large particles(e.g. particulates of coal, ores, aggregates), with a broad range of throughputs from small to thousands of tons per hours [433]–[435]. They also provide setting up flexibility to convey horizontally or inclined and to adapt according to the process requirements and operation site space and usually consume less energy compared to other conveying techniques [433]–[435].

Microwave-compatible conveyor belts have been limited to low-temperature applications due to the need to rely on microwave transparent materials to achieve a relatively uniform treatment [19]. Commercially available high-temperature dielectric belts suitable for use in microwave systems, such as PTFE coated, silicone/glass, Kevlar or basalt fibre belts cannot handle temperatures in excess of 600 °C, and cannot provide the required robustness for continuous operation under harsh conditions [19], [436], [437]. Failure of these belts happens even if the process regularly operates below their threshold temperatures, due to the occurrence of events such as thermal runaway and arcing. Therefore, the belt should be able to handle significantly higher temperatures than expected values due to the likelihood of these to happen, in particular for high-temperature processing, where these events are of frequent occurrence due to hot gas environments given the reduction of voltage threshold for dielectric breakdown [422].

The use of more robust belt materials could provide significant technological step-change to make high-temperature microwave industrial systems a reality. In this chapter, the alternative of using a metallic conveyor belt is investigated, which due to its robustness could provide a platform for operation at much higher temperatures than conventional systems, even able to operate after occasional arcing or thermal runaway events. A configuration consisting of a parallel plate arrangement using a metallic conveyor belt was designed, fabricated and validated experimentally. Some scale-up considerations are discussed, and a large-scale conceptual system is proposed.

7.1 Metallic conveyor belts in the literature

The use of metallic belts is an obvious candidate given its inherent high robustness. Their use as a mean for material transport in microwave systems had received attention mostly as an alternative setup for already established low-temperature processes. Main aspects

considered are improved durability and compliance with hygienic standards in food and pharmaceutical processes (e.g. food and pharmaceutical grade stainless steel) [438]–[443].

Metallic belts might provide a significant enhancement of robustness compared to conventional dielectric belts. Nonetheless, its usage poses several engineering problems, the main one being that the belt will impose a boundary condition that forced the electric field components not perpendicularly polarised against its surface to drop to zero amplitude [22] (i.e. the electric field on the surface of a perfect conductor is perpendicular to the conductor surface as the tangential components cancel out). This reduces the ability to effectively treat the portion of the product that is closer to the belt.

Some solutions have been proposed in the literature. A metal roller conveyor system for filament extrusion [438]. A metal conveyor belt with an absorbent dielectric chamber [439], in which the complementary use of hot air and porous belts are proposed to overcome under heating of materials close to the belt. The use of several parallel waveguides over a metal carrier with junctions on the low field zone, effectively working as multiple waveguides travelling wave system [440]. The use of a tunnel travelling wave applicator with a suspended U or V-shaped conductive belt, fed by a waveguide from the top [441] (Figure 7.1). A set of circular waveguides operating in the TM_{01} mode over a conductive belt, all enclosed in a tank filled with ethylene glycol [442]. A parallel plate structure, with the belt acting as one of the plates, where the microwaves are fed either by an array of monopoles or slotted waveguides in an effort to impinge a mostly vertically polarised (i.e. orthogonal to the belt surface) field that treats the load evenly [443] (Figure 7.2). The apparent weaknesses and strengths of these approaches are summarised in Table 7.1.

Table 7.1 Metallic conveying solutions in the literature – apparent weakness

System description	Weaknesses	Strengths	Ref
Roller for filament	Limited throughput.	Safety.	[438]

extrusion	Limited material presentation.	Uniformity. Controllability.	
Metal belt with the absorbent dielectric chamber	Inherently inefficient due to the absorbent chamber. Possibilities for leakage.	Uniformity.	[439]
Multi-waveguide over carrier	Risk of trapped product and arcing. Limited product presentation. Multiple generators.	Simple.	[440]
Suspended belt in tunnel	Size limitation. MW feeding limitation. Possible arcing.	Low likelyhood of leakage. Uniformity. Controllability. Reliability. Medium possible throughput.	[441]
Circular waveguides over belt enclosed in a tank with ethylene glycol	Inherently inefficient due to the absorbent chamber. Leakage.	-	[442]
Parallel plate structure with belt acting as one of the plates. Array feeding.	Inefficient. Leakage. Limit to product presentation (height).	Large possible throughput. Uniformity.	[443]

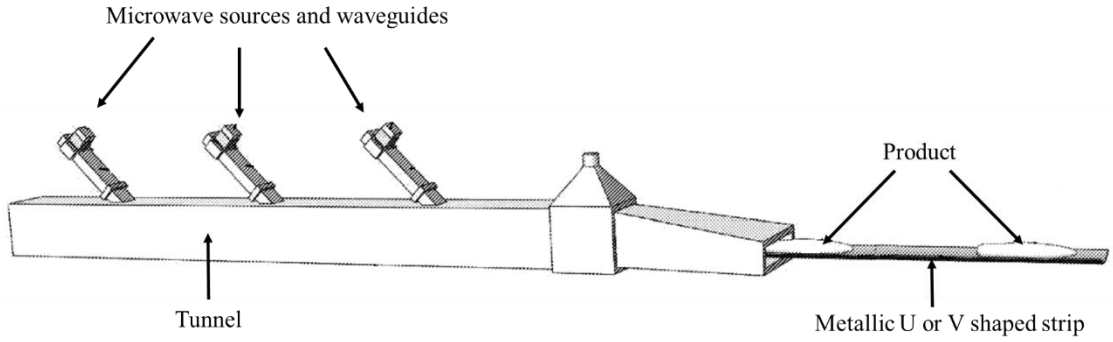


Figure 7.1 Suspended metallic belt in microwave tunnel, adapted from [441]

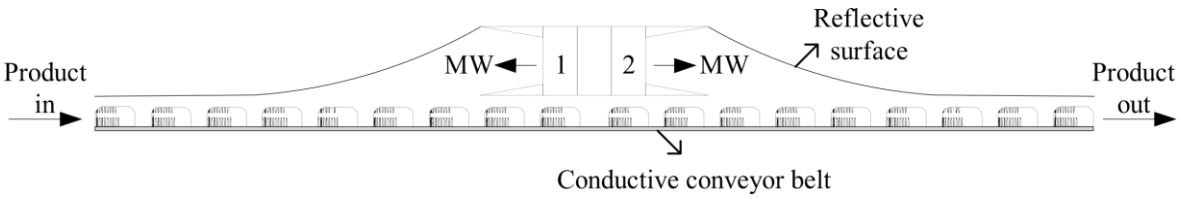


Figure 7.2 Parallel plate applicator schematic, based on the design proposed in [443]

7.2 Prototype applicator concept

In this work, a prototype was developed based on the parallel plate concept [443] with a suspended metal belt within a tunnel in a similar fashion as in [441]. The parallel plate concept proposed in [443] and further detailed in [19] claim to provide uniform treatment and the ability for continuous cooking of food products. The idea behind it is to set a quasi-TEM propagation mode on an approximated parallel plate structure in which one of the plates doubles as a conveyor belt. Such mode is characterised by an electric field polarised normal to the plates, with a uniform amplitude profile in the transverse cross-section. This requires that the sides of the structures are left open.

To excite the structure, uniform illumination of the whole cross section would be needed. Two embodiments are suggested to approximate this in [443], the first one being a slotted waveguide feed, and the second one a monopole array. The use of an inclined tunnel with an aperture in the upper plate is suggested in [19], in which the wavefront created by using an array of sectoral horns.

The slotted waveguide approach was considered a more straightforward feeding strategy. This feed should be able to handle considerable high powers reliably [419], and its single generator excitation makes it attractive for cost and ease of control. The open sides of the parallel plate line suggested in [443] are of significant concern and are needed for a seamless q-TEM propagation. Due to the vertical plate separation, the open sides could lead to significant

microwave leakage, affecting both safety and efficiency, making it not suitable for industrial settings. It was, therefore, necessary to explore alternatives that can overcome these issues, which resulted in the development of a prototype which combines the parallel plate concept with a suspended conveyor belt within a tunnel arrangement, similarly as [441], in a compromise between uniformity versus efficiency and safety. Other investigated solutions were the use of different microwave-absorbing lining on the applicator sides, as in [439], [442]; however, the reduced efficiency and need for cooling of the liner rendered it unpractical.

In such setting the sample presentation would lead to a rather large exposed surface area compared to the volume of sample, thus, leading to a large potential heat loss. Therefore, it is suggested that such applicator require to operate in an hybrid heating configuration to overcome such efficiency limitation.

7.3 Potential applications

The proposed concept could be used for most material presentations given the flexibility and robustness of its mass transport approach. Given the effective volume, applications with moderate to high microwave absorbing properties are likely to be the more suitable, as the achievable power densities are likely to be considerably lower than for small volume systems (e.g., single mode cavities). This makes it particularly suitable as a part of a hybrid heating system in which the products have achieved medium or high microwave absorbent properties by a conventional heating stage, and, given its robustness, for high microwave temperature processes. Among such processes, coke-making from coals and carbonised biomass and direct reduction of iron ore could be particularly attractive applications.

7.3.1 Coke-making

As discussed in chapter 3, coke-making requires relatively high temperatures and long processing cycles; however, research had revealed that microwaves could reduce this process from several hours to minutes, and, furthermore, can allow for the use of low-grade coals as

feedstocks [85], [254], [255]. Nonetheless, the process has been extremely challenging for scale-up, due to several reasons, including the fast change of dielectric properties [82], [85] and frequent occurrences of thermal runaway and consequent damage of lining materials (it is relevant to note that the same phenomena have also been noticed to accelerate the process) [82], [255].

The use of metallic conveyor belts as material transport solution could provide a robust platform to withstand these hostile conditions, even for operation under common occurrences of thermal runaway. The continuous processing is more suitable to adapt to changes of dielectric properties as would effectively behave as in steady state. The contamination of transparent linings and windows can reduced by relying on a staged separated process, as exemplified in Figure 7.3.

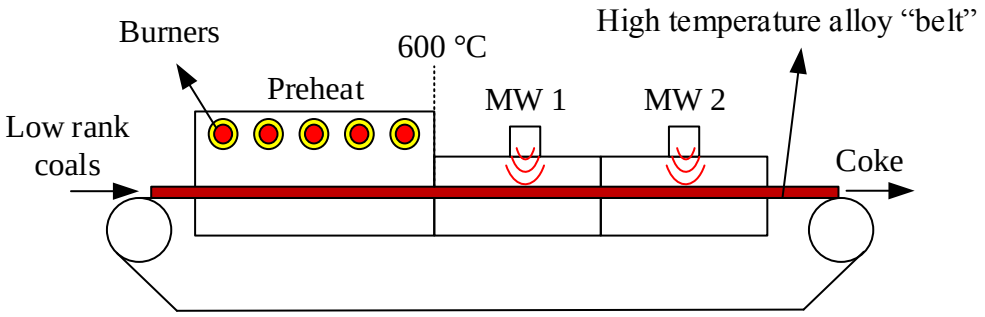


Figure 7.3 Hybrid heating conveyor belt concept for coke-making

First, the coals enter a preheat furnace where they are devolatilised by conventional heating techniques upon a state in which no more release of oily or tarry volatiles occur. Then, the product is handed over to a sequence of microwave heating stages in which microwaves can provide the final heat, fast and efficiently, to reach coking temperatures. The separation in several microwave stages could allow for pre-setting of such systems to optimally deal with the product in its different evolving properties stages. Moreover, the hybridisation of the heating along with adequate setup of insulation could reduce the severe heat loss and consequent low

efficiency that had been observed in most laboratory experiments (i.e. large required energy inputs).

7.3.2 Direct reduction of iron

As revealed in chapter 3, the direct reduction of iron ores (DRI) can be achieved by employing microwaves which can help to overcome a significant issue in conventional reduction, the inability to heat the pellets core fast enough to provide effective gasification of the carbon within it to fuel subsequent reduction. This is thanks to the microwave volumetric heating characteristics. Research has shown that high metallisation degrees can be achieved faster than in conventional processes [82], [108], [109]. Unfortunately, only laboratory scale setups have been successful, as the process scale-up requires an exceptionally robust platform, with material transport solutions that would be exposed to temperatures over 1,200 °C, hot gases, contamination, among other challenges.

In a similar fashion as proposed before for coke-making, a staged approach could be applied for DRI, combining conventional and microwave heating. Nonetheless, the direct use of a metallic belt does not seem plausible in principle due to the possible sticking of metallised particles. However, it can provide a robust platform for the use of a thin refractory layer on top of it, as, at those temperatures, conventional ceramics hearths, as used for example in rotary hearths, could result in an inefficient microwave treatment as a large portion of the microwaves could be absorbed by the hearth volume. The hearth ceramic material can become increasingly microwave abosrbant with temperature and due to its large volume it could dissipate a considerable part of the microwave energy.

Among plausible solutions to combine both technologies, the use a specially designed hearth, consisting in a metallic disc or mesh lined with a low-profile microwave transparent layer on top could overcome such issues, as illustrated in Figure 7.4. This layer does not necessarily need to be a solid ceramic, as it can be made of a variety of low density microwave

transparent materials, as long as they can be screened out and recycled from the process (e.g. alumina sand), which could allow for a permanent maintenance of this lining; therefore, increasing the robustness of the system. Such layer would also perform other relevant roles like improving the penetration of the microwaves into the product by introducing an effective separation from the metallic belt and creating a dielectric barrier that could reduce the likelihood of arcing that may damage permanent parts of the system.

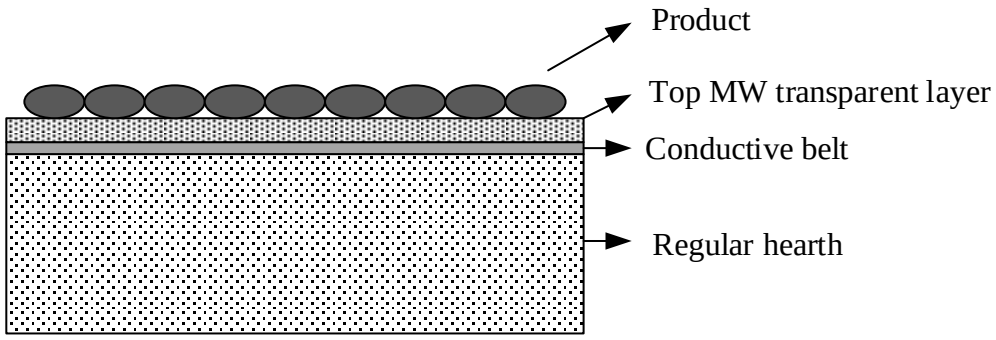


Figure 7.4 Microwave compatible hearth concept.

7.4 Conductive conveyor belt applicator concept and initial design

An initial designed was developed based on the the concept given in Figure 7.2. The product is conveyed through the microwave applicator structure employing a metallic conveyor belt. The applicator structure launches microwave radiation through slotted waveguides, marked 1 and 2. The electromagnetic fields are shaped using a set of three reflective surface sections. Reflectors of wedge geometry in the near vicinity of the waveguides and a curved reflector are used to launch the fields into a parallel plate structure composed by the conveyor belt and an upper reflector plate, which can only sustain fields in vertical polarization to propagate. The reflectors shape and sizes are designed to provide a primary vertical polarisation to the parallel plates for achieving good matching and consistent product treatment. The feeding structure consists of a slotted waveguide. The applicator is mirrored, so the heat pattern on one

side is complementary to the other side in order to improve transverse treatment uniformity as the material pass through both sections.

7.4.1 Slotted waveguide feed

The feeding structure was designed using an antenna array design approach for broad wall slotted waveguides [424], in a similar fashion as for the prototype developed in chapter 6.

A short circuited rectangular waveguide operating in TE_{10} mode result in the setup of a standing wave pattern as shown in Figure 7.5, with a null electric field at the short position, a first maximum at a quarter of guided wavelength from it, and subsequent maximum positioned at half guided wavelength from each other. This corresponds with locations of high surface currents near the broad wall as can be seen in Figure 7.6, as the magnetic fields are tangent to the conductor surface, making them a suitable position for placing a coupling slot. The slots impose an obstacle to the surface current flow, which is forced to go around them inducing an electric field across it.

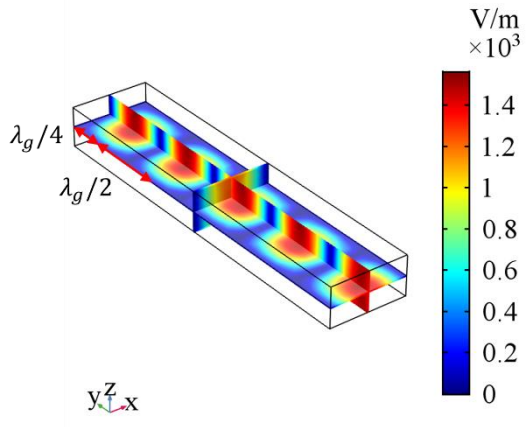


Figure 7.5 Standing wave electric field pattern of a short circuited TE_{10} waveguide

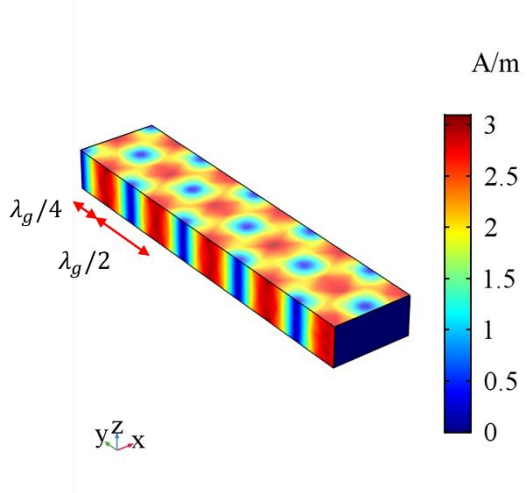


Figure 7.6 Standing wave surface current pattern of a short circuited TE_{10} waveguide.

Therefore, the first slot is positioned at $\lambda_g/4$ from the short-circuited end to coincide with a maximum electric field / high surface current from the standing wave pattern. Each slot is spaced by $\lambda_g/2$ of each other, and are alternated between top and bottom of the centreline, to be fed in phase, with slot length of approximately $\lambda_0/2$ to be resonant. This resulted in the slot pattern shown in Figure 7.7.

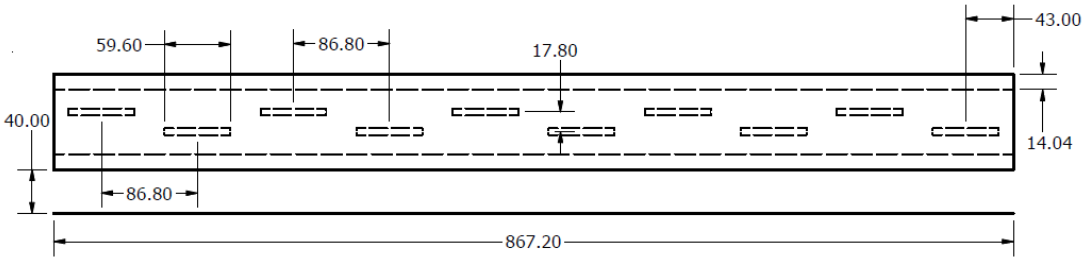


Figure 7.7 Slotted waveguide feed for parallel plate applicator at S-band, 6 mm slot thickness.

Electromagnetic simulations were performed to check their free space radiation properties using COMSOL. For this, a perfect matching layer with outer scattering boundaries (prevents waves to reflect back to the structure) was defined to emulate the behaviour in free space [330], as shown in Figure 7.8, with a far-field radiation pattern (Figure 7.9) showing the expected behaviour with a narrow horizontal and broad vertical beam.

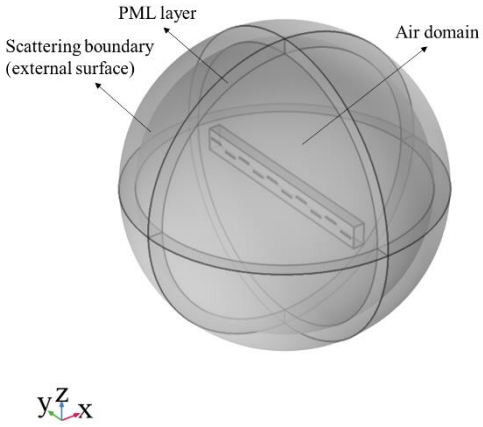


Figure 7.8 Free space model of slotted waveguide design

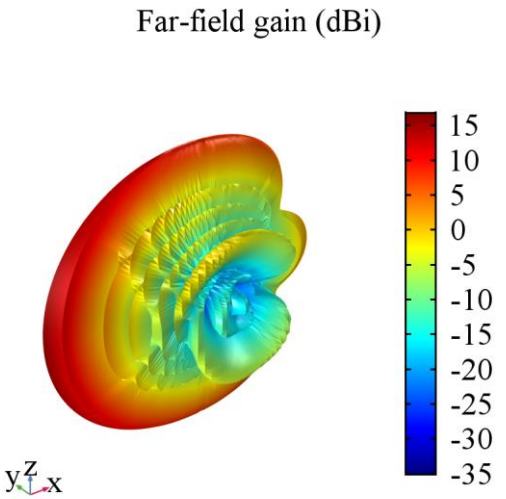


Figure 7.9 Far-field radiation pattern

The near field electric field components are shown in Figure 7.10, Figure 7.11 and Figure 7.12. It is clear that after a small distance, the only substantial contribution to the total fields is polarised in the vertical direction.



Figure 7.10 Electric field X polarisation component (horizontal)

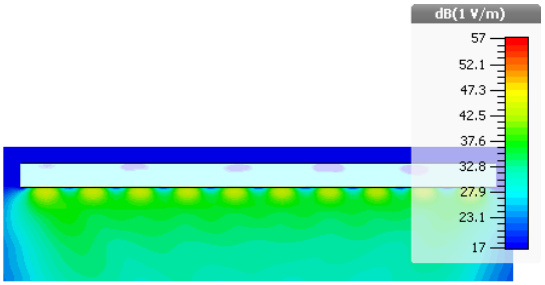


Figure 7.11 Electric field Y polarisation component (vertical)

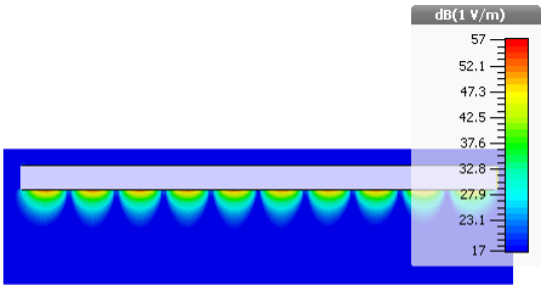
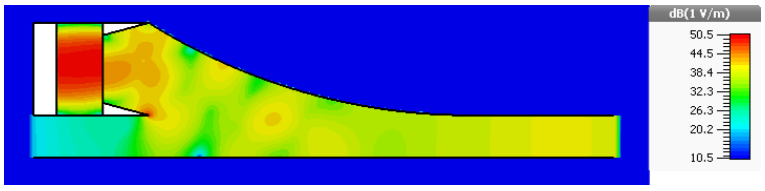


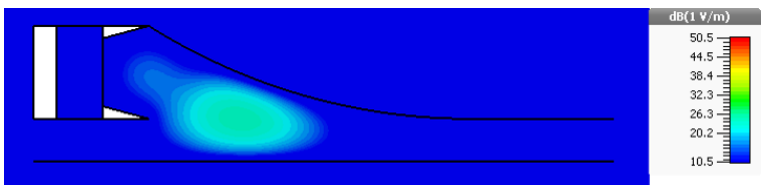
Figure 7.12 Electric field Z polarisation component (horizontal)

7.4.2 Field shapers

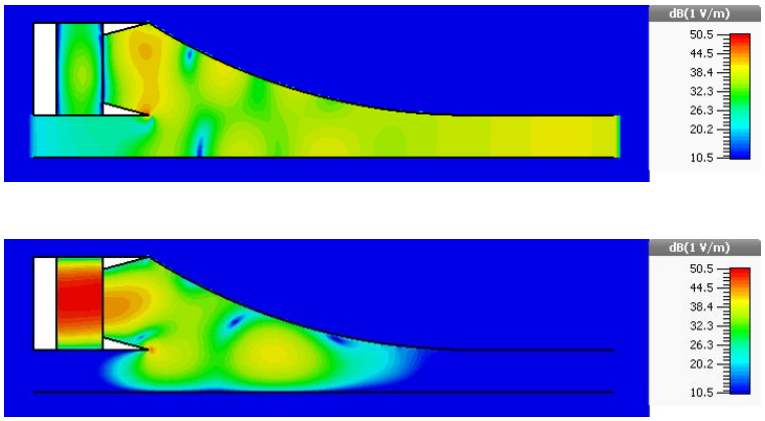
A set of reflective structures, as previously described, were used to shape the electric fields in order to provide a mostly vertical polarisation in the treatment zone, initially assuming an empty applicator. A multiparametric optimisation including wedge length, pitch angle, belt position as well as curvature radius was carried with the goal to achieve high coupling at the central frequency. Goals were partially achieved by manual parametric adjustment, and final dimensions were obtained by using the Trust Region Framework method implemented in CST Microwaves [329]. The electric field components of the resultant structure are illustrated in Figure 7.13, where it is noticeable that most of the heating zone is dominated by vertically polarised field components (Y direction).



(a)



(b)



(c)

(d)

Figure 7.13 Electric field distribution components (a) total, (b) X direction, (c) Y direction and (d) Z direction.

7.4.3 Product load

An undisclosed material (labelled m1) was used as the initial basis for design (details on the nature of the material could not be included in this document due to NDA). The material dielectric properties were measured using CPT in previous internal work with results shown in Figure 7.14. Two material presentations were considered, a matrix of material lumps of 50 mm x 50 mm x 25 mm with rounded edges and uniform spacing of 20 mm (Figure 7.15(a)), representing a typical briquette shape, and a continuous 25 mm height bed of 867 mm width (Figure 7.15(b)), representing a bed of finer particles ranging 10 to 20 mm.

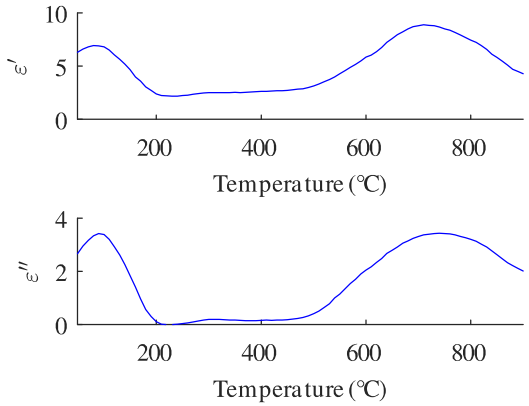
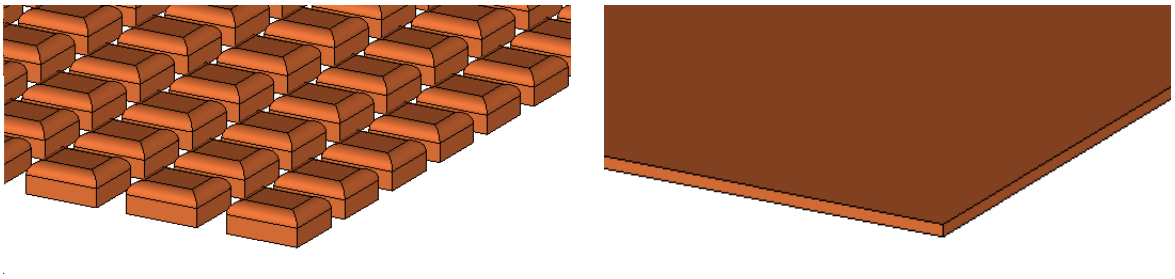


Figure 7.14 Complex permittivity versus temperature of material m1.



(a) (b)

Figure 7.15 Product presentation, (a) 50 mm x 50 mm x 25 mm lump matrix with uniform 20 mm spacing, and (b) continuous 25 mm height bed.

7.4.4 Model simplification

As discussed above, the applicator concept was developed to operate as a mirrored pair to improve treatment uniformity; however, the relatively large size and complexity of the model required a long simulation time. Simplifying the model was essential to allow efficient parametric sweep analysis and optimisation tasks.

The model was reduced to a half, using a conductive plate as a short circuit in the back end. A comparison between the full and half model reflection parameter is shown in Figure 7.16. The similitude between results suggests that the simplification is representative of the behaviour of the full model.

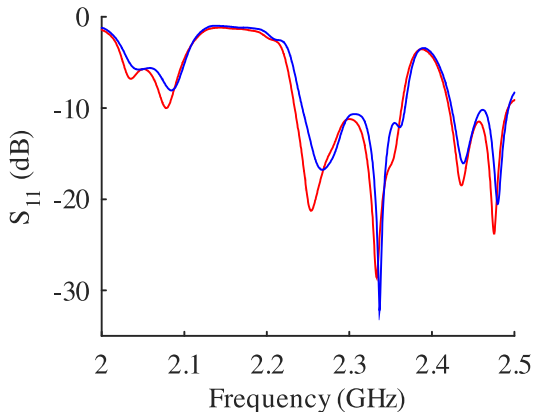


Figure 7.16 Reflection coefficient magnitude of the full mirrored model (red line) and simplified half model (blue line).

7.4.5 Initial results

The structure provides broadband coupling for the whole range of dielectric properties related to the expected variation of temperature during processing, as shown in the reflection coefficient plot in Figure 7.17.

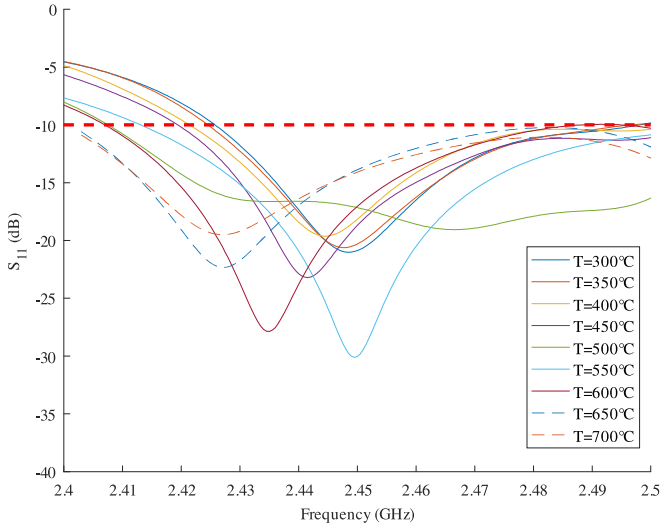


Figure 7.17 Reflection coefficient magnitude of matrix load for different temperature properties.

Power loss density plots for various temperatures are shown in Figure 7.18, Figure 7.19, Figure 7.20 and Figure 7.21. These reveal that for all temperatures, most dissipation occurs in the transition zone between the curved and straight reflector section, with a uniform treatment in the transverse direction. This would lead to good overall treatment uniformity, considering the product displacement through the belt. However, such design has a major flaw from both

efficiency and safety perspective as, in the worst case, up to 20% of the total power is being radiated.

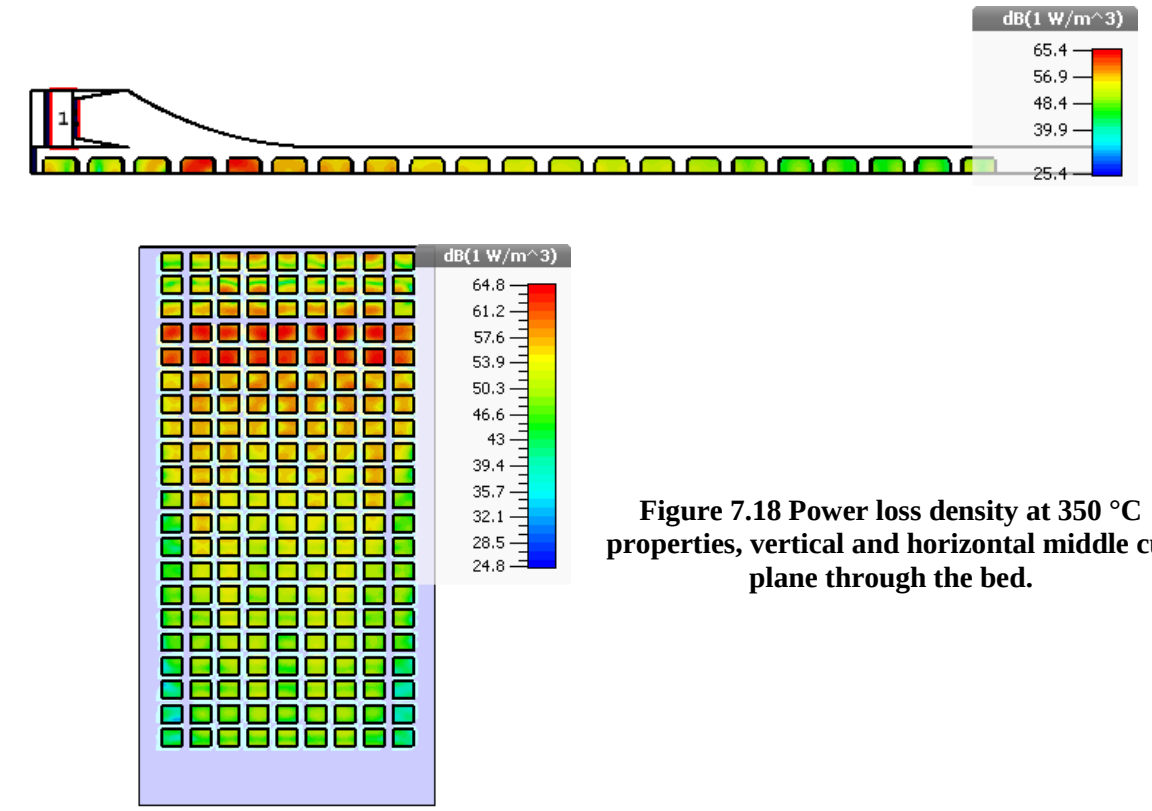
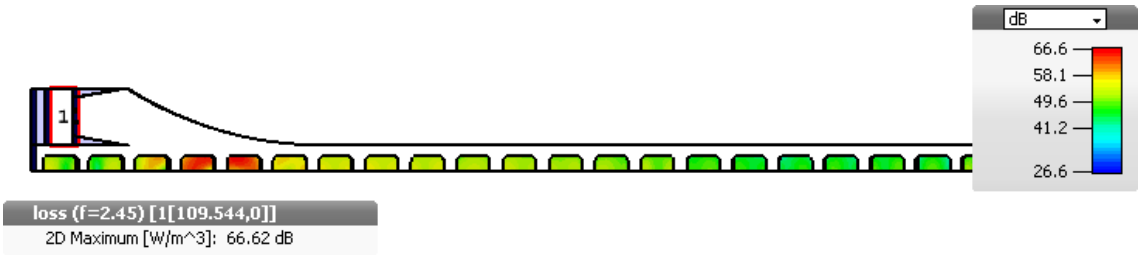


Figure 7.18 Power loss density at 350 °C properties, vertical and horizontal middle cut plane through the bed.



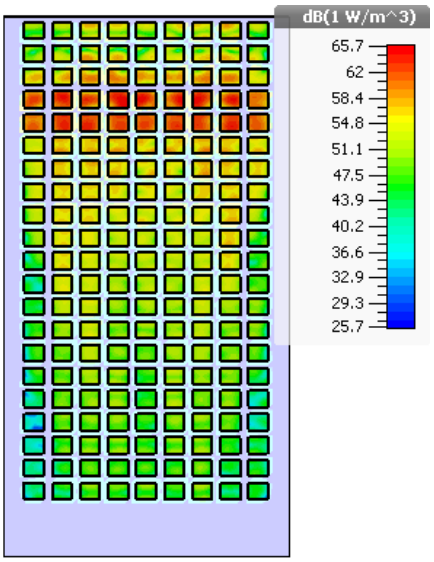
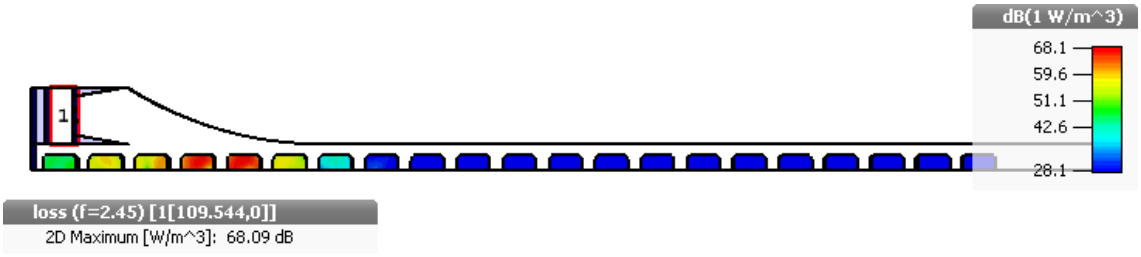


Figure 7.19 Power loss density at 450 °C properties, vertical and horizontal middle cut plane through the bed.



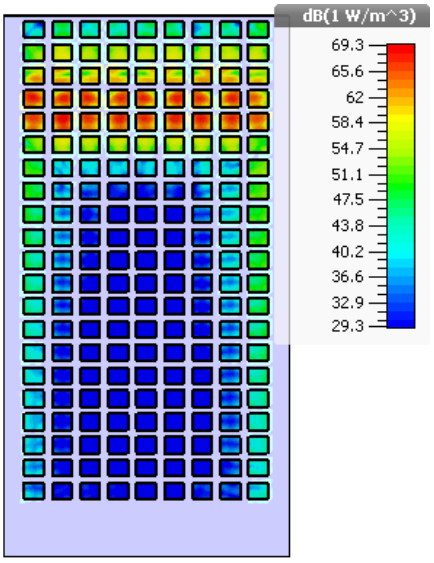


Figure 7.20 Power loss density at 550 °C properties, vertical and horizontal middle cut plane through the bed.

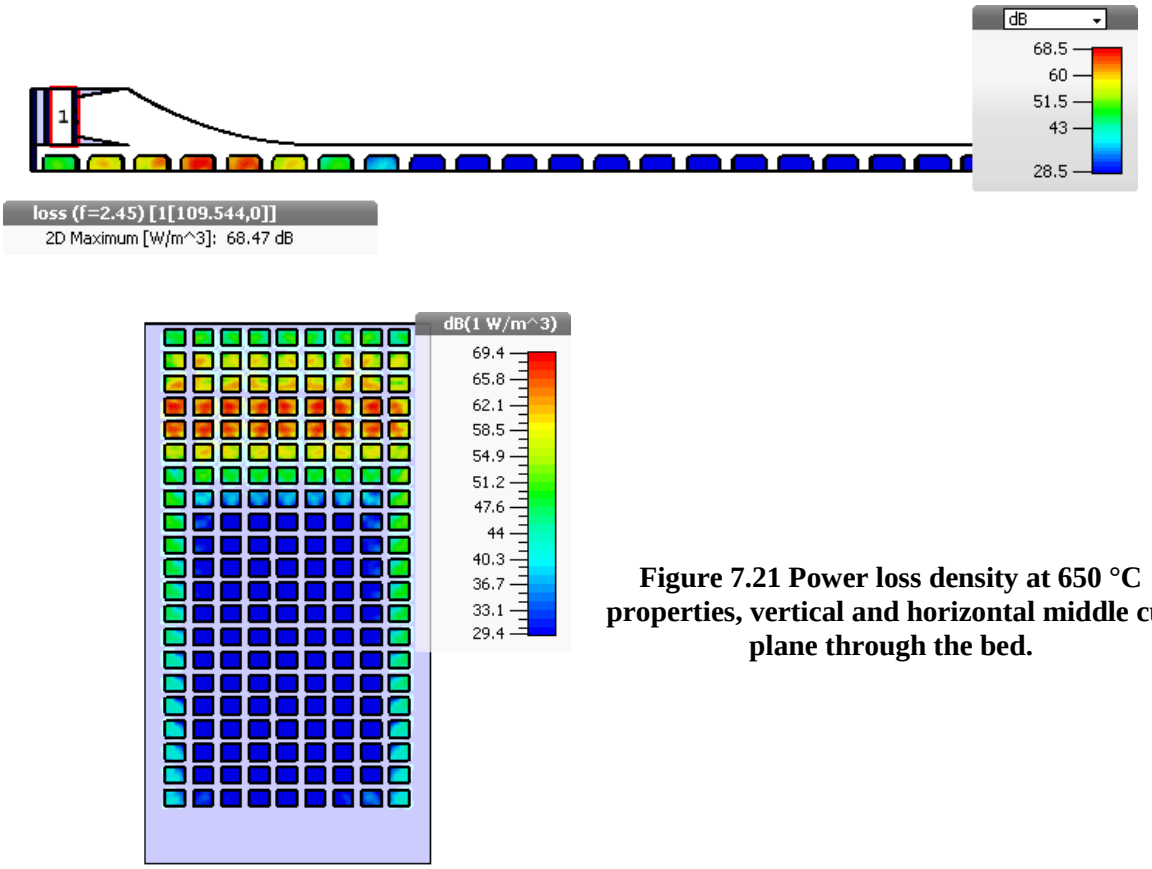


Figure 7.21 Power loss density at 650 °C properties, vertical and horizontal middle cut plane through the bed.

7.4.6 Microwave enclosure

Several attempts relying on dielectric enclosing failed to provide significant field leakage suppression unless high-absorption materials are used as in [439], [442]. However, this implies the inefficient use of energy and the inability to operate continuously without using large cooling systems. On the other hand, the use of metallic enclosing can effectively confine the radiation but introduce a significant reduction of the transverse uniformity. The use of full conductive enclosure was selected as a technical solution for the prototype development as was the only way to use high power inputs effectively in a safe manner. The used of applicator stages in series with complementary feeding patterns is therefore essential to provide uniform treatment homogeneity.

7.5 Prototype development

A static prototype was envisaged to validate numerical results. A broad range of material properties was chosen to evaluate the applicator behaviour. Simulations were carried with a fixed 25 mm height continuous bed. For validation purposes, FOAMGLAS© was selected as test material due to its thermal stability. Reflection coefficient measurements and thermal imaging were used as validation tests. Al tests and simulations were performed using a full metal enclosure spaced 5 cm from each side of the belt, and 36 mm from the belt to the enclosure floor. All simulations in the following sections were performed using COMSOL Multiphysics.

An annotated schematic of the prototype is shown in Figure 7.22, with main dimensions shown in Figure 7.23 and Table 7.2.

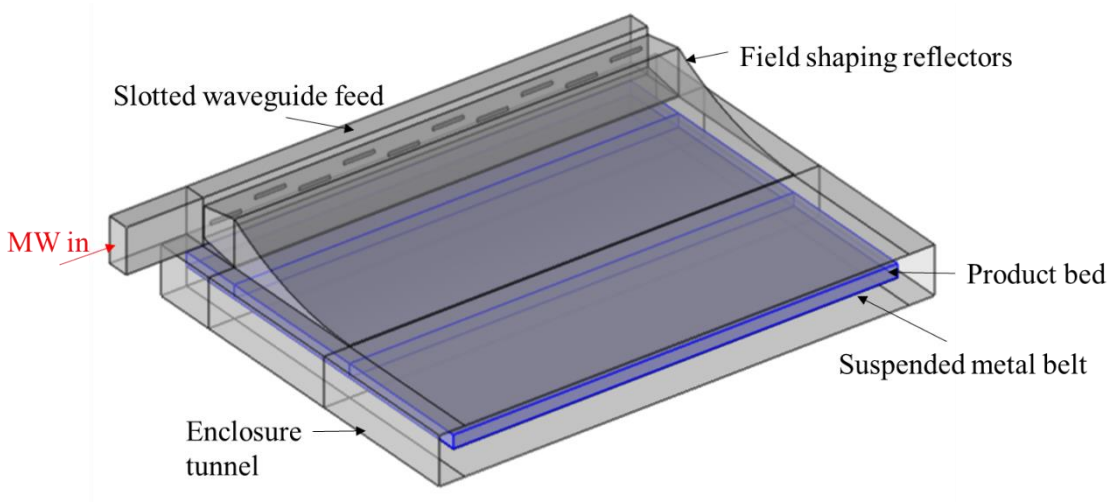


Figure 7.22 Parallel plate metal conveyor belt prototype conceptual schematic.

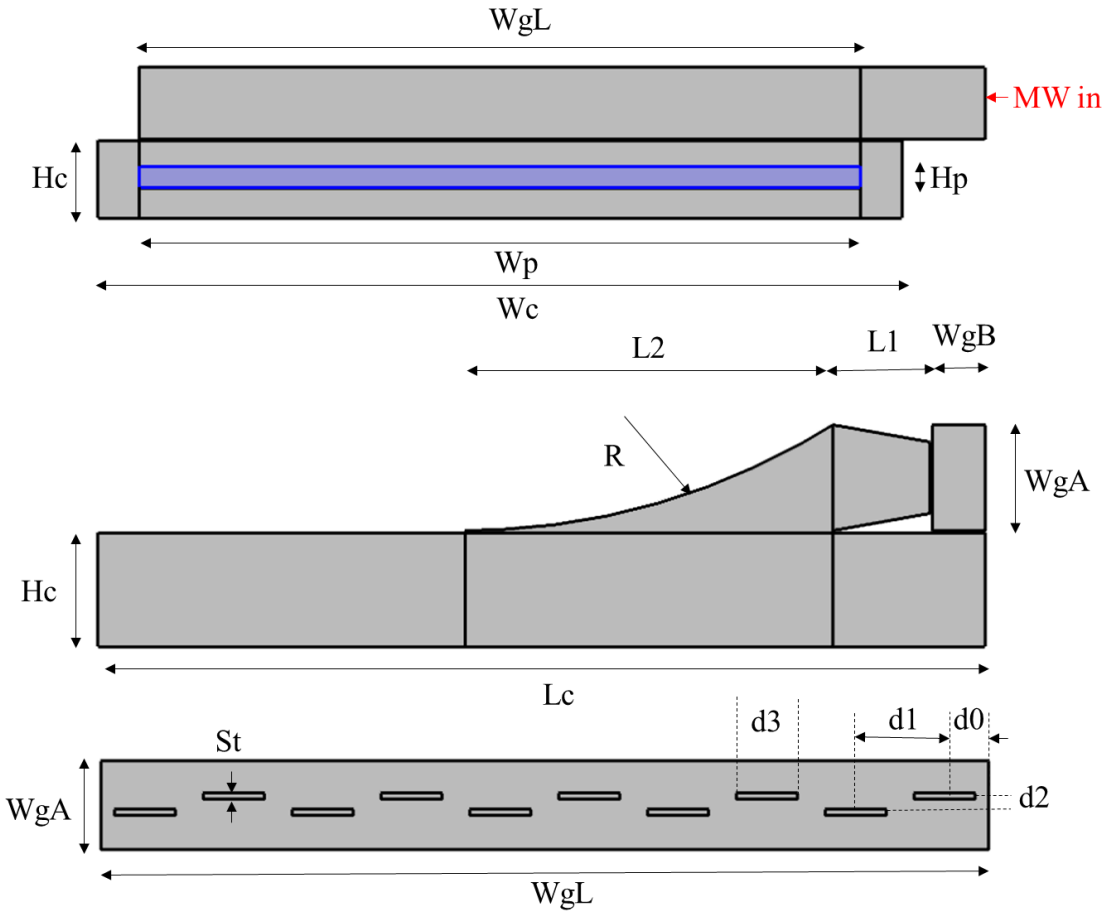


Figure 7.23 Parallel plate metal conveyor belt prototype main dimensions schematic.

Table 7.2 Dimensions of prototype parallel plate metal conveyor belt applicator

Dimension	Abreviation	Value (mm)
Feeding waveguide length	WgL	867.20
Cavity height	Hc	93.00
Cavity width	Wc	967.20
Product/belt width	Wp	20.00
Product height	Hp	25.00
Belt height	t	1.00
Wedge reflector length	L1	79.28
Curved reflector length	L2	300.00
Curved reflector radius of curvature	R	564.26
Waveguide narrow side	WgB	43.18
Waveguide broad side	WgA	86.36
Cavity length	Lc	724.46

Short to first slot centre spacing	d0	43.00
Slot to slot horizontal spacing	d1	86.80
Slot to slot vertical spacing (centred on waveguide centre-line)	d2	15.80
Slot length	d3	59.60
Slot thickness	St	6.00

7.6 Coupling sensitivity to material property change

Several material load properties were simulated demonstrating that the applicator structure has a relatively broad and robust range of operation. Dielectric constant from 1.5 to 15 and loss factors from 0.1 to 2 were studied. For simplicity, the end of the applicator tunnel was modelled as a short circuit plate, mimicking the behaviour of a reactive choke.

The reflection coefficient for each material type provides broadband coupling without the need for any tuning mechanisms as can be seen in Figure 7.24, Figure 7.25, Figure 7.26 and Figure 7.27. The lower loss materials with a loss factor of $\varepsilon_r'' = 0.1$, which are represented in solid lines show a relatively high reflection coefficient for dielectric constants of 4 and 8; nonetheless, these are still over 70% of coupled power for the whole simulated band and can be easily tuned with a network tuner element.

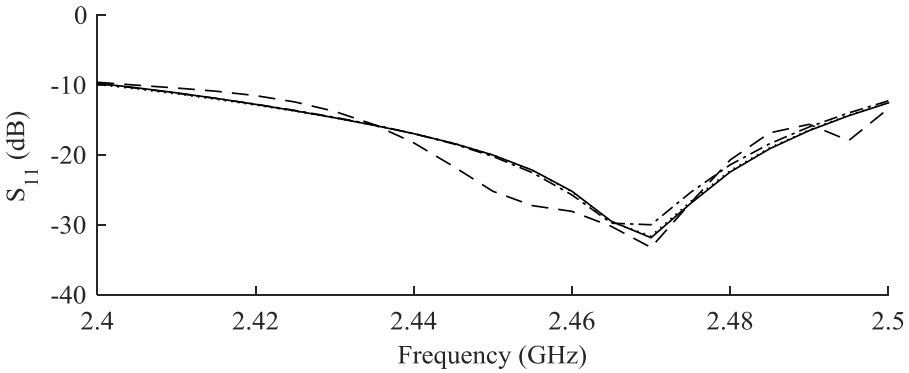


Figure 7.24 S_{11} parameter in (dB) for a 25 mm load with $\varepsilon_r' = 1.5$ and $\varepsilon_r'' = 0.1$ (solid line), $\varepsilon_r'' = 0.5$ (dash line), $\varepsilon_r'' = 1$ (dot line) and $\varepsilon_r'' = 2$ (dash-dot line).

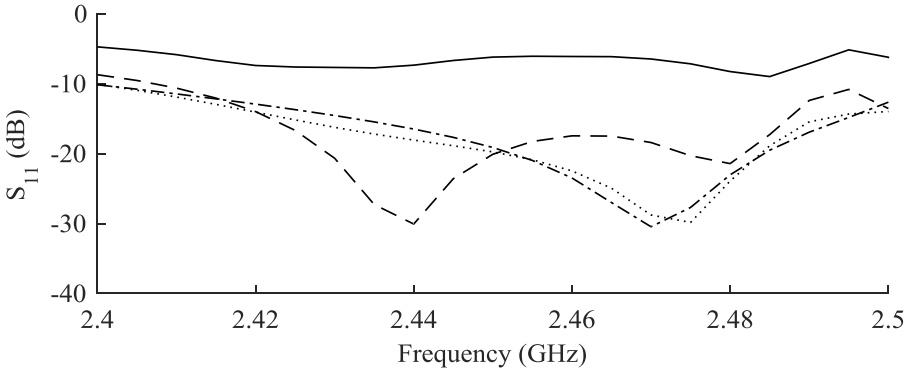


Figure 7.25 S_{11} parameter in (dB) for a 25 mm load with $\varepsilon_r' = 4$ and $\varepsilon_r'' = 0.1$ (solid line), $\varepsilon_r'' = 0.5$ (dash line), $\varepsilon_r'' = 1$ (dot line) and $\varepsilon_r'' = 2$ (dash-dot line).

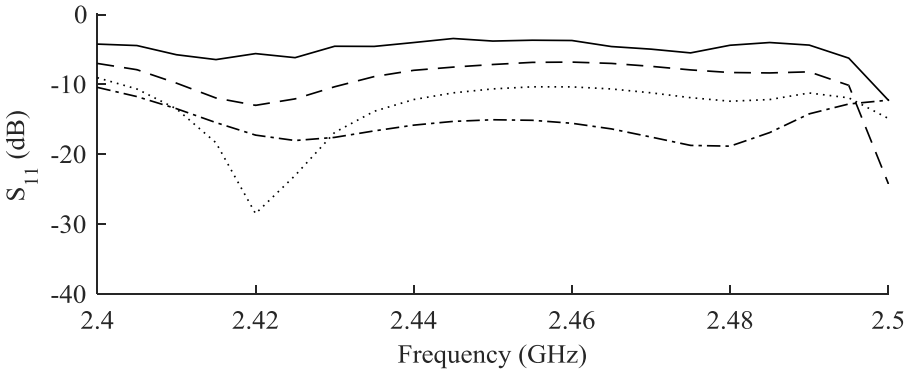


Figure 7.26 S_{11} parameter in (dB) for a 25 mm load with $\varepsilon_r' = 8$ and $\varepsilon_r'' = 0.1$ (solid line), $\varepsilon_r'' = 0.5$ (dash line), $\varepsilon_r'' = 1$ (dot line) and $\varepsilon_r'' = 2$ (dash-dot line).

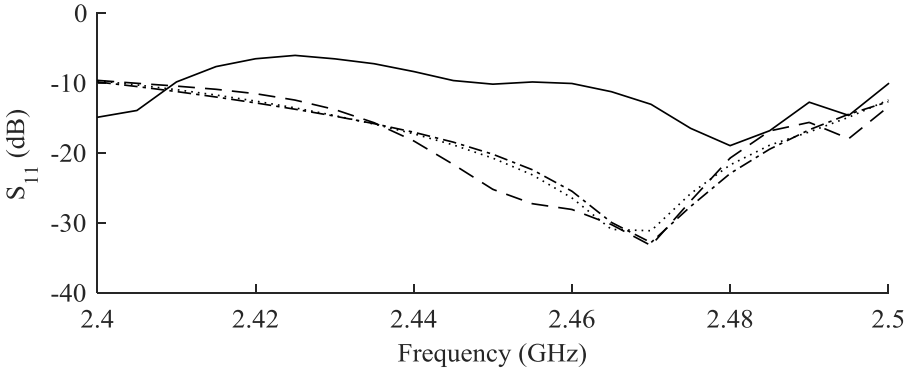


Figure 7.27 S_{11} parameter in (dB) for a 25 mm load with $\varepsilon_r' = 15$ and $\varepsilon_r'' = 0.1$ (solid line), $\varepsilon_r'' = 0.5$ (dash line), $\varepsilon_r'' = 1$ (dot line) and $\varepsilon_r'' = 2$ (dash-dot line).

7.7 Penetration of power and conversion efficiency

The same set of dielectric materials were simulated showing power loss density distribution plots are shown in Figure 7.28, Figure 7.29, Figure 7.30 and Figure 7.31, which

show that for the high loss factor cases the power is completely dissipated in a small area, whereas some of the low loss cases the loss is spread to the straight application section. This suggests that for the treatment of low loss materials the use of a longer applicator tunnel can improve matching characteristics although decreasing the achievable power density levels (i.e. longer tunnel will allow a larger effective heating volume). In all cases, effective heating up the belt interface was achieved. The low dielectric constant case of 1.5 shows preferential heating in the upper to central sections, whereas the higher dielectric constant cases (4, 8 and 15) shows a more evenly distributed power loss density across the vertical direction. Such behaviour can be attributed to the bigger electrical size of the high dielectric constant samples, and the higher reflective characteristics of the sample-air interface, creating the opportunity to set internal more densely populated standing wave patterns.

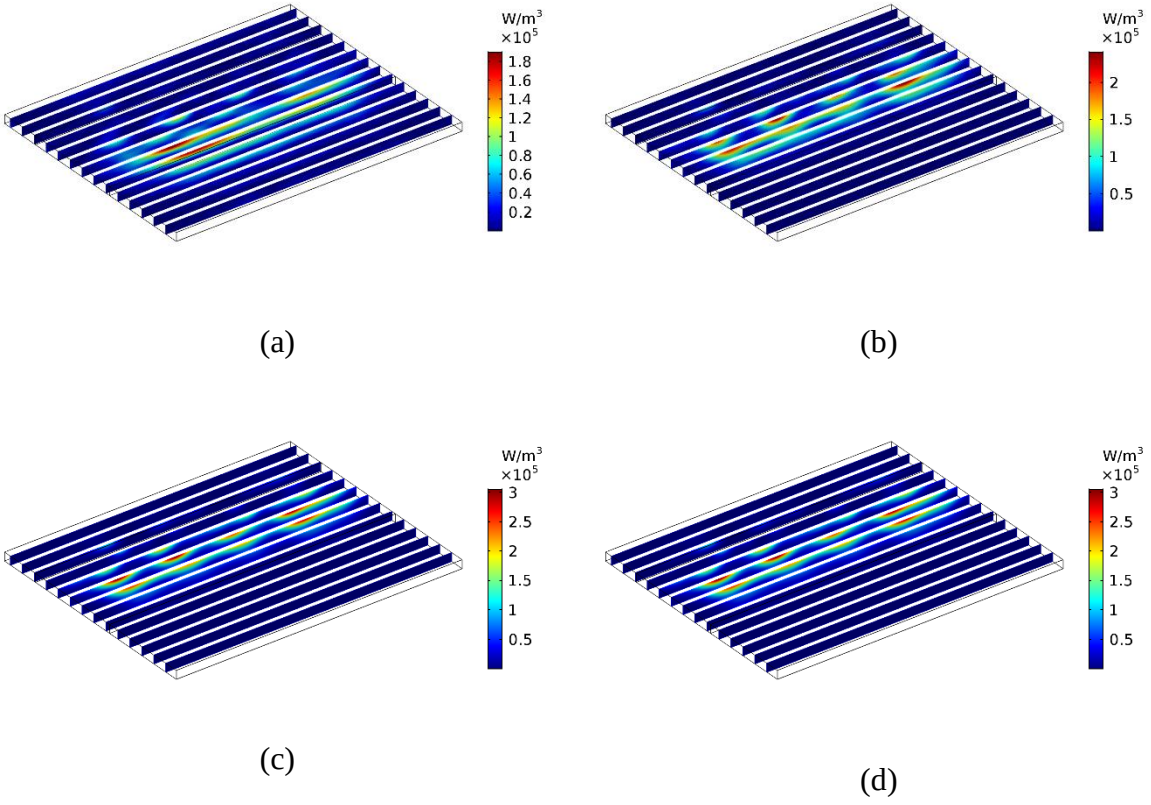


Figure 7.28 Power loss density (W/m^3) for a 25 mm load with $\varepsilon_r' = 1.5$ and $\varepsilon_r'' = 0.1$ (a), $\varepsilon_r'' = 0.5$ (b), $\varepsilon_r'' = 1$ (c) and $\varepsilon_r'' = 2$ (d).

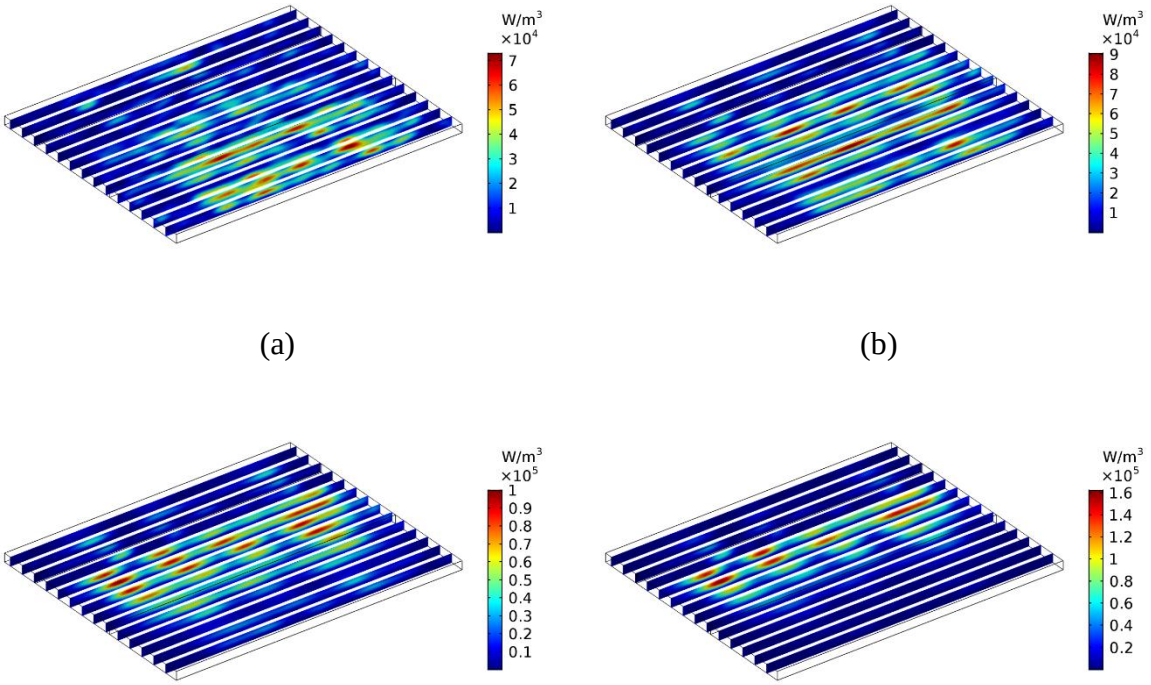
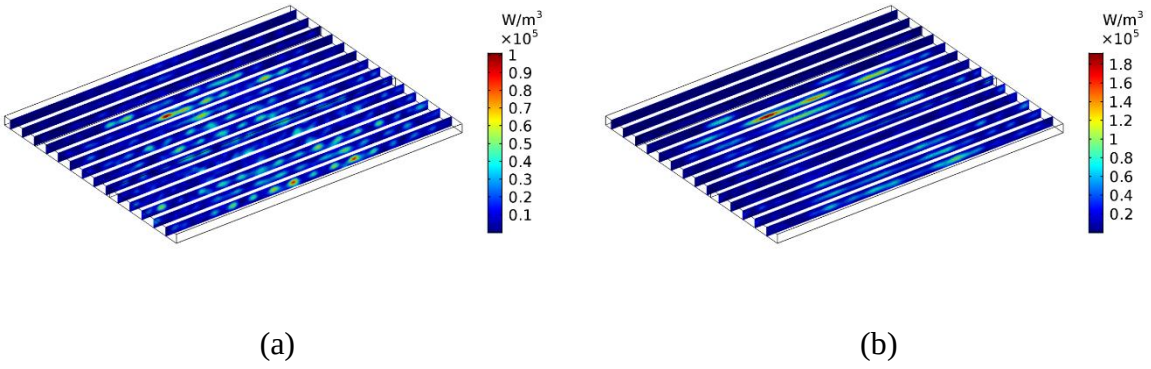
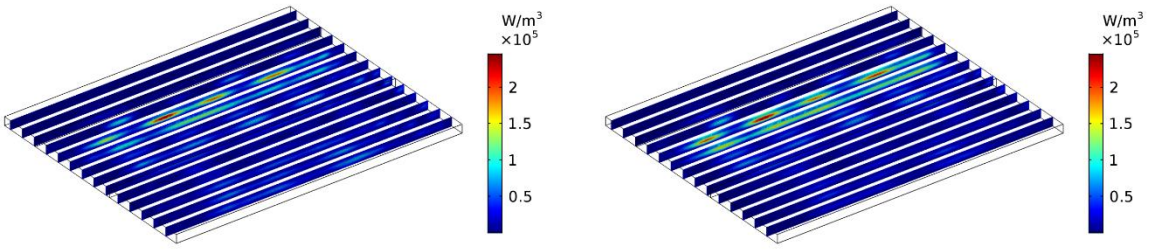


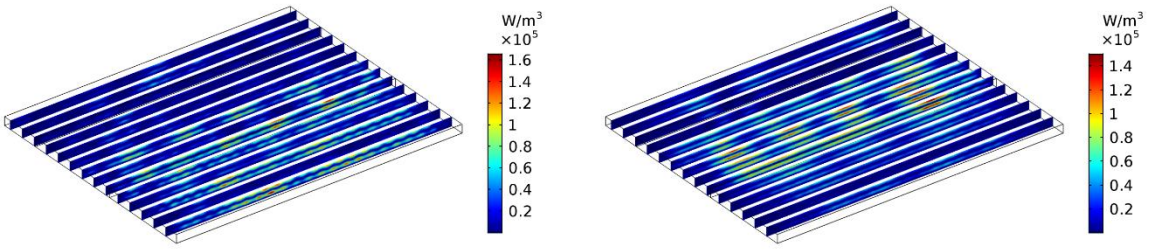
Figure 7.29 Power loss density (W/m^3) for a 25 mm load with $\varepsilon_r{}' = 4$ and $\varepsilon_r'' = 0.1$ (a), $\varepsilon_r'' = 0.5$ (b), $\varepsilon_r'' = 1$ (c) and $\varepsilon_r'' = 2$ (d).



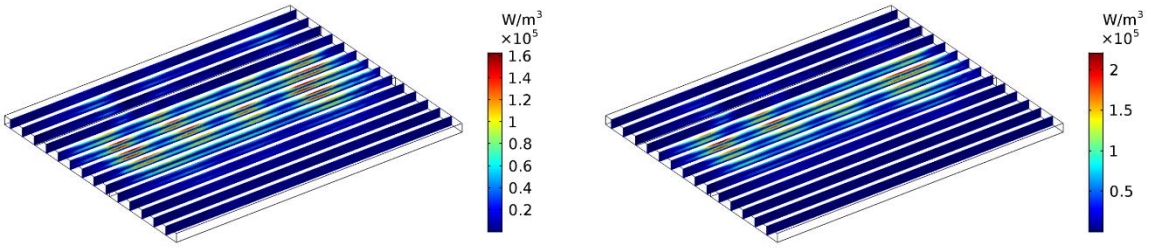


(c) (d)

Figure 7.30 Power loss density (W/m³) for a 25 mm load with $\varepsilon_r' = 8$ and $\varepsilon_r'' = 0.1$ (a), $\varepsilon_r'' = 0.5$ (b), $\varepsilon_r'' = 1$ (c) and $\varepsilon_r'' = 2$ (d).



(a) (b)



(c) (d)

Figure 7.31 Power loss density (W/m³) for a 25 mm load with $\varepsilon_r' = 15$ and $\varepsilon_r'' = 0.1$ (a), $\varepsilon_r'' = 0.5$ (b), $\varepsilon_r'' = 1$ (c) and $\varepsilon_r'' = 2$ (d).

A case of study for a material in which the penetration could be close to critical, a FOAMGLAS® bed of 25 mm height. For such material, the calculated penetration depth is of about 29 mm (~36.8 % of its surface value). Two cases were examined, with the product

directly over the metal belt, and considering a 1 cm dielectric layer ($\varepsilon_r = 3 - j0.01$) between the product and the belt, representing refractory insulation.

7.7.1 Product directly over the belt

The power loss density distribution in the top, middle and bottom of the product bed are shown in Figure 7.32, Figure 7.33 and Figure 7.34 respectively for a power input of 300 W. Similar power distributions are seen for all heights, with a decay to about 51% of the surface value in the middle, and to about 30 % in the bottom plate (calculated in reference to the maximum). Considering the metallic structures as made of stainless steel, a 98 % conversion efficiency is reached.

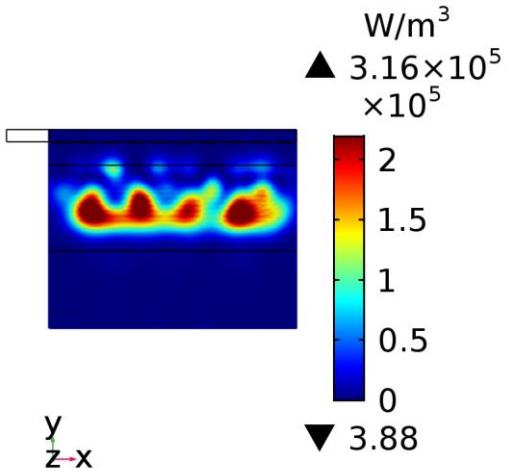


Figure 7.32 Power loss density (W/m^3) for a 25 mm FOAMGLAS® load, at its top surface.

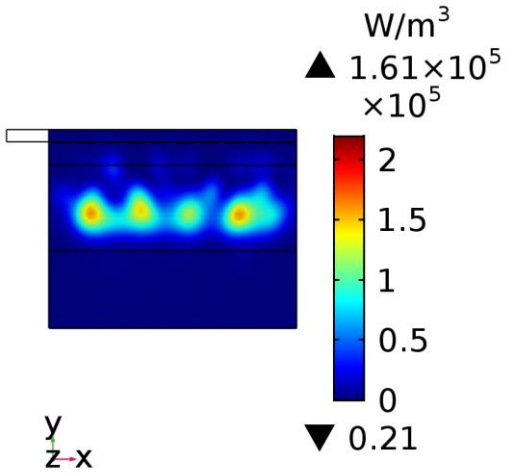


Figure 7.33 Power loss density (W/m^3) for a 25 mm FOAMGLAS® load, at its middle point.

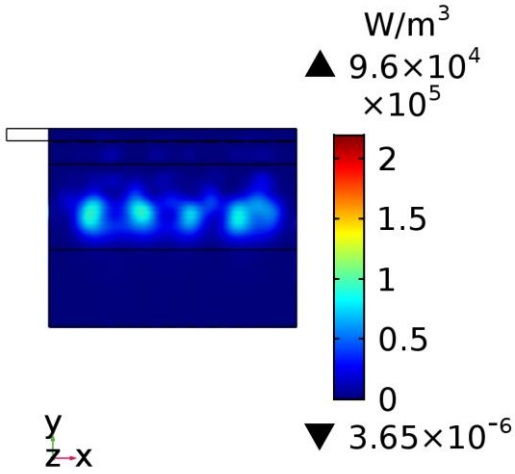


Figure 7.34 Power loss density (W/m3) for a 25 mm FOAMGLAS® load, at its bottom surface.

7.7.2 The dielectric interface between product and belt

The power loss density distribution in the top, middle and bottom of the product bed are shown in Figure 7.35, Figure 7.36 and Figure 7.37 respectively for a power input of 300 W. All zones exhibit a comparable distribution, with a decay to about 72% of the surface value in the middle, and about 47% in the bottom plate (calculated in reference to the maximum). Considering all the metal parts as made of stainless steel, a 98% conversion efficiency is reached, with the rest of the power being dissipated mostly in the metallic structures.

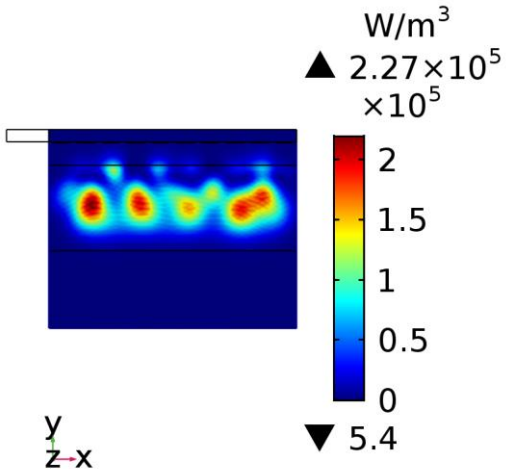


Figure 7.35 Power loss density (W/m³) for a 25 mm FOAMGLAS® load, at its top surface, with a 1 cm refractory layer ($\varepsilon_r = 3 - j0.01$) between belt and product.

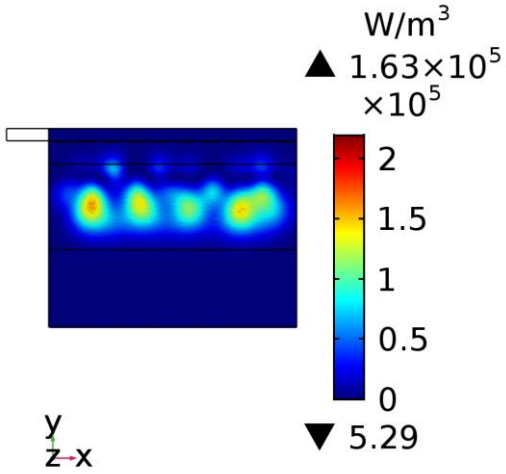


Figure 7.36 Power loss density (W/m³) for a 25 mm FOAMGLAS® load, at its middle point, with a 1 cm refractory layer ($\varepsilon_r = 3 - j0.01$) between belt and product.

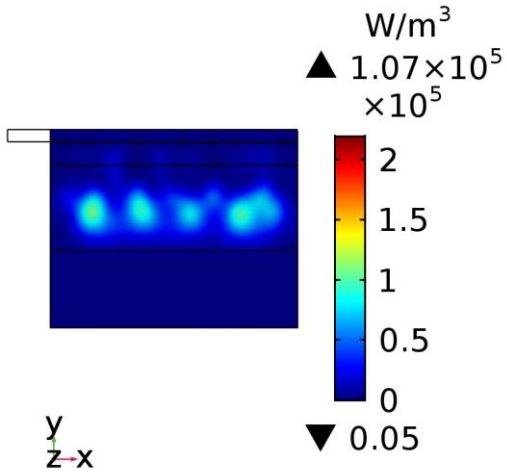


Figure 7.37 Power loss density (W/m3) for a 25 mm FOAMGLAS® load, at its bottom surface, with a 1 cm refractory layer ($\varepsilon_r = 3 - j0.01$) between belt and product.

It is apparent that the use of an interface between the metal belt and the product can effectively provide a suitable way to increase the vertical treatment uniformity.

7.8 Transverse uniformity

In order to illustrate the transverse uniformity of the heating resulting from the material movement through the heating zone, a linear projection of the power loss density on their surface was calculated (i.e. average power loss density along y axis). An estimation of the uniformity of the data, considering the heating zone from x-axis -300 mm to 300 mm was performed by the following relation

$$\%\ Uniformity = \left(1 - \frac{Standard\ deviation}{Average}\right) \times 100\%$$

For example, for a product bed with $\varepsilon_r = 4 - j$, the linear projection is shown in Figure 7.38, revealing a rather uniform transverse heating within a limited heating zone, between -300 and 300 from the x-axis centre. This case results in an estimated 88 % uniformity within this zone. The same estimation was performed for the set of materials properties, with results summarised in Table 7.3, with uniformities ranging from 78 to 92 %.

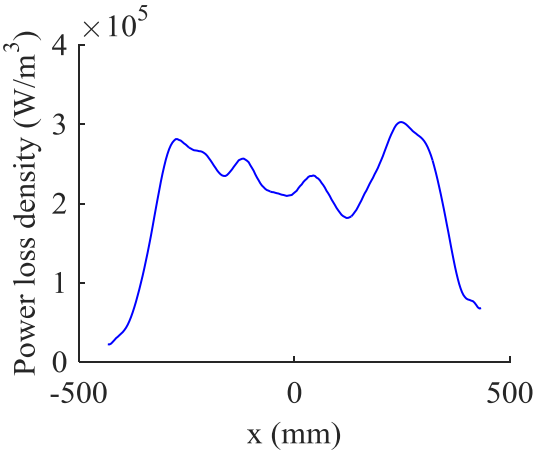


Figure 7.38 Linear projection of the power loss density (W/m³) for a 25 mm load with $\varepsilon_r' = 4$ and $\varepsilon_r'' = 1$ at its top surface.

Table 7.3 Power loss density uniformity across the heating zone.

Dielectric constant	Loss factor	Uniformity in heating zone surface
1.5	0.1	82%
	0.5	80%
	1	77%
	2	78%
4	0.1	83%
	0.5	91%
	1	88%
	2	82%
8	0.1	80%
	0.5	87%
	1	92%
	2	90%

7.9 Cross-coupling in a mirrored setup

In a mirrored setup, the separation between feeding sections needs to be optimised for the minimisation of cross-coupling between ports and depends on the material product properties. A parametric swept comparing the cross-coupling against the separation between feeds is shown in Figure 7.39, for a 25 mm height load of $\varepsilon_r = 4 - j$. Although most positions present relatively low cross-coupling for the example case, this can be a critical feature to optimise for the treatment of low loss products, where a more significant part of the radiation could travel in a backward direction.

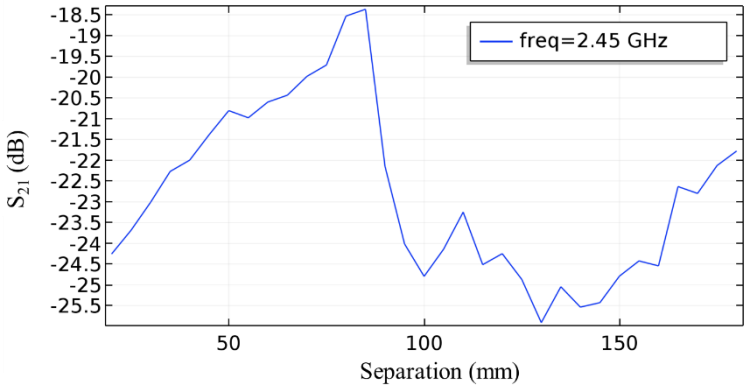


Figure 7.39 Cross-coupling for a 25 mm load with $\varepsilon_r' = 4$ and $\varepsilon_r'' = 1$.

7.10 Coupling tolerance to change of position

To illustrate the robustness of the system to changes of the bed position, various positions were simulated, from the bottom of the enclosure to the top for a FOAMGLAS® 25 mm tall bed. The change of reflection coefficient magnitude at 2.45 GHz with a vertical position of the bed is shown in Figure 7.39.

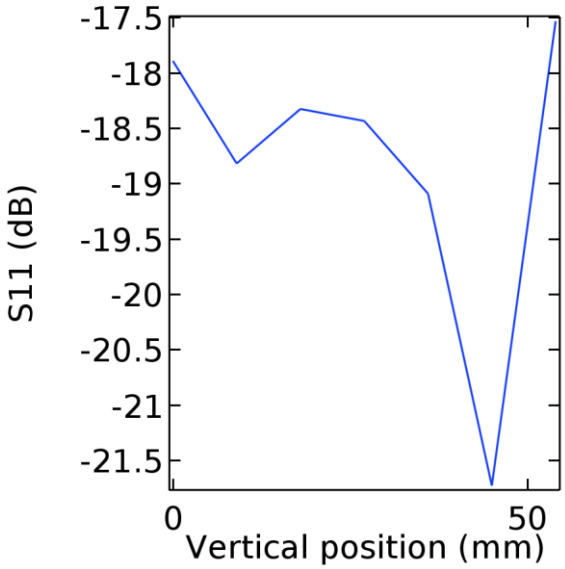


Figure 7.40 Simulation of the reflection coefficient magnitude versus vertical position of the bed for a 25 mm tall FOAMGLAS® bed.

7.11 Experimental validation

A static prototype was built with waveguide parts made of aluminium, and reflective surfaces, the enclosure, and the belt made from steel. The testing setup is shown in Figure 7.42,

using a 25 mm tall bed made of FOAMGLAS® tiles. A thermal image of the product bed after heating for 1 minute at 135 W and cooling for 2 minutes is shown in Figure 7.43, while the simulated power loss density is shown in Figure 7.44. The similarity between both is apparent, although they are some small discrepancies, which can be mostly attributed at the low fabrication accuracy of the prototype. The measured and reflected reflection coefficient are also of similar characteristics as can be seen in Figure 7.45, both with resonance levels slightly below -32 dB and displaced in about 23 MHz, with 69 MHz and 76 MHz -10 dB bandwidths for the experimental and simulation respectively. The reflection coefficient with the tunnel end open or close was the same, as the length is enough for practically full power dissipation. The heating experiments were done with a closed tunnel end.

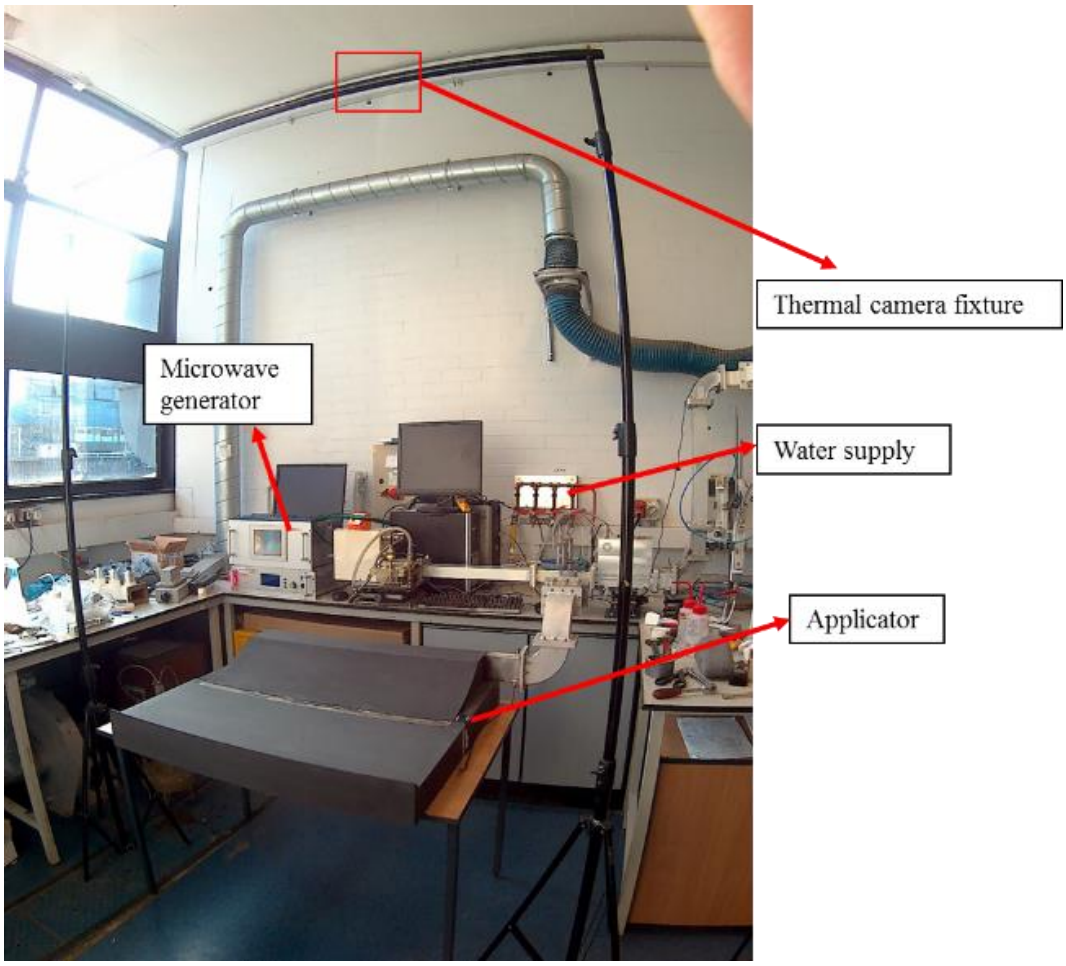


Figure 7.41 Parallel plate applicator testing rig.



Figure 7.42 Parallel plate applicator testing rig product load.

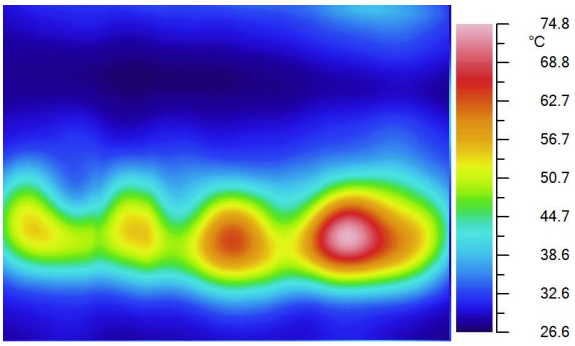


Figure 7.43 Experimental thermal image of a 25 mm tall FOAMGLAS® heated for 1 minute at 135 W and cooled for 2 minutes.

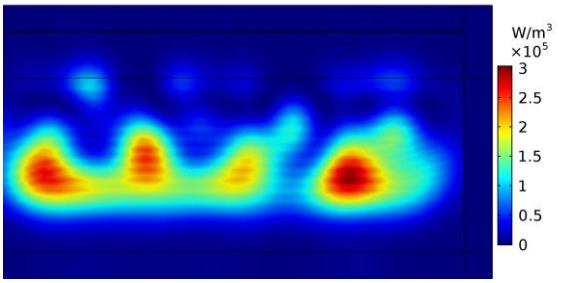


Figure 7.44 Power loss density distribution simulation of a 25 mm height FOAMGLAS® load (300 W input) at 2.45 GHz.

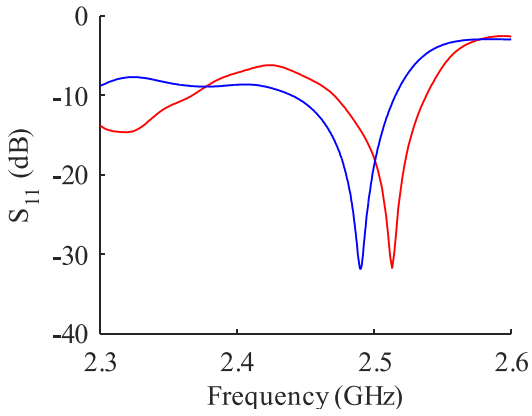


Figure 7.45 Metal conveyor applicator reflection coefficient magnitude simulation (blue line) and experimental measurement (red line).

7.12 Scale-up

The most direct approach to scale-up is by decreasing the operational frequency to 896 MHz. Considering a volumetric scale-up proportional to the wavelength, the frequency change would lead to an increase of the bed volume by a factor of 20. Furthermore, the system could be scaled more by widening it and increasing the number of slots as appropriate. This would require to also scale-up the power capacity of the system proportionally.

As an example, a directly scaled version of the applicator was simulated showing roughly the same behaviour seen before for a FOAMGLAS® bed (dielectric properties at a close frequency of 915 MHz measured by CPT resulting in $\varepsilon_r = 1.555 - j1.43$), as can be seen from the electric field distribution and power loss density distribution plots (Figure 7.46 and Figure 7.47). In this case, the bed height was 68 mm and its width 2.4 m. As seen in the

reflection coefficient magnitude plot (Figure 7.45), a resonance shows slightly above 900 MHz, with a 36 MHz -10 dB bandwidth.

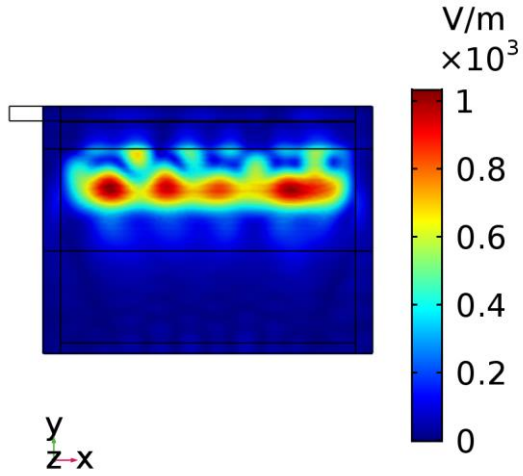


Figure 7.46 Electric field distribution simulation of a 68 mm height FOAMGLAS® load (300 W input) at 896 MHz.

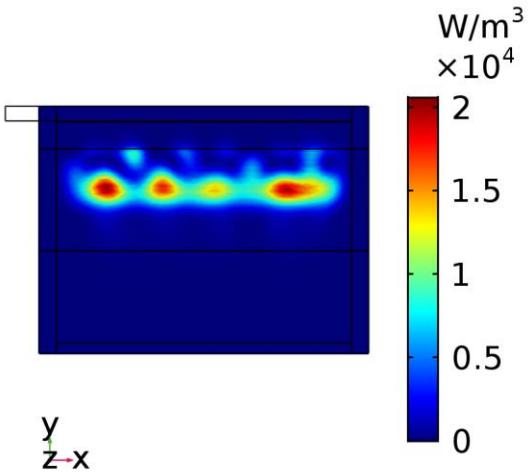


Figure 7.47 Power loss density distribution simulation of a 68 mm height FOAMGLAS® load (300 W input) at 896 MHz.

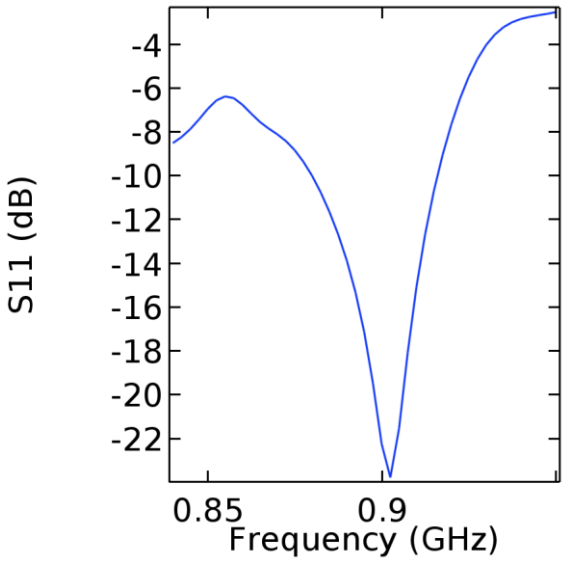


Figure 7.48 Metal conveyor applicator reflection coefficient magnitude simulation for a scaled 896 MHz design.

7.13 Conclusions

A solution for a scalable microwave applicator technology able to handle products of over 10 mm size for the implementation of robust high-temperature processes over 600 °C, where microwave transparent belts become unpractical, was proposed, as current technologies failed to deliver means for scale-up. The concept consists of a parallel plate structure in which the lower plate acts as a material transport carrier (i.e. metal conveyor belt), with a metallic enclosure to prevent leakage. Among possible applications, coke-making and the direct reduction of iron were discussed as attractive candidates.

The proposed concept addressed the major concerns of using a conductive conveyor belt were addressed by the proposed concept. Improved field levels on the material near the belt can be obtained by delivering a predominantly vertical polarisation by a combination of a slotted feed waveguide, reflectors and a parallel plate structure, in which the metal belt acts as the bottom plate. The field penetration could be further improved by the use of a microwave transparent dielectric layer, likely in the form of transparent ceramic sand. The microwave leakage was sorted by the use of a complete microwave enclosure, improving both efficiency and safety of operation.

The use of slotted waveguide feed allows high-power handling and a relatively uniform illumination when using back to back to a mirrored applicator. Given the mostly forward propagation of the power, a relatively low cross-coupling can be observed of less than -20 dB.

A prototype was fabricated and used to validate the simulations models by comparing its heating behaviour and its frequency response, with similar results. However, deviations were apparent which can be attributed mostly to the lack of fabrication accuracy.

The metal conveyor material handling strategy could manage to transport large volumes and therefore high throughputs. The size of the system will be bound by the operational

frequency, which for industrial purposes is likely to be the 896 MHz frequency band. The width of the conveyor belt can be considerably wide, limited mostly by mechanical constraints.

Chapter 8 Conclusions

Microwaves have been proven as a suitable alternative to conventional heating technologies for material processing when significant advantages can be identified. Typically these relate to fast volumetric heating or selective heating and often these mechanisms will be significant where microwave-material processing is most valuable, both technically and commercially. The interaction between microwave energy and materials is controlled by two main material properties, the electrical permittivity and magnetic permeability. These properties are a function of the product and the chemical composition, density, operating frequency and temperature, making knowledge across operational conditions critical for the design of a microwave processing system. Of course, they are also observed to change with temperature making the design of a microwave processing system for elevated temperature a complex task.

The literature review revealed that, although a broad range of microwave heating applications had been successfully demonstrated at laboratory scale, commercial systems have been limited to relatively low-temperature processes, where the product reach less than 250 °C. In high-temperature applications, particular consideration should be given to the selection of material handling techniques, by-product handling, thermal insulation, structural materials, metrology, and control equipment, as well as compatible microwave application technologies and the more common occurrence of effects such as arcing and plasma generation. In many cases this is a non-trivial matter, particularly where the off-gas from the process contaminates the system and carbonises on contact with microwave energy.

Most problems with high-temperature microwave processes appear to be common across different industry sectors. The need for a thorough understanding of microwave and material interactions and detailed characterisation of its properties variations under different process states is key; thus, precise measuring and predictive methods are paramount. System

design needs to account for material volume, material flow, field uniformity and distribution, field or material stirring, power density, temperature distribution, penetration depth, thermal runaway and arcing. Furthermore, systems should be robust and safe for continuous operation under harsh conditions, using adequate construction materials, microwave leakage suppression, thermal insulation, gas handling and atmospheric control. Methods for waste and contamination management, metrology, matching and control of the process are needed to ensure efficiency, safety, and adequate process conditions. All these considerations make the development of high-temperature microwave systems for industrial-scale a highly complex engineering challenge. Due to the diversity of parts involved in the process, the design effort should take a multidisciplinary approach with a holistic view of the problem and, to date, most solutions have only been developed at a laboratory scale without significant prospects or analysis pointing to ways for scale-up.

In this thesis, design and validation frameworks were set and various concepts were developed which provide a clear path for scale-up, with prospects of usage for different applications and for a broad range of product types and properties. Particular attention was given to the compatibility between materials handling and microwave application techniques and system robustness to open the scope to high-temperature applications and to provide a testing platform for the development of new large-scale microwave processes, currently under investigation.

8.1 Design and validation framework

The microwave measurement methodologies, dielectric properties characterisation techniques, and thermal imaging measurement procedures used as a base for modelling and validation of models were defined. A general framework for the electromagnetic modelling of microwave heating systems using COMSOL RF Module was proposed and tested experimentally by network measurements and thermal imaging of a variety of materials in both

a single-mode and multimode systems. These validations supported the suitability of the tool and modelling methodology as an adequate approach for the design of microwave heating systems in the Thesis scope.

8.2 Applicator technology for processing of liquids and fine powders

An alternative to common TE_{10} single-mode application systems was proposed in the form of an elliptical cylindrical cavity. The aim was to provide a stable high power density applicator system without mode degeneracy (i.e. apparition of electric field pattern that shares resonant frequency with the intended operational mode) for operation using higher order modes and for use in high power density experiments in batch and continuous flow.

The operation principles of this concept were described and analysed, and a general design methodology was proposed and validated experimentally by using a test material (i.e. copper ore in granular 3 mm - 4 mm samples). Simulated and experimental results showed a -10 dB bandwidth of 9 MHz and 8 MHz, with quality factors of 198 and 233 respectively, showing good agreement.

Results also suggested that the technology can effectively provide elevated power densities (e.g. near to physical limitations of the product load power densities were achieved at levels which regularly resulted in arcing, plasma formation and burning of test tubes), and can deliver a relatively uniform, reliable and consistent treatment that can be tailored by design. This could serve as a replacement to rectangular and circular cross-section cavities for operation in high order modes without mode degeneracy in systems where the cavity size and stability of the field position is critical.

Although the technology seemed flexible for use with several materials for experimental purposes, examination of material handling limitations showed that effective throughputs could

be considered low, given small sample holder diameters (e.g. 2 cm diameter for a 2,450 MHz reference design). This limitation narrowed the scope of its use for large-scale systems to flow microwave chemistry applications such as the processing of waste oils and plastics, in which the product can be pumped continuously through the system, or for treatment of fine powders. In such systems extreme conditions of pressure and temperature are expected, requiring careful selection of construction materials which are chemically and microwave compatible within the process range. All these applications would require dedicated research on how to handle the different by-products from the processes.

Envisaged alternatives for scale-up included the parallelisation of processing lines and the reduction of operational frequency to handle significantly larger volumes (e.g. about 19 times the volume for a decrease from 2,450 MHz to 915 MHz). Alternatively, a design modification to process considerably larger product loads was introduced in the form of several offset applicators in series, which require the use of microwave choking structures (an example design of such a structure was given).

8.3 Applicator technology for processing of granular products

A novel hybrid heating convection-microwave fluidised bed reactor was proposed for treatment of a broad range of granular products ranging from a few millimetres up to around 2 cm particle size. Several applications could be based on such technology, of which the fast pyrolysis of biomass and coals were discussed as promising candidates to take advantage of its main characteristics. The combination of conventional convection heating by a toroidal fluidised bed with fast volumetric microwave heating provides an effective way to rapidly heat low thermal conduction materials of relatively large size using microwaves efficiently, and by mixing the bed without moving parts within the reactor, can provide a uniform treatment with reduced likelihood of hotspots and arcing events.

Fluidised beds struggle when dealing with a bed of large and irregular feedstocks with low thermal conductivity, due to heat conduction limitations, which can be addressed using volumetric microwave heating. Moreover, conventional fluidising technologies need regularly shaped fine feedstocks to provide consistent fluidisation regimes, while the toroidal fluidising technology had been proven to be able to handle irregular particle size distribution in a single bed up to 2-centimetre sizes whilst also providing a consistent bed.

On the other hand, microwave systems can struggle to provide uniform treatment to highly absorbent materials at high temperatures due to low and highly variable penetration depths, hotspots and arcing occurrence. Also few in any large-scale solutions can be found most likely due to the lack of robustness of microwave compatible conveying solutions and the likely need for metallic moving parts to improve uniformity in large batch systems. These issues can be wholly addressed by the mixing mechanisms of the toroidal fluidised bed. Furthermore, the hybrid heating approach allows heating the bed by convection to surpass the point where microwaves are ineffective (i.e. temperatures where the feedstock is microwave transparent) and to introduce the microwave heating at an optimal processing stage. The emission of volatiles and chemical evolution of the products require careful consideration on the handling. The current concept considere cyclones for capturing solid fines and the use of a scrubber system for the capture of oils. Uncondensable gases will be passed through an afterburner. Materials of construction are mostly stainless-steel and chemically resistant ceramics and liners which are expected to provide a prolonged life of operation under harsh conditions.

Amongst the possible concepts investigated, broad wall and narrow wall slot-waveguides rings feeding energy through a window conformal to the central cone were found to deliver energy deposition throughout the product bed effectively with a power uniformity index of about 0.71 and 0.62 respectively. For low loss or highly variable dielectric properties during processing, the use of automatic tuning equipment and low ripple generators are likely

required as a quality factor close to 2,000 was observed. Nonetheless, for high microwave loss products, the operation is robust even for a considerable variation on the load position and properties.

The models were validated experimentally by use of a prototype which showed good agreement in both resonant frequency and resonance level, with only a 1 MHz difference between experimental and measurement -10 dB bandwidth. The system is currently under in final commissioning stage for batch processing.

A seamless path for large-scale implementation for continuous operation was proposed based on the use of the 896 MHz band with the possibility to extend the reactor diameter to meet process throughput requirements of over 1 tonne/hour continuous processing. Initial estimations revealed better performance regarding efficiency and matching compared to small scale designs. A full-scale plant is expected to start commissioning during 2019.

8.4 Applicator technology for processing of large granular products

A solution able to handle non-fluidizable particle sizes was proposed, useful for the implementation of robust high-temperature processes with product reaching temperatures more than 250 °C as current technologies have failed to deliver enough structural robustness for continuous operation. The concept consists of a parallel plate structure in which the lower plate acts as a material transport carrier, with a metallic enclosure. Among possible applications, coke-making and the direct reduction of iron were discussed as attractive candidates.

Such technology addresses the major concerns of using a conductive conveyor belt. Improved field levels on the material near the belt can be obtained by delivering a predominantly vertical polarisation by a combination of a slotted feed waveguide, reflectors and a parallel plate structure, in which the metal belt acts as the bottom plate. The field

penetration could be further improved using a dielectric layer (likely in the form of transparent ceramic sand) as a hearth layer. The microwave leakage concerns were addressed through using a complete conductive enclosure, improving both efficiency and safety of operation.

The use of a slotted waveguide feed allows for a relatively high-power handling and a uniform illumination when using back to back as a mirrored applicator. Given the mostly forward propagation of the power, low cross-coupling was be observed of less than -20 dB.

A prototype was fabricated and used to validate the simulations models by comparing its heating behaviour and its frequency response. Similar results showing very close resonant levels of -32 dB and 69 MHz and 76 MHz -10 dB bandwidth for the experimental and simulation respectively were produced, with qualitatively similar heating behaviour. The deviations could be mostly attributed to the lack of fabrication accuracy.

The metal conveyor material handling strategy could manage to transport large volumes and therefore high throughputs. The size of the system will be bound by the operational frequency, which for industrial purposes is likely to be the 896 MHz frequency band whereas the width of the conveyor is mostly dependent on the mechanical limitations of the material transport technology.

Some specific applications has been proposed for use with this type of applicator, which in the microwave zone are expected to produce a mostly CO/CO2 atmosphere, with significant changes on the depth of penetration to the bed. This require the utilisation of chemical resitstant construction materials and insulation. The depth of the bed can be adjusted as required by the process to match the expected penetration depths and the uniformity is greatly dependant on the resident time and consequent heat conduction within the bed. Research on considerations such as multistage systems with in between material mixing or turning could also be investigated as alternatives to improve threatment uniformity further.

8.5 Future work

Further work includes the finalisation of commissioning for experimental use in a variety of applications, currently under investigation. The performance of test work that validates the power handling capabilities and robustness of the developed prototypes under different conditions and materials. The implementation of continuous processing strategies in the developed systems to study their engineering performance and commercial prospects.

The following sections comprise some specific work being performed or being planned on future developments for the different proposed systems.

8.5.1 Applicator technology for processing of liquids and fine powders

Solutions for applications are being explored for liquid feedstocks, in particular waste engine oils and plastic waste, for implementing the elliptical cylinder applicator.

8.5.1.1 Processing of waste engine oils

A modified implementation of an elliptical TM_4 is under consideration with the use of two heating zones and microwave feeding by a central T type monopole. Good performance is expected based on preliminary simulations with a PUI of 0.08, a 99.6% power conversion efficiency, and a quality factor of 133. A simulation of the electric field distribution within such system is shown in Figure 8.1.

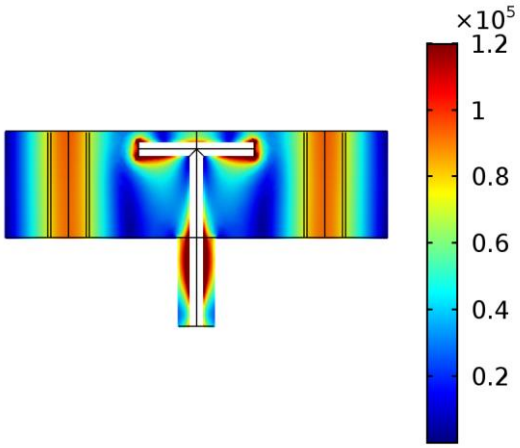


Figure 8.1 Simulated electric field distribution on TM4 elliptical applicator for oil treatment.

The electric field distribution upon material properties variation was also simulated for dielectric constants ranging 2 to 4 and a loss factor of 0.08. The normalised electric field distribution around one of the maximums is shown in Figure 8.2. The maximum field zone narrows with the increase of dielectric constant with a peak position in the range 73.74 ± 1.16 mm. The PUI and quality factors increased with the increase of dielectric constant as shown in **Error! Reference source not found.**.

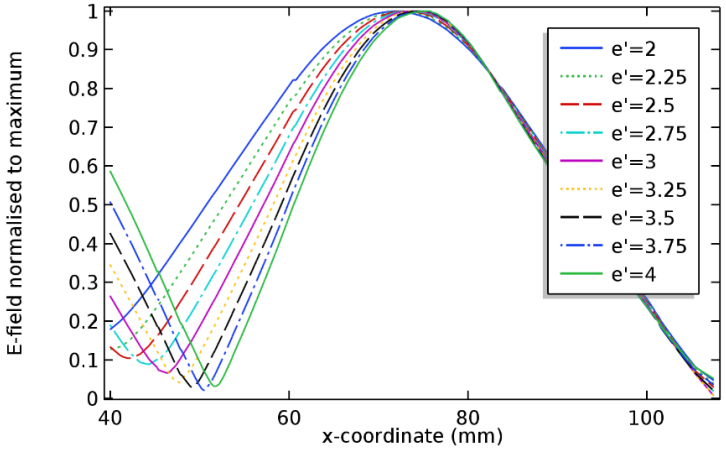


Figure 8.2 Simulated electric field distribution around the maximum for different dielectric constants.

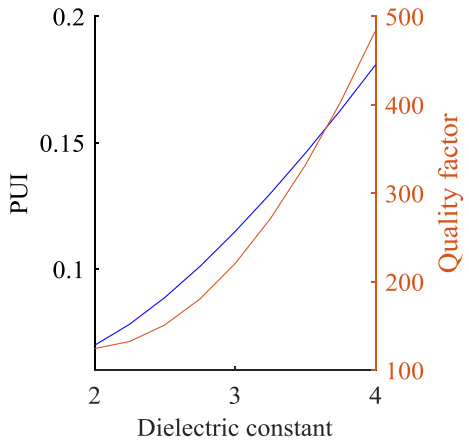


Figure 8.3 Simulated power uniformity index and quality factor for different dielectric constants.

For continuous processing, a multistage system has been envisaged, with several microwave applicator structures in series in a recirculating setup. Temperature monitoring could be accurately performed between microwave stages, overcoming the most commonly reported issue among researchers, which is critical for controlled pyrolysis (see Chapter 3). Each cavity can be controlled independently for optimal processing parameters. Target temperatures ranging 400 - 650°C could be expected depending on the specific process goals, and therefore the system should provide thermal insulation in the whole circuit. The use of ceramic wools within the applicator structures is suggested due to its lack of interaction with the microwaves at high-temperatures and excellent insulation properties.

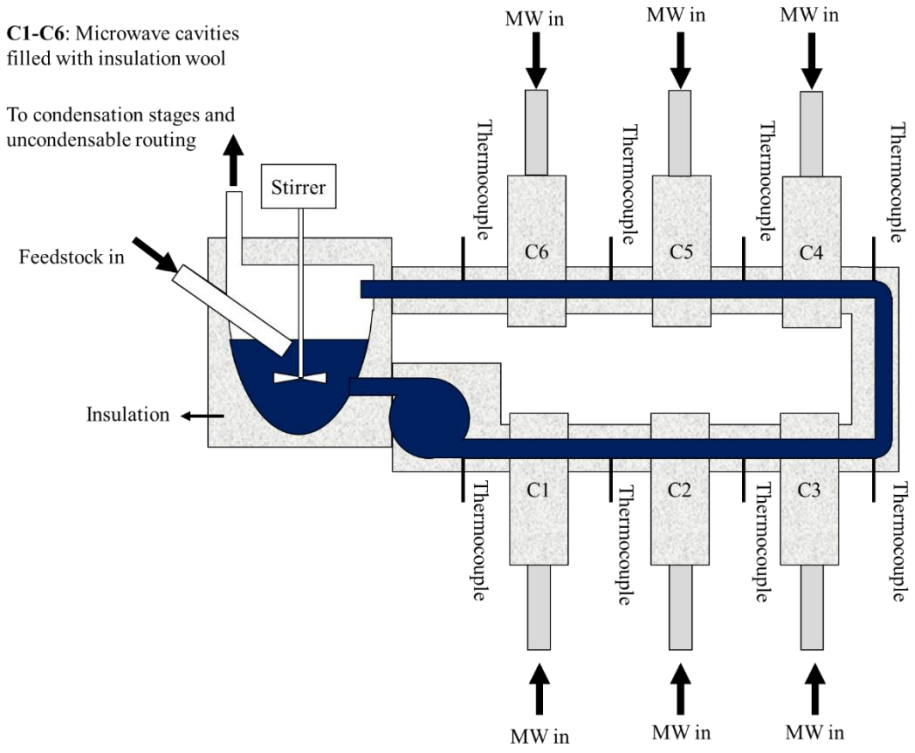


Figure 8.4 Liquid product processing conceptual sketch based on various applicators in series.

8.5.2 Processing of waste plastics

Plastics can be hard to treat due to mostly consisting on relatively transparent to microwave materials, driving research to the use of susceptors for treatment. Researchers have been focused on unlikely scenarios of pure feedstocks as seen in Chapter 3, whereas sorting waste streams by specific polymer types is not likely viable [348]. The composition of non-readily recyclable UK domestic plastic waste streams is roughly composed as shown in Table 8.1. Plastics are typically good thermal insulators and therefore melt slowly by conventional heating means. Microwave and RF heating can provide a faster melting mechanism [444].

Table 8.1 UK domestic plastic waste stream general composition after [348]

Polymer type	Composition (%)
PE	38.5
PP	22.2
PET	15.3
PVC	3.5
PS	4
Contamination	16.5

The low-temperature dielectric constants are in similar ranges as the above-analysed applications within 2 to 5 [24], [25], [349]. However, there is a lack of available information of moderate and especially pyrolytic temperatures properties.

A possible processing route is suggested in Figure 8.5. The waste stream is shredded and fed into an extruding system in the form of small flakes. The extruded plastics pass through a series of microwave applicators and enters a reservoir where volatiles are extracted for processing. The molten product is pumped through a treatment circuit and back to the reservoir where the volatilised products can be collected (e.g. Figure 8.4).

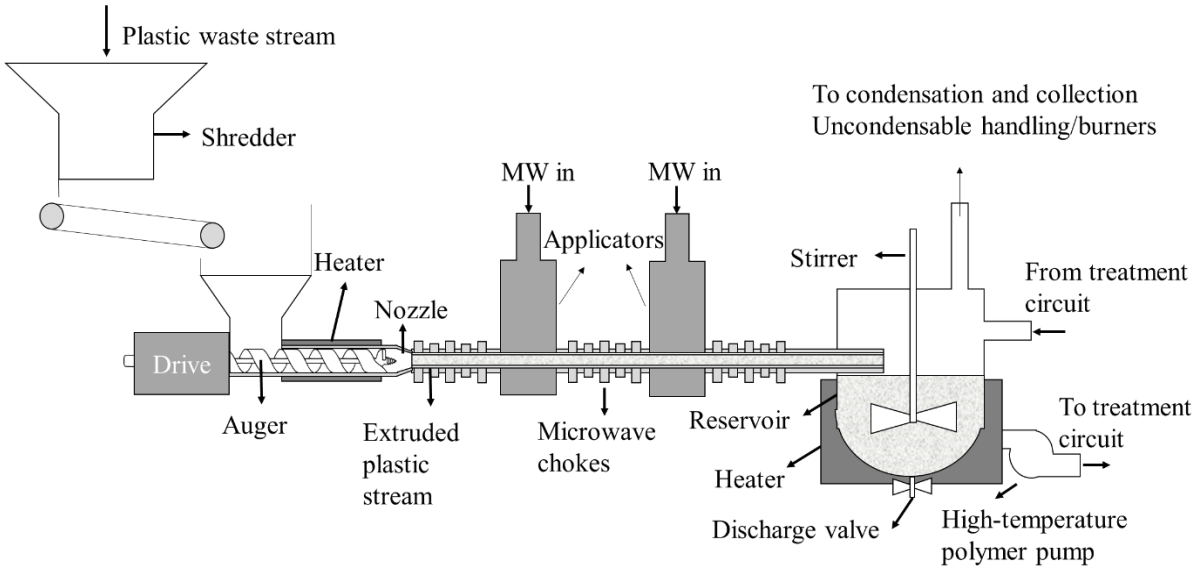


Figure 8.5 Plastic waste microwave processing system conceptual sketch.

8.5.3 Applicator technology for processing of granular products

8.5.3.1 T400 system

The 400 mm system has been commissioned and is currently being tested with a variety of feedstocks, mostly food-stuff in drying, puffing and roasting processes. In the near future the system is going to be modified for use of a ceramic microwave window to allow high-temperature operation. The production of a second unit for microwave retrofit is under study, in particular to modify the atmosphere to an inert gas in order to increase the range of processes it could tackle.

8.5.3.2 T1000 system

Initial design work is being done for the development of a full-scale unit to be fabricated. This will allow for continuous operation and will allow to assess the technoeconomic feasibility study on a variety of products.

8.5.4 Applicator technology for processing of large granular products

A diverse range of possible implementations of the technology is currently being discussed, in particular for pyrometallurgical processes. For example, a hybrid heating system based on a rotary hearth furnace with a microwave heating section is a plausible and compact solution. A schematic of such a concept is shown in Figure 8.6, which could be implemented in an initial experimental setup based on retrofitting the microwave section into a commercial electric rotary hearth furnace as the one shown in Figure 8.7 and Figure 8.8. This system could be used in a diverse range of applications requiring high temperature hybrid processing by adjusting processing parameters.

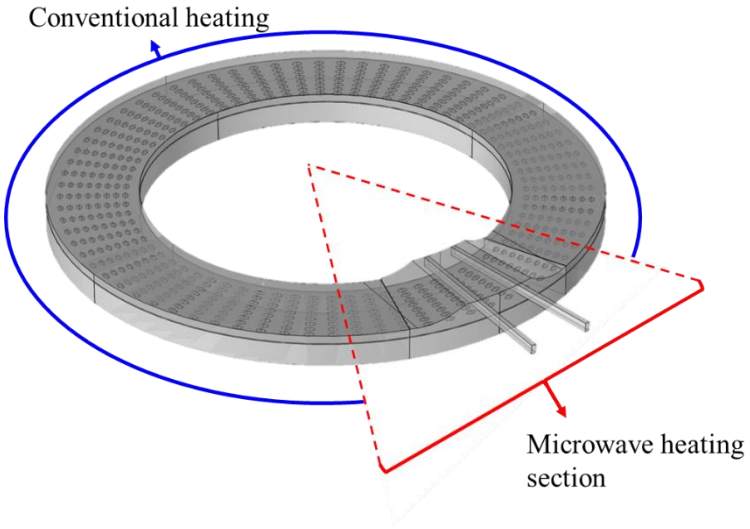


Figure 8.6 Large scale microwave hearth furnace conceptual schematic. Only one microwave heating section represented for simplicity.



Figure 8.7 Laboratory scale rotary hearth furnace Nabertherm DH 3020, from [445]**.**



Figure 8.8 Laboratory scale rotary hearth furnace Nabertherm DH 3020 internals with high-temperature steel plating from [445]**.**

Appendix A – Bessel function roots

Bessel function roots

k	$J_0(x)$	$J_1(x)$	$J_2(x)$	$J_3(x)$	$J_4(x)$	$J_5(x)$
1	2.4048	3.8317	5.1356	6.3802	7.5883	8.7715
2	5.5201	7.0156	8.4172	9.7610	11.0647	12.3386
3	8.6537	10.1735	11.6198	13.0152	14.3725	15.7002
4	11.7915	13.3237	14.7960	16.2235	17.6160	18.9801
5	14.9309	16.4706	17.9598	19.4094	20.8269	22.2178

Derivative of the Bessel function roots

k	$J'_0(x)$	$J'_1(x)$	$J'_2(x)$	$J'_3(x)$	$J'_4(x)$	$J'_5(x)$
1	3.8317	1.8412	3.0542	4.2012	5.3175	6.4156
2	7.0156	5.3314	6.7061	8.0152	9.2824	10.5199
3	10.1735	8.5363	9.9695	11.3459	12.6819	13.9872
4	13.3237	11.7060	13.1704	14.5858	15.9641	17.3128
5	16.4706	14.8636	16.3475	17.7887	19.1960	20.5755

Appendix B – TM_{010} cavity study

A brief study of a single mode TM010 cavity is performed, in similar conditions as the study from Chapter 5, for copper ore treatment.

As the diameter of the sample influence the treatment uniformity, different samples diameters were evaluated. Given the maximum sample diameter of ~40 mm for self-choking behaviour, as shown in Chapter 5, circular cylinder cavities for TM operation were designed and evaluated for diameters ranging 20 to 40 mm. The design approach was a numerical sweep of the cavity size by eigenmode analysis up until TM_{010} resonance occurred at the design frequency of 2.46 GHz. Aluminium cavity walls and a 1.7mm PTFE tube for product containment were considered in the models.

The cavity height does not affect the resonance frequency of the TM_{010} mode; however, it will affect the resonance frequency of modes with longitudinal component (e.g. TE_{111}), which could result in power being coupled to undesired modes. This is illustrated in following table where the resonant frequency of each mode normalised to the dominant mode frequency is shown, for various empty cavity heights. At a height equal to diameter size a critical point is reached where TM_{010} and TE_{111} have the same frequency. The typical design methodology is to select a cavity height large enough to provide a sizeable empty quality factor (i.e. without product) which will improve the power conversion efficiency, but small enough to avoid, as possible, the excitation of undesired modes.

Normalised to dominant mode resonant frequency ($f_{nmq}/f_{nmq-dominant}$) for different cavity height to radius ratio (d/a)

d/a	TM010	TE111	TM110	TM011	TE211	TM111/TE011	TE112	TM210
0	1	-	1.59	-	-	-	-	2.13
0.5	1	2.72	1.59	2.8	2.90	3.06	5.27	2.13
1	1	1.5	1.59	1.63	1.80	2.05	2.72	2.13
2	1	1	1.59	1.19	1.42	1.72	1.5	2.13
3	1.13	1	1.8	1.24	1.52	1.87	1.32	2.41
4	1.2	1	1.91	1.27	1.57	1.96	1.2	2.56

In this case, the height was limited by required power density rather than by modal overlapping, as can be seen in Chapter 5. The maximum volume of 16 cm^3 to achieve the required power density implied that for a maximum height for 20 mm, 30 mm and 40 mm diameters, the cavity height should be 5.1 cm, 2.3 cm and 1.3 cm respectively. The following table shows the quality factor and power uniformity index for TM_{010} evaluated for different sample sizes and the corresponding cavity size. Larger load diameters resulted in lower quality factors and higher PUI.

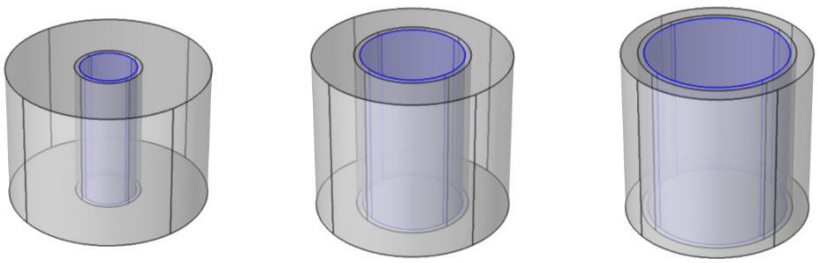
Cavity size, quality factor, and power uniformity index for circular cylinder cavities.

Sample diameter (mm)	Cavity/Sample height (mm)	Cavity diameter (mm)	Q_0	Peff (%)	PUI	E/Emax at sample boundary	E-field 3dB width (mm)
20	51	70.4	44	99.7	0.11	80.0%	24.8
30	23	57.6	30	99.7	0.26	58.2%	24.7
40	13	52.8	27	99.5	0.50	31.5%	24.6

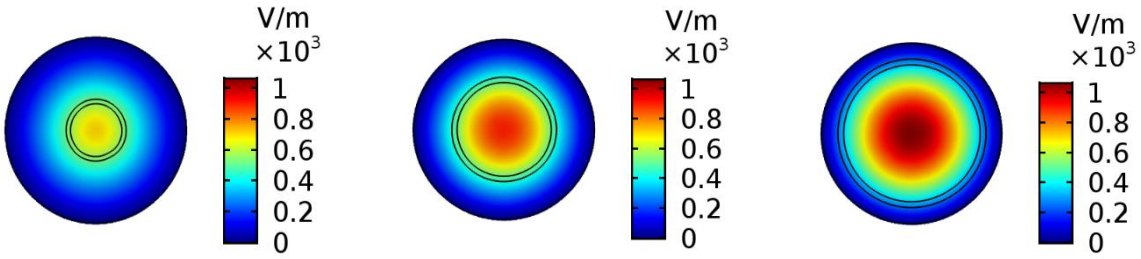
Changing both sample and cavity height does not influence the quality factor and PUI as shown in the next table, for a fixed cavity height of 50 mm. A sketch of the three cavities is shown next followed by their electric field distribution.

Cavity size, quality factor, and power uniformity index for circular cylinder cavities of 50 mm height.

Sample diameter (mm)	Cavity diameter (mm)	Q_0	Peff (%)	PUI	E/Emax at sample boundary	E-field 3dB width (mm)
20	70.4	44	99.7	0.11	80.2%	24.9
30	57.6	30	99.8	0.26	57.9%	24.5
40	52.8	27	99.8	0.50	31.9%	24.3



3D models of circular cylinder cavities for 20, 30 and 40 mm diameter samples (highlighted in blue).



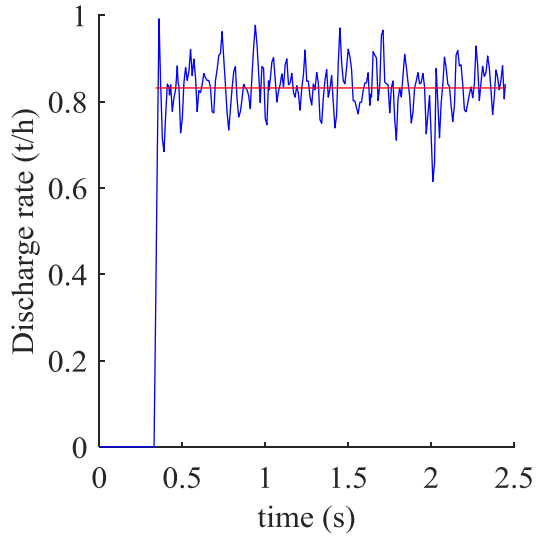
(a) (b) (c)

Electric field distribution for TM_{010} mode for 50 mm height cavities resonant at 2.46 GHz for load diameter of (a) 20 mm, (b) 30 mm, and (c) 40 mm.

The low quality factors translate in ease of matching and good conversion efficiencies of over 99.5% in all cases. Uniformity wise, only the 20 mm comply with the required limit. The three designs provided a considerably small space between the inner tube and cavity ranging from 4.7 to 23.5 mm.

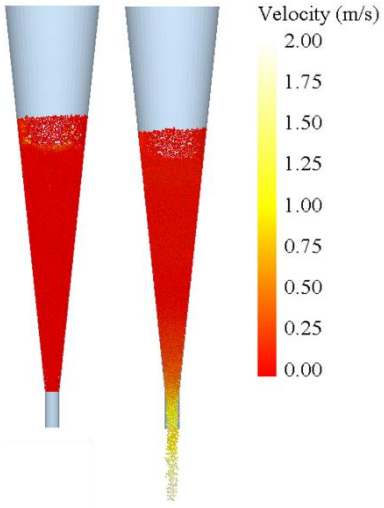
Appendix C – DEM simulation

Three simulations runs were made showing continuous flow without jamming with the model properties discussed in Chapter 5 by using EDEM [369]. The discharge rate for an example run is plotted next. The maximum rate was close to the value obtained via empirical equations at 1 t/h, but the average (after release) was of 0.83 t/h (red line).



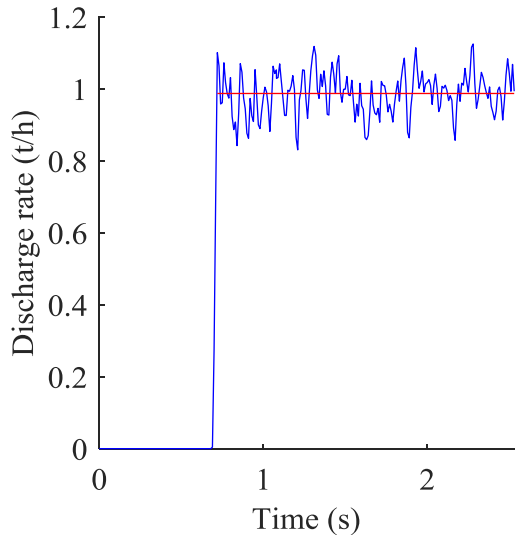
Simulated discharge rate (t/h) for hopper with a top diameter of 130.8 mm (blue line) and average value after opening (red line).

A particle speed distribution graph before and after release is shown next.



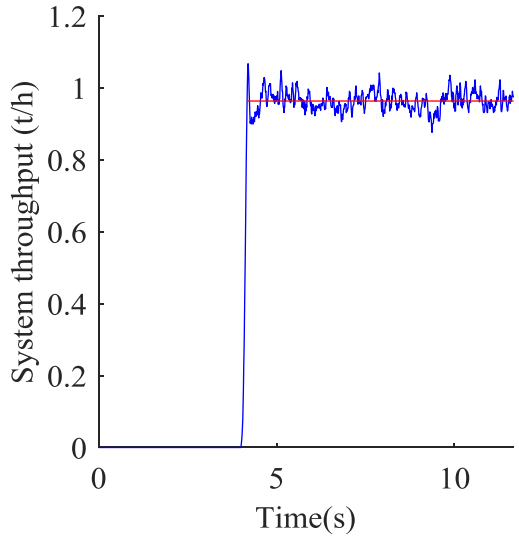
Simulated velocity graph just before hopper opening and after 0.4 s from opening – middle cut view.

A steeper hopper was needed to provide enough discharge rate. A second design with a top diameter of 120 mm and semi-included angle of $\theta = 5.3°$ resulted in an average of 0.99 t/h as seen next.



Simulated discharge rate (t/h) for hopper with a top diameter of 120 mm (blue line) and average value after opening (red line).

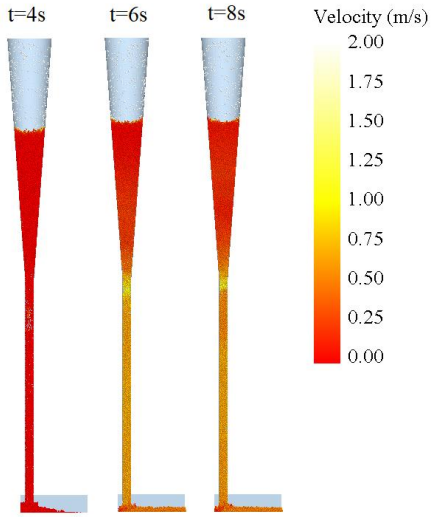
A half-meter 20 mm diameter tube with a 40 mm wide conveyor belt system was simulated in conjunction to check continuous operation. The belt was on stop until initial filling of the system (until t=4 s). A continuous input of 1 t/h was kept on the hopper. With the belt set at 0.5 m/s, an average system throughput of 0.96 t/h was achieved as seen next.



Simulated system throughput (t/h) for hopper with a top diameter of 120mm and belt speed of 0.5m/s (blue line) and average value after opening (red line).

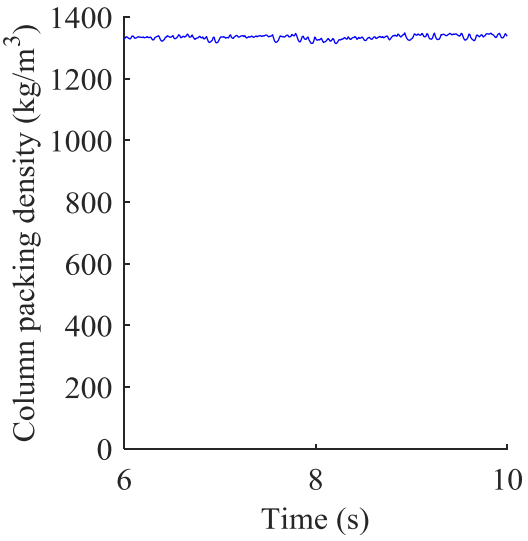
The column speed was maintained relatively constant as can be seen in the next figure, with an average of 0.64 m/s, close to the estimated requirement of 0.63 m/s. The difference

seems to be due to the difference between estimated packing density of 1,400 kg/m^3 (measured in dielectric measurement cell and not in the processing tube) and simulated density within the tube.



Simulated velocity graph just before belt start (t=4s) and after 2 and 4 s – middle cut view.

Simulations show a slightly smaller column packing density with an average of 1,255 kg/m^3 as seen next.



Simulated column packing density over time.

Appendix D – Dielectric properties of some materials

Material	ρ_a (g/cm^3)	f (MHz)	T (°C)	ε_r	Ref	LLM @0.53 g/cm^3	CRI @0.53 g/cm^3
Vermiculite	0.89	934	20	2.13-j0.09	[31]	1.64-j0.05	1.66-j0.05
		2143	20	2.13-j0.1		1.64-j0.05	1.66-j0.06
Anthracite	1.69	915	600	25.05-j20.53	[446]	4.32-j1.86	5.24-j2.84
			700	26.65-j23.23		4.50-2.06	5.49-3.18
			800	28.25-j25.93		4.67-j2.26	5.73-j3.52
			900	38.48-j45.96		5.76-j3.6	7.28-j5.9
			1000	53.48-j78.96		7.26-j5.64	9.45-j9.74
		2450	600	22.34-j12.9		3.96-j1.23	4.78-j1.83
			700	23.74-j14.5		4.11-j1.36	4.99-j2.04
			800	25.14-j16.1		4.26-j1.48	5.2-j2.2
			900	29.64-j39.68		5.01-j3.3	6.09-j5.26
			1000	34.34-j64.68		5.78-j4.99	7.01-j8.26
Indonesian low rank coal	1.04	915	600	8-j9	[83]	3.68-j2.50	3.90-j3.05
			700	51-j5		13.49-j1.05	17.06-j1.47
			800	56-j9		14.55-j1.86	18.54-j2.64
			900	70-j15		17.43-j3.02	22.63-j4.31
		2450	600	9-j8		3.90-j2.20	4.20-j2.69
			700	51-j8		13.50-j1.68	17.07-j2.36
			800	55-j5		14.33-j1.04	18.24-j1.47
			900	68-j9		17.00-j1.82	22.03-j2.60
Sycamore*	0.24	2,450	20	1.37-j0.06	[204]	1.92-j0.17	1.89-j0.16
	0.53			1.92-j0.14		1.92-j0.14	1.92-j0.14
Fe_2O_3 Hematite	2.80	915	700	12.96-j13.83	[247]	2.11-j0.68	2.35-j1.03
			800	26.86-j21.78		2.73-j0.83	3.32-j1.38
			900	39.4-j14.19		3.11-j0.49	4.03-j0.85
			1000	51.25-j13.24		3.49-j0.41	4.71-j0.76
		2450	700	10.01-j6.18		1.86-j0.36	2.03-j0.51
			800	14.61-j13.98		2.18-j0.67	2.46-j1.02

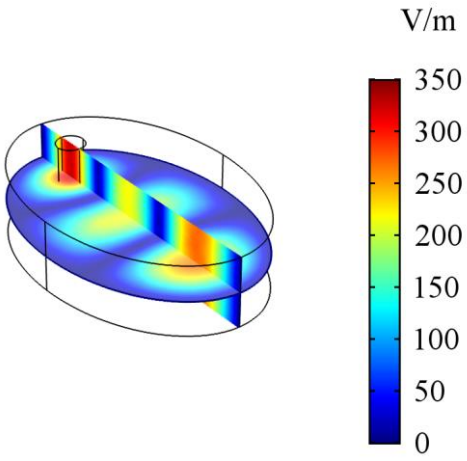
			900	25.69-j18.72		2.66-j0.73	3.22-j1.21
			1000	39.94-j21.83		3.17-j0.73	4.10-j1.29
Fe_3O_4 Magnetite	2.77	915	700	51.23-j48.45	[81]	3.72-j1.46	4.94-j2.73
			800	62.72-j69.1		4.16-j1.92	5.68-j3.74
			900	101.7-j92.56		5.21-j2.24	7.76-j4.70
			1000	139.4-j103.5		6.07-j2.31	9.63-j5.07
		2450	700	48.75-j35.88		3.56-j1.12	4.73-j2.06
			800	69.16-j58.01		4.25-j1.60	5.95-j3.13
			900	92.61-j92.68		5.00-j2.29	7.32-j4.75
			1000	103.3-j115.3		5.36-j2.73	7.95-j5.79
$Fe_{0.925}O$ Wustite	2.43	915	700	82.49-j3.739	[244]	5.19-j0.13	7.63-j0.25
			800	86.85-j3.094		5.34-j0.11	7.92-j0.2
			900	88.57-j3.77		5.40-j0.13	8.04-j0.25
			1000	90.86-j3.86		5.48-j0.13	8.19-j0.25
		2450	700	78.01-j3.74		5.03-j0.13	7.34-j0.25
			800	81.25-j3.09		5.15-0.11	7.55-j0.21
			900	83.44-j3.76		5.22-j0.13	7.70-j0.25
			1000	85.77-j3.86		5.30-j0.13	7.85-j0.25

Appendix E – Rectangular TE_{103} applicator versus elliptical

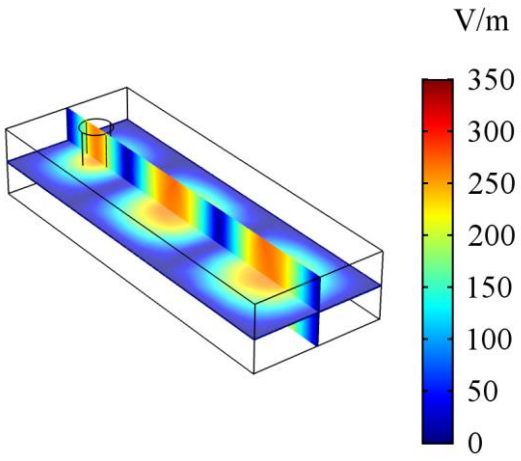
Two comparable systems were analysed: an elliptical and a TE_{103} rectangular applicator, using eigenfrequency numerical simulation using COMSOL Multiphysics. The geometry was initially adjusted for an example load with complex permittivity of $\varepsilon_r = 3 - j0.1$, and the sample was set so a maximum field was present in its centre. The dimensions of both systems are summarised in the following table.

Elliptical			Rectangular	
Minor semi-axis	70 mm		Width	86.36 mm
Major semi-axis	104.5 mm		Height	43.18 mm
Height	50 mm		Length	232.5 mm
Load position (from centre)	71.595 mm		Load position (from centre)	86.845 mm
Load diameter	20 mm		Load diameter	20 mm

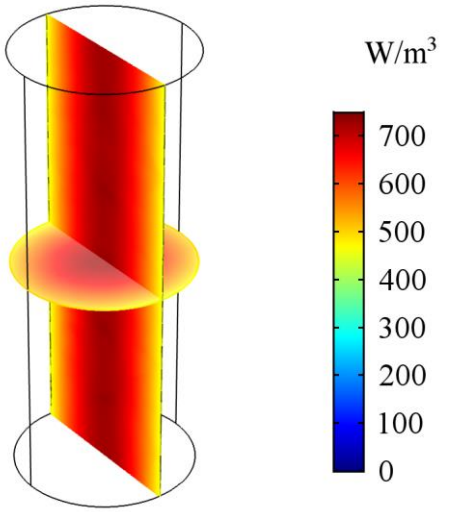
The electric field distribution and power loss density within the samples is shown next for both type of applicators.



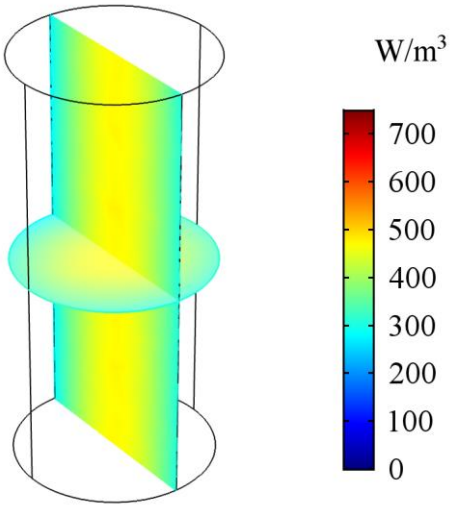
Electric field distribution within elliptical applicator at 2.46 GHz.



Electric field distribution within rectangular TE_{103} applicator at 2.46 GHz.



Power loss density within sample for elliptical applicator at 2.46 GHz.



Power loss density within sample for rectangular TE_{103} applicator at 2.46 GHz.

	Elliptical	Rectangular
Empty Q_0	20,313	16,227
Filled Q_0	149	201
Power Conversion efficiency	99.3%	98.8%
Max field relative to max in overall field	100%	80.6%
Average power loss density	596.4	386.8
PUI	0.105	0.105
Shift of maximum field position with dielectric constant [3, 6, 10] in mm.	[0, 2.2, 4.3]	[0, 3.3, 5.4]

References

[1] R. E. Collin, *Foundations for microwave engineering*. John Wiley & Sons, 2007.

[2] S. Das, *Microwave Engineering*. 2015.

[3] T. V. C. T. Chan and H. C. Reader, *Understanding microwave heating cavities*. Artech House Publishers, 2000.

[4] N. R. Council, *Microwave Processing of Materials*. Washington, DC: The National Academies Press, 1994.

[5] D. Beneroso, T. Monti, E. T. Kostas, and J. Robinson, "Microwave pyrolysis of biomass for bio-oil production: Scalable processing concepts," *Chem. Eng. J.*, vol. 316, pp. 481–498, May 2017.

[6] M. S. Venkatesh and G. S. V. Raghavan, "An overview of microwave processing and dielectric properties of agri-food materials," *Biosyst. Eng.*, vol. 88, no. 1, pp. 1–18, 2004.

[7] M. Gupta and W. Wai Leong Eugene, *Microwaves and Metals*. Singapore: John Wiley & Sons (Asia) Pte Ltd, 2007.

[8] M. Oghbaei and O. Mirzaee, "Microwave versus conventional sintering: A review of fundamentals, advantages and applications," *J. Alloys Compd.*, vol. 494, no. 1–2, pp. 175–189, Apr. 2010.

[9] J. Sun, W. Wang, and Q. Yue, "Review on microwave-matter interaction fundamentals and efficient microwave-associated heating strategies," *Materials (Basel).*, vol. 9, no. 4, 2016.

[10] Y. Zhang *et al.*, "Effects of feedstock characteristics on microwave-assisted pyrolysis – A review," *Bioresour. Technol.*, vol. 230, pp. 143–151, Apr. 2017.

[11] T. T. Chen, J. E. Dutrizac, K. E. Haque, W. Wyslouzil, and S. Kashyap, "The Relative Transparency of Minerals to Microwave Radiation," *Can. Metall. Q.*, vol. 23, no. 3, pp. 349–351, 1984.

[12] A. C. and Metaxas and R. J. Meredith, *Industrial microwave heating*, no. 4. IET, 1983.

[13] T. J. Appleton, R. I. Colder, S. W. Kingman, I. S. Lowndes, and A. G. Read, "Microwave technology for energy-efficient processing of waste," *Appl. Energy*, vol. 81, no. 1, pp. 85–113, 2005.

[14] F. Motasemi and M. T. Afzal, "A review on the microwave-assisted pyrolysis technique," *Renew. Sustain. Energy Rev.*, vol. 28, pp. 317–330, 2013.

[15] C. Yin, "Microwave-assisted pyrolysis of biomass for liquid biofuels production," *Bioresour. Technol.*, vol. 120, pp. 273–284, 2012.

[16] K. E. Haque, "Microwave energy for mineral treatment processes—a brief review," *Int. J. Miner. Process.*, vol. 57, no. 1, pp. 1–24, 1999.

[17] S. Nomanbhay and M. Y. Ong, "A Review of Microwave-Assisted Reactions for Biodiesel Production," *Bioengineering*, vol. 4, no. 2, p. 57, Jun. 2017.

[18] "Dielectric Properties table. Source : A . C Metaxas . R . J Meredith . Industrial Microwave Heating . IEE power engineering series . London . 1983." p. 1983, 1983.

[19] R. Meredith, *Engineers' Handbook of Industrial Microwave Heating*. The Institution of Engineering and Technology, Michael Faraday House, Six Hills Way, Stevenage SG1 2AY, UK: IET, 1998.

[20] S. Das, A. K. Mukhopadhyay, S. Datta, and D. Basu, "Prospects of microwave processing: An overview," *Bull. Mater. Sci.*, vol. 32, no. 1, pp. 1–13, 2009.

[21] S. Chandrasekaran, S. Ramanathan, and T. Basak, "Microwave material processing-a review," *AIChE J.*, vol. 58, no. 2, pp. 330–363, Feb. 2012.

[22] D. Pozar, *Microwave Engineering*, 4th ed. John Wiley & Sons, Inc, 2012.

[23] F. T. Ulaby, U. Ravaioli, and E. Michielssen, *Fundamentals of applied electromagnetics*. Prentice Hall, 2014.

[24] MIT Laboratory for Insulation Research, "Tables of dielectric materials. Volume IV," 1953.

[25] MIT Laboratory for Insulation Research, "Dielecric constant and loss data part II," 1975.

[26] F. Motasemi, A. A. Salema, and M. T. Afzal, "Microwave Dielectric Properties of Agricultural Biomass at High Temperature in an Inert Environment," *Trans. ASABE*, no. June 2016, pp. 869–877, 2015.

[27] J. P. Robinson, S. W. Kingman, R. Barranco, C. E. Snape, and H. Al-Sayegh, "Microwave Pyrolysis of Wood Pellets," *Ind. Eng. Chem. Res.*, vol. 49, no. 2, pp. 459–463, Jan. 2010.

[28] Z. Peng, J.-Y. Hwang, B.-G. Kim, J. Mouris, and R. Hutcheon, "Microwave Absorption Capability of High Volatile Bituminous Coal during Pyrolysis," *Energy & Fuels*, vol. 26, no. 8, pp. 5146–5151, Aug. 2012.

[29] F. Motasemi, M. T. Afzal, and A. A. Salema, "Microwave dielectric characterization of hay during pyrolysis," *Ind. Crops Prod.*, vol. 61, no. January 2016, pp. 492–498, 2014.

[30] G. D. Jiménez, V. H. Montoya, S. Kingman, T. Monti, and E. Binner, "Effect of pyrolysis temperature and microwave frequency on dielectric properties of lignocellulosic material used as carbon precursor," *Boletín del Grup. Español del Carbón*, no. 43, pp. 17–20, 2017.

[31] J. Katrib, O. Folorunso, C. Dodds, G. Dimitrakis, and S. W. Kingman, "Improving the design of industrial microwave processing systems through prediction of the dielectric properties of complex multi-layered materials," *J. Mater. Sci.*, vol. 50, no. 23, pp. 7591–7599, 2015.

[32] A. Sihvola, "Mixing rules with complex dielectric coefficients," *Subsurf. Sens. Technol. Appl.*, vol. 1, no. 4, pp. 393–415, 2000.

[33] R. R. Mishra and A. K. Sharma, "Microwave–material interaction phenomena: Heating mechanisms, challenges and opportunities in material processing," *Compos. Part A Appl. Sci. Manuf.*, vol. 81, pp. 78–97, Feb. 2016.

[34] A. R. von Hippel, "The dielectric relaxation spectra of water, ice, and aqueous solutions, and their interpretation. I. Critical survey of the status-quo for water," *IEEE Trans. Electr. Insul.*, vol. 23, no. 5, pp. 801–816, 1988.

[35] R. Collier, *Transmission lines: Equivalent circuits, electromagnetic theory, and photons*.

Cambridge University Press, 2013.

[36] C. A. Balanis, *Advanced engineering electromagnetics*. 2012.

[37] Agilent Technologies, "Understanding the Fundamental Principles of Vector Network Analysis," *Appl. Note 5965-7707E*, p. 15, 2012.

[38] C. Poole and I. Darwazeh, *Microwave active circuit analysis and design*. Academic Press, 2015.

[39] X. Ren, "High temperature materials characterization and sensor application," University of Central Florida, 2012.

[40] S. O. Nelson, "Dielectric properties measurement techniques and applications," *Trans. ASAE*, vol. 42, no. 2, p. 523, 1999.

[41] Keysight Technologies, "Basics of Measuring the Dielectric Properties of Materials Application Note." .

[42] Rohde&Schwarz, "Measurement of dielectric material properties Application Note." 2006.

[43] M. Mehdizadeh, *Microwave/RF Applicators and Probes*, 2nd Editio. Elsevier, 2015.

[44] B. Chevalier, M. Chataxd-Moulin, J. P. Astier, and P. Y. Guillon, "High temperature complex permittivity measurements of composite materials using an open-ended waveguide," *J. Electromagn. Waves Appl.*, vol. 6, no. 7, pp. 1259–1275, 1992.

[45] D. Misra, M. Chabbra, B. R. Epstein, M. Mirotznik, and K. R. Foster, "Noninvasive Electrical Characterization of Materials at Microwave Frequencies Using an Open-Ended Coaxial Line: Test of an Improved Calibration Technique," *IEEE Trans. Microw. Theory Tech.*, vol. 38, no. 1, pp. 8–14, 1990.

[46] Keysight Technologies, "N1501A Dielectric Probe Kit 10 MHz to 50 GHz: Technical Overview." .

[47] A. Parkash, J. K. Vaid, and A. Mansingh, "Measurement of Dielectric Parameters at Microwave Frequencies by Cavity-Perturbation Technique," *IEEE Trans. Microw. Theory Tech.*, vol. 27, no. 9, pp. 791–795, Sep. 1979.

[48] T. Rydholm, "Measurement of complex permittivity and permeability through a cavity-pertubation method," Chalmers university of technology, 2015.

[49] C. Tsipogiannis, "Microwave materials characterization using waveguides and coaxial probe," Lund University, 2012.

[50] Keysight Technologies, "N1500A Materials Measurement Suite." .

[51] B. J. Wolfson and S. M. Wentworth, "Complex permittivity and permeability measurement at elevated temperatures using rectangular waveguide," *Microw. Opt. Technol. Lett.*, vol. 38, no. 6, pp. 449–453, 2003.

[52] X. Bao *et al.*, "Coplanar waveguide for dielectric material measurements at frequencies from 140 GHz to 220 GHz," in *2017 90th ARFTG Microwave Measurement Symposium (ARFTG)*, 2017, vol. 2018-Janua, no. April 2018, pp. 1–4.

[53] A. Aboutaleb and C. H. Oxley, "Microwave Dielectric Measurement of Solids and Liquids Over 1 To 4 Ghz Using Transmission Line Technique and Coaxial Cavity," in

The 26th ARMMS RF and Microwave Conference, 2013.

[54] A. Vepsalainen, K. Chalapat, and G. S. Paraoanu, "Measuring the microwave magnetic permeability of small samples using the short-circuit transmission line method," *IEEE Trans. Instrum. Meas.*, vol. 62, no. 9, pp. 2503–2510, 2013.

[55] C. Larsson, D. Sjoberg, and L. Elmkvist, "Waveguide Measurements of the Permittivity and Permeability at Temperatures of up to 1000°C," *IEEE Trans. Instrum. Meas.*, vol. 60, no. 8, pp. 2872–2880, Aug. 2011.

[56] A. M. Nicolson and G. F. Ross, "Measurement of the Intrinsic Properties of Materials by Time-Domain Techniques," *IEEE Trans. Instrum. Meas.*, vol. 19, no. 4, pp. 377–382, Nov. 1970.

[57] A.-H. Boughriet, C. Legrand, and A. Chapoton, "Noniterative stable transmission/reflection method for low-loss material complex permittivity determination," *IEEE Trans. Microw. Theory Tech.*, vol. 45, no. 1, pp. 52–57, 1997.

[58] J. Baker-Jarvis, E. J. Vanzura, and W. A. Kissick, "Improved technique for determining complex permittivity with the transmission/reflection method," *IEEE Trans. Microw. Theory Tech.*, vol. 38, no. 8, pp. 1096–1103, Aug. 1990.

[59] P. G. Bartley and S. B. Begley, "A new technique for the determination of the complex permittivity and permeability of materials," in *2010 IEEE Instrumentation & Measurement Technology Conference Proceedings*, 2010, pp. 54–57.

[60] S. A. Barringer, E. A. Davis, J. Gordon, K. G. Ayappa, and H. T. Davis, "Effect of sample size on the microwave heating rate: Oil vs. water," *AIChE J.*, vol. 40, no. 9, pp. 1433–1439, Sep. 1994.

[61] Hyperphysics, "Hysteresis." [Online]. Available: http://hyperphysics.phy-astr.gsu.edu/hbase/Solids/hyst.html. [Accessed: 10-Oct-2018].

[62] D. Agrawal, "Latest global developments in microwave materials processing," *Mater. Res. Innov.*, vol. 14, no. 1, pp. 3–8, Feb. 2010.

[63] R. R., P. M., and R. H.G.A., "Microwave Fast Sintering of Ceramic Materials," in *Sintering of Ceramics - New Emerging Techniques*, InTech, 2012.

[64] S. Singh, D. Gupta, V. Jain, and A. Sharma, "Microwave Processing of Materials and Applications in Manufacturing Industries: A Review," *Mater. Manuf. Process.*, vol. 6914, no. December 2014, pp. 37–41, 2014.

[65] Z. Peng and J.-Y. Hwang, "Microwave-assisted metallurgy," *Int. Mater. Rev.*, vol. 60, no. 1, pp. 30–63, 2015.

[66] M. Bhattacharya and T. Basak, "A review on the susceptor assisted microwave processing of materials," *Energy*, vol. 97, pp. 306–338, Feb. 2016.

[67] A. Porch *et al.*, "Microwave treatment in oil refining," *Appl. Petrochemical Res.*, vol. 2, no. 1–2, pp. 37–44, 2012.

[68] ITU-R, "Radio Regulations - Article No 1.15." 2016.

[69] ITU-R, "Rec. ITU-R SM.1056: LIMITATION OF RADIATION FROM INDUSTRIAL, SCIENTIFIC AND MEDICAL (ISM) EQUIPMENT," 2007.

[70] Peter McNeil, “ISM bands,” *Pasternack*, 2018. [Online]. Available: https://blog.pasternack.com/uncategorized/what-are-the-ism-bands-and-what-are-they-used-for/.

[71] UK Government, *The Control of Electromagnetic Fileds at Work Regulations 2016*. United Kingdom, 2016.

[72] G. Matthaei, L. Young, and E. Jones, “Microwave Filters, Impedance-Matching Networks, and Coupling Structures (Artech Microwave Library),” *Artech House, Febr.*, 1980.

[73] M. Gilden and L. Gould, “Handbook on High Power Capabilities of Waveguide Systems,” MICROWAVE ASSOCIATES INC BURLINGTON MA, 1963.

[74] D. K. Cheng, “Fundamentals of engineering electromagnetics,” 1993.

[75] R. Bansal, *Fundamentals of Electromagnetics*. 2006.

[76] EverythingRF, “Waveguide sizes.” [Online]. Available: https://www.everythingrf.com/tech-resources/waveguides-sizes. [Accessed: 16-Oct-2018].

[77] K. Hara and M. Hayashi, “Continuous Pig Iron Making by Microwave Heating with 12.5 kW at 2.45 GHz,” *J. Microw. Power Electromagn. Energy*, vol. 45, no. 3, pp. 137–147, 2011.

[78] K. Hara, M. Hayashi, M. Sato, and K. Nagata, “Pig Iron Making by Focused Microwave Beams with 20 kW at 2.45 GHz,” *ISIJ Int.*, vol. 52, no. 12, pp. 2149–2157, 2012.

[79] A. J. Buttress, E. Binner, C. Yi, P. Palade, J. P. Robinson, and S. W. Kingman, “Development and evaluation of a continuous microwave processing system for hydrocarbon removal from solids,” *Chem. Eng. J.*, vol. 283, pp. 215–222, 2016.

[80] M. Nuechter, B. Ondruschka, W. Bonrath, and A. Gum, “Microwave assisted synthesis - a critical technology overview,” *Green Chem.*, vol. 6, no. 3, pp. 128–141, 2004.

[81] Z. Peng, J.-Y. Hwang, J. Mouris, R. Hutcheon, and X. Huang, “Microwave Penetration Depth in Materials with Non-zero Magnetic Susceptibility,” *ISIJ Int.*, vol. 50, no. 11, pp. 1590–1596, Nov. 2010.

[82] E. Binner, E. Lester, S. Kingman, C. Dodds, and J. Robinson, “A Review of Microwave Coal Processing,” *J. Microw. Power Electromagn. Energy*, vol. 48, no. 1, pp. 35–60, 2014.

[83] Z. Peng *et al.*, “Dielectric characterization of Indonesian low-rank coal for microwave processing,” *Fuel Process. Technol.*, vol. 156, pp. 171–177, 2017.

[84] A. V. Bridgwater, “Review of fast pyrolysis of biomass and product upgrading,” *Biomass and Bioenergy*, vol. 38, pp. 68–94, 2012.

[85] E. Binner *et al.*, “Factors affecting the microwave coking of coals and the implications on microwave cavity design,” *Fuel Process. Technol.*, vol. 125, pp. 8–17, 2014.

[86] H. S. Uhm, “Influence of chamber temperature on properties of the corona discharge system,” *Phys. Plasmas*, vol. 6, no. 2, p. 623, 1999.

[87] W. Chen, B. Gutmann, and C. O. Kappe, “Characterization of Microwave-Induced

Electric Discharge Phenomena in Metal-Solvent Mixtures," *ChemistryOpen*, vol. 1, no. 1, pp. 39–48, Feb. 2012.

[88] S. C. Brown, "High-Frequency Gas Discharge Breakdown," 1951.

[89] N. S. J. Braithwaite, "Introduction to gas discharges," *Plasma Sources Sci. Technol.*, vol. 9, no. 4, p. 517, 2000.

[90] D. R. Ballal and A. H. Lefebvre, "The influence of spark discharge characteristics on minimum ignition energy in flowing gases," *Combust. Flame*, vol. 24, pp. 99–108, 1975.

[91] F. P. Grosu, A. M. Bologa, M. K. Bologa, and O. V. Motorin, "On temperature dependence of the parameters of corona discharge current–voltage characteristics," *Surf. Eng. Appl. Electrochem.*, vol. 52, no. 1, pp. 85–91, Jan. 2016.

[92] V. Seema and S. Anoop, *FUNDAMENTALS OF MICROWAVE ENGINEERING: PRINCIPLES, WAVEGUIDES, MICROWAVE AMPLIFIERS AND APPLICATIONS*. Prentice-Hall Of India Pvt. Limited, 2009.

[93] Y. V Bykov, K. I. Rybakov, and V. E. Semenov, "High-temperature microwave processing of materials," *J. Phys. D. Appl. Phys.*, vol. 34, no. 13, pp. R55–R75, Jul. 2001.

[94] A. A. Noyes and H. A. Wilson, "The Thermal Ionization of Gaseous Elements at High Temperatures: A Confirmation of the Saha Theory," *Astrophys. J.*, vol. 57, pp. 20–32, 1923.

[95] K. Kashimura *et al.*, "Iron production from Fe 3O 4 and graphite by applying 915MHz microwaves," *Mater. Sci. Eng. A*, vol. 556, pp. 977–979, 2012.

[96] N. Standish and H. Worner, "Microwave Application in the Reduction of Metal Oxides with Carbon," *J. Microw. Power Electromagn. Energy*, vol. 25, no. 3, pp. 177–180, Jan. 1990.

[97] J. A. Menéndez *et al.*, "Microwave heating processes involving carbon materials," *Fuel Process. Technol.*, vol. 91, no. 1, pp. 1–8, 2010.

[98] A. D. Russell, E. I. Antreou, S. S. Lam, C. Ludlow-Palafox, and H. A. Chase, "Microwave-assisted pyrolysis of HDPE using an activated carbon bed," *RSC Adv.*, vol. 2, no. 17, p. 6756, 2012.

[99] E. Ruisánchez, A. Arenillas, E. J. Juárez-Pérez, and J. A. Menéndez, "Pulses of microwave radiation to improve coke grindability," *Fuel*, vol. 102, pp. 65–71, 2012.

[100] K. Yao *et al.*, "Diamond Deposition on Graphite in Hydrogen Microwave Plasma," *J. Coat. Sci. Technol.*, vol. 5, pp. 12–18, 2018.

[101] K. Suzuki, K. Ninomiya, and S. Mishimatsu, "Microwave plasma etching," *Vacuum*, vol. 34, no. 10–11, pp. 953–957, Oct. 1984.

[102] A. Hozumi and O. Takai, "Preparation of ultra water-repellent films by microwave plasma-enhanced CVD," *Thin Solid Films*, vol. 303, no. 1–2, pp. 222–225, Jul. 1997.

[103] S. Guruvenket, G. M. Rao, M. Komath, and A. M. Raichur, "Plasma surface modification of polystyrene and polyethylene," *Appl. Surf. Sci.*, vol. 236, no. 1–4, pp. 278–284, Sep. 2004.

[104] P. Khongkrapan, P. Thanompongchart, N. Tippayawong, and T. Kiatsiriroat,

"Microwave plasma assisted pyrolysis of refuse derived fuels," *Cent. Eur. J. Eng.*, vol. 4, no. 1, pp. 72–79, 2014.

[105] H. Sekiguchi and T. Orimo, "Gasification of polyethylene using steam plasma generated by microwave discharge," *Thin Solid Films*, vol. 457, no. 1, pp. 44–47, Jun. 2004.

[106] G. S. J. Sturm, A. N. Munoz, P. V. Aravind, and G. D. Stefanidis, "Microwave-Driven Plasma Gasification for Biomass Waste Treatment at Miniature Scale," *IEEE Trans. Plasma Sci.*, vol. 44, no. 4, pp. 670–678, Apr. 2016.

[107] K. Huang and B. Lu, "The precise condition of thermal runaway in microwave heating on chemical reaction," *Sci. China, Ser. E Technol. Sci.*, vol. 52, no. 2, pp. 491–496, 2009.

[108] G. Roussy, A. Bennani, and J. Thiebaut, "Temperature runaway of microwave irradiated materials," *J. Appl. Phys.*, vol. 62, no. 4, pp. 1167–1170, Aug. 1987.

[109] A. C. Metaxas, "Microwave heating," *Power Eng. J.*, vol. 5, no. 5, pp. 237–247, 1991.

[110] A. Maryott and E. Smith, "Table of Dielectric Constants of pue Liquids," *Natl. Bur. Stand.*, 1951.

[111] V. V Yakovlev, S. M. Allan, M. L. Fall, and H. S. Shulman, "Computational study of thermal runaway in microwave processing of zirconia," *Microw. RF Power Appl.*, pp. 303–306, 2011.

[112] X. Wu, J. R. Thomas, and W. A. Davis, "Control of thermal runaway in microwave resonant cavities," *J. Appl. Phys.*, vol. 92, no. 6, pp. 3374–3380, 2002.

[113] M. T. Demeuse and A. C. Johnson, "Variable frequency microwave processing of thermoset polymer matrix composites," *MRS Online Proc. Libr. Arch.*, vol. 347, 1994.

[114] R. Behrend, C. Dorn, V. Uhlig, and H. Krause, "Investigations on container materials in high temperature microwave applications," *Energy Procedia*, vol. 120, pp. 417–423, Aug. 2017.

[115] X. Shang, J. Chen, and J. Peng, "Dynamic Transmission Performances of Alumina and Mullite Refractory Ceramics in Microwave High-Temperature Heating," *High Temp. Mater. Process.*, vol. 35, no. 1, pp. 113–119, 2016.

[116] C. E. Holcombe, N. L. Dykes, and M. S. Morrow, "Thermal insulation for high temperature microwave sintering operations and method thereof," 5,449,887, 1995.

[117] E. Khaghanikavkani, "Microwave Pyrolysis of Plastic," *J. Chem. Eng. Process Technol.*, vol. 04, no. 3, 2013.

[118] G. Bond, R. B. Moyes, S. D. Pollington, and D. A. Whan, "Measurement of temperature during microwave heating (chemical reactions enhancement)," *Meas. Sci. Technol.*, vol. 2, no. 6, pp. 571–572, Jun. 1991.

[119] E. Pert *et al.*, "Temperature measurements during microwave processing: the significance of thermocouple effects," *J. Am. Ceram. Soc.*, vol. 84, no. 9, pp. 1981–1986, 2001.

[120] J. Robinson *et al.*, "Microwave Pyrolysis of Biomass: Control of Process Parameters for High Pyrolysis Oil Yields and Enhanced Oil Quality," *Energy & Fuels*, vol. 29, no. 3, pp. 1701–1709, 2015.

[121] D. V. Suriapparao and R. Vinu, “Resource recovery from synthetic polymers via microwave pyrolysis using different susceptors,” *J. Anal. Appl. Pyrolysis*, vol. 113, pp. 701–712, 2015.

[122] Z. Song, Y. Yang, X. Zhao, J. Sun, W. Wang, and Y. Mao, “Journal of Analytical and Applied Pyrolysis Microwave pyrolysis of tire powders : Evolution of yields and composition of products,” *J. Anal. Appl. Pyrolysis*, vol. 123, pp. 152–159, 2017.

[123] L. A. Jermolovicius, E. R. de Castro, J. T. Senise, M. B. Mourao, and C. Takano, “Equipment for microwave enhanced carbothermic reductions,” in *2009 SBMO/IEEE MTT-S International Microwave and Optoelectronics Conference (IMOC)*, 2009, pp. 167–171.

[124] E. Renato de Castro, M. Breda Mourão, L. A. Jermolovicius, C. Takano, and J. Thomaz Senise, “Carbothermal Reduction of Iron Ore Applying Microwave Energy,” *steel Res. Int.*, vol. 83, no. 2, pp. 131–138, Feb. 2012.

[125] S. Farag, A. Sobhy, C. Akyel, J. Doucet, and J. Chaouki, “Temperature profile prediction within selected materials heated by microwaves at 2.45GHz,” *Appl. Therm. Eng.*, vol. 36, no. 1, pp. 360–369, 2012.

[126] A. Hallac and A. C. Metaxas, “Modelling of Industrial Conveyorized Applicators Using Higher Order Vector Finite Elements,” *J. Microw. Power Electromagn. Energy*, vol. 40, no. 2, pp. 101–109, 2005.

[127] D. C. Dibben and R. Metaxas, “Time domain finite element analysis of multimode microwave applicators,” *IEEE Trans. Magn.*, vol. 32, no. 3 PART 2, pp. 942–945, 1996.

[128] P. Plaza-González, J. Monzó-Cabrera, J. M. Catalá-Civera, and D. Sánchez-Hernández, “New approach for the prediction of the electric field distribution in multimode microwave-heating applicators with mode stirrers,” *IEEE Trans. Magn.*, vol. 40, no. 3, pp. 1672–1678, 2004.

[129] R. A. Ehlers and A. C. R. Metaxas, “3-D FE discontinuous sheet for microwave heating,” *IEEE Trans. Microw. Theory Tech.*, vol. 51, no. 3, pp. 718–726, 2003.

[130] S. Bradshaw, S. Delport, and E. Van Wyk, “Qualitative measurement of heating uniformity in a multimode microwave cavity,” *J. Microw. Power Electromagn. Energy*, vol. 32, no. 2, pp. 87–95, 1997.

[131] V. D. Nguyen and K. R. Birdwhistell, “Microwave mapping demonstration using the thermochromic cobalt chloride equilibrium,” *J. Chem. Educ.*, vol. 91, no. 6, pp. 880–882, 2014.

[132] S. L. Semiatin, *Elements of induction heating: design, control, and applications*. ASM International, 1988.

[133] “Indutelec UK,” 2018. [Online]. Available: https://www.inductelec.co.uk/. [Accessed: 09-Oct-2018].

[134] T. Koral, “Considerations for Commercial Success in new RF and Microwave Industrial Heating Applications,” no. September, 2013.

[135] G. Blaker, “Radio Frequency Drying of Ceramics and Fiberglass,” *Ceram. Ind.*, pp. 1–5, 2015.

[136] Q. Zhong, K. P. Sandeep, and K. R. Swartzel, “Continuous flow radio frequency heating

of water and carboxymethylcellulose solutions," *J. Food Sci.*, vol. 68, no. 1, pp. 217–223, 2003.

[137] V. Orsat and G. S. V. Raghavan, "Radio-Frequency Processing," in *Emerging Technologies for Food Processing*, Elsevier, 2014, pp. 385–398.

[138] P. Richardson, *Thermal technologies in food processing*. Taylor & Francis, 2001.

[139] M. Vollmer, "Physics of the microwave oven," *Phys. Educ.*, vol. 39, no. 1, pp. 74–81, 2003.

[140] M. Dunn, "Microwave Heating of Ceramics." [Online]. Available: http://www.ceramicindustry.com/articles/95044-microwave-heating-of-ceramics. [Accessed: 03-May-2016].

[141] J. P. Robinson *et al.*, "Remediation of oil-contaminated drill cuttings using continuous microwave heating," *Chem. Eng. J.*, vol. 152, no. 2–3, pp. 458–463, Oct. 2009.

[142] A. Methlouthi, O. Rouaud, and L. Boillereaux, "Microwave Applicator with Conveyor Belt System," 2010.

[143] M. Nishioka *et al.*, "Single-Mode Microwave Reactor Used for Continuous Flow Reactions under Elevated Pressure," *Ind. Eng. Chem. Res.*, vol. 52, no. 12, pp. 4683–4687, Mar. 2013.

[144] E. R. Binner *et al.*, "Separation of Oil/Water Emulsions in Continuous Flow Using Microwave Heating," *Energy & Fuels*, vol. 27, no. 6, pp. 3173–3178, 2013.

[145] S. Yokozawa *et al.*, "Development of a highly efficient single-mode microwave applicator with a resonant cavity and its application to continuous flow syntheses," *RSC Adv.*, vol. 5, no. 14, pp. 10204–10210, 2015.

[146] L. E. Steed *et al.*, "Continuous flow microwave-assisted processing and aseptic packaging of purple-fleshed sweetpotato purees," *J. Food Sci.*, vol. 73, no. 9, 2008.

[147] IMS, "Continuous Microwave Cylindrical Heating System." 2008.

[148] A. J. Buttress *et al.*, "Towards large scale microwave treatment of ores: Part 1 – Basis of design, construction and commissioning," *Miner. Eng.*, vol. 109, pp. 169–183, Aug. 2017.

[149] A. R. Batchelor *et al.*, "Towards large scale microwave treatment of ores: Part 2 – Metallurgical testing," *Miner. Eng.*, vol. 111, pp. 5–24, 2017.

[150] Y. Wharton, "Microwave Chemistry - out of the lab and into production," *Eur. Process Intensif. Conf.*, vol. 157, no. 157, pp. 117–121, 2011.

[151] Y. Wharton, "Microwave flow chemistry : Faster , cleaner , greener , safer," *Spec. Chem. Mag.*, no. November, pp. 27–28, 2012.

[152] A. Ong, KC Gary and Akbarnezhad, *Microwave-Assisted Concrete Technology: Production, Demolition and Recycling*. CRC Press, 2014.

[153] G. C. Goats, "Microwave diathermy," *Br. J. Sports Med.*, vol. 24, no. 4, pp. 212–218, 1990.

[154] C. L. Brace, "Radiofrequency and microwave ablation of the liver, lung, kidney, and bone: what are the differences?," *Curr. Probl. Diagn. Radiol.*, vol. 38, no. 3, pp. 135–

143, 2009.

[155] M. Sundberg, P. O. Risman, P.-S. Kildal, and T. Ohlsson, “Analysis and Design of Industrial Microwave Ovens Using the Finite Difference Time Domain Method,” *J. Microw. Power Electromagn. Energy*, vol. 31, no. 3, pp. 142–157, Jan. 1996.

[156] D. Agrawal, J. Cheng, H. Peng, and L. Hurt, “Microwave Energy Applied to Processing of High-Temperature Materials variety of ceramic , composite and metallic materials at lower costs .,” *Am. Ceram. Soc. Bull.*, vol. 87, no. 3, pp. 39–44, 2008.

[157] S. S. Lam and H. A. Chase, “A Review on Waste to Energy Processes Using Microwave Pyrolysis,” *Energies*, vol. 5, no. 12, pp. 4209–4232, 2012.

[158] D. Mohan, C. U. Pittman, and P. H. Steele, “Pyrolysis of wood/biomass for bio-oil: A critical review,” *Energy and Fuels*, vol. 20, no. 3, pp. 848–889, 2006.

[159] M. I. Jahirul, M. G. Rasul, A. A. Chowdhury, and N. Ashwath, “Biofuels production through biomass pyrolysis- A technological review,” *Energies*, vol. 5, no. 12, pp. 4952–5001, 2012.

[160] R. Luque, J. A. Menéndez, A. Arenillas, and J. Cot, “Microwave-assisted pyrolysis of biomass feedstocks: the way forward?,” *Energy Environ. Sci.*, vol. 5, no. 2, pp. 5481–5488, 2012.

[161] V. Gude, P. Patil, E. Martinez-Guerra, S. Deng, and N. Nirmalakhandan, “Microwave energy potential for biodiesel production,” *Sustain. Chem. Process.*, vol. 1, no. 1, p. 5, 2013.

[162] F. Mushtaq, R. Mat, and F. N. Ani, “A review on microwave assisted pyrolysis of coal and biomass for fuel production,” *Renew. Sustain. Energy Rev.*, vol. 39, pp. 555–574, 2014.

[163] Y. F. Huang, P. Te Chiueh, and S. L. Lo, “A review on microwave pyrolysis of lignocellulosic biomass,” *Sustain. Environ. Res.*, vol. 26, no. 3, pp. 103–109, 2016.

[164] B. Boundy, S. W. Diegel, L. Wright, and S. C. Davis, “Appendix A,” in *Biomass Energy Data Book*, Oak Ridge National Laboratory, 2011.

[165] R. Geyer, J. R. Jambeck, and K. L. Law, “Production, use, and fate of all plastics ever made,” *Sci. Adv.*, vol. 3, no. 7, p. e1700782, 2017.

[166] C. Ludlow-Palafox and H. A. Chase, “Microwave-Induced Pyrolysis of Plastic Wastes,” *Ind. Eng. Chem. Res.*, vol. 40, no. 22, pp. 4749–4756, Oct. 2001.

[167] A. Undri, L. Rosi, M. Frediani, and P. Frediani, “Efficient disposal of waste polyolefins through microwave assisted pyrolysis,” *Fuel*, vol. 116, pp. 662–671, 2014.

[168] K. N. Aishwarya and N. Sindhu, “Microwave Assisted Pyrolysis of Plastic Waste,” *Procedia Technol.*, vol. 25, no. Raerest, pp. 990–997, 2016.

[169] S. L. Wong, N. Ngadi, T. A. T. Abdullah, and I. M. Inuwa, “Current state and future prospects of plastic waste as source of fuel: A review,” *Renew. Sustain. Energy Rev.*, vol. 50, pp. 1167–1180, 2015.

[170] S. D. Anuar Sharuddin, F. Abnisa, W. M. A. Wan Daud, and M. K. Aroua, “A review on pyrolysis of plastic wastes,” *Energy Convers. Manag.*, vol. 115, no. May, pp. 308–326, May 2016.

[171] X. Zhang, H. Lei, G. Yadavalli, L. Zhu, Y. Wei, and Y. Liu, “Gasoline-range hydrocarbons produced from microwave-induced pyrolysis of low-density polyethylene over ZSM-5,” *Fuel*, vol. 144, pp. 33–42, 2015.

[172] S. R. Juliastuti, N. Hendrianie, P. J. Ramadhan, and D. H. Satria, “Microwave pyrolysis of multilayer plastic waste (LDPE) using zeolite catalyst,” 2017, vol. 110001, p. 110001.

[173] Z. Hussain, K. M. Khan, and K. Hussain, “Microwave-metal interaction pyrolysis of polystyrene,” *J. Anal. Appl. Pyrolysis*, vol. 89, no. 1, pp. 39–43, Sep. 2010.

[174] Z. Hussain, K. M. Khan, N. Basheer, and K. Hussain, “Co-liquefaction of Makarwal coal and waste polystyrene by microwave-metal interaction pyrolysis in copper coil reactor,” *J. Anal. Appl. Pyrolysis*, vol. 90, no. 1, pp. 53–55, Jan. 2011.

[175] Z. Hussain, K. M. Khan, S. Perveen, K. Hussain, and W. Voelter, “The conversion of waste polystyrene into useful hydrocarbons by microwave-metal interaction pyrolysis,” *Fuel Process. Technol.*, vol. 94, no. 1, pp. 145–150, Feb. 2012.

[176] S. J. Goodman, “The Microwave Induced Pyrolysis of Problematic Plastics Enabling Recovery and Component Reuse,” Imperial College London, 2013.

[177] A. Undri, M. Frediani, L. Rosi, and P. Frediani, “Reverse polymerization of waste polystyrene through microwave assisted pyrolysis,” *J. Anal. Appl. Pyrolysis*, vol. 105, pp. 35–42, Jan. 2014.

[178] A. Undri, L. Rosi, M. Frediani, and P. Frediani, “Fuel from microwave assisted pyrolysis of waste multilayer packaging beverage,” *Fuel*, vol. 133, pp. 7–16, Oct. 2014.

[179] L. Rosi, M. Bartoli, and M. Frediani, “Microwave assisted pyrolysis of halogenated plastics recovered from waste computers,” *Waste Manag.*, 2017.

[180] V. Ramopoulos, G. Link, S. Soldatov, and J. Jelonnek, “Industrial scale microwave applicator for high temperature alkaline hydrolysis of PET,” *Int. J. Microw. Wirel. Technol.*, vol. 10, no. 5–6, pp. 709–716, 2018.

[181] World Business Council for Sustainable Development, “Managing End-of-Life Tires,” 2008.

[182] V. K. Sharma, F. Fortuna, M. Mincarini, M. Berillo, and G. Cornacchia, “Disposal of waste tyres for energy recovery and safe environment,” *Appl. Energy*, vol. 65, no. 1–4, pp. 381–394, Apr. 2000.

[183] a. V. Yatsun, P. N. Konovalov, and N. P. Konovalov, “Gaseous products of microwave pyrolysis of scrap tires,” *Solid Fuel Chem.*, vol. 42, no. 3, pp. 187–191, 2008.

[184] F. N. Ani and N. S. Mat Nor, “Microwave induced fast pyrolysis of scrap rubber tires,” in *AIP Conference Proceedings*, 2012, pp. 834–841.

[185] a. V. Yatsun, N. P. Konovalov, and I. S. Efimenko, “Liquid products of the microwave pyrolysis of scrap tires,” *Solid Fuel Chem.*, vol. 47, no. 4, pp. 252–254, 2013.

[186] A. L. Chia Yang and F. N. Ani, “Controlled microwave-induced pyrolysis of waste rubber tires,” *Int. J. Technol.*, vol. 7, no. 2, pp. 314–322, 2016.

[187] A. Undri, S. Meini, L. Rosi, M. Frediani, and P. Frediani, “Microwave pyrolysis of polymeric materials: Waste tires treatment and characterization of the value-added products,” *J. Anal. Appl. Pyrolysis*, vol. 103, pp. 149–158, Sep. 2013.

[188] A. Undri, L. Rosi, M. Frediani, and P. Frediani, “Upgraded fuel from microwave assisted pyrolysis of waste tire,” *Fuel*, vol. 115, pp. 600–608, Jan. 2014.

[189] D. Fitzsimons, *Improving Recycling Markets*, vol. 9789264029. OECD Publishing, 2006.

[190] S. S. Lam, R. K. Liew, A. Jusoh, C. T. Chong, F. N. Ani, and H. A. Chase, “Progress in waste oil to sustainable energy, with emphasis on pyrolysis techniques,” *Renew. Sustain. Energy Rev.*, vol. 53, pp. 741–753, 2016.

[191] S. S. Lam, A. D. Russell, and H. A. Chase, “Microwave pyrolysis, a novel process for recycling waste automotive engine oil,” *Energy*, vol. 35, no. 7, pp. 2985–2991, 2010.

[192] S. S. Lam, S. Russell, and A. Chase, “From waste to valuable fuel: How microwave-heated pyrolysis can recycle waste automotive engine oil,” *Prepr. Pap. Am. Chem. Soc. Div. Fuel Chem.*, vol. 56, no. 1, pp. 19–21, 2011.

[193] S. S. Lam, A. D. Russell, C. L. Lee, S. K. Lam, and H. A. Chase, “Production of hydrogen and light hydrocarbons as a potential gaseous fuel from microwave-heated pyrolysis of waste automotive engine oil,” *Int. J. Hydrogen Energy*, vol. 37, no. 6, pp. 5011–5021, 2012.

[194] S. S. Lam, A. D. Russell, C. L. Lee, and H. A. Chase, “Microwave-heated pyrolysis of waste automotive engine oil: Influence of operation parameters on the yield, composition, and fuel properties of pyrolysis oil,” *Fuel*, vol. 92, no. 1, pp. 327–339, 2012.

[195] S. S. Lam, R. K. Liew, C. K. Cheng, and H. A. Chase, “Catalytic microwave pyrolysis of waste engine oil using metallic pyrolysis char,” *Appl. Catal. B Environ.*, vol. 176–177, no. 1, pp. 601–617, 2015.

[196] H. M. Abo-Dief, A. A. Altalhi, and A. T. Mohamed, “Waste Oil Recycling Using Microwave Pyrolysis Reactors,” *J. Ind. Intell. Inf.*, vol. 2, no. 4, pp. 314–319, 2014.

[197] M. A. Budianto, S. Anis, and W. Sumbodo, “Study of Thermal Heating of Waste Engine Oil in a Microwave Pyrolysis Reactor,” *J. Phys. Sci.*, vol. 29, pp. 39–52, 2018.

[198] N. B. Osman, Y. Uemura, H. Afif, and A. H. R. Aljuboori, “Pyrolyzed Waste Engine Oil Properties by Microwave-Induced Reactor,” *Appl. Mech. Mater.*, vol. 625, pp. 673–676, 2014.

[199] V. L. Budarin *et al.*, “Use of green chemical technologies in an integrated biorefinery,” *Energy Environ. Sci.*, vol. 4, no. 2, pp. 471–479, 2011.

[200] M. Miura, H. Kaga, A. Sakurai, T. Kakuchi, and K. Takahashi, “Rapid pyrolysis of wood block by microwave heating,” *J. Anal. Appl. Pyrolysis*, vol. 71, no. 1, pp. 187–199, 2004.

[201] S. Papari and K. Hawboldt, “A review on the pyrolysis of woody biomass to bio-oil: Focus on kinetic models,” *Renew. Sustain. Energy Rev.*, vol. 52, pp. 1580–1595, 2015.

[202] X. H. Wang, H. P. Chen, X. J. Ding, H. P. Yang, S. H. Zhang, and Y. Q. Shen, “Properties of gas and char from microwave pyrolysis of pine sawdust,” *BioResources*, vol. 4, no. 3, pp. 946–959, 2009.

[203] C. Ravikumar, P. Senthil Kumar, S. K. Subhashni, P. V. Tejaswini, and V. Varshini, “Microwave assisted fast pyrolysis of corn cob, corn stover, saw dust and rice straw: Experimental investigation on bio-oil yield and high heating values,” *Sustain. Mater.*

Technol., vol. 11, pp. 19–27, 2016.

[204] M. Adam, D. Beneroso, J. Katrib, S. Kingman, and J. P. Robinson, "Microwave fluidized bed for biomass pyrolysis. Part I: Process design," *Biofuels, Bioprod. Biorefining*, vol. 11, no. 4, pp. 601–612, Jul. 2017.

[205] M. Adam, D. Beneroso, J. Katrib, S. Kingman, and J. P. Robinson, "Microwave fluidized bed for biomass pyrolysis. Part II: Effect of process parameters," *Biofuels, Bioprod. Biorefining*, vol. 11, no. 4, pp. 613–624, Jul. 2017.

[206] J. A. Menendez, A. Dominguez, M. Inguanzo, and J. J. Pis, "Microwave pyrolysis of sewage sludge: Analysis of the gas fraction," *J. Anal. Appl. Pyrolysis*, vol. 71, no. 2, pp. 657–667, 2004.

[207] A. Dominguez, J. A. Menendez, M. Inguanzo, and J. J. Pis, "Investigations into the characteristics of oils produced from microwave pyrolysis of sewage sludge," *Fuel Process. Technol.*, vol. 86, no. 9, pp. 1007–1020, 2005.

[208] Q. Lin, G. Chen, and Y. Liu, "Scale-up of microwave heating process for the production of bio-oil from sewage sludge," *J. Anal. Appl. Pyrolysis*, vol. 94, pp. 114–119, Mar. 2012.

[209] A. Domínguez *et al.*, "Conventional and microwave induced pyrolysis of coffee hulls for the production of a hydrogen rich fuel gas," *J. Anal. Appl. Pyrolysis*, vol. 79, no. 1-2 SPEC. ISS., pp. 128–135, 2007.

[210] X. Zhao, J. Zhang, Z. Song, H. Liu, L. Li, and C. Ma, "Microwave pyrolysis of straw bale and energy balance analysis," *J. Anal. Appl. Pyrolysis*, vol. 92, no. 1, pp. 43–49, 2011.

[211] P. Li, X. Wang, W. Gong, H. Yang, Y. Chen, and H. Chen, "Effects of metal salt additives on biomass microwave pyrolysis characteristic," *Nongye Jixie Xuebao/Transactions Chinese Soc. Agric. Mach.*, vol. 44, no. 6, pp. 162–167, 2013.

[212] Q. Xie *et al.*, "Fast microwave-assisted catalytic gasification of biomass for syngas production and tar removal," *Bioresour. Technol.*, vol. 156, pp. 291–296, Mar. 2014.

[213] A. A. Salema, M. T. Afzal, and L. Bennamoun, "Pyrolysis of corn stalk biomass briquettes in a scaled-up microwave technology," *Bioresour. Technol.*, vol. 233, pp. 353–362, Jun. 2017.

[214] Z. Du *et al.*, "Microwave-assisted pyrolysis of microalgae for biofuel production," *Bioresour. Technol.*, vol. 102, no. 7, pp. 4890–4896, 2011.

[215] Z. Hu, X. Ma, and C. Chen, "A study on experimental characteristic of microwave-assisted pyrolysis of microalgae," *Bioresour. Technol.*, vol. 107, pp. 487–493, 2012.

[216] D. Beneroso, J. M. Bermúdez, A. Arenillas, and J. A. Menéndez, "Microwave pyrolysis of microalgae for high syngas production," *Bioresour. Technol.*, vol. 144, pp. 240–246, 2013.

[217] N. Ferrera-Lorenzo, E. Fuente, J. M. Bermúdez, I. Suárez-Ruiz, and B. Ruiz, "Conventional and microwave pyrolysis of a macroalgae waste from the Agar-Agar industry. Prospects for bio-fuel production," *Bioresour. Technol.*, vol. 151, pp. 199–206, 2014.

[218] B. Evjen, "Final Report - MICROFUEL (Mobile microwave pyrolysis plant turns

biomass into fuel locally),” 2012.

[219] CORDIS, “Final Report Summary - MICROFUEL,” 2012. [Online]. Available: https://cordis.europa.eu/project/rcn/107623/reporting/en. [Accessed: 10-Jul-2019].

[220] Scandinavian Biofuel Company, “Scandinavian Biofuel Webpage.” [Online]. Available: https://www.sbiofuel.com/index.html. [Accessed: 18-Jun-2019].

[221] J. Li *et al.*, “Biochar from microwave pyrolysis of biomass: A review,” *Biomass and Bioenergy*, vol. 94. Pergamon, pp. 228–244, 01-Nov-2016.

[222] D. Beneroso, A. Albero-Ortiz, J. Monzó-Cabrera, A. Díaz-Morcillo, A. Arenillas, and J. A. Menéndez, “Dielectric characterization of biodegradable wastes during pyrolysis,” *Fuel*, vol. 172, pp. 146–152, May 2016.

[223] X. Li, J. Zhang, C. Liao, H. Chen, Y. Luo, and X. Li, “Mathematical simulation and design of a rectangular cavity of microwave pretreatment equipment used for wood modification,” *BioResources*, vol. 10, no. 1, pp. 527–537, 2015.

[224] A. A. Salema and M. T. Afzal, “Numerical simulation of heating behaviour in biomass bed and pellets under multimode microwave system,” *Int. J. Therm. Sci.*, vol. 91, pp. 12–24, 2015.

[225] S. Gadkari, B. Fidalgo, and S. Gu, “Numerical investigation of microwave-assisted pyrolysis of lignin,” *Fuel Process. Technol.*, vol. 156, pp. 473–484, 2017.

[226] Y. Zhang *et al.*, “Microwave-Assisted Pyrolysis of Biomass for Bio-Oil Production,” in *Pyrolysis*, InTech, 2017.

[227] S. W. Kingman and N. A. Rowson, “Microwave treatment of minerals-a review,” *Miner. Eng.*, vol. 11, no. 11, pp. 1081–1087, 1998.

[228] S. W. Kingman, W. Vorster, and N. A. Rowson, “The influence of mineralogy on microwave assisted grinding,” *Miner. Eng.*, vol. 13, no. 3, pp. 313–327, 2000.

[229] S. W. Kingman, K. Jackson, A. Cumbane, S. M. Bradshaw, N. A. Rowson, and R. Greenwood, “Recent developments in microwave-assisted comminution,” *Int. J. Miner. Process.*, vol. 74, no. 1–4, pp. 71–83, 2004.

[230] M. Al-Harahsheh and S. W. Kingman, “Microwave-assisted leaching - A review,” *Hydrometallurgy*, vol. 73, no. 3–4, pp. 189–203, Jun. 2004.

[231] D. A. Jones, S. W. Kingman, D. N. Whittles, and I. S. Lowndes, “Understanding microwave assisted breakage,” *Miner. Eng.*, vol. 18, pp. 659–669, 2005.

[232] Z. Cao, N. Yoshikawa, and S. Taniguchi, “Directional selectivity of microwave H field heating of Au thin films and non-doped Si plates,” *Mater. Chem. Phys.*, vol. 117, no. 1, pp. 14–17, Sep. 2009.

[233] Z. Cao, N. Yoshikawa, and S. Taniguchi, “Microwave heating behaviors of Si substrate materials in a single-mode cavity,” *Mater. Chem. Phys.*, vol. 124, no. 2–3, pp. 900–903, Dec. 2010.

[234] Z. Peng, J. Y. Hwang, and M. Andriese, “Magnetic loss in microwave heating,” *Appl. Phys. Express*, vol. 5, no. 2, p. 027304, Feb. 2012.

[235] J. Cheng, R. Roy, and D. Agrawal, “Experimental proof of major role of magnetic field

losses in microwave heating of metal and metallic composites," *J. Mater. Sci. Lett.*, vol. 20, no. 17, pp. 1561–1563, 2001.

[236] J. Cheng, R. Roy, and D. Agrawal, "Radically different effects on materials by separated microwave electric and magnetic fields," *Mater. Res. Innov.*, vol. 5, no. 3–4, pp. 170–177, Feb. 2002.

[237] R. Roy, R. Peelamedu, L. Hurtt, J. Cheng, and D. Agrawal, "Definitive experimental evidence for Microwave Effects : radically new effects of separated E and H fields, such as decrystallization of oxides in seconds," *Mater. Res. Innov.*, vol. 6, no. 3, pp. 128–140, Sep. 2002.

[238] J. Luo, C. Hunyar, L. Feher, G. Link, M. Thumm, and P. Pozzo, "Theory and experiments of electromagnetic loss mechanism for microwave heating of powdered metals," *Appl. Phys. Lett.*, vol. 84, no. 25, pp. 5076–5078, Jun. 2004.

[239] K. I. Rybakov, V. E. Semenov, S. V. Egorov, A. G. Eremeev, I. V. Plotnikov, and Y. V. Bykov, "Microwave heating of conductive powder materials," *J. Appl. Phys.*, vol. 99, no. 2, p. 023506, Jan. 2006.

[240] P. Mishra, A. Upadhyaya, and G. Sethi, "Modeling of microwave heating of particulate metals," *Metall. Mater. Trans. B*, vol. 37, no. 5, pp. 839–845, Oct. 2006.

[241] Z. Cao, Z. Wang, N. Yoshikawa, and S. Teniguchi, "Microwave heating origination and rapid crystallization of PZT thin films in separated H field," *J. Phys. D. Appl. Phys.*, vol. 41, no. 9, p. 92003, 2008.

[242] Z. Cao, N. Yoshikawa, and S. Taniguchi, "Microwave heating behavior of nanocrystalline Au thin films in single-mode cavity," *J. Mater. Res.*, vol. 24, no. 01, pp. 268–273, Jan. 2009.

[243] U. S. E. Protection and A. (EPA), "Technical Resource Document: Iron," 1994.

[244] Z. Peng, J. Y. Hwang, J. Mouris, R. Hutcheon, and X. Sun, "Microwave absorption characteristics of conventionally heated nonstoichiometric ferrous oxide," *Metall. Mater. Trans. A Phys. Metall. Mater. Sci.*, vol. 42, no. 8, pp. 2259–2263, 2011.

[245] Z. Peng *et al.*, "Microwave Power Absorption in Materials for Ferrous Metallurgy," *JOM*, vol. 69, no. 2, pp. 178–183, Feb. 2017.

[246] M. Hotta, M. Hayashi, and K. Nagata, "Complex Permittivity and Permeability of α-Fe2O3 and Fe1- xO Powders in the Microwave Frequency Range between 0.2 and 13.5 GHz," *ISIJ Int.*, vol. 50, no. 10, pp. 1514–1516, 2010.

[247] Z. Peng, J.-Y. Hwang, C.-L. Park, B.-G. Kim, M. Andriese, and X. Wang, "Microwave Permittivity, Permeability, and Absorption Capability of Ferric Oxide," *ISIJ Int.*, vol. 52, no. 9, pp. 1535–1538, 2012.

[248] M. Hotta, M. Hayashi, A. Nishikata, and K. Nagata, "Complex Permittivity and Permeability of SiO2 and Fe3O4 Powders in Microwave Frequency Range between 0.2 and 13.5 GHz," *ISIJ Int.*, vol. 49, no. 9, pp. 1443–1448, 2009.

[249] M. Hotta, M. Hayashi, and K. Nagata, "High Temperature Measurement of Complex Permittivity and Permeability of Fe3O4 Powders in the Frequency Range of 0.2 to 13.5 GHz," *ISIJ Int.*, vol. 51, no. 3, pp. 491–497, Mar. 2011.

[250] R. Rajavaram, J. Lee, J. S. Oh, H. G. Kim, and J. Lee, "Microwave heating characteristics

of magnetite ore," *Met. Mater. Int.*, vol. 22, no. 6, pp. 1116–1120, Nov. 2016.

[251] M. Hotta, M. Hayashi, M. T. Lanagan, D. K. Agrawal, and K. Nagata, "Complex Permittivity of Graphite, Carbon Black and Coal Powders in the Ranges of X-band Frequencies (8.2 to 12.4 GHz) and between 1 and 10 GHz," *ISIJ Int.*, vol. 51, no. 11, pp. 1766–1772, 2011.

[252] S. M. Javad and K. Barani, "Microwave Heating Applications in Mineral Processing," in *The Development and Application of Microwave Heating*, InTech, 2012.

[253] IARC, "Coke Production," *IARC Monogr.*, vol. 100F, 2012.

[254] E. Lester, S. Kingman, C. Dodds, and J. Patrick, "The potential for rapid coke making using microwave energy," *Fuel*, vol. 85, no. 14–15, pp. 2057–2063, 2006.

[255] G. Coetzer and M. Rossouw, "Influence of Additives on Cokemaking from a Semi-soft Coking Coal during Microwave Heating," *ISIJ Int.*, vol. 52, no. 3, pp. 369–377, 2012.

[256] Y. Du Hong, B. Q. Lin, H. Li, H. M. Dai, C. J. Zhu, and H. Yao, "Three-dimensional simulation of microwave heating coal sample with varying parameters," *Appl. Therm. Eng.*, vol. 93, pp. 1145–1154, 2016.

[257] Y. Lei, Y. Li, W. Chen, and R. Wan, "Microwave Carbothermic Reduction of Oolitic Hematite," *ISIJ Int.*, vol. 57, no. 5, pp. 791–794, 2017.

[258] J. A. Aguilar and I. Gomez, "Microwaves Applied to carbothermic reduction of iron ore pellets," *J. Microw. Power Electromagn. Energy*, vol. 32, no. 2, pp. 67–73, 1997.

[259] M. B. Mourão, I. P. de Carvalho, Jr., and C. Takano, "Carbothermic Reduction by Microwave Heating," *ISIJ Int.*, vol. 41, no. Suppl, pp. S27–S30, 2001.

[260] K. Ishizaki, K. Nagata, and T. Hayashi, "Production of pig iron from magnetite ore-coal composite pellets by microwave heating," *ISIJ Int.*, vol. 46, no. 10, pp. 1403–1409, 2006.

[261] K. Ishizaki, K. Nagata, and T. Hayashi, "Localized heating and reduction of magnetite ore with coal in composite pellets using microwave irradiation," *ISIJ Int.*, vol. 47, no. 6, pp. 817–822, 2007.

[262] Y. Lei *et al.*, "Carbothermic Reduction of Panzhihua Oxidized Ilmenite in a Microwave Field," *ISIJ Int.*, vol. 51, no. 3, pp. 337–343, 2011.

[263] B. Hu, Z. Huang, L. Yi, and T. Jiang, "Direct reduction of carburized pre-reduced pellets by microwave heating," *J. Cent. South Univ.*, vol. 21, no. 1, pp. 351–357, 2014.

[264] T. Chun, H. Long, Z. Di, P. Wang, and Q. Meng, "Influence of microwave heating on the microstructures of iron ore pellets with coal during reduction," *Ironmak. Steelmak.*, vol. 44, no. 7, pp. 486–491, Aug. 2017.

[265] N. Standish and Pramusanto, "Reduction of microwave irradiated iron ore particles in CO.," *ISIJ Int.*, vol. 31, no. 1, pp. 11–16, 1991.

[266] N. Standish and W. Huang, "Microwave Application in Carbothermic Reduction of lron Ores," *ISIJ Int.*, vol. 31, no. 3, pp. 241–245, 1991.

[267] K. Nishioka, T. Taniguchi, Y. Ueki, K. Ohno, T. Maeda, and M. Shimizu, "Gasification and Reduction Behavior of Plastics and Iron Ore Mixtures by Microwave Heating," *ISIJ Int.*, vol. 47, no. 4, pp. 602–607, 2007.

[268] K. Ishizaki and K. Nagata, “Selectivity of microwave energy consumption in the reduction of Fe3O4 with carbon black in mixed powder,” *ISIJ Int.*, vol. 47, no. 6, pp. 811–816, 2007.

[269] K. Ishizaki and K. Nagata, “Microwave Induced Solid – Solid Reactions between Fe 3 O 4 and Carbon Black Powders,” vol. 48, no. 9, pp. 1159–1164, 2008.

[270] M. Hayashi, K. Takeda, K. Kashimura, T. Watanabe, and K. Nagata, “Carbothermic Reduction of Hematite Powders by Microwave Heating,” *ISIJ Int.*, vol. 53, no. 7, pp. 1125–1130, 2013.

[271] M. S. and M. T. and E. Kouvelos, “Novel applications of microwaves in the metallurgical processing of a nickel-ferrous laterite ore and an aluminum industry waste,” *IOP Conf. Ser. Mater. Sci. Eng.*, vol. 123, no. 1, p. 12049, 2016.

[272] L. Ye *et al.*, “Preparation of core-shell iron ore-biochar composite pellets for microwave reduction,” *Powder Technol.*, vol. 338, no. X, pp. 365–375, 2018.

[273] J. R. Dankwah, B. S. Agbenuvor, and P. Koshy, “Production of Iron Nuggets from the Akpafu-Todzi Iron Ore using Waste Plastics and Waste Biomass as Reductants *,” no. 1, 2016.

[274] K. Nagata *et al.*, “A concept of microwave furnace for steel making in industry scale,” 2007, pp. 87–90.

[275] J. Li, B. Li, J. Han, Z. Cao, and J. Wang, “A Comparative Study on the Reduction Mechanism of Fe2O3 Under Different Heating Methods,” *JOM*, vol. 66, no. 8, pp. 1529–1536, Aug. 2014.

[276] K. Kashimura, K. Nagata, and M. Sato, “Concept of Furnace for Metal Refining by Microwave Heating —A Design of Microwave Smelting Furnace with Low CO2 Emission—,” *Mater. Trans.*, vol. 51, no. 10, pp. 1847–1853, 2010.

[277] X. Huang and J.-Y. Hwang, “Novel Direct Steelmaking By Combining Microwave, Electric Arc, and Exothermal Heating Technologies,” 2005.

[278] J.-Y. Hwang and X. Huang, “MICROWAVE HEATING METHOD AND APPARATUS FOR IRON OXIDE REDUCTION,” US 20080087135A1, 2008.

[279] K. Cherian *et al.*, “Ride the Wave (High temperature microwave processing can be a faster, greener and cheaper alternative to conventional electric and gas-based heating technologies),” *Ceram. Ind.*, no. September, pp. 16–19, 2008.

[280] R. R. Mishra and A. K. Sharma, “A Review of Research Trends in Microwave Processing of Metal-Based Materials and Opportunities in Microwave Metal Casting,” *Crit. Rev. Solid State Mater. Sci.*, vol. 41, no. 3, pp. 217–255, 2016.

[281] V. G. Karayannis, “Microwave sintering of ceramic materials,” *IOP Conf. Ser. Mater. Sci. Eng.*, vol. 161, no. 1, p. 12068, 2016.

[282] B. Yahaya, S. Izman, M. Konneh, and N. Redzuan, “Microwave Hybrid Heating of Materials Using Susceptors - A Brief Review,” *Adv. Mater. Res.*, vol. 845, pp. 426–430, Dec. 2013.

[283] V. V Yakovlev, S. M. Allan, M. L. Fall, and H. S. Shulman, “Computational Study of Microwave Processing of Zirconia : Effects of Frequency and Temperature-Dependent Material Parameters,” in *13th Seminar “Computer Modeling in Microwave Engng &*

Applications," 2011, pp. 59–66.

[284] K. I. Rybakov, E. A. Olevsky, and E. V. Krikun, "Microwave sintering: Fundamentals and modeling," *J. Am. Ceram. Soc.*, vol. 96, no. 4, pp. 1003–1020, Apr. 2013.

[285] K. Cherian and M. Kirksey, "Industrial-Scale Microwave Sintering," *Ceramic Industry*, 2011.

[286] R. Roy, D. Agrawal, J. Cheng, and S. Gedevanlshvili, "Full sintering of powdered-metal bodies in a microwave field," *Nature*, vol. 399, no. 6737, 1999.

[287] S. Gedevanishvili, D. Agrawal, and R. Roy, "Microwave Combustion Synthesis and Sintering of Intermetallics and Alloys," *J. Mater. Sci. Lett.*, vol. 18, no. 9, pp. 665–668, 1999.

[288] R. M. Anklekar, D. K. Agrawal, and R. Roy, "Microwave sintering and mechanical properties of PM copper steel," vol. 44, no. 4, pp. 355–362, 2001.

[289] P. Yadoji, R. Peelamedu, D. Agrawal, and R. Roy, "Microwave sintering of Ni–Zn ferrites: comparison with conventional sintering," *Mater. Sci. Eng. B*, vol. 98, no. 3, pp. 269–278, Apr. 2003.

[290] C. Leonelli, P. Veronesi, L. Denti, A. Gatto, and L. Iuliano, "Microwave assisted sintering of green metal parts," *J. Mater. Process. Technol.*, vol. 205, no. 1–3, pp. 489–496, Aug. 2008.

[291] A. Mondal, D. Agrawal, and A. Upadhyaya, "Microwave sintering of refractory metals/alloys: W, Mo, Re, W-Cu, W-Ni-Cu and W-Ni-Fe alloys.," *J. Microw. Power Electromagn. Energy*, vol. 44, no. 1, pp. 28–44, 2010.

[292] A. Mondal, A. Upadhyaya, and D. Agrawal, "Effect of heating mode and sintering temperature on the consolidation of 90W–7Ni–3Fe alloys," *J. Alloys Compd.*, vol. 509, no. 2, pp. 301–310, Jan. 2011.

[293] R. Roy, R. Peelamedu, C. Grimes, J. Cheng, and D. Agrawal, "Major phase transformations and magnetic property changes caused by electromagnetic fields at microwave frequencies," *J. Mater. Res.*, vol. 17, no. 12, pp. 3008–3011, Dec. 2002.

[294] R. M. Anklekar, D. K. Agrawal, and R. Roy, "Microwave sintering and mechanical properties of PM copper steel," *Powder Metall.*, vol. 44, no. 4, pp. 355–362, Oct. 2001.

[295] Y. Li, F. Xu, X. Hu, Y. Luan, Z. Han, and Z. Wang, "Focusing effect of electromagnetic fields and its influence on sintering during the microwave processing of metallic particles," *J. Mater. Res.*, vol. 30, no. 23, pp. 3663–3670, Dec. 2015.

[296] Maury MW, "VNA Calibration Kits." [Online]. Available: https://www.maurymw.com/Precision/VNA_Cal_Kits.php. [Accessed: 08-Aug-2018].

[297] G. Magerl and K. R. Richter, "A novel method for cavity parameter measurement," *IEEE Trans. Instrum. Meas.*, vol. IM–25, no. 2, pp. 145–151, Jun. 1976.

[298] D. Kajfez, "Q factor measurements, analog and digital," *Univ. Mississippi Dept. Electr. Eng.*, 1999.

[299] T. Berenc and C. Deibele, "Simulation and measurement considerations for resonant cavity couplers and extrapolating results to multiple cells and varying conductivities," *Fermilab RFNote*.

[300] F. Caspers, “RF engineering basic concepts: the Smith chart,” *arXiv Prepr. arXiv1201.4068*, 2012.

[301] Keysight Technologies, “U2000 Series USB Power Sensors.” .

[302] V. Bilik, “Six-port measurement technique: Principles, impact, applications,” in *Invited paper at the International Conference RADIOELEKTRONIKA*, 2002.

[303] G. Tiwari, S. Wang, J. Tang, and S. L. Birla, “Analysis of radio frequency (RF) power distribution in dry food materials,” *J. Food Eng.*, vol. 104, no. 4, pp. 548–556, 2011.

[304] M. Calvo, “Sustainable manufacturing of next generation building materials using microwave energy,” University of Nottingham, 2018.

[305] A. D. Smith *et al.*, “Temperature Dependence of the Dielectric Properties of 2,2′-Azobis(2-methyl-butyronitrile) (AMBN),” *Ind. Eng. Chem. Res.*, vol. 49, no. 6, pp. 3011–3014, Mar. 2010.

[306] B. Garcia-Baños, J. Catalá-Civera, F. Peñaranda-Foix, P. Plaza-González, and G. Llorens-Vallés, “In Situ Monitoring of Microwave Processing of Materials at High Temperatures through Dielectric Properties Measurement,” *Materials (Basel).*, vol. 9, no. 5, p. 349, 2016.

[307] G. Durán-Jiménez, V. Hernández-Montoya, J. Rodríguez Oyarzun, M. Á. Montes-Morán, and E. Binner, “Pb(II) removal using carbon adsorbents prepared by hybrid heating system: Understanding the microwave heating by dielectric characterization and numerical simulation,” *J. Mol. Liq.*, vol. 277, pp. 663–671, Mar. 2019.

[308] Keysight, “TRL and LRM Calibration.” [Online]. Available: http://na.support.keysight.com/plts/help/WebHelp/VNACalAndMeas/TRL_and_LRM_Calibration.htm. [Accessed: 21-Oct-2018].

[309] K. Technologies, “De-Embedding and Embedding S-Parameter Networks Using a Vector Network Analyzer.” 2017.

[310] Soltec Corporation, “NEC H2640 datasheet.” .

[311] Hyperphysics, “Stefan-Boltzmann Law.” [Online]. Available: http://hyperphysics.phy-astr.gsu.edu/hbase/thermo/stefan.html. [Accessed: 10-May-2018].

[312] Hyperphysics, “Radiation Curves.” [Online]. Available: http://hyperphysics.phy-astr.gsu.edu/hbase/bbrc.html#c3. [Accessed: 05-Oct-2018].

[313] Mikron Instrument Company, “Table of Emissivity of Various Surfaces for Infrared Thermometry.” .

[314] Omega, “Emmisivity of common materials.” [Online]. Available: https://www.omega.com/literature/transactions/volume1/emissivitya.html. [Accessed: 08-Oct-2018].

[315] The Engineering Toolbox, “Emmisivity coefficient materials.” [Online]. Available: https://www.engineeringtoolbox.com/emissivity-coefficients-d_447.html. [Accessed: 08-Nov-2018].

[316] F. Cardarelli, *Materials handbook*. Springer, 2000.

[317] Foamglas, “FOAMGLAS ® t4+ Product Datasheet.” 2013.

[318] A. J. Buttress, J. M. Rodriguez, A. Ure, R. S. Ferrari, C. Dodds, and S. W. Kingman, “Production of high purity silica by microfluidic-inclusion fracture using microwave pre-treatment,” *Miner. Eng.*, vol. 131, pp. 407–419, 2019.

[319] coals2u, “NoEcoal50 Smokeless Coal.” [Online]. Available: https://www.coals2u.co.uk/ecoal50.html. [Accessed: 29-Oct-2018].

[320] Vitcas, “Insulating fire bricks.” [Online]. Available: https://www.vitcas.com/insulating-fire-bricks. [Accessed: 29-Oct-2018].

[321] Momentive, “Hot Pressed Boron Nitride,” *Condensed Product Bulletin*. .

[322] B. S. Mitchell, *An Introduction to Materials Engineering and Science*. Hoboken, NJ, USA: John Wiley & Sons, Inc., 2003.

[323] Eddy Current Technology, “Conductivity of Metals Sorted By Resistivity.” [Online]. Available: http://eddy-current.com/conductivity-of-metals-sorted-by-resistivity/. [Accessed: 10-Feb-2017].

[324] British Stainless Steel Association, “Magnetic properties of Stainless Steel,” 2000.

[325] M. F. Iskander, “Computer Modeling and Numerical Simulation of Microwave Heating Systems,” *MRS Bull.*, vol. 18, no. 11, pp. 30–36, 1993.

[326] X. Zhao, L. Yan, and K. Huang, “Review of Numerical Simulation of Microwave Heating Process,” in *Advances in Induction and Microwave Heating of Mineral and Organic Materials*, InTech, 2011, pp. 27–28.

[327] K. Pitchai, “Electromagnetic and Heat Transfer Modeling of Microwave Heating in Domestic Ovens,” University of Nabraska at Lincoln, 2011.

[328] K. Pitchai, S. L. Birla, J. Subbiah, D. Jones, and H. Thippareddi, “Coupled electromagnetic and heat transfer model for microwave heating in domestic ovens,” *J. Food Eng.*, vol. 112, no. 1–2, pp. 100–111, 2012.

[329] CST, “CST Studio Suite ™ 2017.” 2017.

[330] “COMSOL Multiphysics Reference Manual v5.4.” 2018.

[331] W. Frei, “Computational Electromagnetics Modeling, Which Module to Use?,” 2013. [Online]. Available: https://www.comsol.com/blogs/computational-electromagnetics-modeling-which-module-to-use/. [Accessed: 05-May-2017].

[332] Comsol, “The RF Module User Guide.” 2012.

[333] Sairem, “2000 W 2450 MHz Microwave Generator GMP 20K SM 56M230 FST 3 IR.” .

[334] T. Baumann and S. Zunft, “Properties of granular materials as heat transfer and storage medium in CSP application,” *Sol. Energy Mater. Sol. Cells*, vol. 143, pp. 38–47, 2015.

[335] Momentive, “Pyrolytic boron nitride,” *Condensed Product Bulletin*. .

[336] J. H. Whitelaw, “CONVECTIVE HEAT TRANSFER,” in *A-to-Z Guide to Thermodynamics, Heat and Mass Transfer, and Fluids Engineering*, Begellhouse, 2011.

[337] P. Bhartia, S. C. Kashyap, S. S. Stuchly, and M. A. K. Hamid, “Tuning, Coupling and Matching of Microwave Heating Applicators Operating at Higher Order Modes *,” *J.*

Microw. Power, vol. 6, no. 3, pp. 221–228, 1971.

[338] M. Y. El-Ibiary and J. Brown, "The use of lossy material to suppress unwanted modes in cavity resonators," *Proc. IEE Part C Monogr.*, vol. 104, no. 5, p. 25, 1957.

[339] S. Nogi, K. Fukui, M. Kojima, and S. Tanaka, "Effective methods for suppression of undesired cavity modes using microwave absorbers," *Electron. Commun. Japan (Part II Electron.*, vol. 74, no. 9, pp. 31–40, 1991.

[340] J. G. Kretzschmar and F. P. Pietermaat, "Concentrated Microwave Heating in Elliptical Waveguides," *J. Microw. Power*, vol. 6, no. 3, pp. 207–211, Jan. 1971.

[341] V. V Komarov and V. V. Yakovlev, "CAD of efficient TMmn0 single-mode elliptical applicators with coaxial excitation.," *J. Microw. Power Electromagn. Energy*, vol. 40, no. 3, pp. 174–185, 2007.

[342] L. L. Nagy, "Method of detecting soot in engine oil using microwaves," 4,345,202, 1982.

[343] L. L. Nagy, "Apparatus and method for sensing particle and water concentrations in a medium," US 2004/0135585 A1, 2004.

[344] C. Collister, "Electrical measurement of oil quality," US 6,459,995, 2002.

[345] E. Aguilera Bermudez and O. Rodriguez Rico, "Measurement of Complex Dielectric Permittivity in Oils from High-Voltage Transformes Using a Coaxial Probe," *TECCIENCIA*, vol. 11, no. 21, pp. 61–67, Sep. 2016.

[346] Y. Zhang, M. Adam, A. Hart, J. Wood, S. P. Rigby, and J. P. Robinson, "Impact of Oil Composition on Microwave Heating Behavior of Heavy Oils," *Energy and Fuels*, vol. 32, no. 2, pp. 1592–1599, 2018.

[347] R. Correa, G. Gonzalez, and V. Dougar, "Emulsion polymerization in a microwave reactor," *Polymer (Guildf).*, vol. 39, no. 6–7, pp. 1471–1474, Jan. 1998.

[348] S. Foster, *Domestic Mixed Plastics Packaging Waste Management Options*, no. June 2008. 2008.

[349] V. V Komarov, *Handbook of dielectric and thermal properties of materials at microwave frequencies*. Artech house, 2012.

[350] S. Bradshaw *et al.*, "Techno-economic considerations in the commercial microwave processing of mineral ores," *J. Microw. Power Electromagn. Energy*, vol. 40, no. 4, pp. 228–240, 2007.

[351] Y. Wang and N. Djordjevic, "Thermal stress FEM analysis of rock with microwave energy," *Int. J. Miner. Process.*, vol. 130, pp. 74–81, 2014.

[352] J. G. Kretzschmar, "Maximum Longitudinal Electric Field in Hollow Cylindrical Cavities with Elliptical Cross-Section," *J. Microw. Power*, vol. 7, no. 1, pp. 35–42, Jan. 1972.

[353] S. Fujii *et al.*, "Chemical Reaction under Highly Precise Microwave Irradiation," *J. Microw. Power Electromagn. Energy*, vol. 48, no. 2, pp. 89–103, Jan. 2014.

[354] N. Haneishi, S. Tsubaki, M. M. Maitani, E. Suzuki, S. Fujii, and Y. Wada, "Electromagnetic and Heat-Transfer Simulation of the Catalytic Dehydrogenation of Ethylbenzene under Microwave Irradiation," *Ind. Eng. Chem. Res.*, vol. 56, no. 27, pp.

7685–7692, 2017.

[355] Shan-Jie Zhang and Yao-Chun Shen, “Eigenmode sequence for an elliptical waveguide with arbitrary ellipticity,” *IEEE Trans. Microw. Theory Tech.*, vol. 43, no. 1, pp. 227–230, 1995.

[356] J. C. Gutiérrez-Vega, R. M. Rodríguez-Dagnino, M. A. Meneses-Nava, and S. Chávez-Cerda, “Mathieu functions, a visual approach,” *Am. J. Phys.*, vol. 71, no. 3, pp. 233–242, Mar. 2003.

[357] T. V. Davies and N. W. McLachlan, “Theory and Application of Mathieu Functions,” *Math. Gaz.*, vol. 31, no. 297, p. 300, 1947.

[358] Z. L. Mei and F. Y. Xu, “A simple, fast and accurate method for calculating cutoff wavelengths for the dominant mode in elliptical waveguide,” *J. Electromagn. Waves Appl.*, vol. 21, no. 3, pp. 367–374, 2007.

[359] D. L. Young, S. P. Hu, C. W. Chen, C. M. Fan, and K. Murugesan, “Analysis of elliptical waveguides by the method of fundamental solutions,” *Microw. Opt. Technol. Lett.*, vol. 44, no. 6, pp. 552–558, 2005.

[360] Y. Wang and N. Djordjevic, “Thermal stress FEM analysis of rock with microwave energy,” *Int. J. Miner. Process.*, vol. 130, pp. 74–81, 2014.

[361] M. T. Sebastian, R. Ubic, and H. Jantunen, “Low-loss dielectric ceramic materials and their properties,” *Int. Mater. Rev.*, vol. 60, no. 7, pp. 392–412, 2015.

[362] “EIA RF Connectors.” [Online]. Available: http://www.wikiwand.com/en/EIA_RF_Connectors. [Accessed: 02-Dec-2018].

[363] A. L. Drozd, “Selected methods for validating computational electromagnetic modeling techniques,” *IEEE Int. Symp. Electromagn. Compat.*, vol. 1, pp. 301–306, 2005.

[364] J. F. Gerling, “Waveguide Components and Configurations for Optimal Performance in Microwave Heating Systems.” Gerling Applied Enineering, Inc., pp. 1–8, 2000.

[365] Sairem, “Solid State Microwave generator 450W at 2450 MHz.” .

[366] Sairem, “Solid State 915 MHz Microwave Generator 600W.” .

[367] Sairem, “100 kW 915 MHz Microwave Generator.” .

[368] J. F. Gerling and G. Fournier, “Techniques to improve the performance of microwave process systems which utilize high Q cavities,” in *Ceramics transactions 21*, 1991.

[369] EDEM, “EDEM 2.5 Theory Reference Guide.”

[370] S. O. Nelson, “Dielctric Property Measurements and Techniques Useful Relationships Between Dielectric Properties and Bulk Density,” *Am. Inst. Chem. Eng. Annu.*, pp. 136–140, 2004.

[371] Merrick, “Weight belt feeders.” [Online]. Available: http://merrick-inc.com/weigh_belt_feeder. [Accessed: 10-Jun-2016].

[372] D. A. Lelonis, J. W. Tereshko, and C. M. Andersen, “Boron Nitride Powder Alternative for Solid Lubrication,” *GE advanced ceramics*. .

[373] R. M. Nedderman, U. Tüzün, S. B. Savage, and G. T. Houlsby, “The flow of granular

materials—I," *Chem. Eng. Sci.*, vol. 37, no. 11, pp. 1597–1609, Apr. 1982.

[374] K. Mamtani, "Effect of particle shape on hopper discharge rate," The university of Florida, 2011.

[375] G. G. Chase, "Solids notes 10." University of Akron.

[376] H. Heywood, "Calculation of the Specific Surface of a Powder," *Proc. Inst. Mech. Eng.*, vol. 125, no. 1, pp. 383–459, Jun. 1933.

[377] P. Arnold, "Determining the Geometry of Mass-Flow Bins Some Important Considerations," in *11th International Conference on Bulk Materials Storage, Handing and Transportation Australia*, 2013, no. July.

[378] K. Decker, M. Egger, A. Haber, and C. Pillichshammer, "Drive Power of a Discharge Belt Conveyor – Comparison of Calculation, Simulation and Measurement," *FME Trans.*, pp. 272–278, 2016.

[379] J. G. de Gijt and M. L. Broeken, *Quay Walls*, Second Edi. CRC Press, 2013.

[380] P. Kulinowski and P. Kasza, "Properties Bulk Solids." Department of Mining, Dressing and Transport Machines AGH, pp. 1–11, 2014.

[381] K. M. Winter, J. Kalucki, and D. Koshel, *Process technologies for thermochemical surface engineering*. Woodhead Publishing Limited, 2014.

[382] Torftech, "Application Description - Vermiculite Exfoliation," 2015.

[383] F. J. Smith, "Microwave fluidized bed dryer," US 3,528,179, 1970.

[384] J. Manser and G. Dankesreiter, "Method and apparatus for bulk material treatment," US 4,126,945, 1978.

[385] Z. H. Wang and G. Chen, "Theoretical Study of Fluidized-Bed Drying with Microwave Heating," *Ind. Eng. Chem. Res.*, vol. 39, no. 3, pp. 775–782, Mar. 2000.

[386] A. Reyes, S. Cerón, R. Zúñiga, and P. Moyano, "A comparative study of microwave-assisted air drying of potato slices," *Biosyst. Eng.*, vol. 98, no. 3, pp. 310–318, Nov. 2007.

[387] D. Zare and M. Ranjbaran, "Simulation and Validation of Microwave-Assisted Fluidized Bed Drying of Soybeans," *Dry. Technol.*, vol. 30, no. 3, pp. 236–247, Mar. 2012.

[388] G. R. Askari, Z. Emam-Djomeh, and S. M. Mousavi, "Heat and mass transfer in apple cubes in a microwave-assisted fluidized bed drier," *Food Bioprod. Process.*, vol. 91, no. 3, pp. 207–215, Jul. 2013.

[389] M. H. Khoshtaghaza, H. Darvishi, and S. Minaei, "Effects of microwave - fluidized bed drying on quality, energy consumption and drying kinetics of soybean kernels," *J. Food Sci. Technol.*, vol. 52, no. 8, pp. 4749–4760, Aug. 2015.

[390] X. Hu, J. Kurian, Y. Gariepy, and V. Raghavan, "Optimization of microwave-assisted fluidized-bed drying of carrot slices," *Dry. Technol.*, vol. 35, no. 10, pp. 1234–1248, Jul. 2017.

[391] A. G. Whittaker and D. M. P. Mingos, "Microwave-assisted solid-state reactions involving metal powders and gases," *J. Chem. Soc. Dalt. Trans.*, no. 16, p. 2541, 1993.

[392] J. M. Tranquilla, “Method and apparatus for optimization of energy coupling for microwave treatment of metal ores and concentrates in a microwave fluidized bed reactor,” US 6,074,533, 2000.

[393] J. Tranquilla, “Method and apparatus for microwaveinduced pyrolysis of arsenical ores and ore concentrates,” US 2008/0069746 A1, 2008.

[394] A. A. Salema and F. N. Ani, “Microwave induced pyrolysis of oil palm biomass,” *Bioresour. Technol.*, vol. 102, no. 3, pp. 3388–3395, Feb. 2011.

[395] M. Adam, “Understanding Microwave Pyrolysis of Biomass Materials,” University of Nottingham, 2017.

[396] M. Willert-Porada, A. Rosin, A. Schmidt, T. Gerdes, and M. Adam, “Analysis of microwave heating in a fluidized bed reactor,” in *2014 IEEE MTT-S International Microwave Symposium (IMS2014)*, 2014, pp. 1–4.

[397] E. P. Lynch, “Use of microwave energy in conjunction with fluidized bed reactors,” Argonne National Lab., Ill.(USA), 1977.

[398] H. Y. Kim *et al.*, “Fluidized bed reactor heated by microwaves,” US 5,382,412, 1995.

[399] D. Zare and M. Ranjbaran, “Simulation and Validation of Microwave-Assisted Fluidized Bed Drying of Soybeans,” *Dry. Technol.*, vol. 30, no. 3, pp. 236–247, Mar. 2012.

[400] J. Shu, V. . Lakshmanan, and C. . Dodson, “Hydrodynamic study of a toroidal fluidized bed reactor,” *Chem. Eng. Process. Process Intensif.*, vol. 39, no. 6, pp. 499–506, Nov. 2000.

[401] G. A. Wellwood, “Hydrodynamic behaviour of the Torbed(r) reactor operating in fine particle mode,” University of Queensland, 2000.

[402] J. Shu, V. . Lakshmanan, and C. . Dodson, “Hydrodynamic study of a toroidal fluidized bed reactor,” *Chem. Eng. Process. Process Intensif.*, vol. 39, no. 6, pp. 499–506, Nov. 2000.

[403] T. Fouilland, J. R. Grace, and N. Ellis, “Recent advances in fluidized bed technology in biomass processes,” *Biofuels*, vol. 1, no. 3, pp. 409–433, 2010.

[404] P. E. Mason, L. I. Darvell, J. M. Jones, and A. Williams, “Comparative Study of the Thermal Conductivity of Solid Biomass Fuels,” *Energy and Fuels*, vol. 30, no. 3, pp. 2158–2163, 2016.

[405] J. M. Herrin and D. Demirig, “Thermal conductivity of U . S . coals Subbituminous Coal Lignite Bituminous Coal,” *J. Geophys. Res.*, vol. 101, pp. 381–386, 1996.

[406] A. E. Ramazanova, I. M. Abdulagatov, and P. G. Ranjith, “Temperature Effect on the Thermal Conductivity of Black Coal,” *J. Chem. Eng. Data*, vol. 63, no. 5, pp. 1534–1545, 2018.

[407] N. S. Srinivasan, “Reduction of iron oxides by carbon in a circulating fluidized bed reactor,” *Powder Technol.*, vol. 124, no. 1–2, pp. 28–39, 2002.

[408] J. L. Schenk, “Recent status of fluidized bed technologies for producing iron input materials for steelmaking,” *Particuology*, vol. 9, no. 1, pp. 14–23, 2011.

[409] M. Komatina and H.-W. Gudenau, “The Sticking Problem during Direct Reduction of

Fine Iron Ore in the Fluidized Bed," *Metal. Metall.*, pp. 309–328, 2004.

[410] J. F. Gransden and J. S. Sheasby, "The sticking of iron ore during reduction by hydrogen in a fluidized bed," *Can. Metall. Q.*, vol. 13, no. 4, pp. 649–657, 1974.

[411] T. Zhang, C. Lei, and Q. Zhu, "Reduction of fine iron ore via a two-step fluidized bed direct reduction process," *Powder Technol.*, vol. 254, pp. 1–11, 2014.

[412] M. Groszek and B. Laughllin, "Torbed compact bed reactor (CBR)," *Technology Description*. .

[413] M. F. B. and V. R. R. K.V. Vinod, "Study of the Fluid Dynamic Performance of Distributor Type in Torbed Type Reactors," *Eng. e-Transaction*, vol. 6, no. 1, pp. 70–75, 2011.

[414] F. A. L. Dullien, *Porous media: fluid transport and pore structure*. Academic press, 2012.

[415] S. Ebadi and K. Forooraghi, "An annular waveguide slot antenna," *IEEE Antennas Wirel. Propag. Lett.*, vol. 6, no. 1, pp. 525–528, 2007.

[416] C. William *et al.*, "A Slotted-Waveguide Array for High-Power Microwave Transmission," 2001.

[417] T. Ha and R. Canfield, "Design Optimization of a WR-90 Slotted Waveguide Antenna Stiffened Structures," *52nd AIAA/ASME/ASCE/AHS/ASC Struct. Struct. Dyn. Mater. Conf.*, no. April, pp. 1–12, 2011.

[418] A. Johannes and N. Maritz, "Investigation and Design of a Slotted Waveguide Antenna with Low 3D by," no. March, 2010.

[419] H. M. El Misilmani, M. Al-husseini, and K. Y. Kabalan, "Design of Slotted Waveguide Antennas with Low Sidelobes for High Power Microwave Applications," *Prog. Electromagn. Res. C*, vol. 56, no. January, pp. 15–28, 2015.

[420] R. K. Enjiu and M. B. Perotoni, "Slotted Waveguide Antenna Design Using 3D EM Simulation," no. July, 2013.

[421] B. N. Das, J. Ramakrishna, and B. K. Sarap, "Resonant Conductance of Inclined Slots in the Narrow Wall of a Rectangular Waveguide," *IEEE Trans. Antennas Propag.*, vol. 32, no. 7, pp. 759–761, 1984.

[422] H. S. Uhm, S. J. Jung, and H. S. Kim, "Influence of Gas Temperature on Electrical Breakdown in Cylindrical Electrodes," *J. Korean Phys. Soc.*, vol. 42, no. February, pp. 989–993, 2003.

[423] S. S. Sekretarov and D. M. Vavriv, "A wideband slotted waveguide antenna array for SAR systems," *Prog. Electromagn. Res. M*, vol. 11, pp. 165–176, 2010.

[424] P. Wade, *The W1GHZ Online Microwave Antenna Book*. .

[425] J. F. Gerling and G. Fournier, "Techniques to improve the performance of microwave process systems which utilize high Q cavities," GERLING LABS MODESTO CA, 1992.

[426] D. K. Panda and A. Chakraborty, "Design and Simulation of Matched E-Plane Tee," *Int. J. Appl. Eng. Res.*, vol. 10, no. 9, pp. 24681–24691, 2015.

[427] G. Huang, S. Zhou, and T. Chio, "Development of a Symmetric Waveguide T-Junction

Power Divider with Equal-Phase Characteristic," *ACES J.*, vol. 31, no. 3, pp. 309–314, 2016.

[428] Universalmetaltek, "Laminar flow." [Online]. Available: http://www.universalmetaltek.com/industries/laminar-flow/. [Accessed: 01-Feb-2019].

[429] EMCEMI, "EMI shielding aluminium honeycomb ventilation panels." [Online]. Available: https://emcemi.com/product/emi-shielding-aluminium-honeycomb-ventilation-panels/. [Accessed: 02-Jan-2019].

[430] Thorlabs, "Optical substrates." [Online]. Available: https://www.thorlabs.com/newgrouppage9.cfm?objectgroup_id=6973. [Accessed: 15-Feb-2019].

[431] Shalom EO, "Germanium windows for thermal imaging." [Online]. Available: http://shalomeo.com/product/thermal-imaging/ir-windows/ge-windows-5.html. [Accessed: 12-Feb-2019].

[432] Bratney Companies, "Material Handling." [Online]. Available: https://www.bratney.com/equipment/material-handling/. [Accessed: 20-Jan-2019].

[433] Beumer Group, "Advances in Conveyor Technology." .

[434] K. P. Shah, "Construction and Maintenance of Belt Conveyors for Coal and Bulk Material Handling Plants," no. April. pp. 1–269, 2018.

[435] Metso, *Metso Conveyor Solutions Handbook*. 2016.

[436] Yokohama, "Compounds." [Online]. Available: http://www.y-yokohama.com/global/product/mb/conveyor-belts/compounds/. [Accessed: 03-Feb-2017].

[437] Contitech, "Contiflex Vulkan." [Online]. Available: http://www.contitech.de/pages/produkte/transportbaender/cbgindustry/industry_textil_contiflexvulkan_en.html. [Accessed: 03-Feb-2017].

[438] J. E. Gerling, "Metal Roller Conveyor for Microwave Ovens," US3772491, 1973.

[439] M. R. Jeppson, "Conveyorized Microwave Heating Chamber with Dielectric Wall Structure," US4570045, 1986.

[440] C. Marzat, "Microwave Application Device, Particularly for Baking Products on a Metal Carrier," US6153868, 2000.

[441] S. Tastavin, "Microwave treatment device particularly for food products," EP20100306460, 2011.

[442] George M. Harris, "Apparatus and Method for Microwave Heating Using Metallic Conveyor Belt," US20070068939 A1, 2007.

[443] M. R. Shute, P. N. Daines, and R. J. Meredith, "Microwave Ovens Having Conductive Conveyor Band and Applicator Launch Section to Provide Parallel Plate Electric Field," US5457303, 1995.

[444] C. I. Chung, *Extrusion of Polymers Theory & Practice*, Second edi. Hanser Gardner Publications, 2010.

[445] Nabertherm, "Thermal Process Technology / Furnaces for Continuous Processes."

[Online]. Available: https://www.nabertherm.com/produkte/details/en/thermprozesstechnik_1-oefen-fuer. [Accessed: 06-Jun-2018].

[446] Z. Peng *et al.*, “Microwave absorption characteristics of anthracite during pyrolysis,” *Fuel Process. Technol.*, vol. 150, pp. 58–63, 2016.